

---

---

# Assessment of thermally activated dislocation mechanisms via novel indentation approaches

---



TECHNISCHE  
UNIVERSITÄT  
DARMSTADT

**Department of Materials and Earth Science  
Technical University of Darmstadt**

Dissertation approved in fulfilment of the requirements  
for the degree of Doctor of Engineering / Doktor Ingenieur

(Dr.-Ing.)

**M.Sc. Christian Stefan Minnert**

1st Referee:

Prof. Dr. Karsten Durst

2nd Referee:

Prof. Dr. Johann Michler

**Darmstadt 2022**

---



---

---

Assessment of thermally activated dislocation mechanisms via novel indentation approaches

Bestimmung von thermisch aktivierten Versetzungsmechanismen durch neuartige  
Indentierungsmethoden

Genehmigte kumulative Dissertation, vorgelegt von M.Sc. Christian Stefan Minnert

Fachbereich Material- und Geowissenschaften, Technische Universität Darmstadt

Hauptberichterstatter: Prof. Dr. Karsten Durst

Nebenberichterstatter: Prof. Dr. Johann Michler

Tag der Einreichung: 30.05.2022

Tag der Prüfung: 28.07.2022

Veröffentlicht unter CC BY-NC-ND 4.0 International



---

---

## **Declaration of authorship**

---

I herewith formally declare that I, Christian Stefan Minnert, have written the submitted thesis independently pursuant to § 22 paragraph 7 of APB TU Darmstadt. I did not use any outside support except for the quoted literature and other sources mentioned in the thesis. I clearly marked and separately listed all of the literature and all of the other sources which I employed when producing this academic work, either literally or in content. This thesis has not been handed in or published before in the same or similar form.

In the submitted thesis, the written copies and the electronic version for archiving are pursuant to § 23 paragraph 7 of APB identical in content.

Darmstadt, 30.05.2022

---

(Christian Stefan Minnert)



---

---

## Table of contents

---

<b>Declaration of authorship</b>	<b>III</b>
<b>Table of contents</b>	<b>V</b>
<b>Acknowledgements</b>	<b>VII</b>
<b>Complete list of publications</b>	<b>IX</b>
<b>List of abbreviations and symbols</b>	<b>XI</b>
<b>1. Introduction</b>	<b>1</b>
1.1. Motivation	1
1.2. Objectives	3
<b>2. Thermally activated deformation mechanisms</b>	<b>5</b>
2.1. Peierls barrier	6
2.1.1. Brittle-to-ductile transition	8
2.2. Dislocation glide and annihilation	9
2.3. Creep	10
<b>3. Macroscopic test approaches</b>	<b>13</b>
3.1. Strain rate jump experiment	13
3.2. Uniaxial creep experiment	14
<b>4. Depth-sensing indentation testing</b>	<b>17</b>
4.1. Depth-sensing indentation testing instrument	18
4.2. Contact stiffness	19
4.3. Loading protocols	23
4.3.1. Constant strain rate method	24
4.3.2. Cyclic loading method	25
4.3.3. Continuous stiffness measurement technique	25
4.3.4. Strain rate jump method	26
4.3.5. Constant load hold method	27
4.3.6. Constant displacement and stiffness methods	28

---

4.3.7.	High strain rate testing	29
4.4.	Correlation of small-scale and macroscopic experiments	29
4.5.	Size effects	32
4.5.1.	Pop-in	32
4.5.2.	Indentation size effect	32
4.6.	High temperature indentation testing	33
4.6.1.	Thermal drift and temperature management	35
4.6.2.	Environmental effects	36
4.6.3.	Indenter materials and tip wear	36
<b>5.</b>	<b>List of selected publications</b>	<b>39</b>
<b>6.</b>	<b>Synopsis of publications</b>	<b>43</b>
6.1.	Transient indentation testing – method development	43
6.1.1.	Long-term constant contact pressure creep testing	45
6.1.2.	Step load and hold test protocol	56
6.2.	New in-situ high temperature indentation system	58
6.2.1.	Temperature verification and matching	60
6.2.2.	Reference measurements on CG Mo	63
6.2.3.	Tip wear and thermal expansion	64
6.3.	High temperature indentation testing – transient material behavior	66
6.3.1.	Thermally activated dislocation motion in bcc Mo	66
6.3.2.	Indentation creep testing at ultra-high temperatures	70
<b>7.</b>	<b>Summary and conclusion</b>	<b>73</b>
<b>8.</b>	<b>Outlook</b>	<b>77</b>
<b>9.</b>	<b>References</b>	<b>79</b>
<b>10.</b>	<b>Cumulative part of the thesis</b>	<b>93</b>
10.1.	Statement of personal contribution	93
10.2.	Relevant full-text reprints	95

---

---

## Acknowledgements

---

I would like to thank all the people who have directly or indirectly contributed to the success of my PhD thesis.

First and foremost, I would like to thank my supervisor and referee **Prof. Dr. Karsten Durst** for his continuous support, the valuable discussions and the freedom in research that I enjoyed during my time as a PhD student in his research group.

Moreover, I gratefully acknowledge the co-referee **Prof. Dr. Johann Michler**, as well as the further members of the examination committee, **Prof. Dr. Matthias Oechsner** and **Prof. Dr. Jürgen Rödel**.

I would also like to sincerely thank all my colleagues in the **Physical Metallurgy group** for the constructive, pleasant and often very lighthearted working atmosphere. I have enjoyed the time very much. My special thanks to “**die Jungs**” – **Tom Keil, Sebastian Bruns** and **Paul Braun** for fruitful discussions and the shared experiences on and off the job.

Additionally, I express my gratitude to **Dr. Warren Oliver, John Swindeman, Dr. Kurt Johanns, Rich Anthony, Sam Bacon, Chris Rollins, Mike Drake** and all the others of the **Nanomechanics Inc./KLA Instruments team** for their warm welcome, as well as their great support and helpful discussions during the construction and commissioning of the HT indenter in Oak Ridge and Darmstadt.

My heartfelt thanks go to my **family and friends** who have supported and motivated me all the time.

Finally, research can only proceed successfully, if it is adequately funded. I would therefore like to gratefully acknowledge **Deutsche Forschungsgemeinschaft (DFG)** for its financial support within the framework of the project no. 326946902 “*Indentation creep: New machine and test methodology development at various length scales, high temperatures and low deformation rates*”.



---

---

## Complete list of publications

---

1. **Minnert, C.**, Kuhnt, M., Bruns, S., Marshal, A. Pradeep, K., Marsilius, M., Bruder, E. and Durst, K., *Study on the embrittlement of flash annealed Fe<sub>85.2</sub>B<sub>9.5</sub>P<sub>4</sub>Cu<sub>0.8</sub>Si<sub>0.5</sub> metallic glass ribbons*. *Materials & Design*, 2018. **156**: p. 252-261. DOI: 10.1016/j.matdes.2018.06.055.
2. Prach, O., **Minnert, C.**, Johanns, K. and Durst, K., *A new nanoindentation creep technique using constant contact pressure*. *Journal of Materials Research*, 2019. **34**(14): p. 2492-2500. DOI: 10.1557/jmr.2019.188.
3. Bruns, S., Petho, L., **Minnert, C.**, Michler, J. and Durst, K., *Fracture toughness determination of fused silica by cube corner indentation cracking and pillar splitting*. *Materials & Design*, 2020. **186**: p. 108311. DOI: 10.1016/j.matdes.2019.108311.
4. **Minnert, C.**, Oliver, W.C. and Durst, K., *New ultra-high temperature nanoindentation system for operating at up to 1100 °C*. *Materials & Design*, 2020. **192**: p. 108727. DOI: 10.1016/j.matdes.2020.108727.
5. Fang, X., Ding, K., Janocha, S., **Minnert, C.**, Rheinheimer, W., Frömling, T., Durst, K., Nakamura, A. and Rödel, J., *Nanoscale to microscale reversal in room-temperature plasticity in SrTiO<sub>3</sub> by tuning defect concentration*. *Scripta Materialia*, 2020. **188**: p. 228-232. DOI: 10.1016/j.scriptamat.2020.07.033.
6. Fang, X., Ding, K., **Minnert, C.**, Nakamura, A. and Durst, K., *Dislocation-based crack initiation and propagation in single-crystal SrTiO<sub>3</sub>*. *Journal of Materials Science*, 2021. **56**(9): p. 5479-5492. DOI: 10.1007/s10853-020-05587-2<sup>1</sup>.
7. **Minnert, C.**, ur Rehman, H. and Durst, K., *Thermally activated dislocation mechanism in Mo studied by indentation, compression and impact testing*, *Journal of Materials Research*, 2021: p. 1-11. DOI: 10.1557/s43578-021-00126-4.
8. Stich, S., Ding, K., Muhammad, Q. K., Porz, L., **Minnert, C.**, Rheinheimer, W., Durst, K., Rödel, J., Frömling, T. and Fang, X., *Room temperature dislocation plasticity in SrTiO<sub>3</sub> tuned by defect chemistry*. *Journal of the American Ceramic Society*, 2022. **105**(2): p. 1318-1329. DOI: 10.1111/jace.18118.
9. **Minnert, C.** and Durst, K., *Nanoindentation creep testing: Advantages and limitations of the constant contact pressure method*. *Journal of Materials Research*, 2022. **37**(2): p. 567-579. DOI: 10.1557/s43578-021-00445-6.
10. Zhan, Y., Li, W., Grottenmüller, R., **Minnert, C.**, Krasemann, T., Wen, Q. and Riedel, R., *Rapid curing of polysilazane coatings at room temperature via chloride-catalyzed hydrolysis/condensation reactions*, *Progress in Organic Coatings*, 2022. **167**: p. 106872. DOI: 10.1016/j.porgcoat.2022.106872.

---

<sup>1</sup> Awarded the "2021 Robert W. Cahn Prize" of the *Journal of Materials Science*.

- 
11. Keil, T., **Minnert, C.**, Bruder, E. and Durst, K., *Solid solution hardening effects on structure evolution and mechanical properties of nanostructured binary and high entropy alloys after high pressure torsion*, IOP Conference Series: Microstructural variability: Processing, analysis, mechanisms and properties (42<sup>nd</sup> Risø International Symposium), 2022. Accepted for publication.

---

---

## List of abbreviations and symbols

---

### Latin characters and abbreviations

$A_c$	contact area
$b$	Burgers vector
bcc	body centered cubic
BDT	brittle-to-ductile transition
BDTT	brittle-to-ductile transition temperature
BSE	backscattered electron
$C$	constraint factor
$C_f$	load frame compliance
$C_{sys}$	system compliance
CCP	constant contact pressure
CCS	constant contact stiffness
CDH	constant displacement hold
CG	conventionally grained
CLH	constant load hold
CSM	continuous stiffness measurement
CSR	constant strain rate
$d$	slip plane distance
$d_{GS}$	grain size
$d_K$	kink distance
$D_i$	damping coefficient of the instrument
$D_C$	damping coefficient of sample/contact
$D_0$	amplitude of the dynamic load (CSM)
DSI	depth-sensing indentation testing
$E$	Young's modulus
$E_i$	Young's modulus of indenter material
$E_r$	reduced modulus
$f_0$	frequency constant for kink-pair nucleation
$f_0^*$	frequency constant for kink velocity

---

$F$	reduced contact pressure
$G$	shear modulus
$G'$	pre-exponential factor for activation energy
GND	geometrically necessary dislocation
$h$	indentation depth
$\dot{h}$	displacement rate
$h^*$	characteristic length
$h_c$	contact depth
$h_f$	residual penetration depth
$h_K$	kink height
$h_{max}$	maximum penetration depth
$h_0$	amplitude of the dynamic displacement (CSM)
$H$	hardness
$\dot{H}$	time derivative of hardness
$H_0$	macroscopic hardness
HK	Knoop hardness
HT	high temperature
HV	Vickers hardness
ISE	indentation size effect
$k$	pile-up/sink-in parameter
$k_B$	Boltzmann constant
$K_F$	frame stiffness
$K_{i,j}$	material's constants for Norton's creep law
$K_S$	spring stiffness of the column support springs
$m$	strain rate sensitivity coefficient
$m_i$	moving mass of the indenter
$M$	Taylor factor
$n$	stress exponent
$\dot{N}_{KP}$	kink-pair nucleation rate
NC	nanocrystalline
$p_m$	mean contact pressure
$P$	load
$\dot{P}$	loading rate

---

---

$P_{AC0}$	dynamic load component
$P_{DC}$	mean load component
$Q$	activation energy
$Q_c$	activation energy for creep
$Q_N$	kink-pair nucleation energy
$Q_m$	energy for kink migration
$r_c$	contact radius
$R$	universal gas constant
RT	room temperature
$S$	contact stiffness
SE	secondary electron
SLH	step load and hold
SRJ	strain rate jump
SRS	strain rate sensitivity
SSD	statistically stored dislocation
SX	single crystalline
$T$	absolute temperature
$T_{int}$	intersection temperature
$T_k$	knee temperature
$T_m$	melting temperature
$T_{sample}$	sample temperature
$T_{tip}$	temperature of the indenter tip
TBC	thermal barrier coating
UFG	ultra-fine grained
$v_D$	dislocation velocity
$v_K$	kink velocity
$V$	activation volume
$V_{plast}$	volume of plastic zone

### Greek symbols

$\alpha$	geometric constant
$\beta$	geometry correction factor

---

$\dot{\gamma}$	shear deformation rate
$\dot{\gamma}_0$	pre-exponential factor of Orowan equation
$\Delta G$	energy barrier for dislocation motion
$\epsilon$	geometrical constant
$\dot{\epsilon}$	strain rate
$\epsilon_0$	initial strain
$\dot{\epsilon}_c$	creep strain rate
$\dot{\epsilon}_{ind}$	indentation strain rate
$\dot{\epsilon}_r$	representative strain rate
$\dot{\epsilon}_{rel}$	relaxation strain rate
$\dot{\epsilon}_s$	steady state strain rate
$\zeta_i$	geometric constants
$\nu$	Poisson's ratio
$\nu_i$	Poisson's ratio indenter material
$\rho_{GND}$	density of geometrically necessary dislocations
$\rho_K$	kink density
$\rho_m$	mobile dislocation density
$\rho_{SSD}$	density of statistically stored dislocations
$\sigma$	stress
$\sigma^*$	thermal component of the yield strength
$\sigma_a$	athermal component of the yield strength
$\sigma_c$	cleavage strength
$\sigma_r$	representative stress
$\sigma_y$	yield strength
$\tau$	shear stress
$\tau_P$	Peierls force
$\varphi$	inclined face angle
$\phi$	phase angle between force and displacement signals
$\omega$	oscillation frequency of the dynamic displacement (CSM)

---

---

## 1. Introduction

---

### 1.1. Motivation

Climate change is one of the major challenges facing our society today. The emission of greenhouse gases must be stopped or at least drastically reduced in order to keep the impact on nature, society and economy, as well as the associated costs as low as possible [1]. One starting point to achieve this is to further increase the efficiency of jet engines and gas turbines for mobile and stationary applications. Increasing the efficiency of a 1000 MW gas power plant by 1% leads to a reduction in CO<sub>2</sub> emissions of 50,000 ton/year and can save millions of US dollars in fuel and CO<sub>2</sub> certificates over the lifetime of the plant [2, 3]. Two important factors affecting efficiency are the turbine inlet temperature and the clearance between the blade tip and the surrounding casing [4, 5].

Raising the turbine inlet temperature leads to an increase in efficiency [3-5]. This is, however, often limited by the materials used due to severe thermo-mechanical stresses on the turbine blades [6]. The combination of single crystalline (SX) Ni-based superalloys with thermal barrier coatings (TBC) and an active cooling of the blades has made it possible to increase the maximum operating temperatures for long-term applications to 1100-1150 °C in the past decades [6-8]. The actual hot gas temperature of state-of-the-art turbines is even higher than the melting temperature of Ni-base alloys [3, 7].

The materials used must not only exhibit a high oxidation and corrosion resistance as well as a high strength at application temperature, but also a high creep resistance, since the gap between the turbine blades and the housing can be less than a millimeter [4, 7]. Creep deformation caused by a high thermo-mechanical loading leads to a lengthening of the blades over the lifetime of the turbine. This is critical since a contact between the blades and the housing causes catastrophic failure. An increase in clearance is accompanied by a reduction in efficiency and is therefore to be avoided.

The development of new high temperature (HT) materials, such as Ni- or Co-based superalloys, MoSi-based alloys, as well as the improvement of TBCs and bond coats, plays therefore an important role in current research e.g. [3, 6, 9-13]. For all these materials, the local mechanical properties at operation temperatures are largely unknown as they cannot be obtained by conventional testing procedures such as compression or tensile tests. However, knowledge of the mechanical properties of individual microstructural constituents, as those found in Ni-based

superalloys (Fig. 1a), or TBC systems is essential for the improvement and development of new HT materials and composites.

The microstructure of precipitation-hardened SX Ni-based superalloys exhibits two phases (Fig. 1a). The cuboidal  $\gamma'$  precipitates (dark structures) are distributed uniformly in the  $\gamma$  matrix (bright lines), the creep behavior is dominated by the properties of the  $\gamma$  phase. The possibilities of its mechanical characterization are, however, very limited due to the small thickness of the  $\gamma$ -channels by a few tens of nm [14].

The depth-sensing indentation (DSI) technique provides the possibility of local mechanical characterization (Fig. 1) and the identification of the active deformation mechanisms e.g. [15-23]. Its application at elevated temperatures is, however, associated with major challenges in terms of thermal drift and tip wear e.g. [24-30].

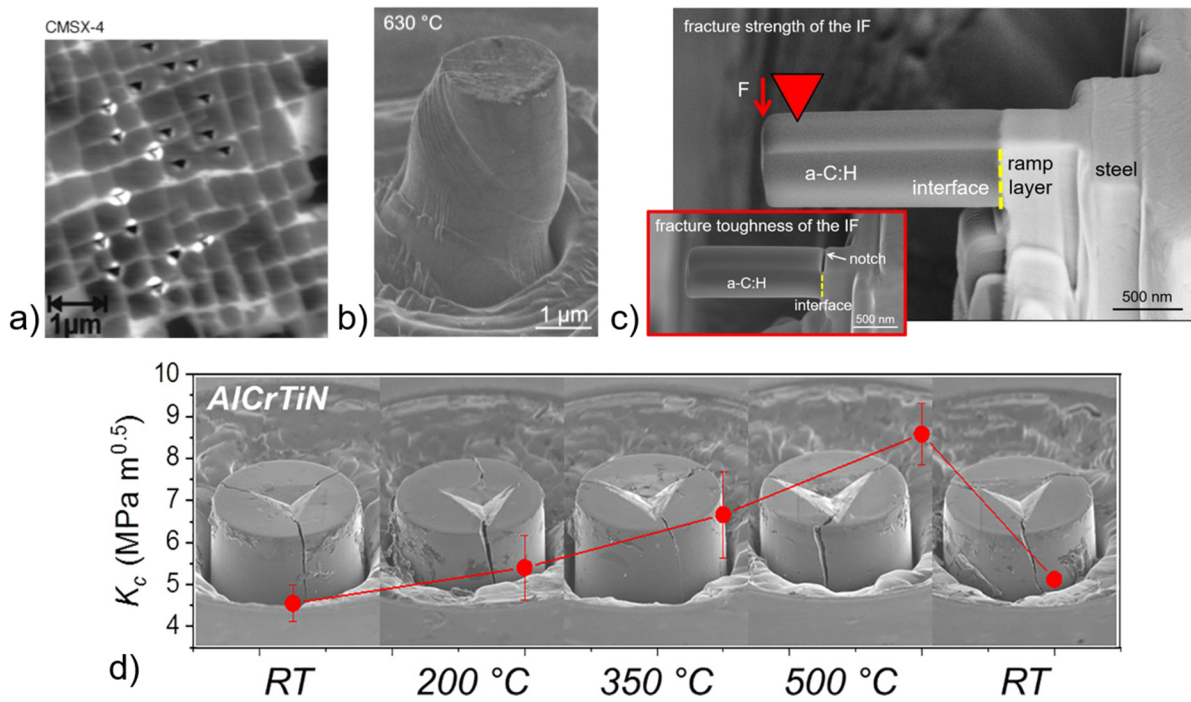


Figure 1: Possible application scenarios of the DSI technique: a) indentation testing of the  $\gamma$ - and  $\gamma'$ - phase of the CMSX-4 Ni-base superalloy [15], b) micropillar compression experiments on the CMSX-4 alloy at 630 °C [21], c) microcantilever testing of the interface strength and toughness between a diamond-like a-C:H layer and a Cr bond coat [23] and d) micropillar splitting experiments for the evaluation of the fracture toughness of ceramic coatings [31]. Reproduced with permission from references [15], [21], [23] and [31], respectively.

---

---

## 1.2. Objectives

This PhD thesis was carried out within the framework of the project “*Indentation creep: New machine and test methodology development at various length scales, high temperatures and low deformation rates*” funded by Deutsche Forschungsgemeinschaft (DFG, project no. 326946902).

In this thesis, the possibilities of depth-sensing indentation testing for studying thermally activated processes is explored, via the development of new experimental approaches and evaluation techniques. Of great importance is the comparability of small-scale and macroscopic mechanical properties, the objectives are therefore twofold:

First, a new depth-sensing indentation system was developed which is able to reliably determine local mechanical properties of high temperature materials such as Ni-based superalloys at or close to their application temperature of  $\leq 1100\text{ °C}$  [32].

Second, new test protocols are to be developed which can be used to study the time, temperature and strain rate ( $\dot{\epsilon}$ ) or stress ( $\sigma$ ) dependent deformation behavior of materials. The focus is particularly on the mechanical properties at elevated temperatures and low deformation rates. Therefore, a new creep method is developed using a constant contact pressure (CCP) approach, similar to conventional uniaxial constant stress and stress dip experiments [33, 34]. Additionally, a new step load and hold (SLH) loading protocol is presented in which the strain rate changes by a factor of  $10^4$  within a few seconds [32]. This allows the determination of material properties over a wide range of strain rates. In consequence, the testing time can be significantly reduced, which is particularly advantageous for testing at high temperatures.

Additional indentation strain rate jump (SRJ) tests are carried out to characterize thermally activated dislocation activity at temperatures close to the brittle-to-ductile transition temperature (BDTT) of body centered cubic (bcc) Mo [35].

The resistance of a material to plastic deformation is related to the active deformation mechanisms, which mechanism is ultimately active depends on the crystal- and microstructure, applied stress, strain rate and temperature. Data from CCP, SLH, and SRJ experiments mentioned above can be used to determine strain rate sensitivity coefficients ( $m$ ) or stress exponents ( $n$ ), but also to calculate activation volumes ( $V$ ) that provide a fingerprint for processes carrying plastic deformation. Therefore, reference experiments were performed on several single phase model materials such as amorphous fused silica, nanocrystalline (NC) and ultra-fine grained (UFG) face centered cubic (fcc) Cu alloys, conventionally grained (CG) bcc

---

Mo and SX fcc Ni. These tests were carried out at temperatures of 20-1100 °C and strain rates ranging from  $10^{-6} - 10^0 \text{ s}^{-1}$ . The new test approaches were finally validated using results from macroscopic experiments as well as literature data.

---

## 2. Thermally activated deformation mechanisms

---

Plastic deformation of crystalline materials is governed by the motion of dislocations or by diffusional processes at elevated temperatures. The activity of both processes is related to the applied load, strain, strain rate and temperature [36]. Therefore, the so-called thermally activated deformation mechanisms play an important role, for instance, in the creep plasticity of UFG and NC metals, but also in the brittle-to-ductile transition (BDT) of bcc metals [36-38].

The macroscopic deformation or strain rate can be correlated with the density ( $\rho_m$ ) and velocity ( $v_D$ ) of mobile dislocations on the active slip systems. This relation is given by the Orowan equation [16, 36, 39]:

$$\dot{\gamma} = b\rho_m v_D = \dot{\gamma}_0 \exp\left(\frac{\Delta G}{k_B T}\right) \quad (1)$$

where  $\dot{\gamma}$  is the applied shear deformation rate,  $b$  the Burgers vector,  $\Delta G$  the energy barrier for dislocation motion,  $k_B$  the Boltzmann constant and  $T$  the absolute temperature. The pre-exponential factor  $\dot{\gamma}_0$  depends on the number of activation sites, the thermally activated vibration frequency and its associated averaged shear strain [40].

Barriers for dislocation motion can be overcome by thermal activation, since the attempt frequency of a dislocation for passing an obstacle is highly temperature dependent. The time available for dislocation motion (i.e. the dislocation velocity) changes with the applied strain rate (Eq. 1). This leads to a strain rate dependence of the resistance to plastic deformation of a material [36-38, 41]. This effect is called strain rate sensitivity (SRS) and is characterized by a strain rate sensitivity coefficient [36]:

$$m = \frac{1}{n} = \frac{1}{T} \frac{\delta \ln \tau}{\delta \ln \dot{\gamma}} \quad (2)$$

where  $\tau$  is the applied shear stress. The activation volume, associated to the number of atoms involved in a deformation process, is defined as [36]:

$$V = k_B T \frac{\partial \ln \dot{\gamma}}{\partial \tau} = k_B T \left( \frac{\partial \ln \rho_m}{\partial \tau} + \frac{\partial \ln v_D}{\partial \tau} \right). \quad (3)$$

Both parameters can be obtained from transient tests such as strain rate jump, creep or relaxation experiments [16, 36] and represent a signature for the respective dominant deformation mechanisms. Strain rate sensitivities in the range of 0.1-1 are discussed for grain boundary sliding or grain rotation processes, whereas  $m$  values below 0.1 are associated with dislocation mediated plasticity [42, 43]. A better understanding of the active deformation mechanisms is provided by the activation volume as  $V$  is normalized by the flow stress.

For fcc metals, activation volumes of  $V > 1000 b^3$  are found for cutting of forest dislocations,  $100 b^3 \leq V \leq 1000 b^3$  are related to dislocation-dislocation interactions and dislocation cross-slip is discussed for  $10 b^3 < V \leq 100 b^3$ . Furthermore, dislocation nucleation processes are related to  $1 b^3 \leq V \leq 10 b^3$ , whereas diffusion controlled processes like Coble or Nabarro-Herring creep (section 2.3) are linked with  $V < 1 b^3$  [20, 42-46].

For bcc metals, small activation volumes ( $V < 20 b^3$ ) are associated with a kink mechanism which is the dominant deformation process at low temperatures. Large  $V$  ( $\sim 200 b^3$ ) are related to dislocation-dislocation interactions as reported for fcc metals [35, 47, 48].

Besides the crystal structure, the SRS is also affected by the grain size ( $d_{GS}$ ), since grain boundaries act as obstacles for dislocation motion causing an additional hardening effect (Hall-Petch strengthening) [49-52] and the possibility of recovery [53, 54]. The strength of fcc metals in the NC ( $d_{GS} < 100$  nm) and UFG ( $100 \leq d_{GS} < 1000$  nm) conditions shows a clear strain rate sensitivity, while CG state ( $d_{GS} \geq 1000$  nm) is mostly strain rate insensitive. For bcc metals, the opposite behavior is observed, i.e.  $m$  decreases with decreasing grain size. This grain size-dependent change in mechanical behavior is related to the activation of different deformation mechanisms [16, 44, 52, 55-62].

## 2.1. Peierls barrier

For metals, dislocation motion across the slip plane can be described by the Peierls model. It is most relevant for the low temperature deformation of bcc metals. The minimum stress, or Peierls force ( $\tau_P$ ), required for moving a single dislocation in the Peierls surface, is given by Equation 4 [63-65]:

$$\tau_P = \frac{2G}{1-\nu} \exp\left(-\frac{2\pi}{(1-\nu)} \frac{d}{b}\right) \quad (4)$$

with shear modulus  $G$ , the slip plane distance  $d$ , Poisson's ratio  $\nu$  and the Burgers vector, which indicates the sliding direction. If the applied force is larger than the Peierls force, the atom moves to the next potential minimum. The crystal segments are then displaced by one Burgers vector. The Peierls force represents a repelling force for dislocation motion and is, thus, responsible for the existence of a yield strength ( $\sigma_y$ ) [63-67].

The Peierls barrier can be overcome in a stepwise manner by forming kinks in the dislocation line. The deformation is then controlled by the nucleation and mobility of kink pairs. The screw dislocation velocity [38]:

$$v_D = \rho_K v_K h_K \quad (5)$$

is related to the steady-state kink density ( $\rho_K$ ), the kink velocity ( $v_K$ ) and its height ( $h_K$ ). The kink-pair nucleation rate ( $\dot{N}_{KP}$ ) shows an Arrhenius type behavior and can be expressed as [38]:

$$\dot{N}_{KP} = f_0 \exp\left(-\frac{Q_N}{k_B T}\right) \quad (6)$$

where  $f_0$  is a frequency constant and  $Q_N$  is the nucleation energy for a kink-pair. The kink velocity is finally given by:

$$v_k = 2d_K f_0^* \sinh\left(\frac{\tau b h_K d_K}{k_B T}\right) \exp\left(-\frac{Q_m}{k_B T}\right) \quad (7)$$

with a frequency constant ( $f_0^*$ ) and the distance ( $d_K$ ) a kink is moving in one step. The energy for kink migration ( $Q_m$ ) is clearly smaller than  $Q_N$  [38].

In contrast to CG fcc metals, the yield strength of bcc metals, depends on the applied strain rate as dislocation motion does not take place along close-packed planes. The Peierls force is therefore comparatively high and clearly more temperature dependent than in the fcc crystal structure [63-65]. This is also the reason why bcc metals exhibit a brittle behavior at low temperatures and a quite ductile behavior at high temperatures. The so-called brittle-to-ductile transition is caused by thermally activated dislocation motion. The temperature at which the BDT takes place is called the brittle-to-ductile transition temperature, which correlates with the applied strain rate [68]. This becomes clear when the attempt frequency of a kink for overcoming the Peierls barrier (Eq. 7) is included in the consideration. The overcoming of barriers is a statistical process which is triggered by the oscillation of a dislocation due to thermal fluctuations that occur with a certain frequency. The number of attempts, thus, depends on the applied strain rate, since at high strain rates the time available for passing the barrier is shorter than at low strain rates [63].

### 2.1.1. Brittle-to-ductile transition

The flow stress of bcc metals is highly temperature and strain rate dependent (Fig. 2). At low temperatures, the plasticity is mainly governed by the mobility of  $a/2 \langle 111 \rangle$  screw dislocations on  $\{110\}$  planes. With increasing temperature, slip along  $\{112\}$  and  $\{123\}$  planes becomes active causing a decrease in  $\sigma_y$  which is given by the sum of an athermal ( $\sigma_a$ ) and a thermal ( $\sigma^*$ ) component [64, 69-74]:

$$\sigma_y = \sigma_a + \sigma^* . \quad (8)$$

Microstructural barriers and long-range internal stresses are responsible for  $\sigma_a$ , whereas  $\sigma^*$  is related to the nucleation and mobility of kink pairs, causing the strain rate dependence. The thermal component and with it  $\sigma_y$  decrease with increasing  $T$  until the knee temperature ( $T_k$ ) is reached (Fig. 2). At  $T_k$ , the thermal component disappears completely ( $\sigma^* = 0$ ) and  $\sigma_y$  becomes almost  $T$  independent. For bcc metals, a knee temperature of about 20% of the melting temperature ( $T_m$ ) is reported, bearing in mind that  $T_k$  also depends on the strain rate applied (Fig. 2) [71, 73-77]. The temperature and strain rate dependence of  $\sigma_y$  leads to a macroscopically brittle behavior at low and a quite ductile behavior at elevated temperatures.

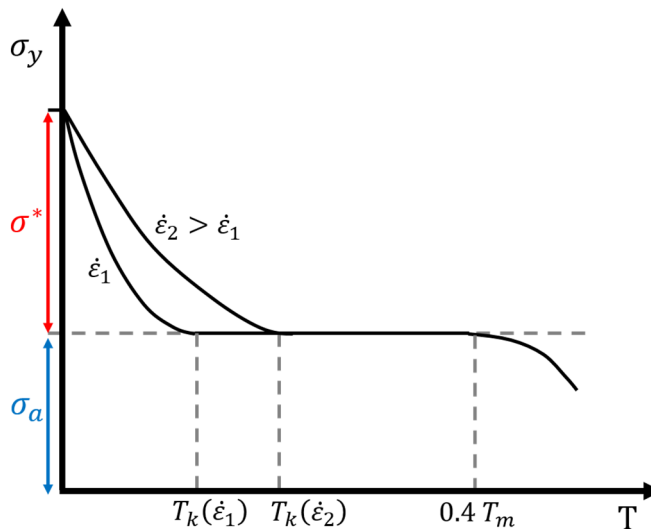


Figure 2: Temperature dependence of the yield strength of bcc metals, adapted from [41].

### Charpy pendulum impact test

The BDT of bcc metals is conventionally studied by Charpy pendulum impact tests. The basic test setup is similar to a three-point bending test but the load is applied abruptly to a notched specimen by impacting a pendulum hammer. The energy absorbed by the specimen is

---

---

determined by the difference in potential energy of the pendulum hammer before and after the impact (minus frictional energy). The absorbed energy increases suddenly in a rather small temperature interval, thus, knowledge of the brittle-to-ductile transition temperature is of great engineering interest. The exact definition of BDTT is challenging and there is no universally applicable definition. Instead, various definitions are used [78].

One approach uses the temperature where a defined absorbed impact energy of e.g. 27 J is measured. According to another definition, BDTT is reached when the absorbed impact energy from the ductile regime drops by 50%. Other definitions are based on a certain shear fracture ratio of 50%, or a certain lateral expansion of e.g. 0.9 mm, for instance [78]. The BDTT is an extrinsic material parameter as it depends on the testing conditions and microstructure of the material [79-81].

## 2.2. Dislocation glide and annihilation

The yield strength of conventional grained fcc metals is clearly less temperature and strain rate dependent than for bcc metals, since dislocation motion in the fcc crystal structure takes place along close packed  $\{111\}\langle 110 \rangle$  slip systems. This results in a similar temperature dependence for bcc and fcc metals for intermediate temperatures, i.e. for temperatures above the knee temperature and below  $0.4 T_m$ , when creep processes become significant (Fig. 2) [41, 65].

A reduction in the grain size of fcc metals leads to both, a strengthening of the material and an increased SRS [52, 82, 83]. The strengthening is caused by an increase in grain boundary density as expressed by the Hall-Petch equation [49, 50]. Dislocations cannot or only to a limited extent be stored inside NC or UFG grains due to their small sizes. In consequence, dislocations are accumulated at high angle grain boundaries. This increases the dislocation generation and annihilation rates significantly and, thus, affects the steady state deformation of the material [84]. Furthermore, the deformation mechanisms are changing with decreasing grain size. For NC and UFG fcc metals, several deformation mechanisms like grain boundary sliding [44, 56, 58, 60, 85-87], grain rotation and grain coalescence [44, 88], shear band formation [44] and stress driven grain boundary migration [89-99] are discussed in literature.

### 2.3. Creep

The term “creep” describes the time-dependent plastic deformation of a material applying a (constant) stress [100-102]. Creep is more pronounced at elevated homologous temperatures of  $>0.4 T_m$  due to thermally activated dislocation glide and climb processes (dislocation creep) as well as enhanced diffusion rates (diffusion creep) [41]. This causes a significant decrease in yield strength as shown in Figure 2.

The different creep mechanisms mentioned above can be summarized in Ashby creep deformation diagrams as schematically illustrated in Figure 3, where the applied stress and temperature are normalized by the shear modulus and melting temperature. The actual diagrams look different for each material as the activation energies of the individual mechanisms are material dependent.

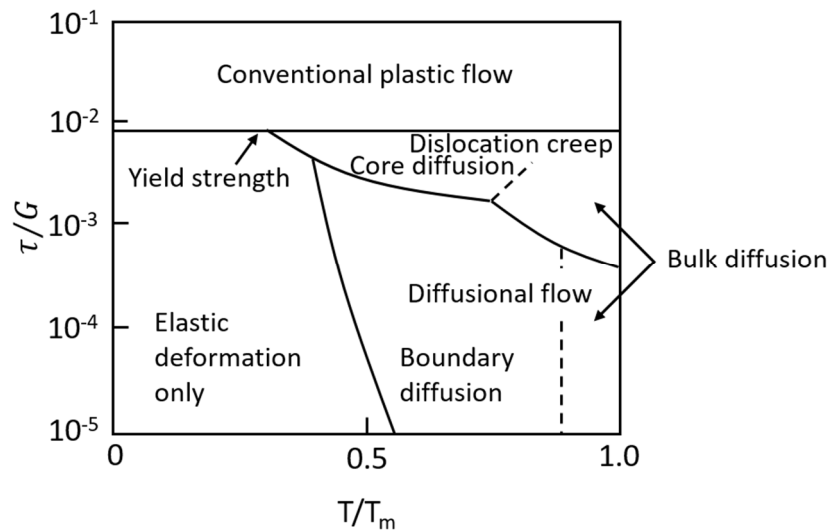


Figure 3: Schematic creep deformation diagram, adapted from [103].

Dislocation creep is associated with dislocation climbing, where obstacles can be overcome at stresses below the flow stress. Diffusion processes cause a vacancy transport from one dislocation (vacancy source) to another dislocation (vacancy sink). Diffusion is temperature dependent and can take place either within a grain (bulk diffusion) or along defects such as dislocations (dislocation core diffusion). Dislocations cause a local distortion of the periodic crystal lattice, this reduces the activation energy required, making dislocation core diffusion preferential at lower temperatures and high stresses. At HT, on the other hand, bulk diffusion is the faster and, therefore, the preferential diffusion path [104].

Thermally activated vacancy flow becomes relevant at high temperatures in addition to vacancy flow-assisted dislocation motion (dislocation creep). This process is called diffusion creep, the

---

vacancy sources and sinks are no longer dislocations but grain boundaries. Diffusion creep can be distinguished into Nabarro-Herring creep [105-108] and Coble creep [109], depending on whether the vacancy diffusion is dominating in the crystal lattice or along grain boundaries.

In summary, diffusion flow dominates at low stresses and high T, while dislocation creep is most relevant at high stresses. Bulk diffusion becomes relevant at higher temperatures, due to increased diffusion rates.



---

### 3. Macroscopic test approaches

---

The macroscopic deformation behavior and its related deformation mechanisms at different stresses and strain rates are conventionally analyzed using macroscopic experiments with varying loading protocols i.e. strain rate jump, creep, or relaxation experiments. The active deformation processes can be identified on the basis of  $m$ ,  $n$ ,  $V$  and the activation energy  $Q$  [36, 110]. In the following sections those macroscopic test procedures are briefly discussed as they are used later on as a blueprint for the implementation of small-scale indentation test procedures.

#### 3.1. Strain rate jump experiment

The coefficient of strain rate sensitivity, as introduced in section 2 (Eq. 2) can be determined in a uniaxial strain rate jump test, where the initially constant strain rate  $\dot{\epsilon}_1$  is suddenly changed to a second strain rate  $\dot{\epsilon}_2$ . For strain rate sensitive materials, this jump in strain rate leads to a rate dependent change in resistance to plastic deformation, i.e. changing yield stress where an increase in  $\dot{\epsilon}$  results in higher strengths. Assuming a constant microstructure,  $m$  can be expressed for a uniaxial test by the following equation [110]:

$$m_{uni} = \frac{1}{n} = \frac{\partial \ln \sigma_y}{\partial \ln \dot{\epsilon}} \quad (2b)$$

The corresponding activation volume can be estimated as [111]:

$$V = \frac{\sqrt{3}k_B T}{m_{uni} \cdot \sigma_y}. \quad (3b)$$

An advantage of the SRJ method compared to two individual tests with different but constant strain rates is, in addition to the shorter test duration, that a quasi-constant volume element and microstructure can be tested and compared. It should be noted, however, that the stress after a strain rate change usually undergoes a short transient, while the steady state stress is used for the analysis [110, 112].

### 3.2. Uniaxial creep experiment

Creep and relaxation experiments are performed to study the long-term transient material response to a constantly applied stress (creep test) e.g. [113-115] or strain (relaxation test) e.g. [116].

In a uniaxial relaxation test, the specimen is first deformed until a predefined strain or stress limit is reached. At this point, the crosshead is stopped ( $\varepsilon(t) = \text{const.}$ ) and the time-dependent course of the stress is analyzed during the relaxation segment. With decreasing stress, the driving force for dislocation motion is continuously decreasing due to relaxation processes.

In a uniaxial creep test, the specimen is initially deformed as in the relaxation test. As soon as the strain or stress limit is reached, the stress is held constant ( $\sigma(t) = \text{const.}$ ) and the change in strain or creep deformation is analyzed within the creep segment. The driving force for dislocation motion is kept at a constant level by controlling the applied stress [100-102].

The material's response during a creep test can be classified into three different regimes: primary, secondary and tertiary creep. A schematic sketch of a creep curve for a uniaxial tensile (blue, solid line) and compression creep test (red, dashed line) is plotted in Fig. 4a. The first part of the creep curve is called "primary creep" or "transient creep".

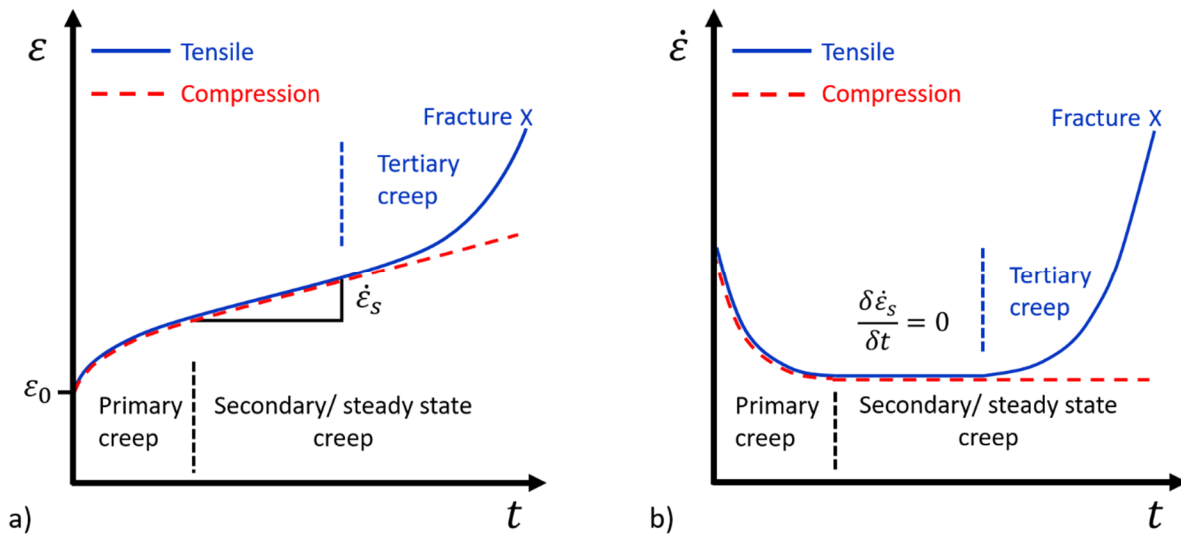


Figure 4: Uniaxial creep testing: a) creep curve: time dependent strain for tensile (solid line) and compression testing (dashed line), b) strain rate as a function of creep time for tensile and compression testing, assuming a constant microstructure, adapted from [104, 117].

The material is initially deformed by a time-independent strain ( $\varepsilon_0$ ) which represents the sum of an elastic and a plastic strain. The creep strain rate is quite high in the beginning (Fig. 4b)

but decreases with increasing creep time due to work hardening of the material [101]. The strain rate declines until a constant or steady state strain rate ( $\dot{\epsilon}_s$ ) is reached. This interval, in which the strain rate is constant and strain changes linearly is called “secondary creep” or “steady state creep”. In this stage, the opposing processes of dislocation nucleation and annihilation compensate each other out resulting in a dynamic equilibrium and a constant dislocation structure [101, 118].

Primarily and secondary creep are comparable for tensile and compression creep tests. In case of tensile creep testing, the strain rate starts to increase again after a certain creep time. This is defined as the “tertiary creep” regime. The increase in strain rate is related to a reduction in the cross-sectional area which finally leads to failure [104]. In a compression creep test, the strain rate remains constant until the end of the experiment, unless the sample cross sectional area changes significantly. Compared to tensile tests, failure occurs usually at much higher strains due to shear band formation.

The minimum creep rate  $\dot{\epsilon}_s$  is described by Norton’s creep law [119] or its combination with the Arrhenius rate equation [120-122]:

$$\dot{\epsilon}_s = K_i \sigma^n = K_j \sigma^n \exp\left(-\frac{Q_c}{RT}\right) \quad (9)$$

where  $K_{i,j}$  are material’s constants. The parameter  $Q_c$  represents the activation energy required for creep deformation and  $R$  is the universal gas constant.

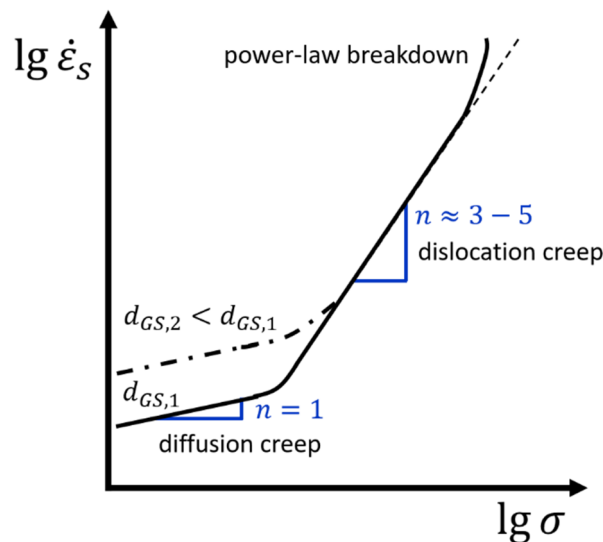


Figure 5: Norton plot, adapted from [120, 123].

---

The stress exponent can be derived from a Norton plot, where the logarithm of the creep rate is plotted against the logarithm of the applied stress. The resulting slope represents  $n$ . A schematic sketch of a Norton plot is illustrated in Figure 5. Dislocation creep in pure metals and single phase alloys is associated with  $n \approx 3 - 5$ , while multi-phase alloys exhibits an stress exponent of up to 40. At low stresses and creep rates, a change in creep mechanisms is observed resulting in  $n \approx 1$  for diffusion creep. A reduction in grain size ( $d_{GS,1} > d_{GS,2}$ ) is accompanied by an increased creep rate. The creep behavior at very high stresses can no longer be described by Norton's law, this is called power-law breakdown. [120, 123].

## 4. Depth-sensing indentation testing

The depth-sensing indentation testing technique offers the possibility to identify the mechanical properties of a material on a small length-scale. This is in contrast to the conventional, macroscopic test procedures presented above, which require fairly large sample volumes (Fig. 6). The DSI technique provides therefore the possibility to independently investigate the mechanical properties of thin coatings such as bond coats or thermal barrier coatings e.g. [18, 30, 124, 125], and of individual microstructural constituents such as the  $\gamma$ - and  $\gamma'$ - phase of Ni-based superalloys e.g. [15]. The technique can not only be applied for simple hardness ( $H$ ) and Young's modulus ( $E$ ) determination [16, 126, 127], but also for studying transients in material plasticity. This allows to determine strain rate sensitivities and activation parameters e.g. [17, 111, 128, 129], as well as creep e.g. [95, 130] and relaxation e.g. [131] properties. Moreover, the fatigue behavior e.g. [132-134], fracture toughness e.g. [22, 23, 135], or the adhesive strength of layers and coatings e.g. [136] can be analyzed using indentation experiments. It is also possible to determine local stress-strain curves e.g. [137, 138], residual stresses e.g. [139-141], the free surface energy [142, 143] or to map the hardness and modulus distribution e.g. [125, 144-146].

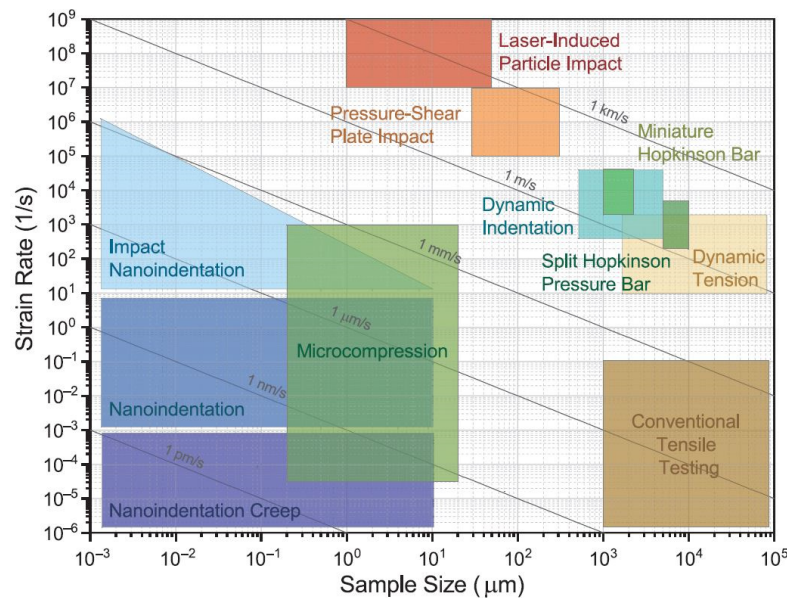


Figure 6: Schematic comparison of strain rate ranges and sample sizes applied in macroscopic and small-scale mechanical experiments. Reprinted with permission from Barnoush et al. [147], Copyright (2019), MRS Bulletin, Springer.

---

Besides the small probed volume ( $V_{plast}$ ), a simple sample preparation, a high sample throughput but also the variety of characterization options are advantages compared to conventional macroscopic test approaches. New instrumented indentation testing systems and loading protocols have been successively designed to semi-automatically characterize the local mechanical properties at different time and length scales (Fig. 6) but also over a wide temperature range e.g. [19, 29, 30, 33, 95, 111, 130, 131, 144, 145, 147-151].

Different loading protocols and instruments allow to investigate the local material properties over a strain rate range of twelve orders of magnitude. Figure 6 provides an overview of strain rates and sample sizes applied in various test procedures from the nano- to the macro-scale [147]. This large range of strain rates cannot be covered by any of the conventional testing techniques. High strain rates in macroscopic tests can only be achieved with rather large test setups such as the Split Hopkinson pressure bar. Indentation systems, on the other hand, are quite compact in comparison.

#### **4.1. Depth-sensing indentation testing instrument**

A schematic sketch of a load-controlled DSI system is illustrated in Figure 7. The system basically consists of an actuator, a shaft, the indenter tip, the frame and the sample stage. The actuator is used to transfer the load via the shaft to the indenter tip and the sample. This is achieved by moving a magnet in a current-carrying coil (magnetic loading unit). Displacements are determined via a plate capacitor (capacitive displacement sensor). Additional support springs hold the assembly in position. The frame is designed for high stiffness to reduce additional displacements due to frame deflection. Its compliance as well as the spring stiffnesses and the tip area function must be recalibrated periodically. The frame compliance as well as the tip area function are calibrated by testing a reference material, e.g. fused silica, with well-known properties [126, 127].

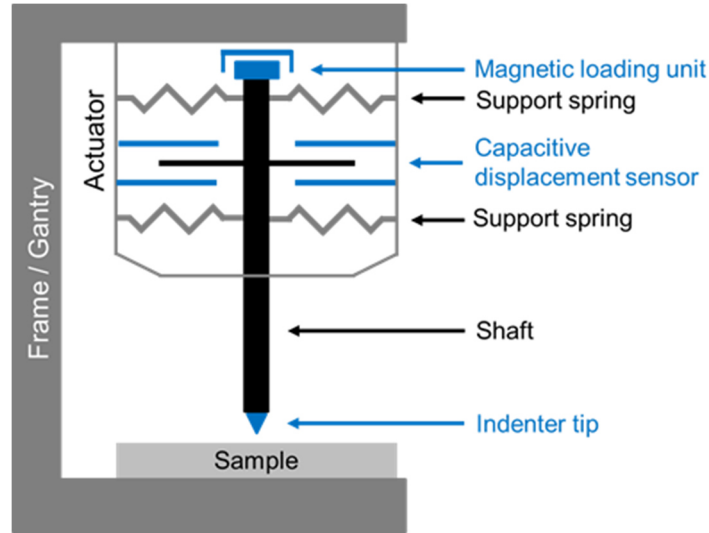


Figure 7: Schematic sketch of a load-controlled instrumented indentation system (not to scale).

## 4.2. Contact stiffness

Based on Sneddon's analysis, the contact stiffness  $S$ :

$$S = \frac{dP}{dh} = 2E_r \sqrt{\frac{A_c}{\pi}} \quad (10)$$

can be determined by the initial unloading slope  $dP/dh$  (red dashed line in Fig. 8) of the load-displacement curve of an DSI experiment, where  $P$  is the applied load and  $h$  is the indentation depth [152-154].  $S$  is thus related on the contact area ( $A_c$ ) and the reduced modulus ( $E_r$ ). The reduced modulus combines the elastic properties of the sample ( $E$ ) and indenter ( $E_i$ ) material and can be expressed by Equation 11 [126, 155]:

$$\frac{1}{E_r} = \frac{1 - \nu^2}{E} + \frac{1 - \nu_i^2}{E_i} \quad (11)$$

where  $\nu$  and  $\nu_i$  are the Poisson's ratios of the sample and the indenter material, respectively. This approach was later on used by Oliver & Pharr [126, 127], who developed the fundamental methodology for evaluating  $H$  and  $E$  from load-displacement curves of DSI experiments in 1992 [156]. In this method,  $S$  is used to determine the actual contact depth  $h_c$ , which is larger than the depth of the residual indent  $h_f$  after final unloading (Fig. 8). The maximum penetration depth before unloading is given by  $h_{max}$ .

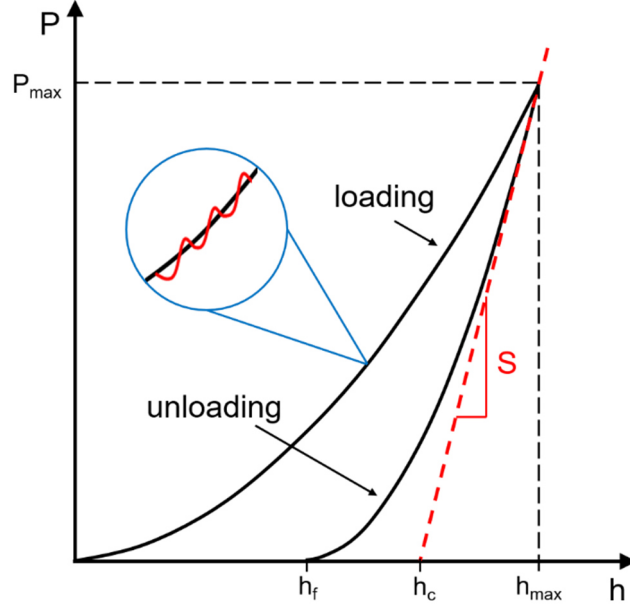


Figure 8: Load-displacement curve of an indentation experiment. The contact stiffness is determined by the initial unloading slope, furthermore, the additional dynamic displacement for the quasi-continuous determination of  $S$  (CSM technique) is illustrated, adapted from [127].

The contact stiffness can be used to determine the actual contact depth [157]:

$$h_c = h_{max} - \epsilon \frac{P_{max}}{S} \quad (12)$$

where  $\epsilon$  is a geometrical constant, depending on the indenter geometry ( $\epsilon = 0.75$  for a Berkovich indenter) [158]. The indentation depth can, furthermore, be used for the calculation of the indentation strain rate  $\dot{\epsilon}_{ind}$  [159]:

$$\dot{\epsilon}_{ind} = \frac{\dot{h}}{h} = \frac{1}{2} \left( \frac{\dot{P}}{P} - \frac{\dot{H}}{H} \right) \approx \frac{1}{2} \frac{\dot{P}}{P} \quad (13)$$

with displacement rate  $\dot{h}$ , loading rate  $\dot{P}$  and the time derivative of the hardness  $\dot{H}$ .

The contact stiffness can also be quasi-continuously determined using the continuous stiffness measurement (CSM) technique, where the loading signal is superimposed with an additional sinusoidal oscillating dynamic displacement (insert in Fig. 8). The amplitude of the dynamic displacement ( $h_0$ ) is constant and usually less than 4 nm, the dynamic frequency ( $\omega$ ) is typically  $\leq 100$  Hz [126, 160-163].

The additional dynamic displacement leads to a dynamic response of the entire indentation system. This in turn must be precisely known and corrected in order to determine accurate dynamic contact stiffnesses, indentation depths and finally hardness and Young's modulus data [126]. The indentation system schematically illustrated in Fig. 7 can be described by a model of a damped harmonic oscillator with one degree of freedom (Fig. 9) [126].

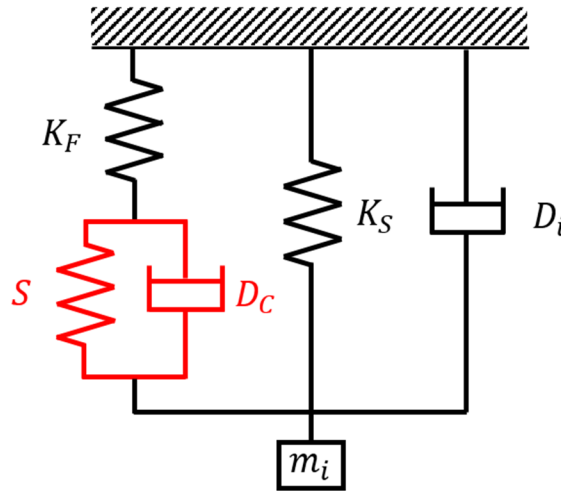


Figure 9: Model of a damped harmonic oscillator representing the indentation system (black components) including the sample/contact (red components), adapted from [126].

The indentation system is represented by two springs with spring stiffnesses  $K_F$  and  $K_S$ , a dashpot with a damping coefficient  $D_i$  and a single mass  $m_i$ . The load frame stiffness is given by  $K_F$ , while  $K_S$  is the spring stiffness of the column support springs. Parameter  $m_i$  sums up the moving mass of the shaft, tip and coil. The damping coefficient of the instrument is mainly related to the aerodynamic resistance of the capacitive displacement sensor and the eddy current within the electromagnetic loading unit [126, 149].

The sample or contact is represented by a simplified model (Fig. 9, sketched in red) containing only a spring with spring stiffness  $S$  and a dashpot with damping coefficient  $D_C$ , since the moving mass of the sample is negligible [126, 149].

Applying the dynamic CSM technique, the load is given by  $P(t) = P_0 \exp(i\omega t)$ , the resulting displacement signal is then  $h(\omega) = h_0 \exp(i(\omega t - \phi))$ . The displacement signal is processed in a phase-sensitive detector (lock-in amplifier). The amplifier has a small time constant of e.g.  $20 \mu s$  [149] and uses a frequency-dependent gain that allows to detect shifts of  $0.001 \text{ nm}$  [126]. The time constant represents the delay between the change of an input and the response of the

signal. The shift between the load and the displacement signal is given by the phase angle  $\phi$ . The dynamic contact stiffness is related to  $h(\omega)$  (Eq. 14) or  $\tan(\phi)$  (Eq.15) [126]:

$$\left| \frac{P_0}{h(\omega)} \right| = \sqrt{\left[ (S^{-1} + K_f^{-1})^{-1} + K_S - m_i \omega^2 \right]^2 + \omega^2 D^2} \quad (14)$$

$$\tan(\phi) = \frac{\omega D}{(S^{-1} + K_f^{-1})^{-1} + K_S - m_i \omega^2} \quad (15)$$

this results in Eq.16 [164]:

$$S = \left[ \frac{1}{\frac{P_0}{h(\omega)} \cos(\phi) - (K_S - m_i \omega^2)} - K_f^{-1} \right]^{-1}. \quad (16)$$

The dynamic damping of the system is given by Eq. 17 [164]:

$$\omega D = \frac{P_0}{h(\omega)} \sin(\phi). \quad (17)$$

Most of the state-of-the art indentation test methods are based on this dynamic technique, as the continuous determination of  $S$  offers several advantages compared to quasi-static loading cycles. The contact stiffness is largely independent of thermal drift and, thus, represents a reliable parameter for the evaluation of the contact including pile-up and sink-in effects. Material pile-up or a sink-in of the specimen surface close to the impression (Fig. 10) can occur due to plastic deformation within the plastic zone below the indenter. The ratio of  $E/\sigma_y$ , as well as the work hardening behavior determine which effect occurs.

Pile-up is expected for non-work hardening materials with a large  $E/\sigma_y$  ratio and  $h_f/h_{max} > 0.7$ . In this case, the plastic zone expands and reaches the free surface of the sample where material flow is no longer constraint. Pile-up formation leads to an underestimation of the contact radius  $r_c$  and thus also of the contact area by up to 60% [165] applying the Oliver-Pharr method [126, 127] (Fig. 10). In consequence, the calculated  $H$  and  $E$  values are too large. For moderate work hardening materials with  $h_f/h_{max} < 0.7$ , on the other hand, sink-in takes place and the contact area, determined by the Oliver-Pharr method, is in good agreement with the actual contact area [127, 165, 166].

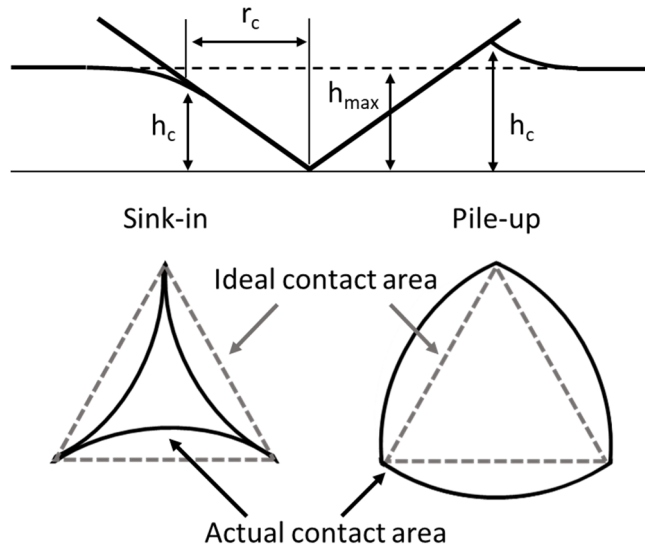


Figure 10: Schematic illustration of sink-in (left) and pile-up (right) formation during indentation testing and its impact on the contact area, adapted from [167].

The hardness or contact pressure is defined by the ratio of the applied load and the contact area. The pile-up effect, as already mentioned, can lead to massive deviations in the evaluation of the projected contact area (Eq. 18) and, consequently, in  $H$ , if the Oliver-Pharr method is applied. The determination of  $A_c$  is also susceptible to thermal drift, which is especially critical for long-term experiments. According to Joslin & Oliver [157], the material's resistance to plastic deformation, can also be expressed in terms of  $S$ , which takes pile-up into account and is independent of thermal fluctuations [126, 157]:

$$H = \frac{P}{A_c} = \frac{4\beta^2 PE_r^2}{\pi S^2} \quad (18)$$

where parameter  $\beta$  is a geometry factor that corrects for the non-axisymmetric indenter geometry of the e.g. Berkovich indenter [168]. For the Berkovich geometry, values of 1.023 to 1.085 have been reported which are slightly higher than for axisymmetric geometries  $\beta = 1$ . However,  $\beta$  can be assumed to be 1.05 [127, 169].

### 4.3. Loading protocols

Loading protocols applying a constant strain, loading or displacement rate are usually applied for basic hardness and Young's modulus measurements. More advanced test procedures like the cyclic loading procedure [157, 170], CSM technique [126, 160-162], SRJ test [111], constant load hold (CLH) [95, 171], constant displacement hold (CDH) [172-179] or the recently

developed constant contact stiffness (CCS) [131] method are used to study the strain rate dependence, respectively the creep and relaxation properties of a material. Furthermore, test methods have been developed for testing at very high strain rates ( $> 10^1 s^{-1}$ ). An overview of various testing protocols developed in the last decades is provided below (Fig. 11).

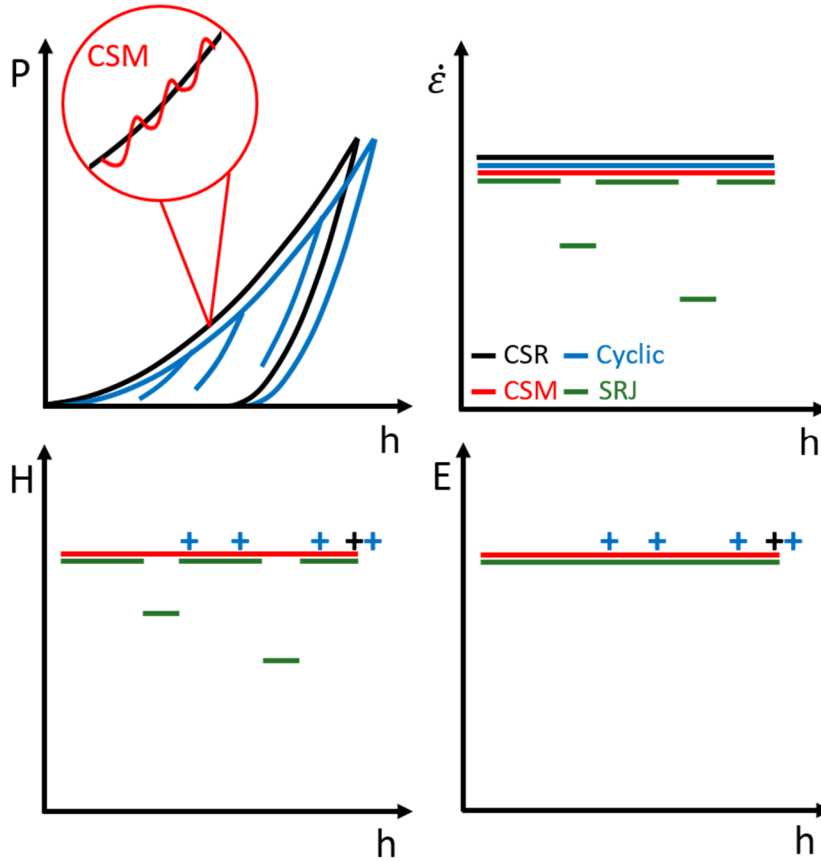


Figure 11: Schematic comparison of the CSR (black), cyclic (blue), CSM (red) and SRJ (green) loading protocol and the associated hardness and Young's modulus profiles. The load-displacement curves of the dynamic SRJ and CSM loading protocols are comparable to the black curve of the CSR method and are therefore not shown separately. The load-displacement curve of the cyclic method is slightly shifted for illustration purposes. The + symbols indicate the H and E values determined at the respective (partial) unloading points, while the lines represent the data obtained from dynamic test procedures in which the CSM technique is applied.

### 4.3.1. Constant strain rate method

Most commercially available DSI systems are load controlled. The loading rate is continuously ramped to keep the quotient  $\dot{P}/P$  and hence  $\dot{\epsilon}_{ind}$  (Eq. 13) constant during the experiment (Fig. 11, black curve). The abortion criterion of a constant strain rate (CSR) experiment is usually a depth or load limit. Once the test limit is reached, the load is first held constant to compensate for creep before the load is relieved quickly. The unloading speed must, according to ISO 14577 [156], be more than ten-times higher than the ratio of the contact creep rate at

---

---

maximum load and the corresponding contact compliance. This becomes particularly relevant for testing at high temperatures [30]. The unloading curve is used to determine  $S$ ,  $E$  and  $H$  at the end of the loading cycle [126].

#### 4.3.2. Cyclic loading method

The depth dependence of  $E$  and  $H$  can be determined by performing several loading cycles, with (partial) unloading at the end of each cycle (Fig. 11, blue curve). This procedure is called cyclic loading method. It allows the determination of  $E$ , respectively  $H$  values at different penetration depths, but a continuous determination of the material parameters is not possible [157, 170].

#### 4.3.3. Continuous stiffness measurement technique

The continuous stiffness measurement technique is an advanced version of the CSR or cyclic method, in which the loading signal is superimposed with an additional sinusoidal oscillating dynamic load respectively displacement (Fig. 11, red curve) [126, 127, 160-162]. The dynamics allows to determine the contact stiffness and, thus,  $E$  and  $H$  quasi-continuously during each partial unloading cycle [127, 180].

An ongoing debate in the field of DSI testing is the influence of the superimposed dynamic oscillation on the test results, as it can reduce the measured hardness value. This is especially the case for low indentation depths and large dynamic displacements [180-182]. It is, however, not fully understood, if this is an intrinsic or extrinsic effect caused by local changes in the microstructure or measurement inaccuracies of the instrument. Furthermore, the difference in hardness between dynamic and quasi-static indentation tests is decreasing with increasing indentation depth [170, 180-182]. Significant differences between quasi-static and dynamic CSM-based methods were found for materials with large  $E/H$  ratios [180, 183, 184].

The loading-unloading within a CSM cycle is not purely elastic, as the mean load is continuously increasing. The applied deformation is therefore both, elastic and elastic-plastic. The plastic deformation leads to periodic discontinuities in the displacement signal resulting in an underestimation of  $S$  and  $E$ , since the data of the phase lock-in amplifier are processed as if the material would deform ideally, i.e. purely elastically [183]. This is known as “plasticity error” [183, 185].

Phani et al. [185, 186], recently came up with the idea of applying a constant ratio of the dynamic load component ( $P_{AC0}$ ) to the mean load ( $P_{DC}$ ) instead of using a constant displacement amplitude. The mean load applied is given by the DC component of the total load while the superimposed dynamic load is defined by the AC component. The total load applied can be written as [185]:

$$P = P_{AC} + P_{DC} = P_{AC0} \cos(2\pi ft) + P_{DC0} e^{\frac{\dot{P}}{P}t} = P_{DC0} e^{\frac{\dot{P}}{P}t} \left[ 1 + \frac{P_{AC0}}{P_{DC}} \cos(2\pi ft) \right]. \quad (19)$$

The amplitude of the dynamic displacement depends then on the relative proportions of the loading and unloading segments and thus on the  $E/H$  ratio and the strain hardening exponent of the material [185, 186].

The approach of applying a constant dynamic load ratio ( $P_{AC0}/P_{DC}$ ) at a simultaneously constant indentation strain rate and oscillation frequency represents a significant improvement in measurement accuracy for load-controlled indentation systems in particular. Additional feedback loops, which are necessary for keeping a constant dynamic displacement, are no longer required. A correction for the time constant of the phase lock-in amplifier is, however, necessary. The higher portion of the elastic segment within a sinus oscillation cycle minimizes the “plasticity error” as demonstrated in [185, 186]. It was found that the phase angle can be used to analyze the “plasticity error” [186]. Furthermore, the load frame stiffness has no influence on the resulting dynamic displacement applied to the sample and the noise level of the contact stiffness is significantly lower [185, 186].

#### 4.3.4. Strain rate jump method

The indentation strain rate jump method was developed in analogy to uniaxial SRJ experiments (see section 3.1). The SRJ method is basically a CSR method where the CSM technique is applied and the indentation strain rate ( $\dot{\epsilon}_{ind} = \dot{P}/2P$ ) is abruptly changed between the individual test segments by controlling  $\dot{P}$  [111]. The change in strain rate leads to a change in hardness if the material is rate sensitive (Fig. 11, green curve). The hardness does not change simultaneously with the strain rate, but usually exhibits a short transient before a plateau value is reached. The strain rate sensitivity coefficient from indentation testing can be calculated using Eq. 2c [111]:

$$m_{ind} = \frac{1}{n} = \frac{\partial \ln H}{\partial \ln \dot{\epsilon}_{ind}}. \quad (2c)$$

The activation volume can be expressed by Eq. 3c similar to uniaxial experiments [111]:

$$V = \frac{C\sqrt{3}k_B T}{m_{ind} \cdot H} \quad (3c)$$

where  $C$  is a constraint factor. The corresponding activation energy in kJ/mol is given by [187]:

$$\frac{H}{E} = G' \cdot \exp\left(\frac{Q}{nRT}\right) \quad (20)$$

with an pre-exponential factor  $G'$ .

Since the SRS is determined from a single experiment (quasi-constant volume element), the effects of material inhomogeneities or changes in the microstructure on  $m$  and  $V$  are significantly reduced. Furthermore, the test duration can be significantly reduced compared to two tests performed at different strain rates. This minimizes the influences of thermal drift. It was demonstrated, that the results from indentation SRJ tests are well comparable with uniaxial SRJ tests which have been used for decades to determine activation parameters [36, 111, 112].

#### 4.3.5. Constant load hold method

Constant load hold indentation creep experiments are frequently used to study the time-dependent behavior of materials e.g. [159, 171, 188, 189]. In this loading protocol, the indenter is pushed into the material with a constant loading, displacement, or strain rate to a defined penetration depth or load limit (Fig. 12a). In the subsequent creep segment, the load is held constant (Fig. 12b) and the resulting temporal change in penetration depth is used for calculating the creep strain rate (Fig. 12c), hardness (Fig. 12d) as well as  $m$ ,  $n$  and  $V$ . A drawback of this method is that the data becomes more and more affected by thermal drift with increasing test duration. In consequence, the actual material behavior can no longer be studied correctly [95].

For this reason, the method was further refined by Maier et al. [95], by applying the CSM technique for the calculation of the stiffness based hardness or contact pressure (Eq. 18). A constant  $E_r$  is assumed for the calculation, therefore an accurate calibration of the frame stiffness is essential. The creep strain rate  $\dot{\epsilon}_c = \dot{h}/h$  is given by Eq. 13.

The volume of the plastic zone, and thus  $A_c$ , increases slightly during the creep segment, resulting in a decline in hardness respectively contact pressure according to Eq. 18. A CLH test

is therefore not exactly comparable with a uniaxial creep experiment performed at a constant stress level [33, 34].

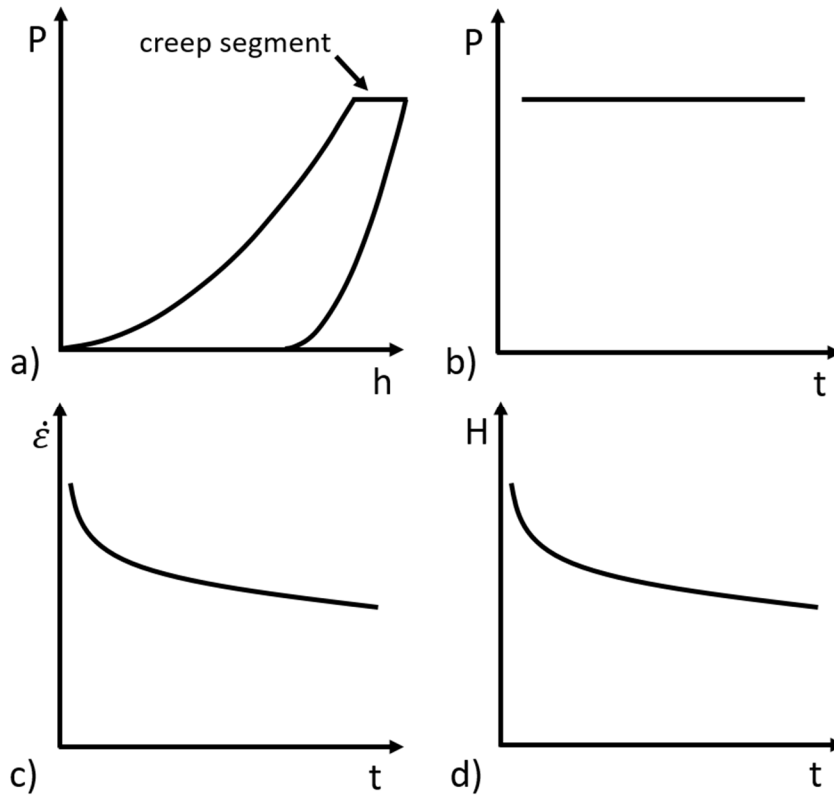


Figure 12: Schematic sketch of the CLH loading protocol: a) load-displacement curve, b) the applied load within the creep segment as well as c) the associated strain rate and d) hardness profiles during creep.

#### 4.3.6. Constant displacement and stiffness methods

Indentation relaxation tests are performed by keeping the penetration depth constant and analyzing the drop in load or contact pressure over time. This test procedure is similar to uniaxial relaxation tests, in which the strain is kept constant and the time dependent stress drop is analyzed [172-179]. However, thermal drift effects during testing cause fluctuations in the actual penetration depth during the experiment. In consequence, the results are affected by thermal drift and do not represent the relaxation behavior of the tested material [174]. These issues have been circumvented by Baral et al. [131, 178] who developed a more advanced relaxation method in which the contact stiffness, rather than penetration depth, is kept constant. In doing so, the size of the plastic zone is not changing with time, only relaxation processes take place. The relaxation strain rate  $\dot{\epsilon}_{rel}$  can be computed using Eq. 21 [131]:

$$|\dot{\epsilon}_{rel}| = \frac{|\dot{\sigma}_r|}{E}. \quad (21)$$

---

### 4.3.7. High strain rate testing

In the past, loading protocols and DSI devices for testing at very high strain rates have been developed to cover the gap between conventional, quasi-static indentation experiments and the high deformation rates, such as those achieved on a macroscopic level in Charpy pendulum impact tests or Split Hopkinson Pressure Bar experiments (Fig. 6).

First DSI tests at high strain rates were carried out by impact experiments using a pendulum-based indentation platform. These systems are often modified to overcome issues like ringing and multiple impacts (rebound effect) on the test results [190-194].

Recently, Phani & Oliver [148, 149] presented a new test method for high strain rate (up to  $4000 \text{ s}^{-1}$ ) testing, which does not require an impact and is therefore suitable for conventional load-controlled DSI systems (Fig. 7) with a high data acquisition rate. Once the tip is in contact with the sample, the load is applied in a step-wise manner and hold constant afterwards. This results in initially very high displacement rates respectively high strain rates, which decrease rapidly during the course of the experiment. In doing so, a wide strain rate range to be investigated within a single test at a quasi-constant volume element.

Another approach is the design of a new indenter setup where a piezo-driven, displacement-controlled, transducer, also called *SmarTip*, was used for testing at strain rates up to  $1000 \text{ s}^{-1}$  [19, 150].

## 4.4. Correlation of small-scale and macroscopic experiments

In previous chapters, macroscopic and local characterization procedures were presented, hence the question of the correlation of local hardness with macroscopic stress arises. The correlation of indentation and uniaxial tests is complex since there are significant differences in the stress and strain states, their uniformity as well as in the constancy of the probed volumes (Fig. 13).

In an indentation test, a stress and strain gradient is present within the plastically probed volume below the indenter tip (gray semicircle in Fig. 13), the stress state is triaxial. The hardness determined represents, thus, the mean contact pressure  $p_m$  within the plastic zone. The average strain applied to a material during indentation depends on the radius or opening angle of the indenter. For self-similar geometries such as the Berkovich geometry, a constant average strain of 7.16% is induced, while sharper indenter geometries such as the Cube corner geometry induce a constant average strain of 21.98% [195]. Furthermore,  $V_{plast}$  expands continuously with increasing penetration depth.

In a compression test, on the other hand, the stress state is uniaxial and the stress distribution is uniform within the sample (Fig. 13). The tested volume is constant but the strain increases with increasing deformation.

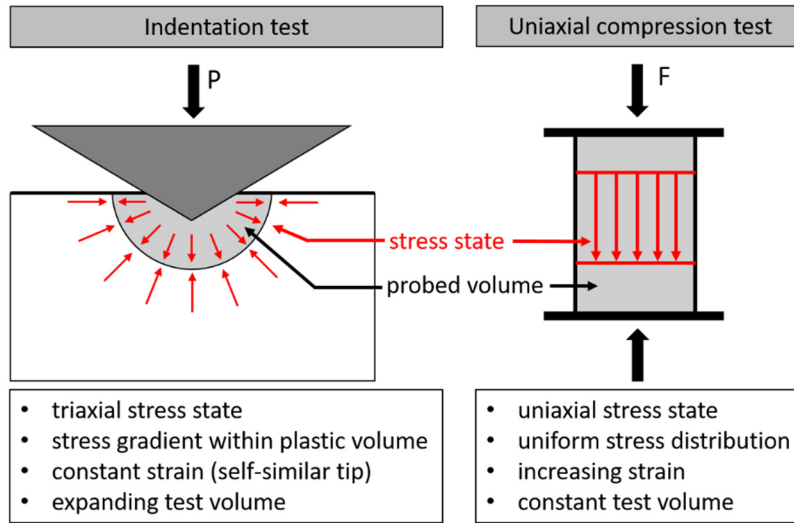


Figure 13: Comparison of indentation and uniaxial compression testing.

On a continuum length scale, different concepts have been derived to relate  $\sigma(\epsilon)$  to  $H(h)$ . For spherical indentation, local plasticity below the indenter occurs if  $p_m$  becomes about 10% higher than the yield stress of the material (Hertzian contact). The initially elastic contact becomes elastic-plastic, the plastic zone below the indenter is first surrounded by purely elastically deformed material. Increasing the load applied to the indenter causes an expansion of the plastic zone until it finally reaches the free surface. Consequently, the material flow is no longer impeded by the surrounding material and the contact becomes fully plastic [155, 196, 197]. At this point of indentation, the contact pressure remains constant, since a further increase in  $P$  is compensated by an expansion of the plastic zone. The correlation of contact pressure and yield strength of the material is then given in Eq. 22 [155, 196, 198]:

$$p_m = C \cdot \sigma_y \tag{22}$$

with a constraint factor. The constraint factor depends on the material, the indenter geometry and the friction coefficient of the interface. For a self-similar, pyramidal Berkovich indenter, it can be assumed to be  $C \approx 3$  for metals and  $C \approx 1.5$  for glasses, in a first approximation [155, 196-198]. Self-similarity means that the indenter tip has a constant ratio of penetration depth and contact radius, causing a constant representative strain.

More advanced equations have been recently developed e.g. by Su et al. [199] and Kermouche et al. [179, 200] for a more accurate calculation of the representative, equivalent uniaxial stress  $\sigma_r$  and the representative, equivalent uniaxial strain rate  $\dot{\epsilon}_r$  from DSI experiments.

The equivalent uniaxial strain rate from indentation creep tests can be expressed as [199]:

$$\dot{\epsilon}_r = \left( \frac{1}{k \tan \theta} \right) \left( \frac{\dot{h}}{h} \right) \quad (23)$$

with equivalent cone angle  $\theta$  ( $\theta = 70.3^\circ$  for Berkovich geometry) and pile-up/sink-in parameter  $k$  [148, 199]. This parameter depends on  $m$  and  $\theta$  [199]:

$$k(m, \theta) = k_0(\theta) + k_1(\theta)m + k_2(\theta)m^2 + k_3(\theta)m^3 \quad (24)$$

the parameters  $k_i(m, \theta)$  are outlined in [199]. The corresponding representative stress is reported by Su et al., as:

$$\sigma_r = \left( \frac{1}{Fk^2} \right) \left( \frac{P}{\pi(h \tan \theta)^2} \right) \quad (25)$$

where  $F$  is the reduced contact pressure [148, 199]. It can be expressed by Eq. 26 [199]:

$$F(m, \theta) = F_0(\theta) + F_1(\theta)m + F_2(\theta)m^2 + F_3(\theta)m^3 + F_4(\theta)m^4 \quad (26)$$

the parameters  $F_i(m, \theta)$  are outlined in [199]. Another expression for  $\sigma_r$  is reported by Kermouche et al. (Eq. 27) [131, 200]:

$$\sigma_r = \frac{\zeta_3 H \tan \varphi}{\zeta_1 \tan \varphi - (1 - \zeta_2) \frac{H}{E}} \quad (27)$$

where  $\varphi$  ( $\varphi = 90^\circ - \theta = 19.7^\circ$  for Berkovich geometry) is the inclined face angle and  $\zeta_i$  are geometric constants. For the Berkovich geometry  $\zeta_1 = 0.66$ ,  $\zeta_2 = 0.216$  and  $\zeta_3 = 0.24$  are applicable [131, 200].

---

## 4.5. Size effects

Care needs to be taken when analyzing and comparing small scale indentation data, since size effects and can influence the measured hardness data.

### 4.5.1. Pop-in

At small indentation depths, sudden jumps in the displacement signal occur, while the applied load remains constant. These jumps in the load-displacement curve are called “pop-ins” and indicate the transition from a purely elastic to plastic deformation. Pop-in events not only indicate the nucleation of dislocations, but can also be evidence for phase transformations or crack formation [201].

### 4.5.2. Indentation size effect

A second size effect is related to strain gradients when testing at penetration depths below approximately  $1\ \mu\text{m}$  [202]. Strain gradients cause an increase in  $H$  with decreasing penetration depths for most applicable materials. This depth dependent behavior is called “indentation size effect” (ISE) [203, 204].

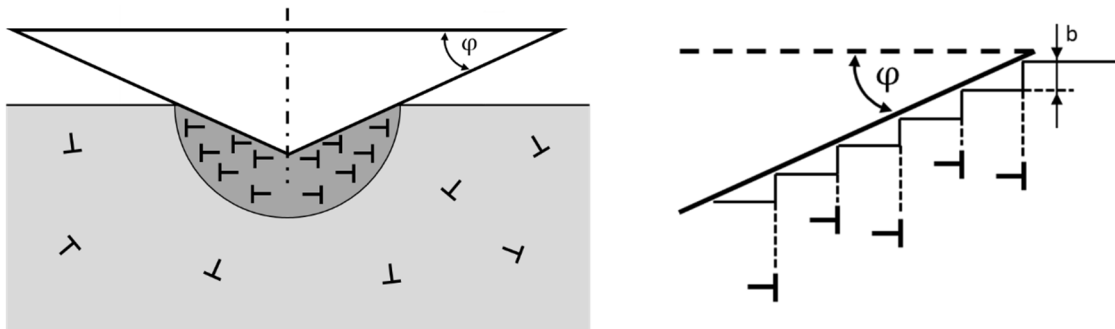


Figure 14: Schematic illustration of the generation of geometric necessary dislocations during indentation with a conical body, adapted from [204].

The ISE can be associated to the formation of geometrically necessary dislocations (GNDs), which are generated in addition to the pre-existing statistically stored dislocations (SSDs) during the indentation process (Fig. 14) [204, 205]. The material forms dislocation rings to mimic the shape of the indenter during plastic deformation, this causes work hardening of the material. The GND density depends on the penetration depth and opening angle of the equivalent cone. The influence of GNDs on  $H$  is larger the smaller the indent, since the gradient

in plastic deformation increases with decreasing penetration depth [206]. The hardness is related to the GND and SSD densities  $\rho_{GND}$  respectively  $\rho_{SSD}$  [204, 207]:

$$H = C\sigma_y = CM\tau = CM\alpha Gb\sqrt{\rho_{GND} + \rho_{SSD}} \quad (28)$$

with Taylor factor  $M$  and a geometric constant  $\alpha$ . At large penetration depths, the hardness reaches a constant level  $H_0$  and is basically determined by the SSD density. The macroscopic hardness can be represented in a simplified equation [204, 207]:

$$H_0 = C\sigma_y = CM\tau = CM\alpha Gb\sqrt{\rho_{SSD}}. \quad (29)$$

This will lead to the expression [204]:

$$\frac{H^2}{H_0^2} = \sqrt{1 + \frac{h^*}{h}} \quad (30)$$

where  $h^*$  the characteristic length is. The hardness is affected by the ISE if  $h < h^*$  [202, 204, 208].

For some time, it was not clear whether the ISE effect is real or caused by systematic errors, such as inadequate sample preparation. Detailed investigations have shown that ISE actual occurs, but can also be caused by systematic errors. A deformation layer and, thus, a hardness gradient may be present in the near-surface volume if the preparation is not carried out carefully. Furthermore, the formation of an oxide layer can lead to high hardness values at small indentation depths. The appearance of the ISE can also be influenced by the surface roughness and tip rounding of the indenter [202, 209-211]. A careful sample preparation is therefore essential.

#### 4.6. High temperature indentation testing

Testing materials at non-ambient temperatures is well established for conventional testing procedures like tensile, compression or creep experiments. Performing nano- and micromechanical experiments at these temperatures, however, is quite challenging due to e.g. a limited thermal stability, oxidation effects and tip wear. For this reasons, various DSI systems and test procedures have been developed for testing at non-ambient conditions in order to reduce the impact on test results [19, 24-30, 130, 147, 148, 150, 151, 155, 212]. The evolution of minimum and maximum test temperatures of DSI systems since the early 1990s is shown in Figure 15.

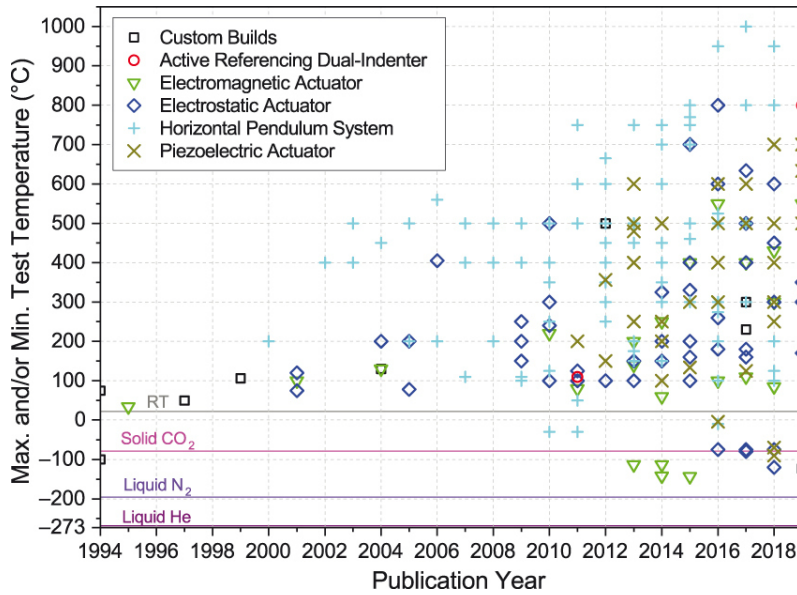


Figure 15: Chronological development of the minimum and maximum test temperatures of DSI systems. Reprinted with permission from Barnoush et al. [147], Copyright (2019), MRS Bulletin, Springer.

Figure 16 summarizes the essential test parameters, challenges and quantifiable material properties of an indentation experiment. The biggest challenge for testing at elevated temperatures is the wear of the indenter tips, which leads to tip rounding. Furthermore, the temperatures of tip and sample surface must be identical (isothermal contact) and precisely controlled to prevent the impact of thermal drift. The major factors affecting HT DSI experiments are briefly discussed in the following.

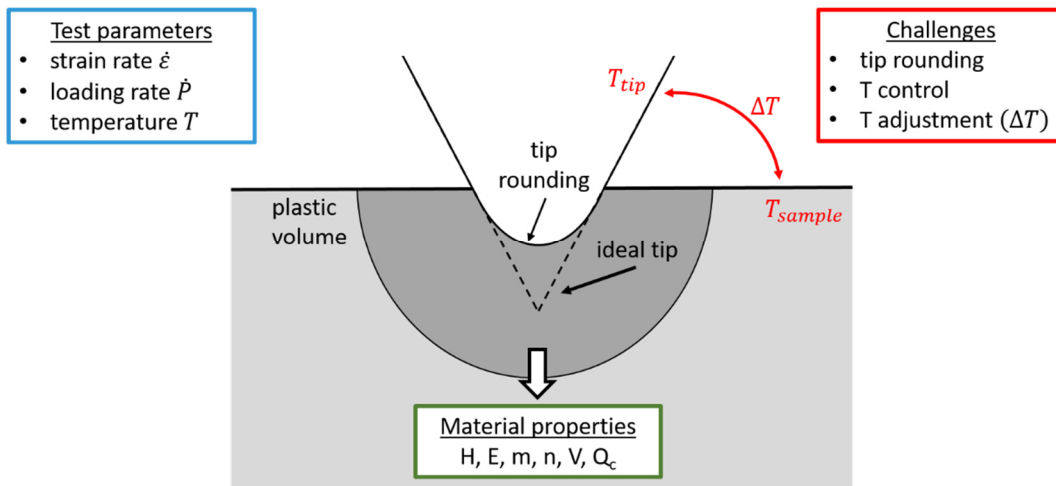


Figure 16: Variables, capabilities and challenges of high temperature indentation experiments.

---

#### 4.6.1. Thermal drift and temperature management

Temperature changes during a DSI experiment lead to thermal expansion or contraction of the indentation system (Fig. 7, tip, shaft, frame and/or specimen, etc.) which significantly influences the signal of the depth channel. A drift correction is, therefore, necessary for accurate data acquisition.

Thermal drift becomes visible by a time dependent change in penetration depth at a constant load. In general, there are two causes for this behavior, creep and thermal drift. For the drift correction, an exact determination of the drift rate without the influence of creep deformation is required. This can be achieved by a load reduction of e.g. 90% at the end of the indentation experiment before holding it constant. The change in depth over time in the partially unloaded state represents the thermal drift rate, which is assumed to be constant for the subsequent correction [167]. However, for long-term experiments as well as for high drift rates, this rather simple correction is insufficiently accurate. In general, experiments should only be performed under stable ambient conditions where drift rates are reasonable small ( $< 0.1 \text{ nm/s}$ ). Furthermore, it is also possible to determine the stiffness based and therefore pile-up and drift independent penetration  $h$  and  $H$  as discussed in section 4.2 (Eq. 12 and 18) [95, 152].

Maintaining constant operating conditions is much more difficult if the experiments are not performed at ambient temperature. The absolute temperature must be accurately measured and controlled. Furthermore, an isothermal contact between tip and specimen has to be ensured such as any temperature mismatch cause thermal drift. Thermal drift can be distinguished between contact drift and system drift.

The system drift is mainly caused by a thermal expansion or contraction during heating or cooling prior to testing. It decreases to zero as soon as a thermal equilibrium has been reached. The system must, therefore, be kept at a constant temperature for a certain time. Contact drift, on the other hand, is related to a temperature mismatch between the tip and the sample surface temperature. For this reason, it is important to match the temperatures before running experiments. This is often accomplished by using two independently controllable heating elements for the specimen and tip as well as advanced temperature matching procedures [28, 29, 212].

During the approach segment, before the tip gets in contact with the sample, successively more radiant heat is transferred. This can lead to temperature changes, especially at the tip, since its heat capacity is lower than that of the sample. The heat transfer to the actuator and the load

---

frame must be minimized in order to keep thermal drift rates low and the frame stiffness high. This requires a sophisticated cooling system [29].

#### **4.6.2. Environmental effects**

High temperature testing in an ambient environment can lead to the formation of oxide layers on the sample surface and a possible oxidation of the indenter material. Diamond, used as indenter material, in particular is susceptible to oxidation even at moderate temperatures starting at about 400 °C [27]. Oxidation effects can be reduced by operating in an inert gas atmosphere or in vacuum. Hydrogen embrittlement may occur when hydrogen-containing inert gases are used, testing under vacuum conditions therefore seems to be the method of choice at high temperatures, but other challenges arise here. The vacuum pumps used must be mechanically well insulated from the vacuum chamber to minimize vibrations, the same applies to the water pump in the cooling circuit. A lamellar water flow is essential for a low noise floor as well. Testing in vacuum complicates the temperature adjustment since there is no convection that can slightly balance out temperature differences [25, 29, 32, 213, 214].

#### **4.6.3. Indenter materials and tip wear**

The limited temperature stability of diamond requires the use of other ceramic indenter materials, such as sapphire ( $\text{Al}_2\text{O}_3$ ), WC, SiC,  $\text{B}_4\text{C}$  or cubic BN for testing at high temperatures. The hardness of these materials (Fig. 17), however, is significantly lower causing a higher mechanical wear of these indenters, especially when testing at high temperatures. In addition to its mechanical stability, the chemical resistance against the sample material is of major importance. Some sample materials based on e.g. Ni, Ti, Cr and Al are very affine to oxygen, carbon or nitrogen, resulting in degradation of the tip. The material of the indenter must therefore be carefully selected to avoid chemical interactions with the sample material [27, 29].

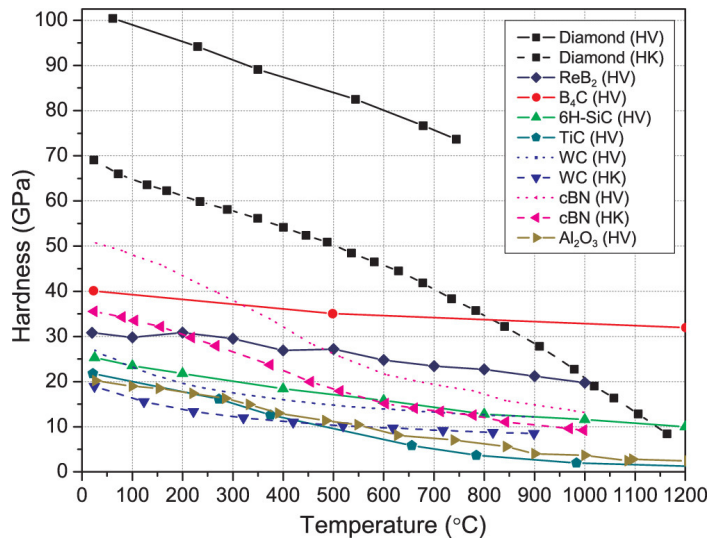


Figure 17: Temperature dependent Vickers (HV) and Knoop (HK) hardness of indenter materials. The dotted lines represent the extrapolated Vickers hardness of materials for which only Knoop hardness data were available. Reprinted with permission from Wheeler & Michler [27], Copyright (2013), Review of Scientific Instruments, American Institute of Physics.



---

---

## 5. List of selected publications

---

This cumulative dissertation reflects the main results of the peer-reviewed publications listed below. The full-text reprints are attached in chapter “10.2 Relevant full-text reprints”.

### Publication A:

#### **A new nanoindentation creep technique using constant contact pressure**

Olena Prach, **Christian Minnert**, Kurt E. Johanns, Karsten Durst

Journal of Materials Research, 34 (2019) p. 2492-2500. DOI: 10.1557/jmr.2019.188.

A new indentation creep method has been developed where a constant contact pressure is applied within the creep segment. The constant contact pressure approach is similar to a uniaxial creep experiment performed at a constant stress level, whereas a simultaneous relaxation of stress and strain rate is observed in case of a constant load and hold indentation creep experiment. The results of the newly developed test procedure are compared with the well-established constant load and hold indentation creep method. For this, long-term creep tests are performed on ultra-fine grained CuZn5, CuZn30 and fused silica. For both methods, the stiffness based indentation depth is used to reduce the influence of thermal drift, sink-in and pile-up effects on the creep data. The minimum strain rates which could be achieved in a long-term CCP test at a constant stress level were in the range of  $5 \cdot 10^{-5} \text{s}^{-1}$ .

---

Publication B:

**Nanoindentation creep testing: Advantages and limitations of the constant contact pressure method**

**Christian Minnert, Karsten Durst**

Journal of Materials Research, 37 (2022) p. 567-579. DOI: 10.1557/s43578-021-00445-6.

The newly developed constant contact pressure creep method is validated by comparing the results with data determined by uniaxial compression creep and stress dip experiments. Tests were carried out on ultrafine-grained Cu and CuAl5. Furthermore, the new CCP method was modified in order to study possible load history effects caused by the loading protocol. Additional indentation strain rate jump and constant load hold indentation creep tests were performed for comparison. The results in terms of strain rate sensitivity coefficients are very similar for uniaxial and constant contact pressure experiments, indicating a change in deformation mechanism at low strain rates. The material's response in a CLH, on the other hand, shows a rather continuous transition already at higher strain rates caused by relaxation effects. The CCP method, thus, represents a significant improvement, making it possible to investigate the local time-dependent mechanical properties of a material reliably and comparably with uniaxial tests.

---

Publication C:

**New ultra-high temperature nanoindentation system for operating at up to 1100 °C**

**Christian Minnert**, Warren C. Oliver, Karsten Durst

Materials & Design, 192 (2020) p. 108727. DOI: 10.1016/j.matdes.2020.108727.

A new ultra-high instrumented indentation system was designed for testing in the temperature range from room temperature to 1100 °C. The indenter is equipped with a 1 N high load actuator and is designed for a high machine stiffness to perform tests from small to large penetration depths. The combination of the dynamic testing capabilities (continuous stiffness measurement technique) and high frame stiffness enables the determination of correct Young's modulus and hardness data up to the maximum operational temperature. A sophisticated temperature management reduces the impact of thermal drift on the results. The indenter is installed inside a scanning electron microscope equipped with a water cooled backscattered electron detector for in-situ testing. Operating in vacuum reduces oxidation effects. The testing capabilities were demonstrated using fused silica and Mo as reference materials. Moreover, a new indentation creep methods and a temperature matching procedure were presented for the first time. Additional short-term creep test using a newly developed step load and hold creep method were performed on single crystalline Ni and compared with results from strain rate jump tests.

---

Publication D:

**Thermally activated dislocation mechanism in Mo studied by indentation, compression and impact testing**

**Christian Minnert, Hamad ur Rehman, Karsten Durst**

Journal of Materials Research, 36 (2021) p. 2397-2407. DOI: 10.1557/s43578-021-00126-4.

The brittle-to-ductile transition of body centered cubic Mo was investigated using indentation, compression and Charpy pendulum impact tests. The brittle-to-ductile transition is related to the mobility of screw dislocations which carries the plastic deformation. A maximum in strain rate sensitivity, determined by strain rate jump tests, was found at the on-set of the transition before decreasing in the ductile regime. At the same time, the activation volume starts to increase and exceeds approx.  $5 b^3$ . It turned out that the analysis of the activation volume, which is independent of the microstructure and testing method, gives an indication of the BDTT, as it depends only on the obstacle spacing. Thus, analyzing the course of the temperature dependent activation volume can be used as a complementary approach to impact testing for determining the BDTT of bcc metals.

---

## 6. Synopsis of publications

---

The following synopsis briefly summarizes the main results of the articles relevant for this thesis. The project focuses on the implementation of new test approaches and a new test device for the investigation of thermally activated deformation processes on small length scales. For this purpose, two new indentation loading protocols as well as a new in-situ indentation system with a maximum operating temperature of 1100 °C have been established.

First, two new test procedures, applying a constant contact pressure (Publications A and B [33, 34]) or a step load and hold approach (Publication C [32]) are introduced and compared in the context of conventional macroscopic experiments. Second, the new custom made high temperature indentation system is presented (Publication C [32]). Finally, HT indentation experiments are carried out to investigate thermally activated dislocation processes using CG Mo (Publication D [35]) and SX Ni [32] as reference materials. Furthermore, an alternative approach for the characterization of the brittle-to-ductile transition temperature will be outlined.

### 6.1. Transient indentation testing – method development

Various indentation test procedures have been developed in the past to investigate the (transient) mechanical response of materials and its associated deformation mechanisms based on strain rate sensitivity, stress exponent or activation volume. The results are supposed to be comparable to uniaxial experiments and at the same time offer the advantage of determining the local mechanical properties. The strain rate range in which CSR and SRJ indentations tests can be performed is, however, typically limited to  $10^{-1} - 10^{-3} \text{ s}^{-1}$  for the most available DSI systems like the G200 indenter (Keysight Technologies, USA) and the *Prometheus* HT indenter (KLA Instruments, USA) used and presented in this dissertation. Testing at very low or high strain rates therefore requires new, more advanced loading protocols.

It was shown that the SRJ method developed by Maier et al., provides comparable results to macroscopic, uniaxial experiments e.g. [111, 112]. However, if one compares indentation creep loading protocols like the CLH method with its uniaxial counterpart, clear differences can be identified in the stress profile ( $\sigma(t)$ ), which raises the question of the comparability of the different testing techniques [34].

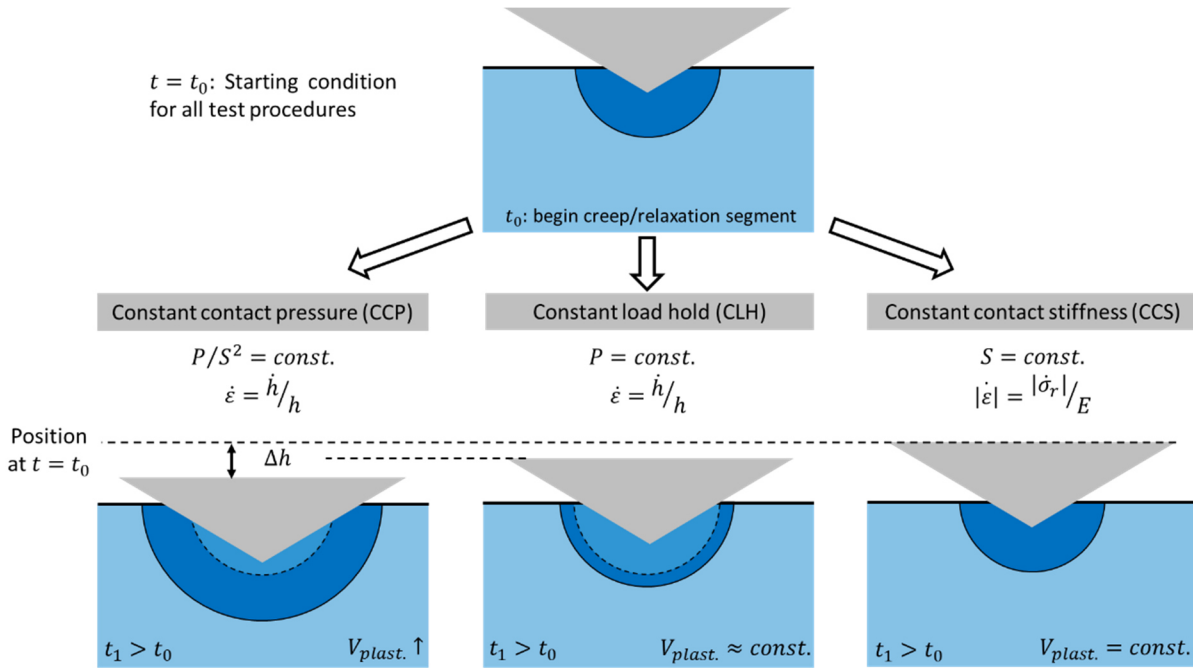


Figure 18: Schematic comparison of different contact situations during a CCP, CLH and CCS indentation creep and relaxations experiments, adapted from [33, 179].

In a CLH indentation creep experiment, the applied load is kept constant and the resulting strain rate is analyzed. Creep deformation causes a slight but continuous expansion of the plastically probed volume and an increase in contact area (Fig. 18). This leads to a decrease in the applied stress or contact pressure, as both are given by the ratio of  $P/A_c$ . The strain field within the plastic volume is self-similar and results in a constant representative strain throughout the test when pyramidal indenter geometries such as the Berkovich geometry are used. This is in contrast to uniaxial creep experiments, where the stress is kept constant and the change in strain rate is analyzed. For this reason, a new indentation creep method using a constant contact pressure approach was developed for testing at small strain rates.

Testing transients in material's response at high strain rates is accomplished by using a modified CLH method where the strain rate changes by four orders of magnitude within a short time scale. This is particularly advantageous for testing at high temperatures where long contact times can lead to severe tip wear. A schematic comparison of the different contact situations and the resulting correlations of strain rate and contact pressure, are sketched in Figure 18 for the CCP, CLH and CCS test protocol.

### 6.1.1. Long-term constant contact pressure creep testing

The CSM-based CCP loading protocol consist of two test segments, the initial strain rate controlled loading up to a predefined load or contact depth limit (here 500 nm) and the subsequent creep segment (here 3000 s). In the beginning of the CCP creep segment, the initially high contact pressure is adjusted to a previously defined, lower stress level which is held constant by controlling  $P/S^2$  (Eq. 18). The methodology is presented below using data from CCP tests on a UFG binary Cu alloy containing 30 wt.% of Zn (CuZn30).

The contact pressure adjustment is evident from the load drops at the beginning of the CCP test segment (Fig. 19a and 19b). Once the new stress level is reached (Fig. 19c), the load is again continuously increased in order to compensate for the enlargement of the plastic zone. This is in contrast to the well-established CLH indentation creep method, where the load is kept constant throughout the creep experiment. The resulting loading rate during CCP tests is significantly decreasing with contact pressure (Fig. 19b).

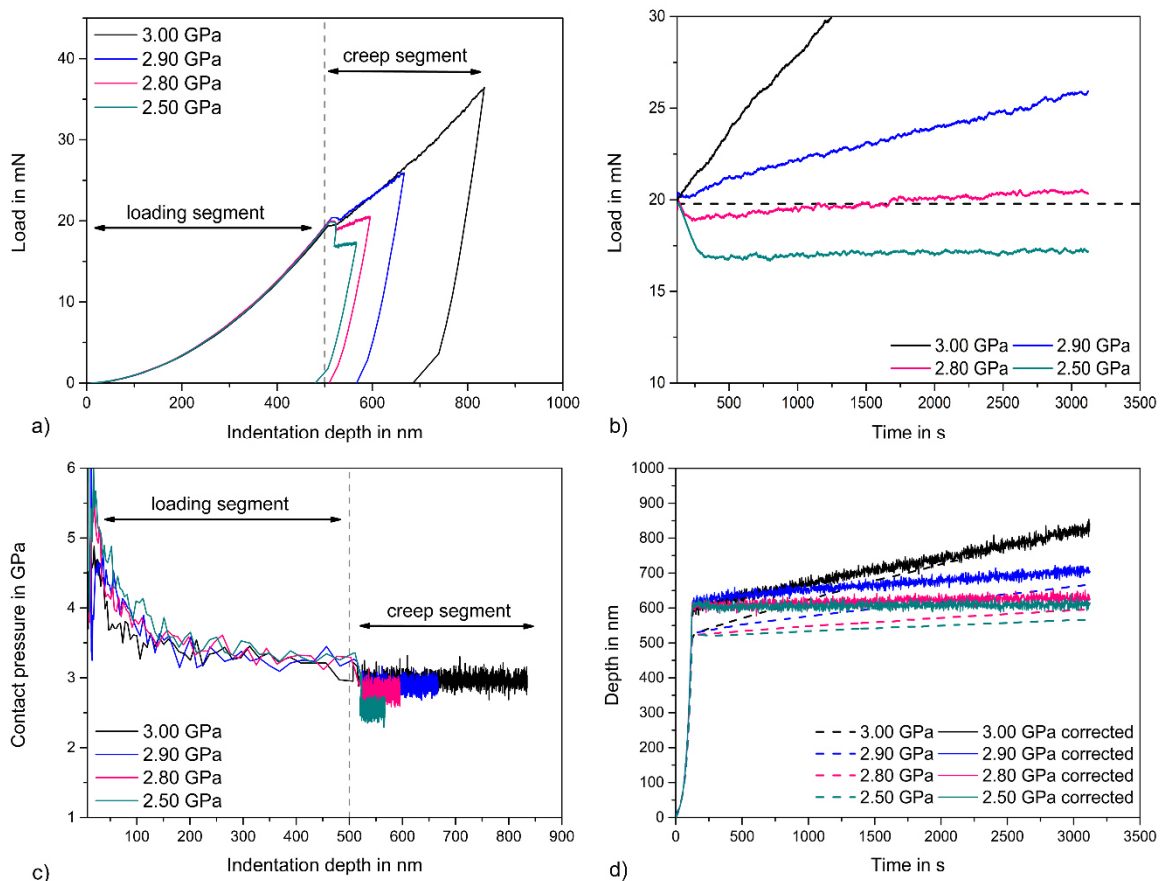


Figure 19: Constant contact pressure experiments on UFG CuZn30: a) load-displacement curves, b) applied load as a function creep time, c) contact pressure vs. depth and d) raw and corrected indentation depth over time. Reproduced with permission from Prach et al. [33], Copyright (2019), Journal of Materials Research, Springer Nature.

The contact stiffness, determined at a high frequency of e.g. 45 Hz, is used to determine an indentation depth (Fig. 19d) which is unaffected by thermal drift, pile-up and sink-in effects (Eq. 12) and used for the calculation of the creep strain rate (Eq. 13). The reduced modulus, used as an input for the calculation of the contact pressure (Eq. 18), is assumed to be depth independent.

Some differences become apparent by comparing data from a CLH and a CCP test. Figure 20a and 20b shows the raw contact pressure plotted as a function of time and indentation depth for both test methods using UFG CuZn30 as model material. In both test protocols, the load is initially applied at a constant strain rate until the depth limit of 500 nm is reached. The data in this initial segment are therefore congruent for both test procedures (Fig. 20a and 20b). The initial drop in contact pressure observed in the loading segment can be attributed to an ISE. The contact pressure is, however, constant at penetration depths of approx. 300 nm and above (Fig. 20b), the ISE is therefore not influencing the creep data determined later on.

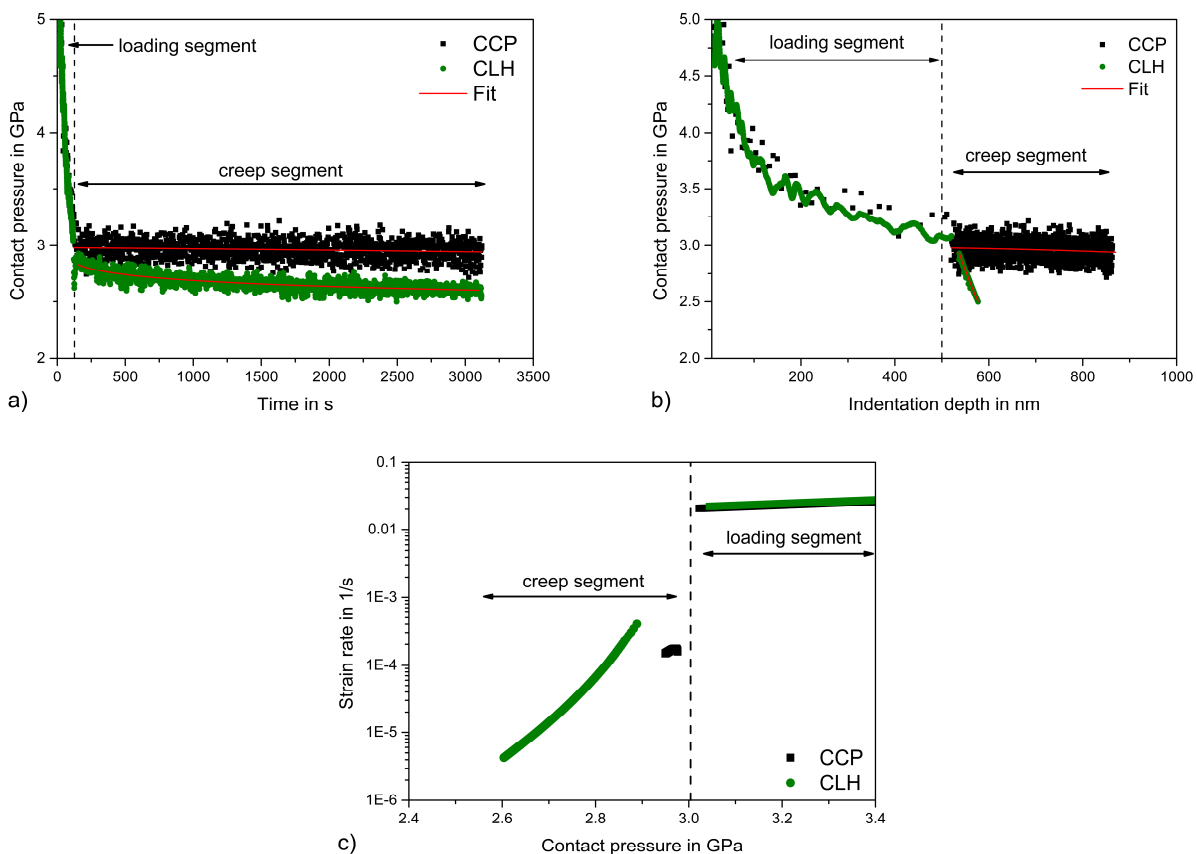


Figure 20: Comparative analysis of contact pressure and strain rate during a CCP and a CLH experiment on UFG CuZn30: a) contact pressure vs. time, b) contact pressure vs. indentation depth and c) the resulting strain rate vs. contact pressure. Reproduced with permission from Prach et al. [33], Copyright (2019), Journal of Materials Research, Springer Nature.

In the creep segment, the contact pressure is kept constant in the case of the CCP method, while it exhibits a clear transient behavior during a CLH experiment (Fig. 20a and 20b). The strain rate (Fig. 20c) changes only slightly during a CCP test due to the constantly applied driving force within the considered creep period of 3000 s. In a CLH test, the driving force decreases continuously, causing the creep strain rate to decline much more sharply. Figure 21 compares the contact pressures (Fig. 21a) and strain rates (Fig. 21b) of CCP experiments performed at different stress levels with a CLH experiment according to Maier et al. [95]. Strain rates from CCP experiments show a kind of steady state behavior already after a quite short creep time. The creep strain rate depends on the selected contact pressure. CCP tests at very low contact pressures, such as 2.5 GPa in the example presented, display a similar transient behavior as a CLH test. This behavior becomes clear considering the load-time curves shown in Figure 19b. Large contact pressures reductions to e.g. 2.5 GPa result in very small loading rates. The applied load is therefore approximately constant and thus similar to a CLH test.

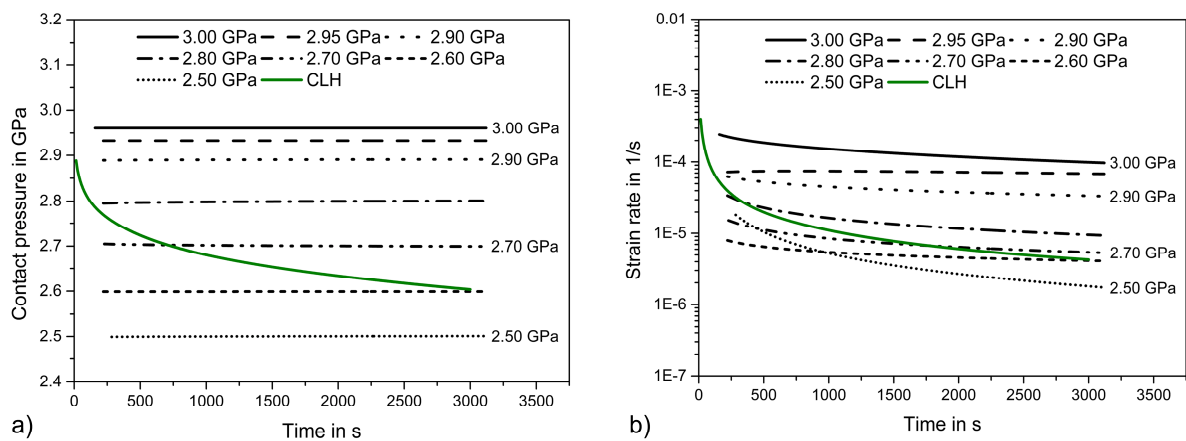


Figure 21: Comparison of CCP and CLH experiments: a) evolution of contact pressure and b) strain rate with creep time on UFG CuZn30. Reproduced with permission from Prach et al. [33], Copyright (2019), Journal of Materials Research, Springer Nature.

Finally, the residual penetration depths for both test methods are compared after different creep periods of up to 3000 s (Fig. 22). For this purpose, CCP experiments at a constant contact pressure of 3 GPa and CLH experiments at a constant load of 20 mN (similar initial stress level, Fig. 19a) were performed on CuZn30. The residual depth profiles were captured using a 3D-Laser scanning microscope (LEXT OLS4000, Olympus, USA). The penetration depth during CCP experiments increases by approx. 440 nm within 3000 s, while only a minor increase of approx. 20 nm is recorded for the equivalent CLH experiment. The marginal increase in depth during the CLH tests finally causes a stress relaxation as discussed above.

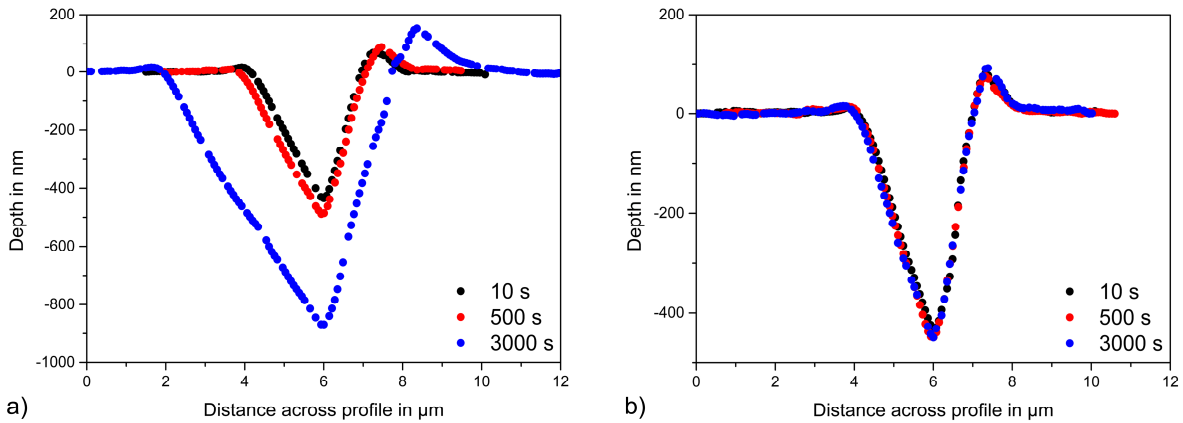


Figure 22: Depth profiles of the residual indents of a) CCP and b) CLH tests on UFG CuZn30 after different creep durations. Reproduced with permission from Prach et al. [33], Copyright (2019), Journal of Materials Research, Springer Nature.

### Application of the CCP Method

The new CCP method presented above was applied to amorphous fused silica, UFG Cu ( $d_{GS} = 425 \pm 115 \text{ nm}$ ) and binary NC or UFG Cu-X alloys. The binary Cu-X alloys contain 5 wt.% of Al (CuAl5,  $d_{GS} = 133 \pm 46 \text{ nm}$ ), Sn (CuSn5,  $d_{GS} = 62 \pm 26 \text{ nm}$ ), Zn (CuZn5,  $d_{GS} = 304 \pm 142 \text{ nm}$ ) or 30 wt.% of Zn (CuZn30,  $d_{GS} = 100 \pm 50 \text{ nm}$ ), respectively [34, 215]. All model materials exhibit a largely depth-independent hardness which is important to exclude an influence of the ISE on the results. In addition, NC and UFG metals show an increased creep deformation compared to the CG state due to the grain size dependent change in the deformation mechanisms [216].

The relations of strain rate and applied contact pressure are presented in Figure 23. Fused silica (Fig. 23a) exhibits a quite linear correlation between contact pressure and strain rate. This results in a constant strain rate sensitivity coefficient of 0.014. Data determined by the CCP and SRJ method agree well, indicating the validity of the CCP data at high strain rates. The material's response of NC and UFG Cu-X alloys, on the other hand, can be classified into a high and low stress regime, indicated by constant but different strain rate sensitivity coefficients (Fig. 23b). A similar behavior was found in literature for nanostructured Cu [42]. In the high stress regime, strain rate sensitivities and activation volumes of  $0.012/23 \text{ b}^3$  (CuSn5) to  $0.037/19 \text{ b}^3$  (CuZn5) could be determined by CSR, SRJ and CCP experiments. These data match well with results from conventional indentation SRJ tests ( $m = 0.024$  for CuAl5 [217];  $m = 0.011$  for CuSn5 [215];  $m = 0.027$  for CuZn5 [33, 215];  $m = 0.019$  for CuZn30 [33, 215]).

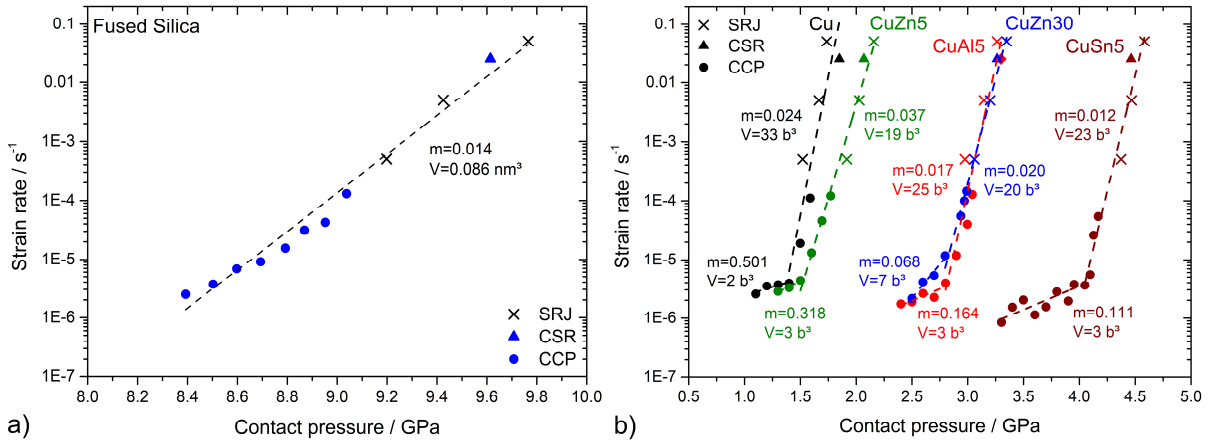


Figure 23: Correlation of strain rate and contact pressure determined by indentation SRJ, CSR and CCP experiments. Results are shown for a) fused silica, b) binary NC and UFG Cu-X alloys. Figure a) is reproduced with permission from Prach et al. [33], Copyright (2019), Journal of Materials Research, Springer Nature.

For all materials investigated, a further reduction in contact pressure results in an apparent increase in strain rate. This effect is illustrated in Figure 24 for UFG CuAl5, where a negative strain rate sensitivity coefficient of -0.547 was found. Therefore, the question arises about the limits of the CCP method in terms of the maximum possible reduction in contact pressure and the existence of a loading history effect.

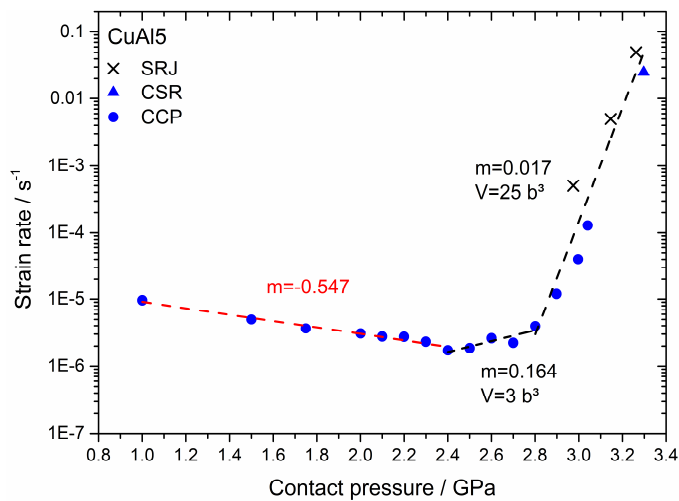


Figure 24: Apparent increase in strain rate at large contact pressure reductions in a CCP experiment, exemplified for UFG CuAl5.

## Loading history effect

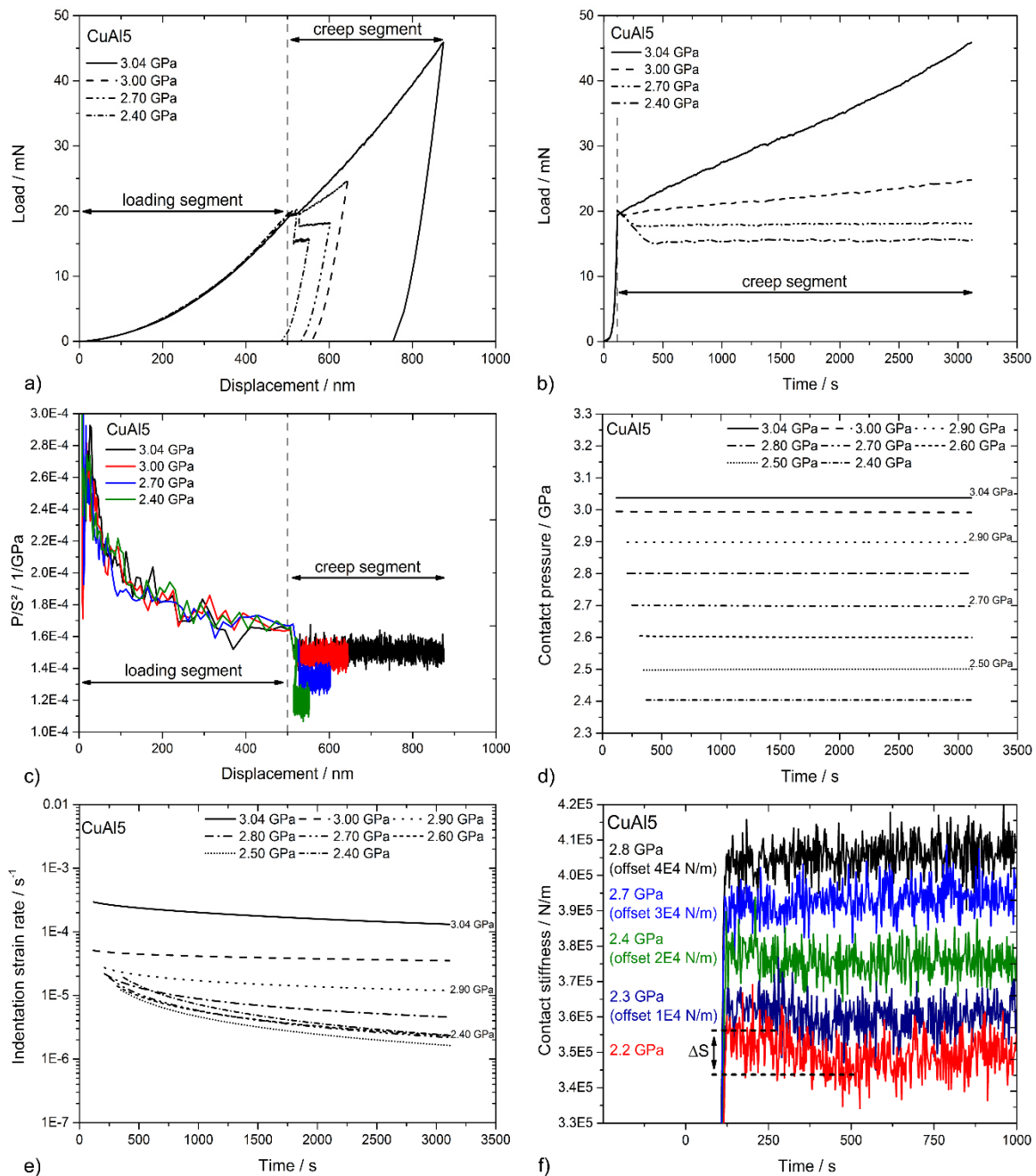


Figure 25: Constant contact pressure experiments on UFG CuAl5: a) load-displacement curves, b) applied load over time, c)  $P/S^2$  over displacement, d) fitted contact pressure profiles over time, e) resulting indentation strain rate over time and f) time dependent raw contact stiffness for different contact pressures applied. Reprinted with permission from Minnert et al. [34], Copyright (2021), Journal of Materials Research, Springer Nature.

Additional tests were performed on UFG Cu and UFG CuAl5 to address these questions and to study potential changes in the contact situation caused by the partial unloading at the beginning of the CCP segment. The potential loading history effect is investigated by CCP experiments with incremental  $H$  reduction events which are compared to the “standard” CCP method

---

presented in section 6.1.1. Finally, the CCP method was validated by uniaxial constant stress and stress dip experiments [34].

The load-displacement and load-time plots of single unloading CCP tests applying contact pressures between 2.40 and 3.04 GPa on UFG CuAl5 are shown in Figure 25a and 25b. The general behavior is similar to previously discussed data on UFG CuZn30 (Fig. 19a and 19b). The  $P/S^2$  data controlled within the creep segment to keep the contact pressure (Fig. 25d) constant are displayed in Figure 25c. A reduction in contact pressure results in lower strain rates (Fig. 25e). For low contact pressures (e.g. 2.2 GPa and 2.3 GPa for CuAl5), the analysis of the contact stiffness exhibits an initial decrease ( $\Delta S$ ) of up to 3% at the beginning of the creep segment (Fig. 25f) before increasing again with progressing creep time and penetration depth. In this situation, an apparent increase in deformation strain rate and consequently a negative  $m$  is observed, as mentioned earlier.

The occurrence of a negative SRS is associated with a slight decrease in  $S$ . The contact stiffness or its decrease at the beginning of the CCP creep segment (Fig. 25f) can, thus, be identified as the limiting factor for the maximum stress reduction since a changing  $S$  is related to changes in the contact situation. At large stress reductions, the contact may no longer be fully plastic and the elastic properties of the sample may become dominant. For UFG Cu and CuZn5, the stress could be reduced most by 37% while for fused silica, the maximum reduction is only 12%. All other alloys investigated allow a stress reduction of 14-26% [34].

Additional CCP experiments with incremental unloading events ( $\Delta H = 0.1 - 0.2 \text{ GPa}$ ) were performed to investigate the potential presence of a loading history effect. The load-displacement data of these tests are illustrated in Figure 26a. The unfiltered raw data of contact pressure is plotted in Figure 26b as a function of creep time. The comparison of CCP data from experiments with a single or multiple stress reduction events (Fig. 26c) shows a good agreement. Moreover, the minimum contact pressure could not be further reduced by the incremental unloading procedure. This clearly demonstrates that the results are not affected by a loading history effect [34].

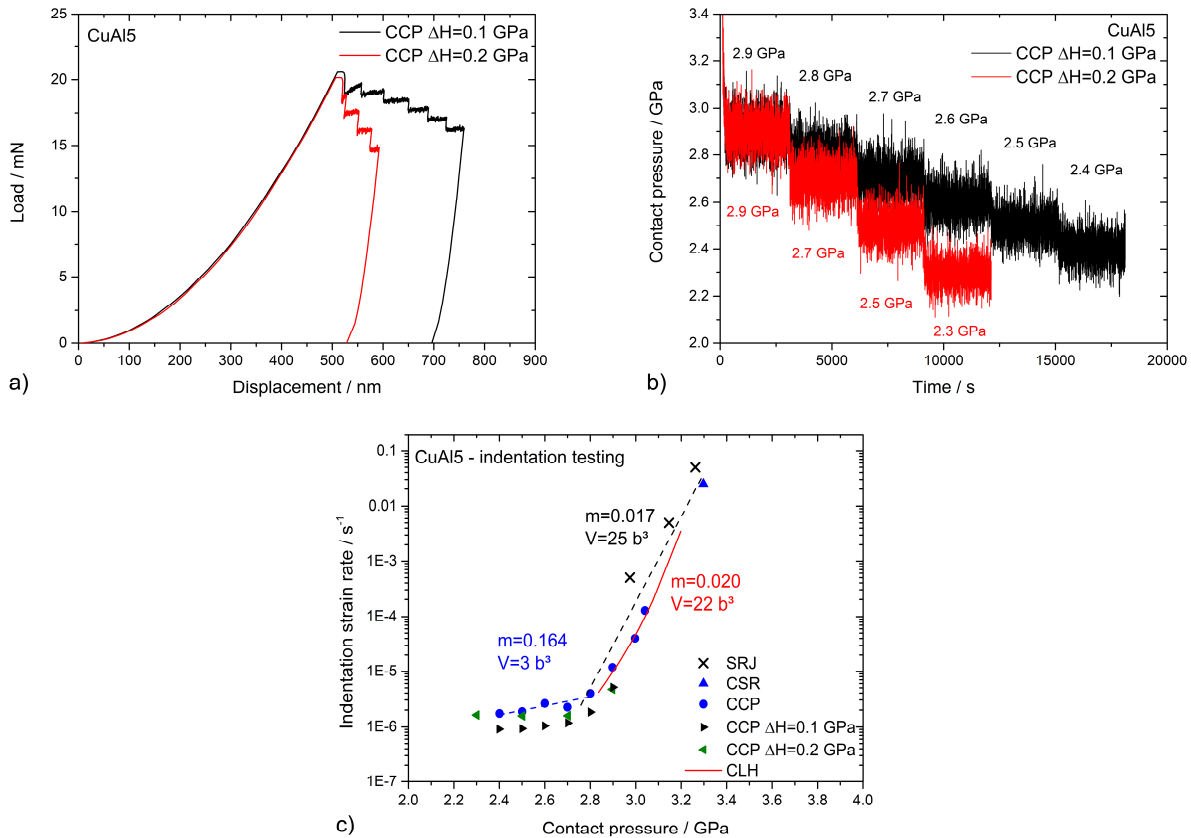


Figure 26: Constant contact pressure test with incremental unloading events: a) load-displacement curves, b) raw contact pressures over time and c) indentation strain rate over contact pressure for SRJ, CSR, CCP and CLH experiments. An equal creep duration of 3000 s was chosen for CCP and CLH experiments. Reproduced with permission from Minnert et al. [34], Copyright (2021), Journal of Materials Research, Springer Nature.

### Validation of the CCP method

The newly developed CCP method was validated using macroscopic, compression stress dip tests on UFG Cu and CuAl5. The results are plotted in Figure 27. The indentation stress or contact pressure is converted to an equivalent uniaxial stress (Eq. 22) by a constraint factor of 3.0 for UFG Cu and 2.8 for UFG CuAl5 [95, 111]. The comparison of indentation and uniaxial test data clearly shows the same trend and can be distinguished in a high and a low stress regime. For UFG Cu, a very similar course of indentation and uniaxial data was found, whereas some differences occur in the low stress regime of UFG CuAl5. This behavior might be related to grain coarsening within the plastic zone below the indenter, which is more pronounced than in compression samples due to the higher stresses applied [90, 217-219].

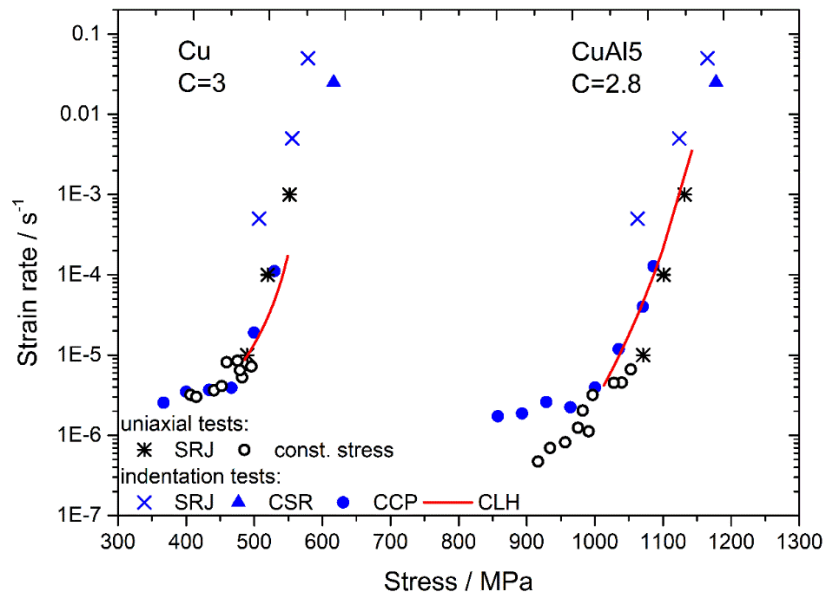


Figure 27: Comparison of uniaxial constant stress, stress dip experiments and indentation data on UFG CU and UFG CuAl5. Reprinted with permission from Minnert et al. [34], Copyright (2021), Journal of Materials Research, Springer Nature.

Dislocation annihilation and stress-assisted grain growth led to a softening of the material. The microstructure of UFG Cu is most susceptible to stress mediated grain growth and also exhibits the largest change in rate sensitivity between the two regimes. Alloying with substitutional atoms like Al, Sn and Zn causes pinning effects at grain boundaries and dislocations. The microstructure is, thus, more stable resulting in a less pronounced change in  $m$ . In the low stress regime of CuAl5, the difference between indentation and uniaxial data can be attributed to different driving forces for stress-driven grain coarsening. This is consistent with previous studies, where stronger grain coarsening was also observed within the plastic zone below an indent than in a compression specimen, due to the three-times higher stresses applied in an indentation experiment [90, 217-219].

The material's response of fused silica and Cu-X alloys is analyzed in terms of  $m$  and  $V$ . Alloy-specific Burgers vectors were used for the calculation of the activation volumes [220, 221]. The results of DSI and uniaxial experiments are summarized in Table 1 and Table 2.

Table 1: Results from indentation CSR, SRJ, CCP and CLH experiments. Data taken from [33, 34, 215].

Material	$d_{GS}$ in nm	Method	High stress regime			Low stress regime		
			$m$	$V$ in nm <sup>3</sup>	$V$ in b <sup>3</sup>	$m$	$V$ in nm <sup>3</sup>	$V$ in b <sup>3</sup>
Fused silica	-	CCP <sup>2</sup>	0.014	0.086	-	-	-	-
Cu	425 ±115	CCP <sup>2</sup>	0.024	0.551	33	0.501	0.033	2
		CLH	0.047	0.301	18	-	-	-
CuAl5	133 ±46	CCP <sup>2</sup>	0.017	0.422	25	0.164	0.051	3
		CLH	0.020	0.371	22	-	-	-
CuSn5	62 ±26	CCP <sup>2</sup>	0.012	0.401	23	0.111	0.052	3
CuZn5	304 ±142	CCP <sup>2</sup>	0.037	0.321	19	0.318	0.051	3
CuZn30	100 ±50	CCP <sup>2</sup>	0.020	0.356	20	0.068	0.124	7

Table 2: Results from compression strain rate jump and constant stress experiments [34, 215].

Material	$d_{GS}$ in nm	High stress regime			Low stress regime		
		$m$	$V$ in nm <sup>3</sup>	$V$ in b <sup>3</sup>	$m$	$V$ in nm <sup>3</sup>	$V$ in b <sup>3</sup>
Cu	425 ±115	0.026	0.534	32	0.140	0.117	7
CuAl5	133 ±46	0.012	0.557	33	0.048	0.152	9

In the indentation high stress regime, strain rate sensitivities of 0.012-0.037 and activation volumes of 19-33 b<sup>3</sup> could be determined by CSR, SRJ and CCP experiments on UFG Cu and NC or UFG Cu-X alloys. The SRS coefficient of UFG Cu coincide with values of 0.009-0.031 published in literature and uniaxial experiments of this work [52, 217, 222-227]. Furthermore, good consistency with reference values from literature was also found for the other alloys investigated [33, 215, 217]. In the low stress regime, considerably higher  $m$  values of 0.068-0.501 and activation volumes of 2-7 b<sup>3</sup> were found indicating a change in deformation mechanism [42, 43].

The well-established CLH indentation creep method provides strain rate sensitivity coefficients and activation volumes of 0.047/18 b<sup>3</sup> for UFG Cu and 0.020/22 b<sup>3</sup> for UFG CuAl5, which is somewhere in between the data determined in the high and low stress regime of CCP tests. The change in  $m$  is rather continuous indicating relaxation processes to be dominating the materials

<sup>2</sup> Results of the high stress regime are based on CSR, SRJ and CCP tests.

---

---

behavior. This behavior is comparable to the results of uniaxial stress relaxation tests on Cu [43].

For fused silica a constant  $m$  value of 0.0139 was found correlating with an activation volume of  $0.0861\text{nm}^3$ . However, the data show a slight scatter, so that a low and high stress regime might be identified here as well [33]. Nevertheless, the  $m$  and  $V$  values agree with data from *Zehnder et al.* [228], who found a SRS coefficient of 0.0143 and an activation volume of  $0.0793\text{ nm}^3$ . The constant SRS implies that there is no strain rate dependent change in the deformation behavior of amorphous fused silica.

### **Deformation mechanisms in binary NC and UFG Cu alloys**

According to Blum et al. [53, 54, 102, 229-233], Milička [234-236] and Sun et al. [54, 233], the material's response of a uniaxial stress dip depends on the amount of stress reduction. It is related to the dislocation motion and the balance of dislocation generation and annihilation processes. For small stress reductions, dislocation glide and dislocation generation is dominating the deformation behavior, while for large stress reductions relaxation processes become significant. Relaxation processes are related to a reversal of the dislocation motion direction so that annihilation at the grain boundaries takes place. Thus, the strain rate immediately after stress reduction is caused by the net flow (forward and backward flow) of dislocations, so that negative strain rates can be observed if the backward flow is dominant. With increasing test duration and progressive deformation, dislocation generation dominates again and the deformation behavior enters a kind of steady state.

A similar behavior can be identified from the determined activation volumes in this work. Large  $V$  in the high stress regime indicate deformation based on dislocation nucleation and motion, while low values at large stress reductions can be attributed to dislocation annihilation and grain boundary mediated processes [20, 42, 43]. It should be noted, however, that multiple deformation mechanisms may be involved simultaneously during deformation. This is in particular relevant when testing a transient material behavior where no steady state condition has been reached. The calculated activation volume reflects, thus, only an average with limited significance for individual processes.

The constant stress approach was implemented for the first time in an DSI method. It is equivalent to a uniaxial constant stress test, yielding to very similar results, whereas the CLH

---

method is a kind of a relaxation-creep method. The creep properties at low strain rates ( $< 10^5 s^{-1}$ ) cannot be determined correctly using the CLH loading protocol as it is significantly affected by relaxation effects. Nevertheless, there are also clear differences between the standardized uniaxial test methods and the new experimental approach presented here.

In a uniaxial test, the sample volume is constant and the applied strain is continuously increasing. This is in contrast to an indentation creep experiment, where mostly self-similar indenter geometries are used which applies a constant average plastic strain, e.g. 7.16% for a Berkovich indenter [195]. Furthermore, in a CCP test, the probed volume is continuously increasing as the load has to be ramped in order to keep the contact pressure constant (Eq. 18, Fig. 19a-c). In consequence, new previously undeformed material will be consumed by the expanding plastic zone. It is therefore not clear whether primary or secondary creep mechanisms control the creep response of the material. A steady state in microstructure can, thus, never be reached in an indentation creep experiment. However, also the uniaxial constant stress experiments do not reach a steady state behavior for the applied test parameters in this work. A steady state condition might be achieved if the test duration will be significantly extended and the microstructure does not change with deformation. However, the expanding test volume also offers an advantage over macroscopic test procedures. In the case of very unstable microstructures, where grain coarsening can occur even during a uniaxial compression test, new material in its initial state is continuously deformed. This might reduce the effect of grain coarsening on the determined creep parameters.

### **6.1.2. Step load and hold test protocol**

Indentation testing at high temperatures is quite challenging, as a sophisticated thermal management must be established to achieve low thermal drift rates. In addition, tip wear is currently the biggest issue when testing materials such as Ni-based superalloys at high temperatures due to their high hot hardness and chemical interaction with the indenter material used. The amount and impact of tip wear on test results can be reduced by analyzing data at large penetration depths as well as by reducing the contact times between tip and specimen. The reduction of contact time requires the development of new loading protocols, in which, the transient material behavior can be investigated on a short time scale. For this purpose, a modified loading protocol was developed for testing transients in the high to intermediate strain rate regime. The method is based on a quasi-static CLH method with an initial step-like loading which was developed by Phani and Oliver [148, 149].

The newly developed test procedure, in the following called, step load and hold method, consists of two different test segments. In the first segment, the tip is slowly brought into contact with the sample (no impact) and afterwards loaded in a stepwise manner (Fig. 28a-c). A high indentation strain rate can be achieved by applying a load of e.g. 95 mN with a loading rate of e.g. 200 mN/s. The load will then hold constant for a short time e.g. 1.5 s before the static load is superimposed with a dynamic displacement (CSM technique) in the second test segment [32]. The dynamic displacement was accomplished, by applying a constant load fraction ( $P_{AC_0}/P_{DC}$ ) as suggested by Phani et al. [185, 186] (section 4.3.3). For the experiments performed in this work, a load fraction of 0.1 was used. At the same time, the mean load was slightly decreased by about 0.2% compared to the load at the end of the first test segment to compensate for the superimposed dynamic load. The corresponding load-displacement and load-time curves are shown in Figure 28a and 28b.

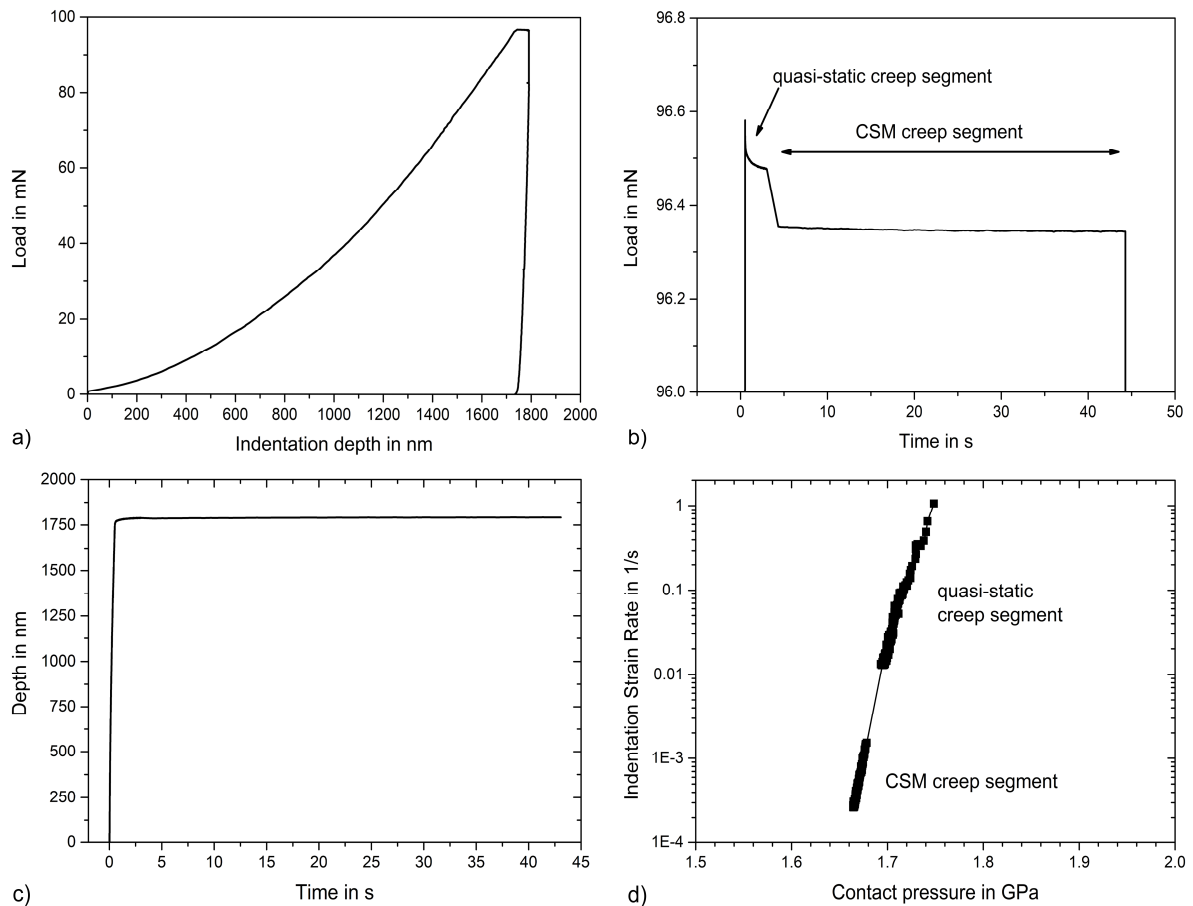


Figure 28: Step load and hold test on SX Ni: In a) load-displacement curve, b) applied load over time, c) time-dependence of indentation depth and d) indentation strain rate over hardness. Data reproduced with permission from Minnert et al. [32], Copyright (2020), Materials & Design, Elsevier Ltd.

---

The impact of thermal drift on the hardness ( $H = P/A_c$ ) is negligible during the first test segment, due to the short test duration. In the second test segment, the continuously determined contact stiffness (CSM) is used to determine a pile-up and drift independent contact depth and hardness (Eq. 12 and 18). The change in depth, as well as the resulting strain rate as a function of hardness is shown in Figure 28c and 28d. A broad strain rate interval can be scanned within a short time interval (Fig. 28d) by the combination of the step load (high strain rate regime) and the CSM based CLH segment (intermediate to low strain rate regime) [32].

Engineering materials frequently exhibits local inhomogeneities. Applying a wide range of strain rates at an almost constant sample volume also has the advantage that these inhomogeneities do not affect the measured transient data as much as testing two different volume elements of the sample. In addition, due to the short contact times, more tests can be carried out, which improves the statistics of the results [148]. The long-term behavior or the response at very slow strain rates ( $< 10^{-5} \text{ s}^{-1}$ ), however, cannot be determined with adequate accuracy. The reasons for this are discussed in the next section.

## 6.2. New in-situ high temperature indentation system

The novel, custom made in-situ high temperature DSI system presented below was developed by *KLA Instruments* (Oak Ridge, TN, USA) [32]. The operation temperature ranges from room temperature (RT) to 1100 °C. This provides, for the first time, the ability to characterize the local mechanical properties of superalloys or TBC systems at or close to their actual operating temperature.

An illustration of the device is shown in Figure 29. The system is equipped with a load-controlled actuator. Its maximum load of 1 N can be applied with a load resolution of 6 nN, a noise floor of 0.9  $\mu\text{N}$  was found. The maximum displacement of the system is 80  $\mu\text{m}$ . The displacement signal can be determined with a resolution of 0.04 nm, where the noise floor is less than 0.1 nm. The frame stiffness is considerably higher than 1 MN/m even at the maximum test temperature. Dynamic tests can be performed with a maximum frequency of 1 kHz, which allows a continuous determination of contact stiffness (CSM technique) [32]. Moreover, testing at high dynamic frequencies provide higher (partial-) unloading rates than in quasi-static experiments. This ensures that the required minimum unloading rate (ISO 14577) is exceeded even at high creep rates and provides therefore reliable data [156].

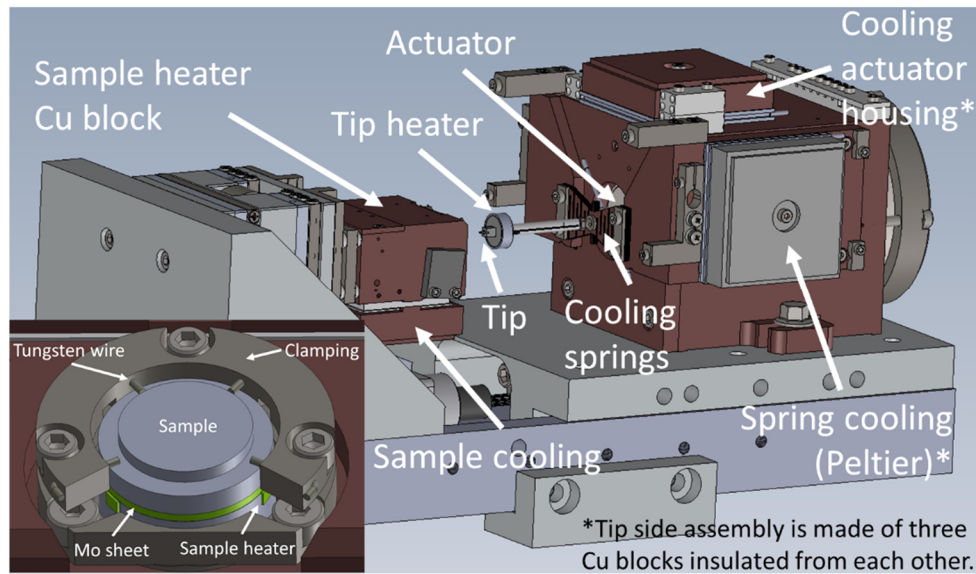


Figure 29: Illustration of the Prometheus in-situ high temperature indenter. The heat shield has been omitted for presentation reasons. Reprinted with permission from Minnert et al. [32], Copyright (2020), Materials & Design, Elsevier Ltd.

Two independently adjustable heating elements on the sample and the tip side allow the setting of an isothermal contact. The temperatures are measured by means of thermocouples type K and controlled via PID loops. One thermocouple is placed close to the tip to measure its temperature ( $T_{tip}$ ) as accurately as possible. The second thermocouple for measuring the sample temperature ( $T_{sample}$ ) is placed between the sample heating element and the sample, for this purpose a slot was cut into the Mo sheet which protects the sample heater (insert Fig. 29). Alternatively, the thermocouple can also be inserted into a lateral drill hole of the specimen (Fig. 30).

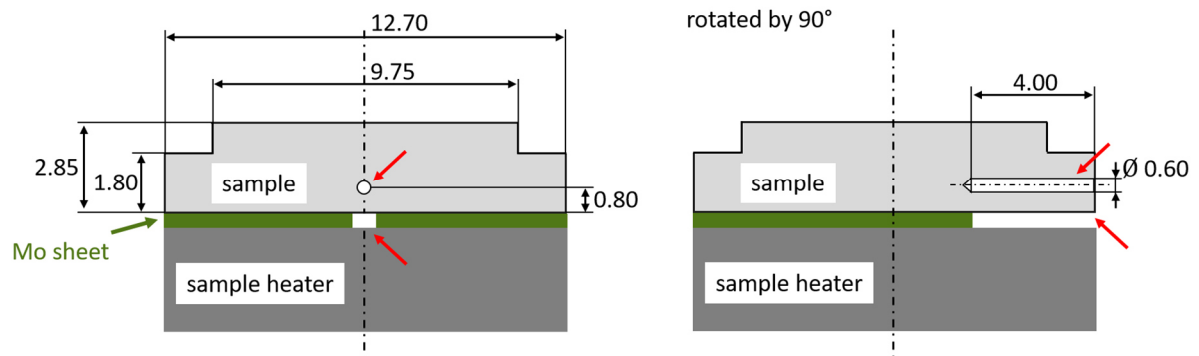


Figure 30: Schematic cross-section of a standard sample, the Mo sheet beneath and the sample heater. The thermocouple for measuring the sample temperature can be inserted either into a slot in the Mo sheet or into a lateral bore inside the specimen. The two positions for the thermocouple are marked by the red arrows.

The specifications of the system are not changing with operation temperature due to a sophisticated cooling system, which keeps the actuator always close to room temperature. The cooling system consists of a heat shield, cooling springs, Peltier elements, and actively cooled Cu blocks [32].

The indenter is installed in a W-cathode VEGA 3 GMH (Tescan, Czech Republic) scanning electron microscope equipped with an active vibration damping unit of the vacuum chamber, a secondary electron (SE) as well as a water cooled backscattered electron (BSE) detector for imaging at up to 1100 °C [32].

The capabilities of the new system were demonstrated by test measurements on reference materials like fused silica (low temperature range) and Mo (high temperature range).

### 6.2.1. Temperature verification and matching

The accuracy of the temperature measurement was verified by examining the  $\alpha$ - $\gamma$  phase transition of pure iron. For this, a Fe sample was mounted and the thermocouple was placed into the lateral drill hole (Fig. 30). The sample temperature (Fig. 31, black curve) was continuously increased by 2 K/min and the corresponding heating power (blue curve) was monitored. The onset of the endothermic phase transition, indicated by oscillations of the temperature slope, is observed at about 927.5 °C. This is close to the phase transition temperature reported in literature (911 °C) [237].

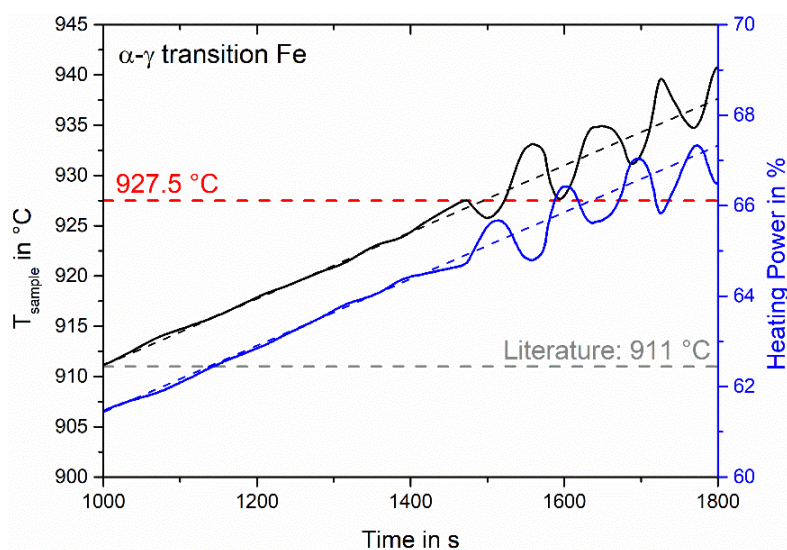


Figure 31: Sample temperature and applied heating power plotted as a function of time at the endothermic  $\alpha$ - $\gamma$  phase transition of pure iron (Armco). A constant heating ramp of 2 K/min was used in the experiment.

The small offset between literature and experimentally determined transition temperature can be explained by a temperature gradient during heating. The experimentally determined transition temperature is thus about 1.4% (in absolute T) higher than the expected transition temperature. This demonstrates the accuracy of the measurement of the absolute test temperature.

The indenter tip was used as a temperature probe for adjusting the sample surface temperature to ensure an isothermal contact. Even slight temperature mismatches can be detected as the tip temperature is very sensitive due to its small heat capacity. The isothermal contact was achieved by applying a semi-automated temperature matching procedure before testing. This procedure was first presented in Publication D [32].

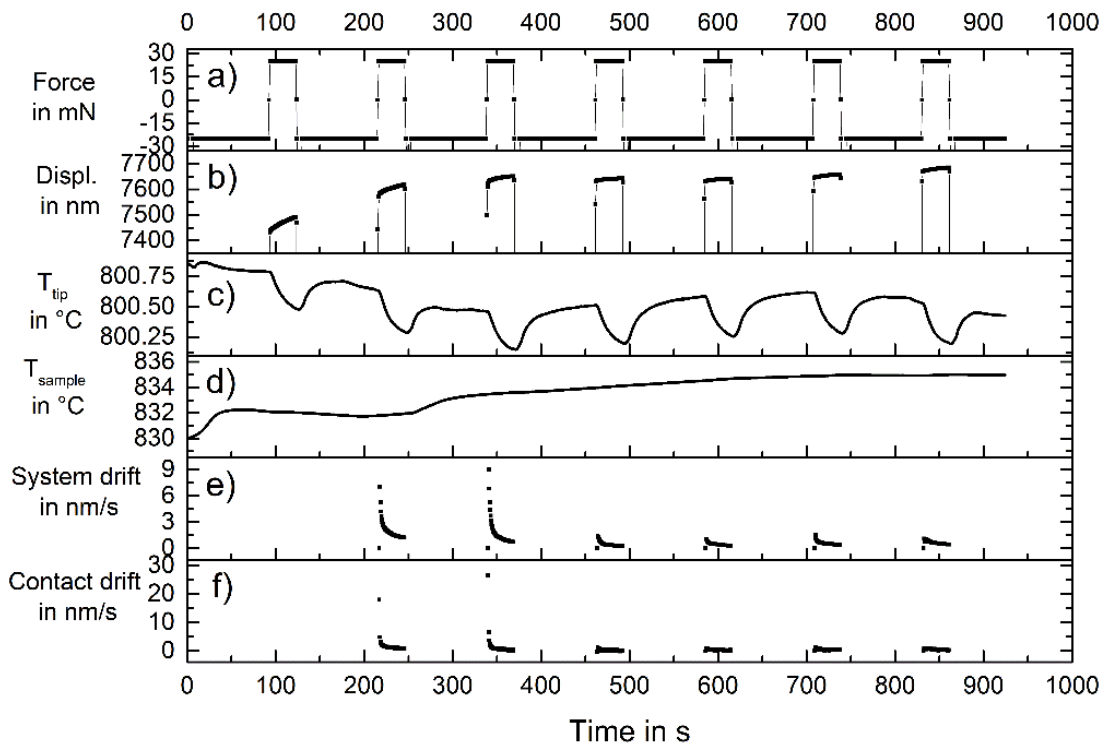


Figure 32: Semi-automated temperature matching procedure for setting an isothermal contact, exemplarily illustrated for SX Ni at 800 °C: a) applied force, b) resulting displacement, c) tip temperature, d) sample temperature, e) system drift and d) contact drift plotted vs. time. Reprinted with permission from Minnert et al. [32], Copyright (2020), Materials & Design, Elsevier Ltd.

In the first step, the tip was brought in contact with the sample surface by applying a force of 30 mN for 30 s (Fig. 32a). If a temperature difference between tip and sample is present, thermal expansion or contraction, mainly on the tip side (smaller heat capacity) will occur,

causing a change in the displacement signal (Fig. 32b). After a contact time of 30 s, the tip is removed from the sample for 90 s to allow the temperature to settle (Fig. 32c and 32d) before it is brought back into contact. The thermal drift can be determined by analyzing the displacement signal during the contact and between the individual contact cycles.

A distinction between system drift (Fig. 32e) and contact drift (Fig. 32f) can be made. The system drift is caused by a thermal expansion/contraction of the frame, which mainly occurs during the heating or cooling process. It can be determined by the change in displacement between the individual loading cycles (Fig. 32b). The contact drift, on the other hand, is a measure of the temperature difference between the tip and the sample surface. It can be identified by the slope of the displacement signal during contact (Fig. 32b). The contributions of system and contact drift can be determined largely independently of each other, which significantly reduces the time required for the temperature adjustment. The impact of creep deformation on the displacement signal is reduced by testing the same position repetitively. The relevant test parameters during the  $T$  matching procedure at 800 °C are plotted in Figure 32 as an example.

The temperature profiles during CSR experiments on fused silica at 200 °C and Mo at 1100 °C are plotted in Figure 33. A very good temperature stability was achieved after matching the temperature resulting in low thermal drift rates of less than 0.2 nm/s even at the maximum test temperature. The difference between tip and sample temperature (Fig. 33b) is due to the offset in the positions of the thermocouples and the temperature gradient within the sample.

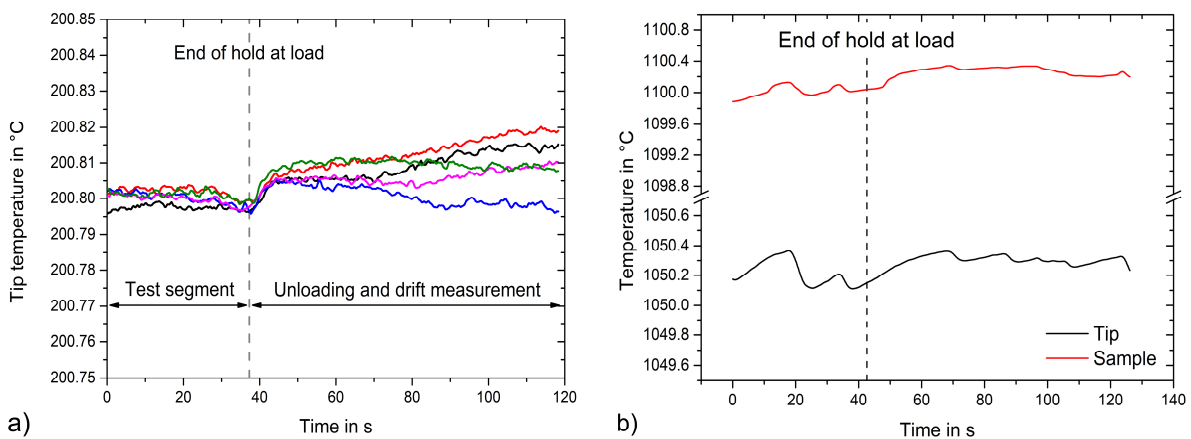


Figure 33: Temperature profiles of the tip, respectively, tip and sample when testing a) fused silica (low temperature range) and b) Mo (maximum temperature). Reproduced with permission from Minnert et al. [32], Copyright (2020), Materials & Design, Elsevier Ltd.

## 6.2.2. Reference measurements on CG Mo

Reference measurements were performed on commercially pure (99,95%, ASTM-B-387 Type 361) Mo to demonstrate the functionality of the system up to its maximum operating temperature. A CSM-based CSR method and a sapphire Berkovich indenter was used for these tests.

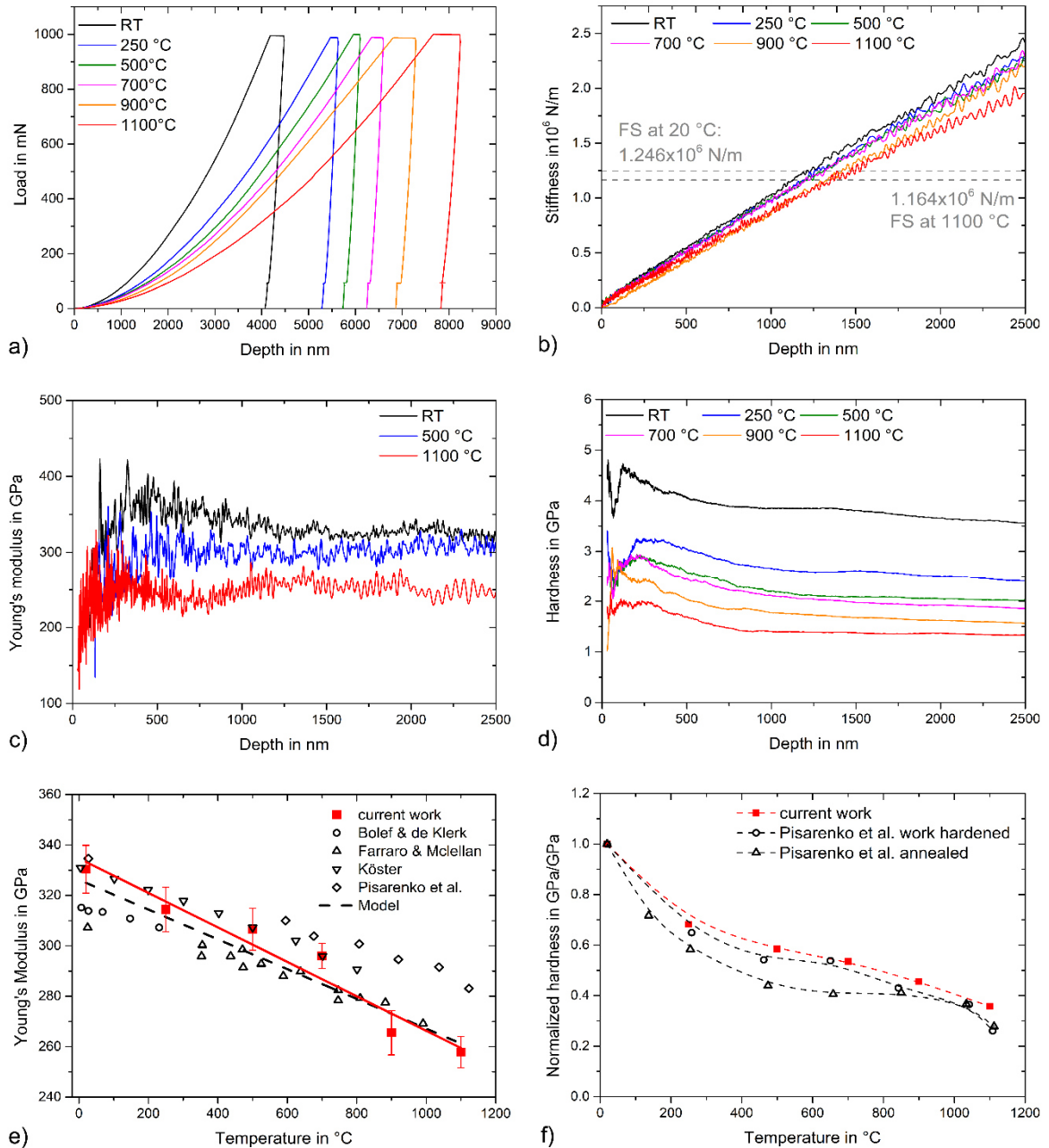


Figure 34: Constant strain rate test on Mo at different temperatures: a) load-displacement curves, b) corresponding contact stiffness, c) Young's modulus profiles, d) hardness profiles, e) averaged  $E$  and f) normalized hardness. Reprinted with permission from Minnert et al. [32], Copyright (2020), Materials & Design, Elsevier Ltd.

---

Representative load-displacement curves determined at different temperatures are illustrated in Figure 34a. Increasing the test temperature leads to a softening of the material and thus to larger indentation depths. More interesting, however, is the depth-dependent course of the contact stiffness (Fig. 34b). The contact stiffness increases linearly with penetration depth, which is essential for the correct determination of Young's modulus data. Stiffness data recorded at 900 °C and 1100 °C differ slightly from data determined at lower temperatures. Nevertheless, also at 900 °C and above, a linear relationship up to a penetration depth of about 1500 nm can be observed. Data at higher penetration depths was therefore not considered in the analysis.

The slight decrease in stiffness with increasing temperature can be attributed to an increasing compliance of the indentation system (tip, shaft, frame, specimen holder, etc.). This is taken into account in the analysis by an adjustment of the frame stiffness to achieve a depth independent  $E$ . Furthermore, the temperature dependence of sapphire's Young's modulus is considered in the data evaluation. The frame stiffnesses at room temperature and 1100 °C are shown as dashed lines in Fig. 34b for comparison. It drops only slightly due to the sophisticated thermal management where the temperature of most components does not change significantly.

The temperature and depth dependent  $E$  and  $H$  profiles are visualized in Figure 34c and 34d. The averaged modulus data are plotted in Figure 34e in comparison with literature data determined by pulse-echo methods. An excellent coincidence was found for both, normalized  $H$  and  $E$ , up to 1100 °C. This is the first time that Young's moduli have been correctly determined at temperatures of 1000 °C and above using DSI technology. Previous test systems were not able to accomplish this as they did not apply the CSM technique and did not achieve the high unloading rates required [30, 156].

### 6.2.3. Tip wear and thermal expansion

Nevertheless, indentation testing at high temperatures remains challenging. Tip wear is currently the biggest issue, in particular when testing materials such as Ni-based superalloys at high temperatures due to their high hot hardness and chemical interaction of the indenter and sample material. The indenter material must therefore be carefully selected to be compatible with the specimen material and test conditions (temperature and atmosphere). The high temperature experiments on Mo and Ni are performed with Berkovich indenters made of sapphire.

The extent of tip wear is evident by the change in depth-dependent contact area after testing Mo and Ni at different temperatures. It is obvious that there is no significant change when testing Mo (Fig. 35a). This implies that Mo and sapphire are largely inert to each other and the mechanical wear is insignificant. This is in accordance to literature [27]. If, on the other hand, Ni is tested, strong changes in the tip shape function already occur in the medium temperature range (Fig. 35b). This is caused by dissolution of sapphire on contact with Ni [27]. For this reason, the tip had to be replaced after testing at 1009 °C.

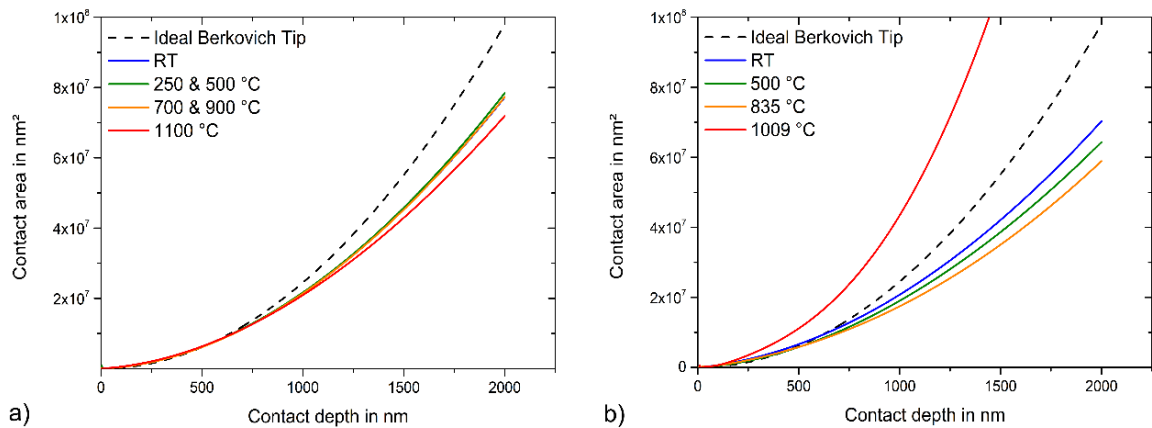


Figure 35: Changes in contact area of Berkovich sapphire tips used for testing a) Mo and b) Ni at high temperatures. Reprinted with permission from Minnert et al. [32], Copyright (2020), Materials & Design, Elsevier Ltd.

Another parameter affecting accurate data determination besides tip wear is thermal expansion of the indenter tip. The tip area function is commonly determined using reference measurements on a material with well-known properties, such as fused silica at room temperature. It is then assumed to be constant and temperature independent [127].

This assumption is valid for self-similar, conical or pyramidal indenter geometries as long as the coefficient of thermal expansion is isotropic as for diamond. Real indenter tips, however, always exhibit a certain amount of manufacturing-related tip rounding, which increases progressively during operation. The tip radius of the spherical region near the apex of the indenter therefore increases with increasing temperature. This results in a temperature dependent deviation in the tip area function of typically  $\leq 0.5\%$  at temperatures of up to 1000 °C for the most indenter materials except sapphire and tungsten carbide. These exhibit a larger thermal expansion coefficient [24, 27].

For high temperature experiments in this work, large penetration depths were chosen where the indentation depth is significantly larger than the tip radius. The effect of the temperature

---

dependent change in tip radius can therefore be neglected. The sapphire tips used, however, do not exhibit an isotropic thermal expansion behavior. This results in a temperature dependent change of the equivalent cone angle of the self-similar tip geometry.

Considering the anisotropy in thermal expansion of a sapphire single crystal, the projected contact area at 1100 °C ( $\Delta T = 1080 K$ ) is slightly overestimated by approx. 0.18%. This estimation is based on the assumption of two constant thermal expansion coefficients for the *c*-axis (indentation axis) and the *a*-axis (orthogonal to the indentation axis) of the crystal [238]. Thermal expansion of the indenter tip was not considered in the data evaluation in this work due to its minor influence on the results and the fact that the exact orientation of the tip is not known since it is not routinely checked by the tip manufacturers.

### **6.3. High temperature indentation testing – transient material behavior**

In the following, the high temperature indentation technique is applied to study thermally activated dislocation motion and its related BDT using bcc Mo as reference material. Additional uniaxial compression and Charpy pendulum impact tests are carried out to evaluate the results [35]. Furthermore, the newly developed HT indenter is used in combination with the SLH method to investigate the transient material response of Ni at temperatures of up to 1100 °C. The results are then assessed on the basis of data from conventional experiments [32].

#### **6.3.1. Thermally activated dislocation motion in bcc Mo**

Dislocation mobility in bcc metals like Mo is strongly temperature and strain rate dependent, causing a brittle behavior at low and a ductile behavior at high temperatures as discussed before. The BDT is conventionally investigated using Charpy pendulum impact tests (section 2.1.1) in order to determine the BDTT. Its exact determination is quite challenging and can vary depending on the definition used [78]. A better understanding of the active deformation mechanisms might be provided by the activation volume.

The question therefore arises as to how the activation volume determined by a SRJ experiment correlates with the dislocation mobility and whether it can be used for the definition or at least as an indicator for the BDTT as it is an extrinsic material parameter dependent on testing conditions and microstructure of the material [79-81].

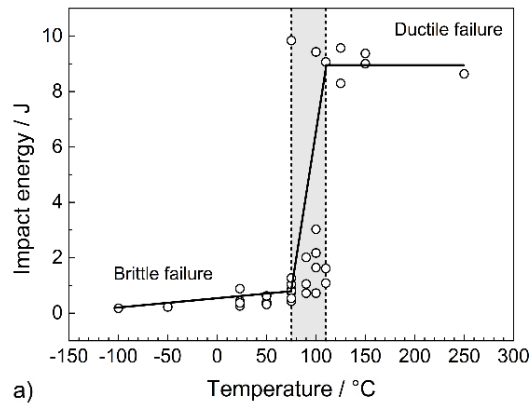


Figure 36: Brittle-to-ductile transition of CG Mo investigated by Charpy pendulum impact experiments: a) the absorbed energy shown for different test temperatures, the BDT range is highlighted by the gray area. Representative samples tested at different temperatures ranging from RT to 250 °C clearly indicates the transition from b) the brittle (0.26 J) to c) the transition (3.03 J) and finally to d) the ductile (8.64 J) state. Reproduced with permission from Minnert et al. [35], Copyright (2021), Journal of Materials Research, Springer Nature.

In Publication D, compression and indentation SRJ tests were performed in comparison with Charpy pendulum impact tests. In an impact test, the specimen is deformed abruptly leading to high strain rates and a three-dimensional stress state in the notch base. A similar stress-state is present within the plastic zone below the indenter tip but the strain rate is much smaller. Additional compression SRJ tests were performed in which the strain rate is comparable to indentation SRJ tests, while the stress state is uniaxial and thus clearly different.

The temperature dependent impact energy determined via Charpy pendulum impact tests is plotted in Figure 36a. The data show two plateaus where the absorbed energy is approximately independent of the test temperature. In the low temperature range (-100-75 °C), brittle fracture was observed (Fig. 36b) resulting in an impact energy of about 0.2 J. In the high temperature range (110-250 °C), on the other side, specimens deform in a ductile manner (Fig. 36d). In consequence, the energy absorbed by the sample is increasing to approx. 9 J. A clear transition behavior can be found in the temperature range between approx. 75-110 °C (Fig. 36c). This overall behavior is well known for bcc metals and was already reported in literature e.g. [81].

The analysis of the temperature dependent SRS determined by indentation and compression SRJ tests shows a maximum close to the transition range (50-110 °C, highlighted in gray) determined by impact experiments (Fig. 37a). For comparison, additional literature data for polycrystalline (Nemat-Nasser [75] and Cheng et al. [76]) and single crystalline (Seeger & Hollang [73]) Mo are plotted as well.

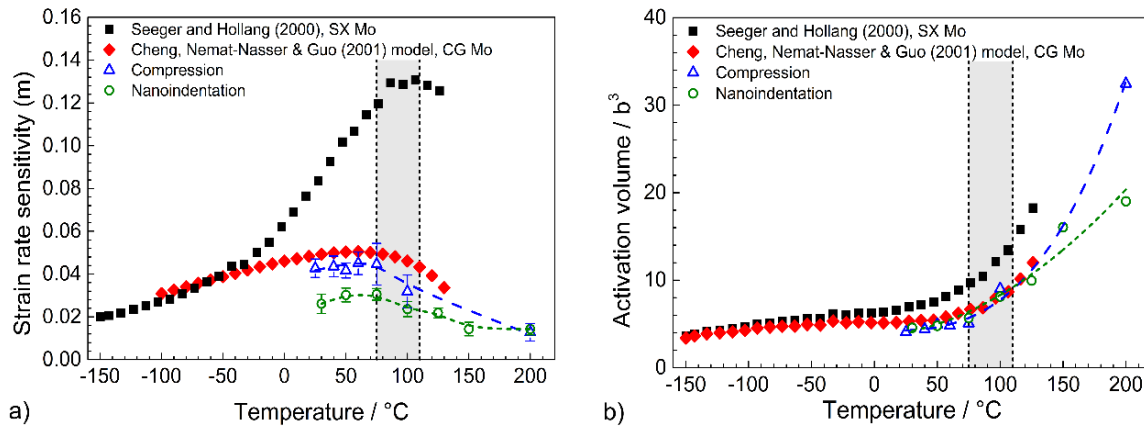


Figure 37: Temperature dependent a) strain rate sensitivity and b) activation volume of Mo. The brittle to ductile transition range determined by Charpy pendulum impact experiments is highlighted in gray. Reproduced with permission from Minnert et al. [35], Copyright (2021), Journal of Materials Research, Springer Nature.

A maximum in SRS was determined for polycrystalline Mo at about 50-80 °C according to literature (Nemat-Nasser [75] and Cheng et al. [76]) and compression and indentation test results of this work. The overall course of  $m$  is consistent with observations made on bcc tungsten [239]. Both materials exhibit a maximum in  $m$  at similar homologous temperatures of  $0.13 T_m$  (Mo) and  $0.17 T_m$  (tungsten), which is close to  $T_k \approx 0.2 \cdot T_m$  for bcc metals [74]. Comparing the absolute  $m$  values of polycrystalline Mo, very similar results are obtained for compression and literature data. In contrast, SRS coefficients determined by indentation testing are smaller. This might be related to the different, triaxial stress state within the plastic zone below the indenter.

The SX data (Seeger & Hollang [73]) show significantly higher rate dependencies with a maximum in  $m$  at about 100 °C. The higher strain rate dependence can be attributed to the lower strength of a single crystal compared to a polycrystal, where grain boundaries provide an additional strengthening effect. Differences between SX and polycrystalline data as well as different test procedures causing different deformation rates can be understood by analyzing the activation volume (Fig. 37b).

It is noticeable that  $V$  is almost independent of the microstructure (single or polycrystalline) and the applied test method (stress state and strain rate) as it is normalized by  $\sigma_y$  or  $H$  respectively (Eq. 3b and 3c). Small activation volumes of about  $5 \text{ b}^3$  were found in the brittle low temperature regime, this is comparable with  $V$  of  $4\text{-}7 \text{ b}^3$  found for SX bcc tungsten and chromium [47]. Activation volumes of  $\leq 5 \text{ b}^3$  indicate that the deformation is governed by a kink mechanism [47]. This process takes place rather locally, so only a few atoms are involved in this process, resulting in a small activation volume. The motion of kink pairs, on the other hand, is the limiting process at high temperatures, where activation volumes of  $>20 \text{ b}^3$  were found and the material deforms ductile.

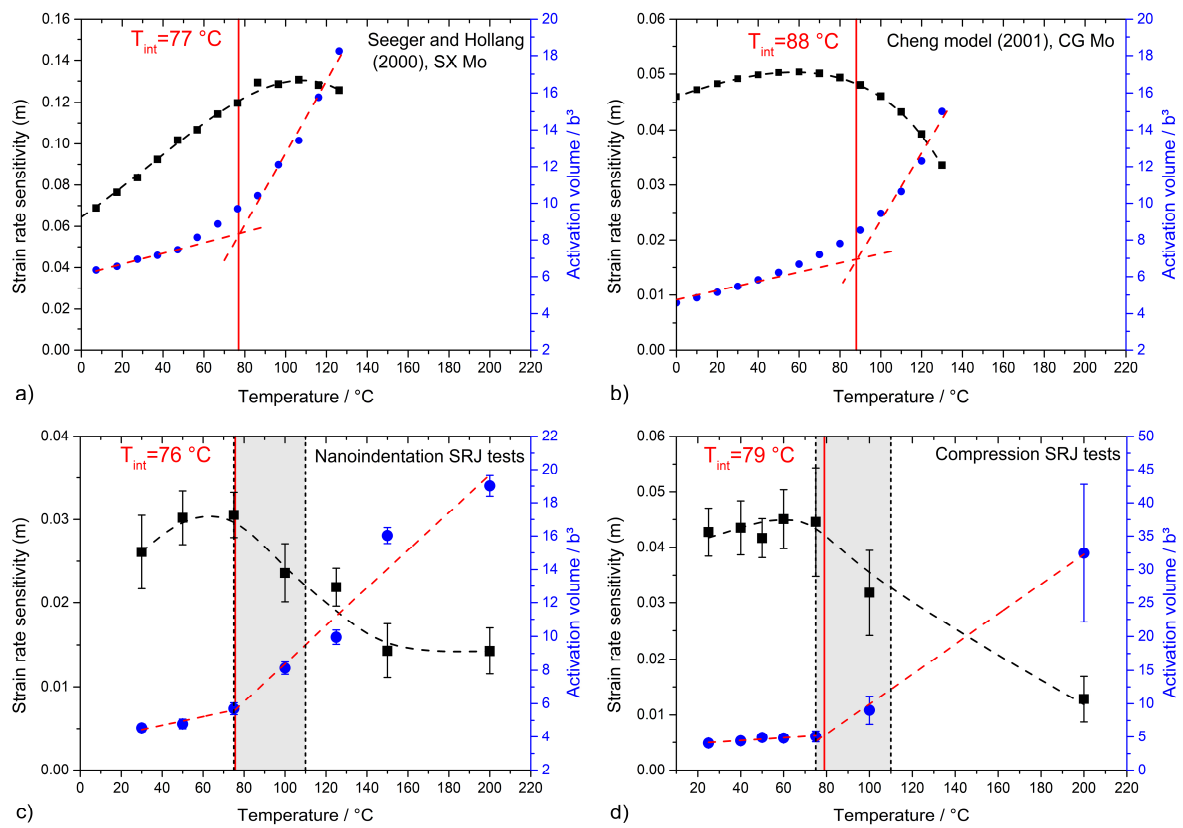


Figure 38: Intersection temperatures of a) SX Mo [73], b) CG Mo [75, 76] as well as indentation and compression SRJ data determined by a linear fitting approach. Reproduced with permission from Minnert et al. [35], Copyright (2021), Journal of Materials Research, Springer Nature.

The course of  $V$  as a function of temperature can be described by approximation with two linear fitting functions (Fig. 38). The literature data for SX Mo (Fig. 38a) and CG Mo (Fig. 38b) show a rather continuous transition, whereas the indentation (Fig. 38c) and compression data (Fig. 38d) of this work shows two linear regimes. Calculating the temperature at which the two fitting lines intersect results in an intersection temperature  $T_{int}$  of approx.  $77 \text{ }^\circ\text{C}$  for SX Mo and  $76\text{-}88 \text{ }^\circ\text{C}$  ( $0.13\text{-}0.14 T_m$ ) for polycrystalline Mo. Comparing the intersection temperatures with

---

the BDT range determined by Charpy pendulum impact tests (highlighted in gray), it is noticeable that  $T_{int}$  (marked in red) approximately corresponds to its lower limit. The maximum in SRS was observed at slightly lower temperatures.

The knee temperature is the temperature at which the thermal component of the yield stress becomes zero (Fig. 2) and the material exhibits a ductile deformation behavior. It can therefore be assumed that  $T_k$  represents a theoretical limit for the maximum BDTT, however,  $T_k$  does not necessarily correspond to the BDTT determined by impact tests. For SX Mo, a  $T_k$  of 450 K (177 °C) was found [71]. At  $T < T_k$ , the thermal component of  $\sigma_y$  is non-zero, meaning that the mobility of screw dislocations is the limiting factor for plastic deformation [79, 80, 240]. Depending on the remaining dislocation mobility and applied deformation rate, the material exhibits a brittle or a semi-brittle/semi-ductile behavior.

Based on the present data,  $T_{int}$  represents an alternative for the estimation of the BDTT. The correlation with  $V$  connects the rather empirically determined BDTT from impact tests with metal-physical parameters. For the sake of clarity, it must be noted that the analysis presented here, only allows an estimate of the BDTT, since the change in  $V$  can also be continuous, as shown in Figure 38a and 38b. In this case an exact description with the use of linear fitting functions is limited and may cause some inaccuracies.

The transition temperature determined in this manner may represent the actual BDTT for the material. For technical applications, however,  $T_{int}$  is presumably of little interest since the ductility is insufficient high. Nevertheless, a definition of BDTT related to physical parameters, such as the activation volume, is useful since different data sets can be compared, regardless of the specimen geometry or the test equipment used. This is not possible with the conventional Charpy pendulum impact experiments where the difference in potential energy is analyzed.

### 6.3.2. Indentation creep testing at ultra-high temperatures

Step load and hold experiments were carried out on single crystalline Ni in  $\langle 100 \rangle$  orientation at temperatures between RT-1100 °C using the presented HT indentation system. Additional SRJ tests were performed for comparison. In Figure 39a, the time dependent depth signal of a SLH experiment is plotted for the different temperatures applied. The resulting strain rates are plotted as a function of  $H$  in Figure 39b. It is obvious that the material gets softer with increasing temperature, resulting in higher penetration depths and lower hardness values. Furthermore, the indentation strain rates are increasing as well. The largest change in strain rate occur within

the first 1.5 s of the experiment (first test segment) illustrated by the upper part of Figure 39b. In the subsequent 40 s creep segment (lower part of Fig. 39b), the strain rate decreases by only about one order of magnitude. However, both creep segments correlate well, resulting in a linear relationship over the whole strain rate range of about four orders of magnitude (Fig. 39b). The results from SLH and SRJ indentation testing are compared with literature data using the temperature compensated uniaxial strain rate (Eq. 23) and the corresponding uniaxial stress (Eq. 25) data normalized by the shear modulus of the material (Norton plot, Fig. 39c).

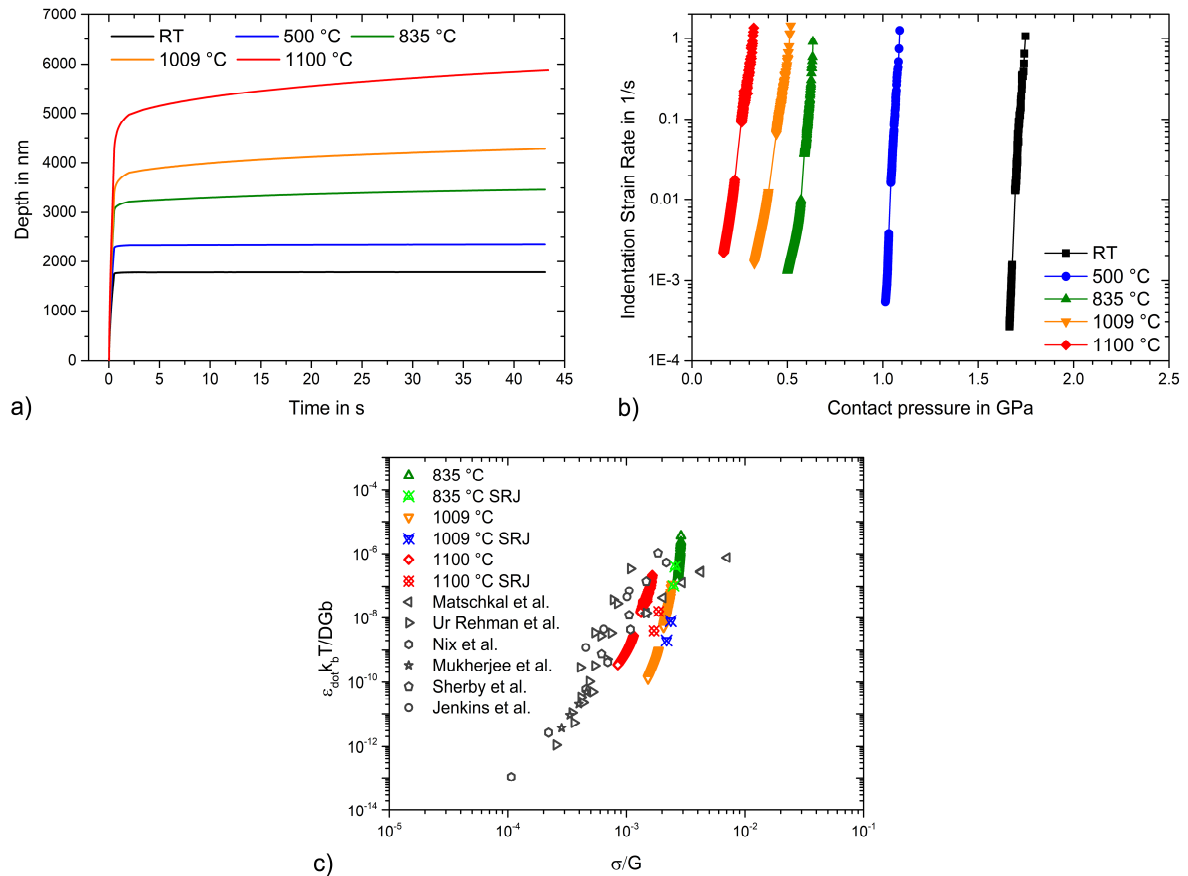


Figure 39: Step load and hold test on SX Ni at various temperatures: a) load-displacement curve, b) indentation strain rate over contact pressure and c) temperature compensated strain rates versus normalized uniaxial stresses. Reproduced with permission from Minnert et al. [32], Copyright (2020), Materials & Design, Elsevier Ltd.

A very good correlation between the SRJ and SLH data as well as reference values from literature, determined by uniaxial and indentation testing, was found. This clearly shows the possibilities of the newly developed method to determine the material behavior within a short test period in a wide strain rate range. Moreover, the present data yields to an activation energy for creep of  $216 \pm 22$  kJ/mol (evaluated at  $\dot{\epsilon}_c = 0.002$  s<sup>-1</sup>). The activation energy from SLH experiments is thus slightly lower than literature data of 243- 285 kJ/mol which correspond to

---

the activation energy for self-diffusion in Ni [241-246]. The deviation may be due to the complex, three-dimensional stress state within the plastic zone and the non-steady state condition in deformation rate caused by the short creep time. Moreover, a steady state condition has not yet been achieved due to the rather short creep time. Low strain rates as they usually occur during creep deformation can only be achieved by a significant extension of the test duration. Analyzing data at lower creep strain rates would result in slightly higher activation energies

The SLH method is, therefore, well suited to study the transient material behavior at high and medium strain rates, but not at very low strain rates, due to strong tip wear (Fig. 35b) and relaxation processes within the plastic zone as discussed earlier for CLH tests.

---

## 7. Summary and conclusion

---

This PhD thesis was carried out within the DFG project (project no. 326946902) “*Indentation creep: New machine and test methodology development at various length scales, high temperatures and low deformation rates*”. Focus of the thesis was, therefore, on the investigation of the thermally activated deformation behavior of materials at high temperatures and low strain rates applying the DSI technique. This required the development of new loading protocols as well as the improvement of the design of indentation systems.

Mechanical properties of materials including their stress and strain rate dependent deformation behavior is strongly correlated to thermally activated mechanisms such as generation, annihilation and motion of dislocations. These processes are traditionally characterized by macroscopic test procedures. The DSI technique provides, however, the possibility to determine mechanical properties at a local scale. This allows individual microstructural constituents like individual phases to be characterized. Moreover, a rather simple sample preparation is required, since a single polished, plane-parallel, specimen is sufficient to perform thousands of tests. For these reasons, new test procedures and test platforms have been under development for several decades, making the semi-automated depth-sensing indentation testing technique a powerful characterization tool e.g. [16, 22, 23, 126, 131, 134, 137, 142, 145, 147].

Two new indentation loading protocols for studying the time-dependent deformation behavior of materials have been presented in this thesis [32-34]. The constant contact pressure method provides information on the deformation resistance at low deformation rates and long timescales. This loading protocol is comparable with conventional uniaxial creep or stress dip experiments. Different contact pressures can be applied by controlling  $P/S^2$ , where the maximum contact pressure is limited by the velocity of the control loops of the systems. The maximum stress in the creep segment is therefore always smaller than the initial stress at the end of the first test segment. The minimum contact pressure is limited by the contact situation. The comparison of experiments with single and incremental unloading events do not show any differences, hence, the influence of a loading history effect can be excluded. Furthermore, it could be proven that indentation data agree well with macroscopic uniaxial stress dip tests. An advantage of the incremental contact pressure reduction approach is the shorter test duration, which is particularly important for testing at elevated temperatures.

---

The SLH method can be applied for testing the transient plastic deformation behavior at high and medium strain rates. High strain rates in the order of  $10^0 \text{ s}^{-1}$  can be achieved in the first second of the experiment using the presented *Prometheus* HT indentation system. The resulting strain rate drops sharply down to  $10^{-4} \text{ s}^{-1}$  within seconds. This method can, thus, be used to analyze a large strain rate range in a short time scale, reducing the contact times required to a minimum. The results on SX Ni show excellent agreement with reference data in the normalized Norton plot [32]. The linear relationship of the two test segments indicates that there is no change in the active deformation mechanisms under the test conditions investigated. The activation energy is with 216 kJ/mol comparable to literature data [241-244].

Furthermore, a newly developed in-situ indentation system with a maximum operation temperature of 1100 °C is presented. The advanced design of the instrument has eliminated or evaded several issues with previous indenters [29, 30]. The sophisticated thermal management leads to low thermal drift, while the combination of the high load actuator and the high machine stiffness enables the possibility of testing at large penetration depths respectively large contact areas. Experiments performed at large penetration depths are less affected by tip wear, which is currently the biggest challenge in the field of HT indentation testing [27, 29]. The dynamic testing capabilities of the instrument are essential for an accurate determination of  $S$ , since the maximum unloading rates of previous, quasi-static systems are not high enough to measure correct Young's modulus data at 1000 °C and beyond [30]. Furthermore, the contact stiffness can be used to determine a drift and pile-up independent indentation depth and hardness [33, 34, 95, 157]. The outstanding performance of the new instrument was demonstrated by reference measurements on fused silica and Mo, whose results correlate well with literature data [32]. As a result, reliable Young's modulus values could be determined for the first time applying small-scale DSI testing at temperatures beyond 1000 °C.

Thermally activated dislocation mechanisms at the brittle-to-ductile transition of bcc Mo were investigated using the DSI technique, macroscopic compression tests and Charpy pendulum impact tests. A significant increase in activation volume, starting from about  $5 \text{ b}^3$ , could be observed at the onset of the BDT range determined by impact experiments. An intersection temperature can be determined by linear fitting of the temperature dependent activation volumes in the low and high temperature range. The BDTT is an extrinsic material parameter which can be related to dislocation mobility. The intersection temperature was, thus, identified as an alternative approach for the estimation of the BDTT.

---

In this thesis, the limits of DSI were pushed a little further. The CCP method provides the possibility to perform indentation creep tests at constant equivalent stresses similar and comparable to conventional uniaxial experiments. In addition, it has been demonstrated for, the first time, that reliable DSI experiments can be carried out at temperatures of up to 1100 °C. However, the biggest hurdle for a broader application of the small-scale DSI technique at high temperatures remains the limited lifetime of the indenter tips. In order to reduce the effect of tip wear, new indenter materials are required which can withstand the harsh test conditions [27]. A possible work around has been realized with the SLH method by significantly reducing the test duration and, thus, also diffusion-related wear



---

---

## 8. Outlook

---

In future, alternative indenter materials must be found that are both mechanically robust and chemically inert to a large number of materials [27]. Potential candidates are e.g. HfC, TaC and HfTaC compositions as they are reported as the materials with the highest melting temperature and good mechanical and chemical properties [247-249]. Besides this, it is also possible to use blunter indenter geometries like flat punches or spherical indenters. These indenter geometries exhibit large contact areas even at small penetration depths. A slight change in contact area, caused by tip wear, is therefore insignificant to a certain extent.

The contact size of a flat punch indenter is well defined and will not change throughout the experiment. A new approach for creep testing with flat punch indenters was, therefore, recently presented by Matschkal-Amberger et al. [130]. These experiments must be supported by finite element simulations to determine correct conversion factors. In addition, an accurate orthogonal alignment of the specimen surface to the indenter axis is challenging and an additional alignment procedure is required for this. The use of large punches also necessitates high loads and a very high frame stiffness of the indentation device. This difficulty can be overcome by testing free-standing structures such as micropillars. Micropillar testing also allows stress-strain diagrams to be recorded and the strain hardening behavior to be investigated. The fabrication of these free-standing structures, however, is associated with a high preparative effort.

Local stress-strain diagrams can also be determined by using spherical indenters [137, 138]. The production of ideal spherical indenters is complex, particularly since they are grinded manually. The determination of a representative tip area function is, therefore, challenging as even slight deviations can cause an inaccurate representation of the actual material behavior.

Testing with non-self-similar indenter geometries requires an adaptation or the development of new loading protocols. The interesting aspect of using a spherical geometry is, on the one hand, a more homogeneous stress distribution compared to three-sided pyramidal indenters like the Berkovich geometry used in this thesis. On the other hand, the applied strain increases with increasing penetration depth, i.e. with increasing creep duration. This is in contrast to a self-similar indenter geometry where the applied strain remains constant. An increase in strain is also observed in a uniaxial constant stress experiment. This may provide an even better correlation between indentation and uniaxial experiments.



---

## 9. References

---

1. United Nations, U.N.E.P., *Emissions Gap Report 2021: The Heat Is On - A World of Climate Promises Not Yet Delivered*. 2021, United Nations, United Nations Environment Programme (2021): Nairobi.
2. Jansohn, P., *Introduction to gas turbines*, in *Modern Gas Turbine Systems: High Efficiency, Low Emission, Fuel Flexible Power Generation*. 2013, Elsevier Science. p. 1-20.
3. Saini, A. and Pollock, T., *High-temperature materials increase efficiency of gas power plants*. MRS Bulletin, 2012. **37**(6): p. 550-551. DOI: 10.1557/mrs.2012.124.
4. Bringhenti, C. and Barbosa, J.o.R. *Effects of turbine tip clearance on gas turbine performance*. in *Turbo Expo: Power for Land, Sea, and Air*. 2008. DOI: <https://doi.org/10.1115/GT2008-50196>.
5. Badran, O.O., *Gas-turbine performance improvements*. Applied Energy, 1999. **64**(1-4): p. 263-273. DOI: [https://doi.org/10.1016/S0306-2619\(99\)00088-4](https://doi.org/10.1016/S0306-2619(99)00088-4).
6. Perepezko, J.H., *The Hotter the Engine, the Better*. Science, 2009. **326**(5956): p. 1068. DOI: 10.1126/science.1179327.
7. Schulz, U., et al., *Some recent trends in research and technology of advanced thermal barrier coatings*. Aerospace Science and Technology, 2003. **7**(1): p. 73-80. DOI: [https://doi.org/10.1016/S1270-9638\(02\)00003-2](https://doi.org/10.1016/S1270-9638(02)00003-2).
8. Maier, H.J., Niendorf T., Bürgel R., *Hochtemperaturlegierungen*, in *Handbuch Hochtemperatur-Werkstofftechnik*. 2019, Springer Vieweg, Wiesbaden. p. 333-496. DOI: <https://doi.org/10.1007/978-3-658-25314-1>.
9. Webler, R., et al., *Evolution of microstructure and mechanical properties of coated Co-base superalloys during heat treatment and thermal exposure*. Materials Science and Engineering: A, 2015. **628**: p. 374-381. DOI: <https://doi.org/10.1016/j.msea.2015.01.060>.
10. Obert, S., Kauffmann, A., and Heilmaier, M., *Characterisation of the oxidation and creep behaviour of novel Mo-Si-Ti alloys*. Acta Materialia, 2020. **184**: p. 132-142. DOI: <https://doi.org/10.1016/j.actamat.2019.11.045>.
11. Darolia, R., *Development of strong, oxidation and corrosion resistant nickel-based superalloys: critical review of challenges, progress and prospects*. International Materials Reviews, 2019. **64**(6): p. 355-380. DOI: 10.1080/09506608.2018.1516713.
12. Volz, N., et al., *Thermophysical and Mechanical Properties of Advanced Single Crystalline Co-base Superalloys*. Metallurgical and Materials Transactions A, 2018. **49**(9): p. 4099-4109. DOI: 10.1007/s11661-018-4705-1.
13. Liu, B., et al., *Advances on strategies for searching for next generation thermal barrier coating materials*. Journal of Materials Science & Technology, 2019. **35**(5): p. 833-851. DOI: <https://doi.org/10.1016/j.jmst.2018.11.016>.
14. Pollock, T. and Argon, A., *Creep resistance of CMSX-3 nickel base superalloy single crystals*. Acta Metallurgica et Materialia, 1992. **40**(1): p. 1-30. DOI: [https://doi.org/10.1016/0956-7151\(92\)90195-K](https://doi.org/10.1016/0956-7151(92)90195-K).
15. Durst, K. and Göken, M., *Micromechanical characterisation of the influence of rhenium on the mechanical properties in nickel-base superalloys*. Materials Science and Engineering: A, 2004. **387-389**: p. 312-316. DOI: <https://doi.org/10.1016/j.msea.2004.03.079>.
16. Durst, K. and Maier, V., *Dynamic nanoindentation testing for studying thermally activated processes from single to nanocrystalline metals*. Current Opinion in Solid State and Materials Science, 2015. **19**(6): p. 340-353. DOI: <https://doi.org/10.1016/j.cossms.2015.02.001>.
17. Wheeler, J.M., et al., *Activation parameters for deformation of ultrafine-grained aluminium as determined by indentation strain rate jumps at elevated temperature*. Materials Science and Engineering: A, 2013. **585**: p. 108-113. DOI: <https://doi.org/10.1016/j.msea.2013.07.033>.

18. Shang, F., et al., *Determination of high temperature mechanical properties of thermal barrier coatings by nanoindentation*. Surface engineering, 2014. **30**(4): p. 283-289. DOI: <https://doi.org/10.1179/1743294413Y.0000000227>.
19. Best, J.P., et al., *High temperature impact testing of a thin hard coating using a novel high-frequency in situ micromechanical device*. Surface and Coatings Technology, 2018. **333**: p. 178-186. DOI: <https://doi.org/10.1016/j.surfcoat.2017.10.072>.
20. Monclús, M. and Molina-Aldareguia, J., *High temperature nanomechanical testing*. Handbook of Mechanics of Materials; Hsueh, CH, Schmauder, S., Chen, C.-S., Chawla, KK, Chawla, N., Chen, W., Kagawa, Y., Eds, 2018.
21. Korte, S., et al., *High temperature microcompression and nanoindentation in vacuum*. Journal of materials research, 2012. **27**(1): p. 167-176. DOI: <https://doi.org/10.1557/jmr.2011.268>.
22. Sebastiani, M., et al., *Measurement of fracture toughness by nanoindentation methods: Recent advances and future challenges*. Current Opinion in Solid State and Materials Science, 2015. **19**(6): p. 324-333. DOI: <https://doi.org/10.1016/j.cossms.2015.04.003>.
23. Ast, J., et al., *A review of experimental approaches to fracture toughness evaluation at the micro-scale*. Materials & Design, 2019. **173**: p. 107762. DOI: <https://doi.org/10.1016/j.matdes.2019.107762>.
24. Schuh, C.A., Packard, C.E., and Lund, A.C., *Nanoindentation and contact-mode imaging at high temperatures*. Journal of Materials Research, 2006. **21**(3): p. 725-736. DOI: [10.1557/jmr.2006.0080](https://doi.org/10.1557/jmr.2006.0080).
25. Trenkle, J.C., Packard, C.E., and Schuh, C.A., *Hot nanoindentation in inert environments*. Review of Scientific Instruments, 2010. **81**(7): p. 073901. DOI: [10.1063/1.3436633](https://doi.org/10.1063/1.3436633).
26. Wheeler, J., Brodard, P., and Michler, J., *Elevated temperature, in situ indentation with calibrated contact temperatures*. Philosophical Magazine, 2012. **92**(25-27): p. 3128-3141. DOI: <https://doi.org/10.1080/14786435.2012.674647>.
27. Wheeler, J. and Michler, J., *Invited Article: Indenter materials for high temperature nanoindentation*. Review of Scientific Instruments, 2013. **84**(10): p. 101301. DOI: <https://doi.org/10.1063/1.4824710>.
28. Wheeler, J.M. and Michler, J., *Elevated temperature, nano-mechanical testing in situ in the scanning electron microscope*. Review of Scientific Instruments, 2013. **84**(4): p. 045103. DOI: [10.1063/1.4795829](https://doi.org/10.1063/1.4795829).
29. Wheeler, J.M., et al., *High temperature nanoindentation: The state of the art and future challenges*. Current Opinion in Solid State and Materials Science, 2015. **19**(6): p. 354-366. DOI: <https://doi.org/10.1016/j.cossms.2015.02.002>.
30. Gibson, J.S.K.L., et al., *On extracting mechanical properties from nanoindentation at temperatures up to 1000 °C*. Extreme Mechanics Letters, 2017. **17**: p. 43-49. DOI: <https://doi.org/10.1016/j.eml.2017.09.007>.
31. Best, J.P., et al., *High temperature fracture toughness of ceramic coatings evaluated using micro-pillar splitting*. Scripta Materialia, 2019. **162**: p. 190-194. DOI: <https://doi.org/10.1016/j.scriptamat.2018.11.013>.
32. Minnert, C., Oliver, W.C., and Durst, K., *New ultra-high temperature nanoindentation system for operating at up to 1100 °C*. Materials & Design, 2020. **192**: p. 108727. DOI: <https://doi.org/10.1016/j.matdes.2020.108727>.
33. Prach O., et al., *A new nanoindentation creep technique using constant contact pressure*. Journal of Materials Research, 2019. **34**(14): p. 2492-2500. DOI: [10.1557/jmr.2019.188](https://doi.org/10.1557/jmr.2019.188).
34. Minnert, C. and Durst, K., *Nanoindentation creep testing: Advantages and limitations of the constant contact pressure method*. Journal of Materials Research, 2022. **37**(2): p. 567-579. DOI: <https://doi.org/10.1557/s43578-021-00445-6>.
35. Minnert, C., Ur Rehman, H., and Durst, K., *Thermally activated dislocation mechanism in Mo studied by indentation, compression and impact testing*. Journal of Materials Research, 2021: p. 1-11. DOI: <https://doi.org/10.1557/s43578-021-00126-4>.

36. Caillard D. and J.L., M., *Thermally Activated Mechanisms in Crystal Plasticity*. Pergamon Materials Series, ed. Cahn, R.W. Vol. 8. 2003.
37. Kocks, U.F., Argon, A., and Ashby, M., *Thermodynamics and kinetics of slip*. 1975.
38. Duesbery, M.S. and Richardson, G.Y., *The dislocation core in crystalline materials*. Critical Reviews in Solid State and Materials Sciences, 1991. **17**(1): p. 1-46. DOI: 10.1080/10408439108244630.
39. Orowan, E., *Problems of plastic gliding*. Proceedings of the Physical Society, 1940. **52**(1): p. 8-22. DOI: 10.1088/0959-5309/52/1/303.
40. Wei, Q., *Strain rate effects in the ultrafine grain and nanocrystalline regimes—influence on some constitutive responses*. Journal of materials science, 2007. **42**(5): p. 1709-1727. DOI: <https://doi.org/10.1007/s10853-006-0700-9>.
41. Mughrabi, H., *Materials Science and Technology, Volume 6, Plastic Deformation and Fracture of Materials*. Materials Science and Technology, 1996. **6**.
42. Yang, X.-S., et al., *Time-, stress-, and temperature-dependent deformation in nanostructured copper: Creep tests and simulations*. Journal of the Mechanics and Physics of Solids, 2016. **94**: p. 191-206. DOI: <https://doi.org/10.1016/j.jmps.2016.04.021>.
43. Yang, X.-S., et al., *Time, stress, and temperature-dependent deformation in nanostructured copper: stress relaxation tests and simulations*. Acta Materialia, 2016. **108**: p. 252-263. DOI: <https://doi.org/10.1016/j.actamat.2016.02.021>.
44. Meyers, M.A., Mishra, A., and Benson, D.J., *Mechanical properties of nanocrystalline materials*. Progress in Materials Science, 2006. **51**(4): p. 427-556. DOI: <https://doi.org/10.1016/j.pmatsci.2005.08.003>.
45. Dao, M., et al., *Toward a quantitative understanding of mechanical behavior of nanocrystalline metals*. Acta Materialia, 2007. **55**(12): p. 4041-4065. DOI: <https://doi.org/10.1016/j.actamat.2007.01.038>.
46. Wang, Y.-J., Ishii, A., and Ogata, S., *Transition of creep mechanism in nanocrystalline metals*. Physical Review B, 2011. **84**(22): p. 224102. DOI: 10.1103/PhysRevB.84.224102.
47. Kiener, D., et al., *Rate limiting deformation mechanisms of bcc metals in confined volumes*. Acta Materialia, 2019. **166**: p. 687-701. DOI: <https://doi.org/10.1016/j.actamat.2019.01.020>.
48. Seeger, A., *The temperature and strain-rate dependence of the flow stress of body-centred cubic metals: a theory based on kink-kink interactions*. International Journal of Materials Research, 1981. **72**(6): p. 369-380. DOI: <https://doi.org/10.1515/ijmr-1981-720601>.
49. Hall, E., *The deformation and ageing of mild steel: III discussion of results*. Proceedings of the Physical Society. Section B, 1951. **64**(9): p. 747.
50. Petch, N., *The cleavage strength of polycrystals*. Journal of the iron and steel institute, 1953. **174**: p. 25-28.
51. Cordero, Z.C., Knight, B.E., and Schuh, C.A., *Six decades of the Hall–Petch effect – a survey of grain-size strengthening studies on pure metals*. International Materials Reviews, 2016. **61**(8): p. 495-512. DOI: 10.1080/09506608.2016.1191808.
52. Wei, Q., et al., *Effect of nanocrystalline and ultrafine grain sizes on the strain rate sensitivity and activation volume: fcc versus bcc metals*. Materials Science and Engineering: A, 2004. **381**(1): p. 71-79. DOI: <https://doi.org/10.1016/j.msea.2004.03.064>.
53. Blum, W., et al., *Strain Rate Contribution due to Dynamic Recovery of Ultrafine-Grained Cu–Zr as Evidenced by Load Reductions during Quasi-Stationary Deformation at 0.5 Tm*. Metals, 2019. **9**(11): p. 1150. DOI: 10.3390/met9111150.
54. Sun, Z., et al., *Dynamic recovery in nanocrystalline Ni*. Acta Materialia, 2015. **91**: p. 91-100. DOI: <https://doi.org/10.1016/j.actamat.2015.03.033>.
55. Moser, B., Schwaiger, R., and Dao, M., *Size Effects on Deformation and Fracture of Nanostructured Metals*, in *Nanostructures Coatings*, Cavaleiro, A. and Hosson, J.T.M.D., Editors. 2006. p. 27-77.

- 
56. Meyers, M.A., Mishra, A., and Benson, D.J., *The deformation physics of nanocrystalline metals: Experiments, analysis, and computations*. JOM, 2006. **58**(4): p. 41-48. DOI: 10.1007/s11837-006-0214-6.
  57. Valiev, R., et al., *Paradox of strength and ductility in metals processed by severe plastic deformation*. Journal of Materials research, 2002. **17**(1): p. 5-8. DOI: <https://doi.org/10.1557/JMR.2002.0002>.
  58. Kumar, K.S., Van Swygenhoven, H., and Suresh, S., *Mechanical behavior of nanocrystalline metals and alloys* *The Golden Jubilee Issue—Selected topics in Materials Science and Engineering: Past, Present and Future*, edited by S. Suresh. Acta Materialia, 2003. **51**(19): p. 5743-5774. DOI: <https://doi.org/10.1016/j.actamat.2003.08.032>.
  59. Mungole, T., et al., *A critical examination of the paradox of strength and ductility in ultrafine-grained metals*. Journal of Materials Research, 2014. **29**(21): p. 2534-2546. DOI: 10.1557/jmr.2014.272.
  60. Hahn, H., Mondal, P., and Padmanabhan, K.A., *Plastic deformation of nanocrystalline materials*. Nanostructured Materials, 1997. **9**(1): p. 603-606. DOI: [https://doi.org/10.1016/S0965-9773\(97\)00135-9](https://doi.org/10.1016/S0965-9773(97)00135-9).
  61. Segal, V.M., *Deformation mode and plastic flow in ultra fine grained metals*. Materials Science and Engineering: A, 2005. **406**(1): p. 205-216. DOI: <https://doi.org/10.1016/j.msea.2005.06.035>.
  62. Dao, M., et al., *Strength, strain-rate sensitivity and ductility of copper with nanoscale twins*. Acta Materialia, 2006. **54**(20): p. 5421-5432. DOI: <https://doi.org/10.1016/j.actamat.2006.06.062>.
  63. Rösler, J., Harders, H., and Bäker, M., *Mechanisches Verhalten der Metalle*, in *Mechanisches Verhalten der Werkstoffe*. 2008, Springer-Verlag. p. 165-226.
  64. Hull, D. and Bacon, D.J., *Strength of Crystalline Solids*, in *Introduction to dislocations*. 2011, Elsevier. p. 205-249.
  65. Gottstein, G., *Mechanische Eigenschaften*, in *Physikalische Grundlagen der Materialkunde*. 2007, Springer-Verlag Berlin Heidelberg. p. 197-301. DOI: 10.1007/978-3-540-71105-6.
  66. Peierls, R., *The size of a dislocation*. Proceedings of the Physical Society, 1940. **52**(1): p. 34-37. DOI: 10.1088/0959-5309/52/1/305.
  67. Cottrell, A.H., *Theory of dislocations*. Progress in Metal Physics, 1953. **4**: p. 205-264. DOI: [https://doi.org/10.1016/0502-8205\(53\)90018-5](https://doi.org/10.1016/0502-8205(53)90018-5).
  68. Giannattasio, A. and Roberts, S.G., *Strain-rate dependence of the brittle-to-ductile transition temperature in tungsten*. Philosophical Magazine, 2007. **87**(17): p. 2589-2598. DOI: <https://doi.org/10.1080/14786430701253197>.
  69. Vitek, V. and Kroupa, F., *Dislocation theory of slip geometry and temperature dependence of flow stress in BCC metals*. physica status solidi (b), 1966. **18**(2): p. 703-713. DOI: <https://doi.org/10.1002/pssb.19660180222>.
  70. Suzuki, T., Takeuchi, S., and Yoshinaga, H., *Dislocations in bcc metals and their motion*, in *Dislocation Dynamics and Plasticity*. 1991, Springer. p. 77-98. DOI: [https://doi.org/10.1007/978-3-642-75774-7\\_6](https://doi.org/10.1007/978-3-642-75774-7_6).
  71. Hollang, L., Hommel, M., and Seeger, A., *The Flow Stress of Ultra-High-Purity Molybdenum Single Crystals*. physica status solidi (a), 1997. **160**(2): p. 329-354. DOI: 10.1002/1521-396x(199704)160:2<329::Aid-pssa329>3.0.Co;2-o.
  72. Vitek, V., *Core structure of screw dislocations in body-centred cubic metals: relation to symmetry and interatomic bonding*. Philosophical Magazine, 2004. **84**(3-5): p. 415-428. DOI: <https://doi.org/10.1080/14786430310001611644>.
  73. Seeger, A. and Hollang, L., *The flow-stress asymmetry of ultra-pure molybdenum single crystals*. Materials Transactions, JIM, 2000. **41**(1): p. 141-151. DOI: <https://doi.org/10.2320/matertrans1989.41.141>.

74. Seeger, A., *Why anomalous slip in body-centred cubic metals?* Materials Science and Engineering: A, 2001. **319-321**: p. 254-260. DOI: [https://doi.org/10.1016/S0921-5093\(01\)00958-3](https://doi.org/10.1016/S0921-5093(01)00958-3).
75. Nemat-Nasser, S., Guo, W., and Liu, M., *Experimentally-based micromechanical modeling of dynamic response of molybdenum*. Scripta materialia, 1999. **40(7)**: p. 859-872.
76. Cheng, J., Nemat-Nasser, S., and Guo, W., *A unified constitutive model for strain-rate and temperature dependent behavior of molybdenum*. Mechanics of materials, 2001. **33(11)**: p. 603-616. DOI: [https://doi.org/10.1016/S0167-6636\(01\)00076-X](https://doi.org/10.1016/S0167-6636(01)00076-X).
77. Maier, V., et al., *Microstructure-dependent deformation behaviour of bcc-metals-indentation size effect and strain rate sensitivity*. Philosophical Magazine, 2015. **95(16-18)**: p. 1766-1779. DOI: <https://doi.org/10.1080/14786435.2014.982741>.
78. DIN, *Metallic materials - Charpy pendulum impact test - Part 1: Test method (ISO 148-1:2016); German version EN ISO 148-1:2016*. 2016.
79. Bonnekoh, C., et al., *The brittle-to-ductile transition in cold rolled tungsten plates: Impact of crystallographic texture, grain size and dislocation density on the transition temperature*. International Journal of Refractory Metals and Hard Materials, 2019. **78**: p. 146-163. DOI: <https://doi.org/10.1016/j.ijrmhm.2018.09.010>.
80. Butler, B.G., et al., *Mechanisms of deformation and ductility in tungsten – A review*. International Journal of Refractory Metals and Hard Materials, 2018. **75**: p. 248-261. DOI: <https://doi.org/10.1016/j.ijrmhm.2018.04.021>.
81. Babinsky, K., et al., *Fracture behavior and delamination toughening of molybdenum in Charpy impact tests*. Jom, 2016. **68(11)**: p. 2854-2863. DOI: <https://doi.org/10.1007/s11837-016-2075-y>.
82. May, J., Höppel, H.W., and Göken, M., *Strain rate sensitivity of ultrafine-grained aluminium processed by severe plastic deformation*. Scripta Materialia, 2005. **53(2)**: p. 189-194. DOI: <https://doi.org/10.1016/j.scriptamat.2005.03.043>.
83. Vehoff, H., et al., *The effect of grain size on strain rate sensitivity and activation volume—from nano to ufg nickel*. International journal of materials research, 2007. **98(4)**: p. 259-268. DOI: <https://doi.org/10.3139/146.101464>.
84. Blum, W. and Zeng, X., *A simple dislocation model of deformation resistance of ultrafine-grained materials explaining Hall–Petch strengthening and enhanced strain rate sensitivity*. Acta Materialia, 2009. **57(6)**: p. 1966-1974. DOI: <https://doi.org/10.1016/j.actamat.2008.12.041>.
85. Van Swygenhoven, H. and Derlet, P.M., *Grain-boundary sliding in nanocrystalline fcc metals*. Physical Review B, 2001. **64(22)**: p. 224105. DOI: [10.1103/PhysRevB.64.224105](https://doi.org/10.1103/PhysRevB.64.224105).
86. Chinh, N.Q., et al. *The effect of grain boundary sliding and strain rate sensitivity on the ductility of ultrafine-grained materials*. in *Materials Science Forum*. 2011. Trans Tech Publ.
87. Hahn, H. and Padmanabhan, K.A., *A model for the deformation of nanocrystalline materials*. Philosophical Magazine B, 1997. **76(4)**: p. 559-571. DOI: [10.1080/01418639708241122](https://doi.org/10.1080/01418639708241122).
88. Margulies, L., Winther, G., and Poulsen, H.F., *In Situ Measurement of Grain Rotation During Deformation of Polycrystals*. Science, 2001. **291(5512)**: p. 2392. DOI: [10.1126/science.1057956](https://doi.org/10.1126/science.1057956).
89. Zhang, K., Weertman, J., and Eastman, J., *The influence of time, temperature, and grain size on indentation creep in high-purity nanocrystalline and ultrafine grain copper*. Applied Physics Letters, 2004. **85(22)**: p. 5197-5199. DOI: <https://doi.org/10.1063/1.1828213>.
90. Zhang, K., Weertman, J., and Eastman, J., *Rapid stress-driven grain coarsening in nanocrystalline Cu at ambient and cryogenic temperatures*. Applied Physics Letters, 2005. **87(6)**: p. 061921. DOI: <https://doi.org/10.1063/1.2008377>.

- 
91. Ma, X.L. and Yang, W., *Dislocation-assisted grain growth in nanocrystalline copper under large deformation*. Scripta Materialia, 2008. **59**(7): p. 792-795. DOI: <https://doi.org/10.1016/j.scriptamat.2008.06.022>.
  92. Gianola, D.S., et al., *Stress-assisted discontinuous grain growth and its effect on the deformation behavior of nanocrystalline aluminum thin films*. Acta Materialia, 2006. **54**(8): p. 2253-2263. DOI: <https://doi.org/10.1016/j.actamat.2006.01.023>.
  93. Legros, M., Gianola, D.S., and Hemker, K.J., *In situ TEM observations of fast grain-boundary motion in stressed nanocrystalline aluminum films*. Acta Materialia, 2008. **56**(14): p. 3380-3393. DOI: <https://doi.org/10.1016/j.actamat.2008.03.032>.
  94. Mompious, F., Legros, M., and Caillard, D., *Stress assisted grain growth in ultrafine and nanocrystalline aluminum revealed by in-situ TEM*. MRS Online Proceedings Library, 2008. **1086**(1): p. 1-6. DOI: <https://doi.org/10.1557/PROC-1086-U09-04>.
  95. Maier, V., et al., *An improved long-term nanoindentation creep testing approach for studying the local deformation processes in nanocrystalline metals at room and elevated temperatures*. Journal of Materials Research, 2013. **28**(9): p. 1177-1188. DOI: [10.1557/jmr.2013.39](https://doi.org/10.1557/jmr.2013.39).
  96. Cahn, J.W. and Taylor, J.E., *A unified approach to motion of grain boundaries, relative tangential translation along grain boundaries, and grain rotation*. Acta Materialia, 2004. **52**(16): p. 4887-4898. DOI: <https://doi.org/10.1016/j.actamat.2004.02.048>.
  97. Winning, M., Gottstein, G., and Shvindlerman, L.S., *Stress induced grain boundary motion*. Acta Materialia, 2001. **49**(2): p. 211-219. DOI: [https://doi.org/10.1016/S1359-6454\(00\)00321-9](https://doi.org/10.1016/S1359-6454(00)00321-9).
  98. Winning, M., Gottstein, G., and Shvindlerman, L.S., *On the mechanisms of grain boundary migration*. Acta Materialia, 2002. **50**(2): p. 353-363. DOI: [https://doi.org/10.1016/S1359-6454\(01\)00343-3](https://doi.org/10.1016/S1359-6454(01)00343-3).
  99. Molodov, D.A., Gorkaya, T., and Gottstein, G., *Dynamics of grain boundaries under applied mechanical stress*. Journal of materials science, 2011. **46**(12): p. 4318-4326. DOI: <https://doi.org/10.1007/s10853-010-5233-6>.
  100. Kassner, M.E., *Chapter 1 - Fundamentals of Creep in Materials*, in *Fundamentals of Creep in Metals and Alloys (Third Edition)*, Kassner, M.E., Editor. 2015, Butterworth-Heinemann: Boston. p. 1-6. DOI: <https://doi.org/10.1016/B978-0-08-099427-7.00001-3>.
  101. Blum, W., *Creep of crystalline materials: experimental basis, mechanisms and models*. Materials Science and Engineering: A, 2001. **319-321**: p. 8-15. DOI: [https://doi.org/10.1016/S0921-5093\(00\)02010-4](https://doi.org/10.1016/S0921-5093(00)02010-4).
  102. Blum, W., Eisenlohr, P., and Breutingger, F., *Understanding creep—a review*. Metallurgical and Materials Transactions A, 2002. **33**(2): p. 291-303. DOI: <https://doi.org/10.1007/s11661-002-0090-9>.
  103. Ashby, M.F. and Jones, D.R., *Engineering materials 1: an introduction to properties, applications and design*. Vol. 1. 2012: Elsevier.
  104. Joachim Roesler, H.H., Martin Baeker, *Creep*, in *Mechanical Behaviour of Engineering Materials*. 2007, Springer-Verlag Berlin Heidelberg. p. 383-406. DOI: [10.1007/978-3-540-73448-2](https://doi.org/10.1007/978-3-540-73448-2).
  105. Nabarro, F., *Report of a Conference on the Strength of Solids*. The Physical Society, London, 1948. **75**.
  106. Herring, C., *Diffusional viscosity of a polycrystalline solid*. Journal of applied physics, 1950. **21**(5): p. 437-445.
  107. Nabarro, F.R.N., *Steady-state diffusional creep*. The Philosophical Magazine: A Journal of Theoretical Experimental and Applied Physics, 1967. **16**(140): p. 231-237. DOI: [10.1080/14786436708229736](https://doi.org/10.1080/14786436708229736).
  108. Nabarro, F., *Creep at very low rates*. Metallurgical and Materials Transactions A, 2002. **33**(2): p. 213-218.

109. Coble, R., *A model for boundary diffusion controlled creep in polycrystalline materials*. Journal of applied physics, 1963. **34**(6): p. 1679-1682.
110. Hart, E.W., *Theory of the tensile test*. Acta Metallurgica, 1967. **15**(2): p. 351-355. DOI: [https://doi.org/10.1016/0001-6160\(67\)90211-8](https://doi.org/10.1016/0001-6160(67)90211-8).
111. Maier, V., et al., *Nanoindentation strain-rate jump tests for determining the local strain-rate sensitivity in nanocrystalline Ni and ultrafine-grained Al*. Journal of Materials Research, 2011. **26**(11): p. 1421-1430. DOI: 10.1557/jmr.2011.156.
112. Wehrs, J., et al., *Comparison of In Situ Micromechanical Strain-Rate Sensitivity Measurement Techniques*. JOM, 2015. **67**(8): p. 1684-1693. DOI: 10.1007/s11837-015-1447-z.
113. DIN, *DIN EN ISO 204:2018 Metallic material - Uniaxial creep testing in tension - Method of test*. 2018.
114. DIN, *DIN EN 2002-005:2007 Aerospace series – Test methods for metallic materials – Part 005: Uninterrupted creep and stress-rupture testing*. 2007.
115. ASTM, *E139-11 Standard Test Methods for Conducting Creep, Creep-Rupture, and Stress-Rupture Tests of Metallic Materials*. 2018. DOI: 10.1520/E0139-11R18.
116. DIN, *DIN EN 10319-1 Metallic materials - Tensile stress relaxation testing - Part 1: Procedure for testing machines*. 2003.
117. Ashby, M.F. and Jones, D.R.H., *Chapter 20 - Creep and Creep Fracture*, in *Engineering Materials 1 (Fourth Edition)*, Ashby, M.F. and Jones, D.R.H., Editors. 2012, Butterworth-Heinemann: Boston. p. 311-324. DOI: <https://doi.org/10.1016/B978-0-08-096665-6.00020-9>.
118. Blum, W. and Eisenlohr, P., *Dislocation mechanics of creep*. Materials Science and Engineering: A, 2009. **510-511**: p. 7-13. DOI: <https://doi.org/10.1016/j.msea.2008.04.110>.
119. Norton, F.H., *The creep of steel at high temperatures*. 1929: McGraw-Hill Book Company, Incorporated.
120. Maier, H.J., Niendorf T., Bürgel R., *Hochtemperaturfestigkeit und -verformung*, in *Handbuch Hochtemperatur-Werkstofftechnik*. 2019, Springer Vieweg, Wiesbaden. p. 85-194. DOI: <https://doi.org/10.1007/978-3-658-25314-1>.
121. Golan, O., et al., *The applicability of Norton's creep power law and its modified version to a single-crystal superalloy type CMSX-2*. Materials Science and Engineering: A, 1996. **216**(1-2): p. 125-130. DOI: [https://doi.org/10.1016/0921-5093\(96\)10400-7](https://doi.org/10.1016/0921-5093(96)10400-7).
122. Brunner, M., et al., *Creep properties beyond 1100°C and microstructure of Co–Re–Cr alloys*. Materials Science and Engineering: A, 2010. **528**(2): p. 650-656. DOI: <https://doi.org/10.1016/j.msea.2010.09.035>.
123. Chokshi, A.H., *Unusual stress and grain size dependence for creep in nanocrystalline materials*. Scripta Materialia, 2009. **61**(1): p. 96-99. DOI: <https://doi.org/10.1016/j.scriptamat.2009.03.009>.
124. Zotov, N., Bartsch, M., and Eggeler, G., *Thermal barrier coating systems — analysis of nanoindentation curves*. Surface and Coatings Technology, 2009. **203**(14): p. 2064-2072. DOI: <https://doi.org/10.1016/j.surfcoat.2009.02.008>.
125. Vignesh, B., et al., *Critical assessment of high speed nanoindentation mapping technique and data deconvolution on thermal barrier coatings*. Materials & Design, 2019. **181**: p. 108084. DOI: <https://doi.org/10.1016/j.matdes.2019.108084>.
126. Oliver, W.C. and Pharr, G.M., *An improved technique for determining hardness and elastic modulus using load and displacement sensing indentation experiments*. Journal of Materials Research, 1992. **7**(6): p. 1564-1583. DOI: 10.1557/JMR.1992.1564.
127. Oliver, W.C. and Pharr, G.M., *Measurement of hardness and elastic modulus by instrumented indentation: Advances in understanding and refinements to methodology*. Journal of Materials Research, 2004. **19**(1): p. 3-20. DOI: 10.1557/jmr.2004.19.1.3.

128. Mayo, M.J. and Nix, W.D., *A micro-indentation study of superplasticity in Pb, Sn, and Sn-38 wt% Pb*. Acta Metallurgica, 1988. **36**(8): p. 2183-2192. DOI: [https://doi.org/10.1016/0001-6160\(88\)90319-7](https://doi.org/10.1016/0001-6160(88)90319-7).
129. Maier-Kiener, V. and Durst, K., *Advanced nanoindentation testing for studying strain-rate sensitivity and activation volume*. Jom, 2017. **69**(11): p. 2246-2255. DOI: <https://doi.org/10.1007/s11837-017-2536-y>.
130. Matschkal-Amberger, D., et al., *New flat-punch indentation creep testing approach for characterizing the local creep properties at high temperatures*. Materials & Design, 2019. **183**: p. 108090. DOI: <https://doi.org/10.1016/j.matdes.2019.108090>.
131. Baral, P., et al., *A new long-term indentation relaxation method to measure creep properties at the micro-scale with application to fused silica and PMMA*. Mechanics of Materials, 2019. **137**: p. 103095. DOI: <https://doi.org/10.1016/j.mechmat.2019.103095>.
132. Merle, B. and Höppel, H., *Microscale high-cycle fatigue testing by dynamic micropillar compression using continuous stiffness measurement*. Experimental Mechanics, 2018. **58**(3): p. 465-474. DOI: <https://doi.org/10.1007/s11340-017-0362-3>.
133. Lavenstein, S. and El-Awady, J.A., *Micro-scale fatigue mechanisms in metals: Insights gained from small-scale experiments and discrete dislocation dynamics simulations*. Current Opinion in Solid State and Materials Science, 2019. **23**(5): p. 100765. DOI: <https://doi.org/10.1016/j.cossms.2019.07.004>.
134. Gabel, S. and Merle, B., *Small-scale high-cycle fatigue testing by dynamic microcantilever bending*. MRS Communications, 2020. **10**(2): p. 332-337. DOI: 10.1557/mrc.2020.31.
135. Bruns, S., et al., *Fracture toughness determination of fused silica by cube corner indentation cracking and pillar splitting*. Materials & Design, 2020. **186**: p. 108311. DOI: <https://doi.org/10.1016/j.matdes.2019.108311>.
136. Huang, Y.-C., Chang, S.-Y., and Chang, C.-H., *Effect of residual stresses on mechanical properties and interface adhesion strength of SiN thin films*. Thin Solid Films, 2009. **517**(17): p. 4857-4861. DOI: <https://doi.org/10.1016/j.tsf.2009.03.043>.
137. Leitner, A., Maier-Kiener, V., and Kiener, D., *Essential refinements of spherical nanoindentation protocols for the reliable determination of mechanical flow curves*. Materials & Design, 2018. **146**: p. 69-80. DOI: <https://doi.org/10.1016/j.matdes.2018.03.003>.
138. Pathak, S. and Kalidindi, S.R., *Spherical nanoindentation stress-strain curves*. Materials Science and Engineering: R: Reports, 2015. **91**: p. 1-36. DOI: <https://doi.org/10.1016/j.mser.2015.02.001>.
139. Swadener, J.G., Taljat, B., and Pharr, G.M., *Measurement of residual stress by load and depth sensing indentation with spherical indenters*. Journal of Materials Research, 2001. **16**(7): p. 2091-2102. DOI: 10.1557/JMR.2001.0286.
140. Jang, J.I., *Estimation of residual stress by instrumented indentation: A review*. J. Ceram. Process. Res, 2009. **10**(3): p. 391-400.
141. Xiao, L., Ye, D., and Chen, C., *A further study on representative models for calculating the residual stress based on the instrumented indentation technique*. Computational Materials Science, 2014. **82**: p. 476-482. DOI: <https://doi.org/10.1016/j.commatsci.2013.10.014>.
142. Rossi, E., et al., *A novel nanoindentation protocol to characterize surface free energy of superhydrophobic nanopatterned materials*. Journal of Materials Research, 2021: p. 1-14. DOI: <https://doi.org/10.1557/s43578-021-00127-3>.
143. De Santis, S., et al., *A Nanoindentation Approach for Time-Dependent Evaluation of Surface Free Energy in Micro- and Nano-Structured Titanium*. Materials, 2022. **15**(1): p. 287.
144. Roa, J.J., et al., *Mapping of mechanical properties at microstructural length scale in WC-Co cemented carbides: Assessment of hardness and elastic modulus by means of high speed massive nanoindentation and statistical analysis*. International Journal of Refractory

- Metals and Hard Materials, 2018. **75**: p. 211-217. DOI: <https://doi.org/10.1016/j.ijrmhm.2018.04.019>.
145. Sudharshan Phani, P. and Oliver, W.C., *A critical assessment of the effect of indentation spacing on the measurement of hardness and modulus using instrumented indentation testing*. Materials & Design, 2019. **164**: p. 107563. DOI: <https://doi.org/10.1016/j.matdes.2018.107563>.
  146. Chang, Y., et al., *Revealing the relation between microstructural heterogeneities and local mechanical properties of complex-phase steel by correlative electron microscopy and nanoindentation characterization*. Materials & Design, 2021. **203**: p. 109620. DOI: <https://doi.org/10.1016/j.matdes.2021.109620>.
  147. Barnoush, A., et al., *In situ small-scale mechanical testing under extreme environments*. MRS Bulletin, 2019. **44**(6): p. 471-477. DOI: 10.1557/mrs.2019.126.
  148. Phani, P.S. and Oliver, W., *A direct comparison of high temperature nanoindentation creep and uniaxial creep measurements for commercial purity aluminum*. Acta Materialia, 2016. **111**: p. 31-38. DOI: <https://doi.org/10.1016/j.actamat.2016.03.032>.
  149. Sudharshan Phani, P. and Oliver, W., *Ultra high strain rate nanoindentation testing*. Materials, 2017. **10**(6): p. 663. DOI: <https://doi.org/10.3390/ma10060663>.
  150. Guillonneau, G., et al., *Nanomechanical testing at high strain rates: New instrumentation for nanoindentation and microcompression*. Materials & Design, 2018. **148**: p. 39-48. DOI: <https://doi.org/10.1016/j.matdes.2018.03.050>.
  151. Conte, M., et al., *Novel high temperature vacuum nanoindentation system with active surface referencing and non-contact heating for measurements up to 800° C*. Review of Scientific Instruments, 2019. **90**(4): p. 045105. DOI: <https://doi.org/10.1063/1.5029873>.
  152. Sneddon, I.N., *The relation between load and penetration in the axisymmetric Boussinesq problem for a punch of arbitrary profile*. International journal of engineering science, 1965. **3**(1): p. 47-57. DOI: [https://doi.org/10.1016/0020-7225\(65\)90019-4](https://doi.org/10.1016/0020-7225(65)90019-4).
  153. Doerner, M.F. and Nix, W.D., *A method for interpreting the data from depth-sensing indentation instruments*. Journal of Materials Research, 1986. **1**(4): p. 601-609. DOI: 10.1557/JMR.1986.0601.
  154. Pharr, G.M., Oliver, W.C., and Brotzen, F.R., *On the generality of the relationship among contact stiffness, contact area, and elastic modulus during indentation*. Journal of Materials Research, 1992. **7**(3): p. 613-617. DOI: 10.1557/JMR.1992.0613.
  155. Johnson, K.L. and Johnson, K.L., *Contact mechanics*. 1987: Cambridge university press.
  156. DIN, *Metallic materials - Instrumented indentation test for hardness and materials parameters - Part 1: Test methods (ISO 14577-1:2015); German version EN ISO 14577-1:2015*. 2015.
  157. Joslin, D.L. and Oliver, W.C., *A new method for analyzing data from continuous depth-sensing microindentation tests*. Journal of Materials Research, 1990. **5**(1): p. 123-126. DOI: 10.1557/JMR.1990.0123.
  158. Merle, B., et al., *Experimental determination of the effective indenter shape and  $\epsilon$ -factor for nanoindentation by continuously measuring the unloading stiffness*. Journal of Materials Research, 2012. **27**(1): p. 214-221. DOI: <https://doi.org/10.1557/jmr.2011.245>.
  159. Lucas, B. and Oliver, W., *Indentation power-law creep of high-purity indium*. Metallurgical and materials Transactions A, 1999. **30**(3): p. 601-610. DOI: <https://doi.org/10.1007/s11661-999-0051-7>.
  160. Pethica, J. and Oliver, W., *Tip surface interactions in STM and AFM*. Physica Scripta, 1987. **1987**(T19A): p. 61. DOI: <https://doi.org/10.1088/0031-8949/1987/T19A/010>.
  161. Pethica, J.B. and Oliver, W.C., *Mechanical Properties of Nanometre Volumes of Material: use of the Elastic Response of Small Area Indentations*. MRS Online Proceedings Library, 1988. **130**(1): p. 13-23. DOI: 10.1557/PROC-130-13.

162. Oliver, W.C. and Pethica, J.B., *Method for continuous determination of the elastic stiffness of contact between two bodies*. US patent no. 4 848 141, 1989: USA.
163. Guillonneau, G., et al., *Extraction of Mechanical Properties with Second Harmonic Detection for Dynamic Nanoindentation Testing*. *Experimental Mechanics*, 2012. **52**(7): p. 933-944. DOI: 10.1007/s11340-011-9561-5.
164. Maier, V., *Verformungsverhalten von ultrafeinkörnigen Metallen untersucht mittels neu entwickelter Nanoindentierungsmethoden*, in *Technische Fakultät*. 2013, Friedrich-Alexander-Universität Erlangen-Nürnberg.
165. Bolshakov, A. and Pharr, G.M., *Influences of pileup on the measurement of mechanical properties by load and depth sensing indentation techniques*. *Journal of Materials Research*, 1998. **13**(4): p. 1049-1058. DOI: 10.1557/JMR.1998.0146.
166. Elmustafa, A., *Pile-up/sink-in of rate-sensitive nanoindentation creeping solids*. *Modelling and Simulation in Materials Science and Engineering*, 2007. **15**(7): p. 823. DOI: <https://doi.org/10.1088/0965-0393/15/7/008>.
167. Fischer-Cripps, A.C., *Factors affecting nanoindentation test data*, in *Nanoindentation*. 2011, Springer-Verlag New York. p. 77-104. DOI: 10.1007/978-1-4419-9872-9.
168. Khrushchov, M. and Berkovich, E., *Methods of determining the hardness of very hard materials: the hardness of diamond*. *Industrial diamond review*, 1951. **11**(2): p. 42-49.
169. Strader, J.H., et al., *An experimental evaluation of the constant  $\beta$  relating the contact stiffness to the contact area in nanoindentation*. *Philosophical Magazine*, 2006. **86**(33-35): p. 5285-5298. DOI: 10.1080/14786430600567747.
170. Leitner, A., Maier-Kiener, V., and Kiener, D., *Dynamic nanoindentation testing: is there an influence on a material's hardness?* *Materials research letters*, 2017. **5**(7): p. 486-493. DOI: <https://doi.org/10.1080/21663831.2017.1331384>.
171. Raman, V. and Berriche, R., *An investigation of the creep processes in tin and aluminum using a depth-sensing indentation technique*. *Journal of Materials Research*, 1992. **7**(3): p. 627-638. DOI: 10.1557/JMR.1992.0627.
172. Hannula, S. and Li, C.-Y., *Repeated load relaxations of type 316 austenitic stainless steel*. *Scripta metallurgica*, 1984. **18**(3): p. 225-229. DOI: [https://doi.org/10.1016/0036-9748\(84\)90512-X](https://doi.org/10.1016/0036-9748(84)90512-X).
173. LaFontaine, W., et al., *Indentation load relaxation experiments with indentation depth in the submicron range*. *Journal of Materials Research*, 1990. **5**(10): p. 2100-2106. DOI: <https://doi.org/10.1557/JMR.1990.2100>.
174. Goodall, R. and Clyne, T., *A critical appraisal of the extraction of creep parameters from nanoindentation data obtained at room temperature*. *Acta materialia*, 2006. **54**(20): p. 5489-5499. DOI: <https://doi.org/10.1016/j.actamat.2006.07.020>.
175. Mattice, J.M., et al., *Spherical indentation load-relaxation of soft biological tissues*. *Journal of Materials Research*, 2006. **21**(8): p. 2003-2010. DOI: <https://doi.org/10.1557/jmr.2006.0243>.
176. Zhang, C.Y., et al., *Extracting the elastic and viscoelastic properties of a polymeric film using a sharp indentation relaxation test*. *Journal of Materials Research*, 2006. **21**(12): p. 2991-3000. DOI: 10.1557/jmr.2006.0395.
177. Stegall, D.E., et al., *Repeated load relaxation testing of pure polycrystalline nickel at room temperature using nanoindentation*. *Applied Physics Letters*, 2014. **104**(4): p. 041902. DOI: 10.1063/1.4862799.
178. Baral, P., et al., *Theoretical and experimental analysis of indentation relaxation test*. *Journal of Materials Research*, 2017. **32**(12): p. 2286-2296. DOI: 10.1557/jmr.2017.203.
179. Baral, P., et al., *Indentation creep vs. indentation relaxation: A matter of strain rate definition?* *Materials Science and Engineering: A*, 2020. **781**: p. 139246. DOI: <https://doi.org/10.1016/j.msea.2020.139246>.
180. Pharr, G.M., Strader, J.H., and Oliver, W., *Critical issues in making small-depth mechanical property measurements by nanoindentation with continuous stiffness*

- measurement. *Journal of Materials Research*, 2009. **24**(3): p. 653-666. DOI: <https://doi.org/10.1557/jmr.2009.0096>.
181. Cordill, M., et al., *The Nano-Jackhammer effect in probing near-surface mechanical properties*. *International journal of plasticity*, 2009. **25**(11): p. 2045-2058. DOI: <https://doi.org/10.1016/j.ijplas.2008.12.015>.
  182. Siu, K. and Ngan, A., *Oscillation-induced softening in copper and molybdenum from nano-to micro-length scales*. *Materials Science and Engineering: A*, 2013. **572**: p. 56-64. DOI: <https://doi.org/10.1016/j.msea.2013.02.037>.
  183. Merle, B., Maier-Kiener, V., and Pharr, G.M., *Influence of modulus-to-hardness ratio and harmonic parameters on continuous stiffness measurement during nanoindentation*. *Acta Materialia*, 2017. **134**: p. 167-176. DOI: <https://doi.org/10.1016/j.actamat.2017.05.036>.
  184. Merle, B., Higgins, W.H., and Pharr, G.M., *Critical issues in conducting constant strain rate nanoindentation tests at higher strain rates*. *Journal of Materials Research*, 2019. **34**(20): p. 3495-3503. DOI: <https://doi.org/10.1557/jmr.2019.292>.
  185. Phani, P.S., Oliver, W., and Pharr, G., *Understanding and modeling plasticity error during nanoindentation with continuous stiffness measurement*. *Materials & Design*, 2020. **194**: p. 108923. DOI: <https://doi.org/10.1016/j.matdes.2020.108923>.
  186. Phani, P.S., Oliver, W., and Pharr, G., *An experimental assessment of methods for mitigating plasticity error during nanoindentation with continuous stiffness measurement*. *Materials & Design*, 2020. **194**: p. 108924. DOI: <https://doi.org/10.1016/j.matdes.2020.108924>.
  187. Sherby, O. and Armstrong, P., *Prediction of activation energies for creep and self-diffusion from hot hardness data*. *Metallurgical and Materials Transactions B*, 1971. **2**(12): p. 3479-3484. DOI: <https://doi.org/10.1007/BF02811630>.
  188. Poisl, W.H., Oliver, W.C., and Fabes, B.D., *The relationship between indentation and uniaxial creep in amorphous selenium*. *Journal of Materials Research*, 1995. **10**(8): p. 2024-2032. DOI: [10.1557/JMR.1995.2024](https://doi.org/10.1557/JMR.1995.2024).
  189. Choi, I.-C., et al., *Indentation creep revisited*. *Journal of Materials Research*, 2012. **27**(1): p. 3. DOI: [10.1557/jmr.2011.213](https://doi.org/10.1557/jmr.2011.213).
  190. Beake, B., Goodes, S., and Smith, J., *Micro-impact testing: A new technique for investigating thin film toughness, adhesion, erosive wear resistance, and dynamic hardness*. *Surface engineering*, 2001. **17**(3): p. 187-192. DOI: <https://doi.org/10.1179/026708401101517755>.
  191. Jennett, N.M. and Nunn, J., *High resolution measurement of dynamic (nano) indentation impact energy: a step towards the determination of indentation fracture resistance*. *Philosophical Magazine*, 2011. **91**(7-9): p. 1200-1220. DOI: <https://doi.org/10.1080/14786435.2010.485585>.
  192. Zehnder, C., et al., *High strain rate testing at the nano-scale: A proposed methodology for impact nanoindentation*. *Materials & Design*, 2018. **151**: p. 17-28. DOI: <https://doi.org/10.1016/j.matdes.2018.04.045>.
  193. Wheeler, J.M., Dean, J., and Clyne, T., *Nano-impact indentation for high strain rate testing: The influence of rebound impacts*. *Extreme Mechanics Letters*, 2019. **26**: p. 35-39. DOI: <https://doi.org/10.1016/j.eml.2018.11.005>.
  194. Rueda-Ruiz, M., Beake, B.D., and Molina-Aldareguia, J.M., *New instrumentation and analysis methodology for nano-impact testing*. *Materials & Design*, 2020. **192**: p. 108715. DOI: <https://doi.org/10.1016/j.matdes.2020.108715>.
  195. Leitner, A., Maier-Kiener, V., and Kiener, D., *Extraction of flow behavior and Hall-Petch parameters using a nanoindentation multiple sharp tip approach*. *Advanced Engineering Materials*, 2017. **19**(4): p. 1600669. DOI: <https://doi.org/10.1002/adem.201600669>.
  196. Tabor, D., *The Hardness of Metals*. 1951: Clarendon Press.
  197. Fischer-Cripps, A.C., *Contact Mechanics*, in *Nanoindentation*. 2011, Springer-Verlag New York. p. 1-20. DOI: [10.1007/978-1-4419-9872-9](https://doi.org/10.1007/978-1-4419-9872-9).

- 
198. Johnson, K.L., *The correlation of indentation experiments*. Journal of the Mechanics and Physics of Solids, 1970. **18**(2): p. 115-126. DOI: [https://doi.org/10.1016/0022-5096\(70\)90029-3](https://doi.org/10.1016/0022-5096(70)90029-3).
  199. Su, C., et al., *Measurement of power-law creep parameters by instrumented indentation methods*. Journal of the Mechanics and Physics of Solids, 2013. **61**(2): p. 517-536. DOI: <https://doi.org/10.1016/j.jmps.2012.09.009>.
  200. Kermouche, G., Loubet, J.L., and Bergheau, J.M., *Extraction of stress-strain curves of elastic-viscoplastic solids using conical/pyramidal indentation testing with application to polymers*. Mechanics of Materials, 2008. **40**(4): p. 271-283. DOI: <https://doi.org/10.1016/j.mechmat.2007.08.003>.
  201. Lorenz, D., et al., *Pop-in effect as homogeneous nucleation of dislocations during nanoindentation*. Physical Review B, 2003. **67**(17): p. 172101. DOI: [10.1103/PhysRevB.67.172101](https://doi.org/10.1103/PhysRevB.67.172101).
  202. Pharr, G.M., Herbert, E.G., and Gao, Y., *The indentation size effect: a critical examination of experimental observations and mechanistic interpretations*. Annual Review of Materials Research, 2010. **40**: p. 271-292. DOI: <https://doi.org/10.1146/annurev-matsci-070909-104456>.
  203. Mc Elhaney, K.W., Vlassak, J.J., and Nix, W.D., *Determination of indenter tip geometry and indentation contact area for depth-sensing indentation experiments*. Journal of Materials Research, 1998. **13**(5): p. 1300-1306. DOI: [10.1557/JMR.1998.0185](https://doi.org/10.1557/JMR.1998.0185).
  204. Nix, W.D. and Gao, H., *Indentation size effects in crystalline materials: A law for strain gradient plasticity*. Journal of the Mechanics and Physics of Solids, 1998. **46**(3): p. 411-425. DOI: [https://doi.org/10.1016/S0022-5096\(97\)00086-0](https://doi.org/10.1016/S0022-5096(97)00086-0).
  205. Ashby, M., *The deformation of plastically non-homogeneous materials*. The Philosophical Magazine: A Journal of Theoretical Experimental and Applied Physics, 1970. **21**(170): p. 399-424. DOI: <https://doi.org/10.1080/14786437008238426>.
  206. Elmustafa, A.A. and Stone, D.S., *Nanoindentation and the indentation size effect: Kinetics of deformation and strain gradient plasticity*. Journal of the Mechanics and Physics of Solids, 2003. **51**(2): p. 357-381. DOI: [https://doi.org/10.1016/S0022-5096\(02\)00033-9](https://doi.org/10.1016/S0022-5096(02)00033-9).
  207. Durst, K., Göken, M., and Pharr, G.M., *Indentation size effect in spherical and pyramidal indentations*. Journal of Physics D: Applied Physics, 2008. **41**(7): p. 074005. DOI: [10.1088/0022-3727/41/7/074005](https://doi.org/10.1088/0022-3727/41/7/074005).
  208. Swadener, J.G., George, E.P., and Pharr, G.M., *The correlation of the indentation size effect measured with indenters of various shapes*. Journal of the Mechanics and Physics of Solids, 2002. **50**(4): p. 681-694. DOI: [https://doi.org/10.1016/S0022-5096\(01\)00103-X](https://doi.org/10.1016/S0022-5096(01)00103-X).
  209. Kim, J.-Y., et al., *Influence of surface-roughness on indentation size effect*. Acta Materialia, 2007. **55**(10): p. 3555-3562. DOI: <https://doi.org/10.1016/j.actamat.2007.02.006>.
  210. Qu, S., et al., *Indenter tip radius effect on the Nix-Gao relation in micro- and nanoindentation hardness experiments*. Journal of Materials Research, 2004. **19**(11): p. 3423-3434. DOI: [10.1557/JMR.2004.0441](https://doi.org/10.1557/JMR.2004.0441).
  211. Iost, A. and Bigot, R., *Indentation size effect: reality or artefact?* Journal of Materials Science, 1996. **31**(13): p. 3573-3577. DOI: [10.1007/BF00360764](https://doi.org/10.1007/BF00360764).
  212. Everitt, N., Davies, M., and Smith, J., *High temperature nanoindentation—the importance of isothermal contact*. Philosophical Magazine, 2011. **91**(7-9): p. 1221-1244. DOI: <https://doi.org/10.1080/14786435.2010.496745>.
  213. Duan, Z.C. and Hodge, A.M., *High-temperature nanoindentation: New developments and ongoing challenges*. JOM, 2009. **61**(12): p. 32. DOI: [10.1007/s11837-009-0177-5](https://doi.org/10.1007/s11837-009-0177-5).
  214. Li, Y., et al., *In situ measurement of oxidation evolution at elevated temperature by nanoindentation*. Scripta Materialia, 2015. **103**: p. 61-64. DOI: <https://doi.org/10.1016/j.scriptamat.2015.03.008>.

215. Bruder, E., et al., *Influence of solute effects on the saturation grain size and rate sensitivity in Cu-X alloys*. Scripta Materialia, 2018. **144**: p. 5-8. DOI: <https://doi.org/10.1016/j.scriptamat.2017.09.031>.
216. Conrad, H., *Grain size dependence of the plastic deformation kinetics in Cu*. Materials Science and Engineering: A, 2003. **341**(1-2): p. 216-228. DOI: [https://doi.org/10.1016/S0921-5093\(02\)00238-1](https://doi.org/10.1016/S0921-5093(02)00238-1).
217. Maier-Kiener, V., et al., *Influence of solid solution strengthening on the local mechanical properties of single crystal and ultrafine-grained binary Cu-ALX solid solutions*. Journal of Materials Research, 2017. **32**(24): p. 4583-4591. DOI: 10.1557/jmr.2017.320.
218. Brandstetter, S., et al., *Grain coarsening during compression of bulk nanocrystalline nickel and copper*. Scripta Materialia, 2008. **58**(1): p. 61-64. DOI: <https://doi.org/10.1016/j.scriptamat.2007.08.042>.
219. Chen, W., et al., *Mechanically-induced grain coarsening in gradient nano-grained copper*. Acta Materialia, 2017. **125**: p. 255-264. DOI: <https://doi.org/10.1016/j.actamat.2016.12.006>.
220. Edalati, K., et al., *Influence of dislocation-solute atom interactions and stacking fault energy on grain size of single-phase alloys after severe plastic deformation using high-pressure torsion*. Acta Materialia, 2014. **69**: p. 68-77. DOI: <https://doi.org/10.1016/j.actamat.2014.01.036>.
221. Sidot, E., et al., *The lattice parameter of  $\alpha$ -bronzes as a function of solute content: application to archaeological materials*. Materials Science and Engineering: A, 2005. **393**(1): p. 147-156. DOI: <https://doi.org/10.1016/j.msea.2004.10.001>.
222. Gray, G.T., et al., *Influence of strain rate & temperature on the mechanical response of ultrafine-grained Cu, Ni, and Al-4Cu-0.5Zr*. Nanostructured Materials, 1997. **9**(1): p. 477-480. DOI: [https://doi.org/10.1016/S0965-9773\(97\)00104-9](https://doi.org/10.1016/S0965-9773(97)00104-9).
223. Wang, Y. and Ma, E., *Temperature and strain rate effects on the strength and ductility of nanostructured copper*. Applied physics letters, 2003. **83**(15): p. 3165-3167. DOI: <https://doi.org/10.1063/1.1618370>.
224. Li, Y., Zeng, X., and Blum, W., *Transition from strengthening to softening by grain boundaries in ultrafine-grained Cu*. Acta Materialia, 2004. **52**(17): p. 5009-5018. DOI: <https://doi.org/10.1016/j.actamat.2004.07.003>.
225. Cheng, S., et al., *Tensile properties of in situ consolidated nanocrystalline Cu*. Acta materialia, 2005. **53**(5): p. 1521-1533. DOI: <https://doi.org/10.1016/j.actamat.2004.12.005>.
226. Chen, J., Lu, L., and Lu, K., *Hardness and strain rate sensitivity of nanocrystalline Cu*. Scripta Materialia, 2006. **54**(11): p. 1913-1918. DOI: <https://doi.org/10.1016/j.scriptamat.2006.02.022>.
227. Suo, T., et al., *Compressive behavior and rate-controlling mechanisms of ultrafine grained copper over wide temperature and strain rate ranges*. Mechanics of Materials, 2013. **61**: p. 1-10. DOI: <https://doi.org/10.1016/j.mechmat.2013.02.003>.
228. Zehnder, C., et al., *Influence of Cooling Rate on Cracking and Plastic Deformation during Impact and Indentation of Borosilicate Glasses*. Frontiers in Materials, 2017. **4**(5). DOI: 10.3389/fmats.2017.00005.
229. Blum, W., et al., *Two mechanisms of dislocation motion during creep*. Acta Metallurgica, 1989. **37**(9): p. 2439-2453. DOI: [https://doi.org/10.1016/0001-6160\(89\)90041-2](https://doi.org/10.1016/0001-6160(89)90041-2).
230. Kapoor, R., et al., *Creep transients during stress changes in ultrafine-grained copper*. Scripta Materialia, 2006. **54**(10): p. 1803-1807. DOI: <https://doi.org/10.1016/j.scriptamat.2006.01.032>.
231. Blum, W., Eisenlohr, P., and Hu, J., *Interpretation of unloading tests on nanocrystalline Cu in terms of two mechanisms of deformation*. Materials Science and Engineering: A, 2016. **665**: p. 171-174. DOI: <https://doi.org/10.1016/j.msea.2016.04.013>.
232. Blum, W. and Durst, K., *Kinetics of deformation and recovery of nanocrystalline Ni studied by stress reductions*. 2016.

- 
233. Sun, Z., et al., *Grain size and alloying effects on dynamic recovery in nanocrystalline metals*. Acta Materialia, 2016. **119**: p. 104-114. DOI: <https://doi.org/10.1016/j.actamat.2016.08.019>.
234. Milička, K., *Constant structure creep in metals after stress reduction in steady state stage*. Acta metallurgica et materialia, 1993. **41**(4): p. 1163-1172. DOI: [https://doi.org/10.1016/0956-7151\(93\)90164-N](https://doi.org/10.1016/0956-7151(93)90164-N).
235. Milička, K., *Constant structure experiments in high temperature primary creep of some metallic materials*. Acta metallurgica et materialia, 1994. **42**(12): p. 4189-4199. DOI: [https://doi.org/10.1016/0956-7151\(94\)90195-3](https://doi.org/10.1016/0956-7151(94)90195-3).
236. Milička, K., *Constant structure creep experiments on aluminium*. Kovove Mater, 2011. **49**: p. 307-318.
237. Goodwin, F., et al., *Part 3 Classes of Materials*, in *Springer Handbook of Condensed Matter and Materials Data*, Martienssen, W. and Warlimont, H., Editors. 2005, Springer, Berlin, Heidelberg. p. 159-574. DOI: <https://doi.org/10.1007/3-540-30437-1>.
238. Yim, W. and Paff, R., *Thermal expansion of AlN, sapphire, and silicon*. Journal of Applied Physics, 1974. **45**(3): p. 1456-1457. DOI: <https://doi.org/10.1063/1.1663432>.
239. Brunner, D. and Glebovsky, V., *Analysis of flow-stress measurements of high-purity tungsten single crystals*. Materials letters, 2000. **44**(3-4): p. 144-152. DOI: [https://doi.org/10.1016/S0167-577X\(00\)00017-3](https://doi.org/10.1016/S0167-577X(00)00017-3).
240. Trefilov, V., Milman, Y.V., and Gridneva, I., *Characteristic temperature of deformation of crystalline materials*. Crystal Research and Technology, 1984. **19**(3): p. 413-421. DOI: <https://doi.org/10.1002/crat.2170190321>.
241. Weertman, J. and Shahinian, P., *Creep of Polycrystalline Nickel*. JOM, 1956. **8**(10): p. 1223-1226. DOI: [10.1007/bf03377854](https://doi.org/10.1007/bf03377854).
242. Richardson, G.J., Sellars, C.M., and Tegart, W.J.M., *Recrystallization during creep of nickel*. Acta Metallurgica, 1966. **14**(10): p. 1225-1236. DOI: [https://doi.org/10.1016/0001-6160\(66\)90240-9](https://doi.org/10.1016/0001-6160(66)90240-9).
243. Karashima, S., Oikawa, H., and Motomiya, T., *Steady-State Creep Characteristics of Polycrystalline Nickel in the Temperature Range 500° to 1000°C*. Transactions of the Japan Institute of Metals, 1969. **10**(3): p. 205-209. DOI: [10.2320/matertrans1960.10.205](https://doi.org/10.2320/matertrans1960.10.205).
244. Oikawa, H., Kato, T., and Karashima, S., *Activation Parameters of High-Temperature Creep in Nickel, and in Ni-9.5at% Cr and Ni-10.3at% W Alloys*. Transactions of the Japan Institute of Metals, 1973. **14**(5): p. 389-395. DOI: [10.2320/matertrans1960.14.389](https://doi.org/10.2320/matertrans1960.14.389).
245. Wazzan, A.R., *Lattice and grain boundary self-diffusion in nickel*. Journal of Applied Physics, 1965. **36**(11): p. 3596-3599. DOI: <https://doi.org/10.1063/1.1703047>.
246. Maier, H.J., Niendorf T., Bürgel R., *Grundlagen*, in *Handbuch Hochtemperatur-Werkstofftechnik*. 2019, Springer Vieweg, Wiesbaden. p. 1-36. DOI: <https://doi.org/10.1007/978-3-658-25314-1>.
247. Fahrenholtz, W.G. and Hilmas, G.E., *Ultra-high temperature ceramics: Materials for extreme environments*. Scripta Materialia, 2017. **129**: p. 94-99. DOI: <https://doi.org/10.1016/j.scriptamat.2016.10.018>.
248. Silvestroni, L., et al., *Microstructure and properties of HfC and TaC-based ceramics obtained by ultrafine powder*. Journal of the European Ceramic Society, 2011. **31**(4): p. 619-627. DOI: <https://doi.org/10.1016/j.jeurceramsoc.2010.10.036>.
249. Scholz, B., *Untersuchung an TaC-HfC-Hartstoffen mit und ohne Bindemetall*, in *Institut für Material- und Festkörperforschung, Gesellschaft für Kernforschung*. 1974, Universität (TH) Karlsruhe: Karlsruhe.

---

## 10. Cumulative part of the thesis

---

### 10.1. Statement of personal contribution

#### Publication A



**Olena Prach:** Software, Methodology, Investigation, Data Curation, Formal Analysis, Validation, Visualization, Writing – Original Draft, Writing – Review & Editing. **Christian Minnert:** Investigation, Data Curation, Formal Analysis, Validation, Visualization, Writing – Review & Editing. **Kurt E. Johanns:** Software, Methodology, Data Curation, Writing – Review & Editing. **Karsten Durst:** Conceptualization, Methodology, Resources, Writing – Review & Editing, Supervision, Project Administration, Funding Acquisition.

#### Publication B



**Christian Minnert:** Conceptualization, Software, Methodology, Investigation, Data Curation, Formal Analysis, Validation, Visualization, Writing – Original Draft, Writing – Review & Editing. **Karsten Durst:** Conceptualization, Methodology, Resources, Writing – Review & Editing, Supervision, Project Administration, Funding Acquisition.

## Publication C

Materials and Design 192 (2020) 108727

Contents lists available at ScienceDirect

 **Materials and Design** 

journal homepage: [www.elsevier.com/locate/matdes](http://www.elsevier.com/locate/matdes)

---

New ultra-high temperature nanoindentation system for operating at up to 1100 °C 

Christian Minnert<sup>a,\*</sup>, Warren C. Oliver<sup>b</sup>, Karsten Durst<sup>a</sup>

<sup>a</sup> Physical Metallurgy, Materials Science Department, Technical University of Darmstadt, Germany  
<sup>b</sup> Nanomechanics Inc./KLA, Oak Ridge, TN, USA

**Christian Minnert:** Investigation, Formal Analysis, Data Curation, Visualization, Writing – Original Draft, Writing – Review & Editing. **Warren C. Oliver:** Methodology, Writing – Review & Editing, Resources, Supervision. **Karsten Durst:** Conceptualization, Writing – Review & Editing, Supervision, Resources, Funding Acquisition, Project Administration.

## Publication D

 Journal of MATERIALS RESEARCH Article  
DOI:10.1557/s43578-021-00126-4

**ADVANCED NANOMECHANICAL TESTING** 

**Thermally activated dislocation mechanism in Mo studied by indentation, compression and impact testing**

Christian Minnert<sup>1,a)</sup> , Hamad ur Rehman<sup>1</sup>, Karsten Durst<sup>1</sup>

<sup>1</sup> Physical Metallurgy, Materials Science Department, Technical University of Darmstadt, Darmstadt, Germany

**Christian Minnert:** Investigation, Data Curation, Formal Analysis, Validation, Visualization, Writing – Original Draft, Writing – Review & Editing. **Hamad ur Rehman:** Conceptualization, Investigation, Data Curation, Formal Analysis, Validation, Visualization, Writing – Original Draft, Writing – Review & Editing, Project Administration. **Karsten Durst:** Conceptualization, Methodology, Resources, Writing – Review & Editing, Supervision, Project Administration, Funding Acquisition.

---

## 10.2. Relevant full-text reprints

### **Publication A**

Reproduced full text article with permission from Springer Nature.

Copyright (2019), Journal of Materials Research.

# A new nanoindentation creep technique using constant contact pressure

Olena Prach<sup>1,a)</sup>, Christian Minnert<sup>1</sup>, Kurt E. Johanns<sup>1</sup>, Karsten Durst<sup>1</sup>

<sup>1</sup>Physical Metallurgy, Materials Science, Technische Universität Darmstadt, Darmstadt 64287, Germany

<sup>a)</sup>Address all correspondence to this author. e-mail: prach@phm.tu-darmstadt.de

Received: 7 February 2019; accepted: 9 May 2019

A new constant contact pressure (CCP) indentation creep method is presented, which is based on keeping the mean contact pressure as defined through Sneddon's hardness constant, until a steady-state strain rate is achieved. This is in contrast to the conventional constant load–hold (CLH) creep experiments, where the load is held constant and relaxation in both hardness and strain rate occurs at the same time. Besides controlling the mean contact pressure, the dynamic stiffness is furthermore used to assess the indentation depth, thereby minimizing thermal drift influence and pile-up or sink-in effects during long-term experiments. The CCP method has been tested on strain rate sensitive ultrafine-grained (UFG) CuZn30 and UFG CuZn5 as well as on fused silica, comparing the results with those of strain rate jump tests as well as the CLH nanoindentation creep tests. With the CCP method, strain rates from  $5 \times 10^{-4} \text{ s}^{-1}$  down to  $5 \times 10^{-6} \text{ s}^{-1}$  can be achieved, keeping the mean contact pressure constant over a long period of time, in contrast to the CLH method. The CCP technique thus offers the possibility of performing long-term creep experiments while retaining the contact stress underneath the tip constant.

## Introduction

Instrumented indentation testing is a versatile tool commonly applied for measuring mechanical properties, such as hardness, Young's modulus, and fracture toughness on a localized scale [1, 2, 3, 4, 5]. In recent years, significant advances have been made, which have allowed the measurement of thermally activated processes using indentation testing [6, 7, 8, 9, 10, 11, 12, 13]. Nanoindentation creep experiments play a significant role in determining the thermally activated properties on the nanoscale. The loading conditions for indentation creep tests reported in literature are fundamentally different from those for a conventional creep test, where deformation is observed under constant stress [6, 14, 15]. The pioneers in the nanoindentation creep testing are Mulhearn and Tabor [9]. Later, the constant loading-rate test, which was proposed by Mayo and Nix [16], enables an accurate determination of the strain rate sensitivity (SRS)  $m$  of the material. In the indentation load relaxation experiments [13], the position of the indenter is fixed after reaching a predetermined penetration depth and a decrease in the indentation load is monitored as a function of time. Nevertheless, it is rather difficult to keep the penetration depth constant, as a result of the continuous load and displacement change, which makes the

analysis rather difficult [17]. The constant load test [12] is rather similar to the conventional uniaxial creep experiments. At the peak load, a change in hardness is found during the short dwell time. The strain rate can be determined from the displacement rate divided by the indentation depth  $\dot{h}/h$ , and finally, the log–log plot of stress against strain rate helps to find the stress exponent  $n$ . Last, constant strain rate test, developed by Lucas and Oliver [18], proposes to control the indentation strain rate during the loading sequence by the means of the loading rate divided by load  $\dot{P}/P$ . Since multiple tests are performed, the changes in the hardness from test to test should be carefully considered in this method. With the strain rate jump (SRJ) method, the SRS can be determined from a single indentation test, by varying the indentation strain rate during certain depth ranges during the indentation [7]. Long-term indentation creep tests suffer from thermal drift influences, which can be overcome based on the dynamic stiffness, as has been shown by Goldsby and colleagues [19] and has been recently implemented in a method developed by Maier et al. [8]. Due to this, the dwell time of the experiment can be increased to several hours excluding any influence of thermal drift. Despite these improvements, the stress underneath the indenter tip decreases during long-term experiments, which leads in turn to stress relaxation [8, 10].

The present work was initiated with the above challenges in mind. A new indentation creep testing method is proposed, where the mean contact pressure is kept constant. An approach of the proposed method is quite different from conventional indentation creep experiments, where the load on the sample is kept constant and the hardness is constantly decreasing due to the increasing contact depth/area. By using the contact stiffness for controlling the experiments, thermal drift correction is also considered, and effects from pile-up or sink-in on the determination of the contact area do not affect the results of the presented method.

For the method development, ultrafine-grained (UFG) materials CuZn5 and CuZn30 after high-pressure torsion (HPT) have been used [20]. In contrast to single crystalline materials, the UFG materials do not exhibit a strong indentation size effect (ISE) [21, 22]. At larger indentation depths, many thousand grains are deformed and the hardness stays constant with the increase in indentation depth for a given indentation strain rate. Thus, the material hardness is in a steady-state condition [7, 10, 20].

### Constant contact pressure method— theoretical background

Figure 1 schematically illustrates the contact geometry with the plastic zone underneath the indenter, as well as indentation strains for the SRJ and load–hold indentation creep method [8], in comparison with the new constant contact pressure (CCP) method.

During SRJ tests [Fig. 1(a)], the indentation rate ( $\dot{P}/2P$ ) is controlled after the target depth is reached. During a single indentation, appropriate changes in strain rate can be performed up to a target depth over a short time, which significantly reduces thermal drift effects. After

a jump, the plastic zone extends further, leading at the same time to a material-dependent transient in hardness [23]. The SRS is then simply determined from the constant hardness values at each strain rate. Since the new strain rate is reached very fast, a minimal transient period can be found. However, due to the control of the strain rate during the experiment, only strain rates down to  $10^{-3} \text{ s}^{-1}$  can be kept constant.

In the constant load–hold (CLH) method, the load is fixed and held constant ( $P = \text{constant}$ ) during a prescribed time period, after reaching a predetermined target depth value [Fig. 1(b)]. Since the applied load is held constant, the indentation depth and thereby the size of the plastic zone vary only slightly with time and mainly relaxation takes place. The tip sinks slightly into the material and the hardness as well as the applied mean contact pressure decrease until a further displacement into the surface is no longer detectable. The method has the advantage that low strain rate down to  $10^{-6} \text{ s}^{-1}$  can be achieved. However, during the test, the material is in a transient condition and a steady state is never reached.

In the CCP method after reaching the target depth value, a fixed mean contact pressure value (hardness value) is held constant [Fig. 1(c)]. Any increase in the size of the contact leads to an increase in the load to keep the stress level constant. With the increasing indentation depth, also the plastic zone is expanding until a steady state in indentation strain rate is reached. Which also leads to a more significant increase in the indentation depth compared to CLH. The indentation strain rate is declining during that time period until the prescribed mean contact pressure (hardness) and a constant strain rate is achieved. Since the mean contact pressure is used to control the experiments, also small strain rates down to  $10^{-6} \text{ s}^{-1}$  can be achieved with this method.

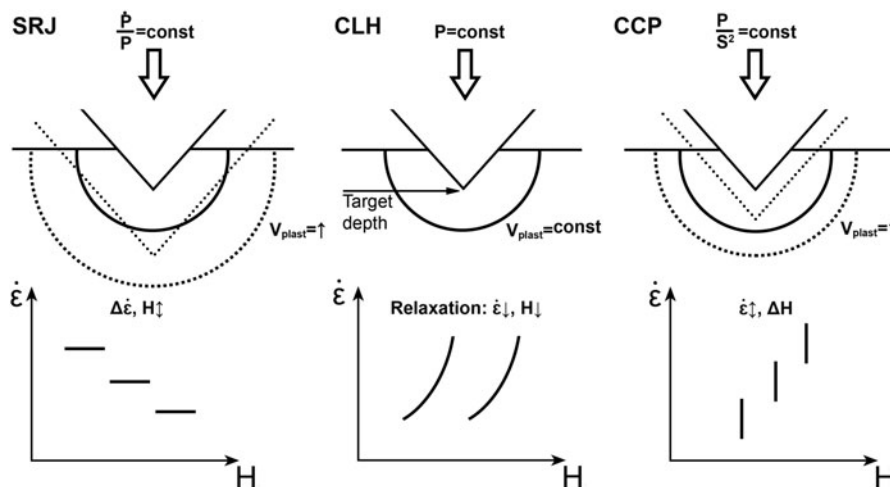


**Figure 1:** Schematic illustration of the resulting strain rate and plastic zone volume  $V_{\text{plast}}$  evolution underneath an indenter during SRJ, CLH, and CCP tests.

To prevent pile-up and thermal drift effects [10, 24] for the final result determined from the CLH and CCP methods, the contact pressure (hardness) is calculated based on Sneddon's equation [Eq. (1)] [1, 25], which was not done in the original SRJ method. Therefore, through this paper, the Sneddon's hardness is also calculated for the SRJ test, based on the harmonic contact stiffness  $S$ :

$$S = \frac{2\beta}{\sqrt{\pi}} \cdot E_R \cdot \sqrt{A_c} \quad (1)$$

where  $E_r$  is the reduced modulus,  $A_c$  is a contact area, and  $\beta$  is a constant, which depends on the geometry of the indenter [1, 25].

Extracting the contact area  $A_c$  from Eq. (1), the pile-up corrected hardness, based on the thermal drift independent contact stiffness channel, can be presented as:

$$H = \frac{P}{A_c} = P \cdot \frac{4 \cdot \beta^2}{\pi} \cdot \frac{E_R^2}{S^2} \quad (2)$$

where  $P$  is the applied load.

In the CCP experiments, the main controlling parameter is the set mean contact pressure (or hardness value), which is kept constant over the whole creep part. At the beginning of the creep segment, to achieve the set mean contact pressure value, a transient in hardness takes place. Therefore, only the segment with a constant hardness value is taken into account.

By knowing the contact area and the tip area function, the contact depth is given as follows:

$$h = h_c + \varepsilon \cdot \frac{P}{S} \quad (3)$$

where  $\varepsilon$  is a constant that depends on the indenter geometry, which for a Berkovich tip  $\varepsilon = 0.75$  [3, 8].

The strain rate was calculated according to Nix and Mayo [16], i.e., the indentation strain rate  $\dot{\varepsilon}$  is the time derivative of the indentation depth  $\dot{h}$  or the applied load  $\dot{P}$  divided by the indentation depth  $h$  or the applied load  $P$  [Eq. (4)] [9, 18].

$$\dot{\varepsilon} = \frac{\dot{h}}{h} = \frac{1}{2} \left( \frac{\dot{P}}{P} - \frac{\dot{H}}{H} \right) \approx \frac{1}{2} \frac{\dot{P}}{P} \quad (4)$$

The SRS and activation volume are calculated with Eqs. (5) and (6) [7, 8]:

$$m = \frac{d(\ln H)}{d(\ln \dot{\varepsilon})} \quad (5)$$

$$A = C \cdot \sqrt{3kT} \cdot \left( \frac{d(\ln \dot{\varepsilon})}{dH} \right) \quad (6)$$

where  $C$  is a constrain factor,  $k$  is the Boltzmann constant, and  $T$  is a temperature.

## Results and discussion

In Fig. 2, the general approach of the CCP test is shown for UFG CuZn30 for different contact pressures of 3.0, 2.9, 2.8, and 2.5 GPa. The initial loading segment for the CCP tests was performed under strain rate control up to a target indentation depth of 500 nm [Fig. 2(a)]. All indentation tests overlap during the initial test segment and a constant depth independent hardness level of 3.1 GPa is reached at an indentation

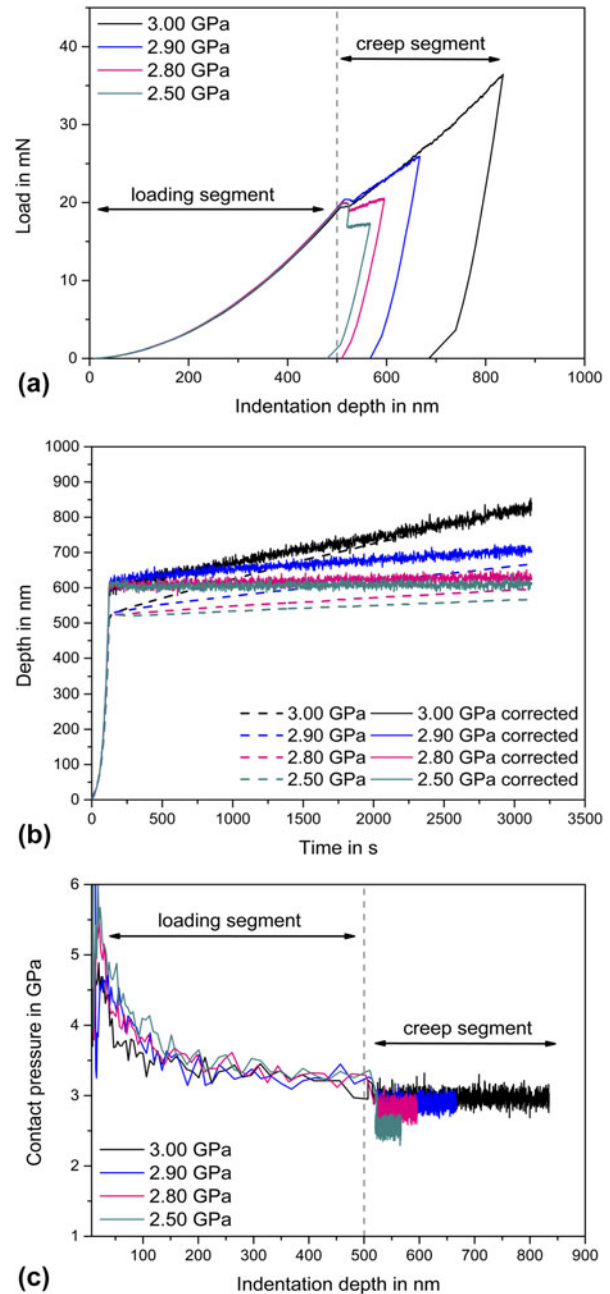


**Figure 2:** The CCP experiments on the UFG CuZn30: (a) load versus depth, (b) raw indentation and corrected indentation depth versus time, and (c) contact pressure versus time.

depth of approximately 400 nm [Fig. 2(c)]. As soon as the target depth is reached, the control software is switched to the CCP test, in which Sneddon's hardness [Eq. (2)] is kept constant at the chosen values, by controlling the  $P/S^2$  signal [Fig. 2(c); raw hardness values at CCP segment]. Switching to a lower mean contact pressures leads to a transient regime until a CCP is held for a certain time period. If the contact stiffness increases with time due to, e.g., creep effects, the machine adjusts the load level accordingly [Fig. 2(a)]. The required adjustment of the load and the loading rate therefore depends on the set  $P/S^2$  or CCP values. To keep the mean CCP constant at a high level (3.0 GPa), a higher loading rate is required as compared with the lower CCP of 2.5 GPa [Fig. 2(a)]. During the CCP segment, the indentation depth and the corrected indentation depth [Eq. (3)] are continuously recorded [Fig. 2(b)]. The depth correction with Eq. (3) is required to account for the thermal drift effect during the long-time creep experiments [Fig. 2(b)]. The strain rate  $\dot{\epsilon}$  during the CCP test is then calculated using  $\dot{h}/h$  Eq. (4). The strain rate analysis in the current work is based on  $\dot{h}/h$ , since the channel provide the smallest noise level.  $\dot{P}/P$  and  $\dot{S}/S$  provide the same strain rate levels. The resulting true indentation depth and load data as well as the hardness values were fitted with a three-parameter power-law function to smooth the raw data. The initial part of the creep segment, where slight unloading is observed, was excluded from the analysis.

Next, the CCP results are compared with the CLH test results (Fig. 3). During the approach segment, both CLH and CCP tests run with the same CSR (constant strain rate) parameters, using the same strain rate value and target depth [Figs. 3(b) and 3(c)]. The starting conditions for the two test approaches are thus the same. At the beginning of the CCP segment, some time is needed to reach the set contact pressure, whereas in the CLH segment the contact pressure evaluation starts from the very beginning of the creep segment [Fig. 3(b)]. This leads to a difference in the contact pressure values at the start of the creep segment [Figs. 3(a)–3(c)]. It is also quite apparent that the contact pressure value in the CCP method is constant during the whole creep segment and a significant increase in indentation depth is found with time [Fig. 3(b)]. The CLH test, however, shows a declining contact pressure value and only a limited increase in indentation depth. Figure 3(c) shows the evaluation of the data by analyzing the strain rate as a function of the contact pressure throughout the indentation test. In the loading segment, until reaching the target depth, a decline in hardness due to the initial ISE is found. However, the hardness is relatively constant at a depth of larger than 300 nm and the ISE does not play a role in the creep segment. In the CLH test segment, the hardness and the indentation strain rate are continuously dropping and neither contact pressure nor hardness value reaches a steady state. In the CCP test, however,

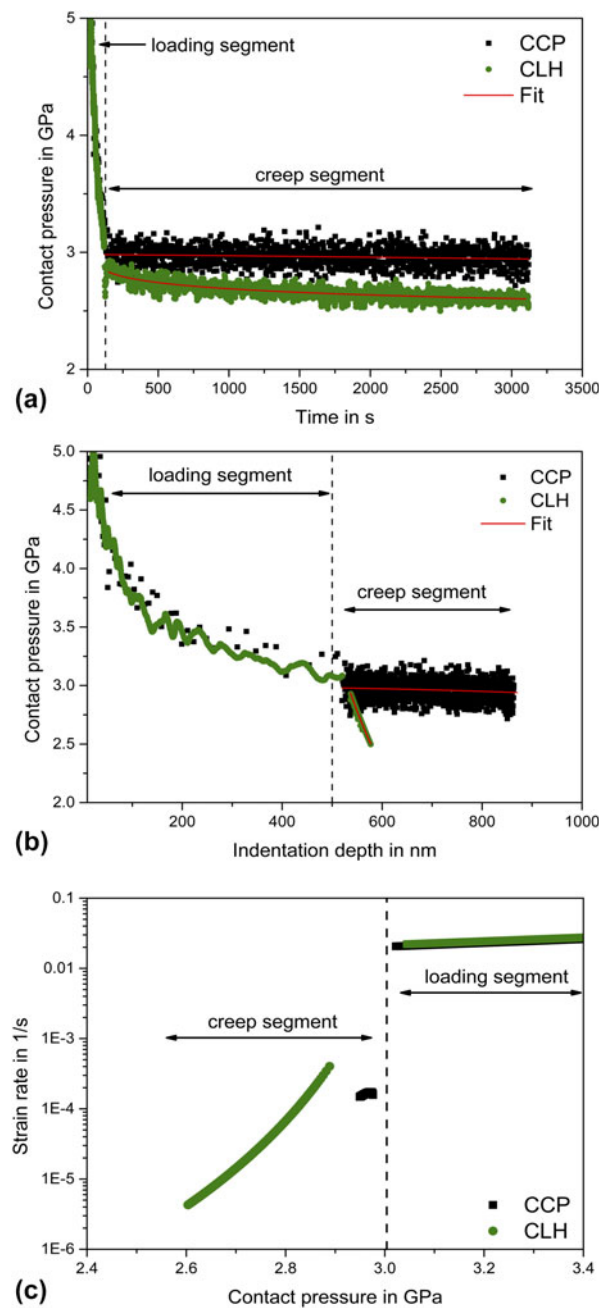


**Figure 3:** (a) Raw contact pressure values versus time, (b) raw contact pressure values versus indentation depth, and (c) strain rate versus contact pressure for CCP and CLH experiments of the UFG CuZn30.

the strain rate and the contact pressure are constant after a certain time period.

In Figs. 4(a) and 4(b), results from the CCP tests at different contact pressure levels are compared with the results of a load–hold indentation experiment at a load of 20 mN, analyzing only the test segment results. The CLH experiment was performed at the same target depth of 500 nm, and the load level at that indentation depth was kept constant. The

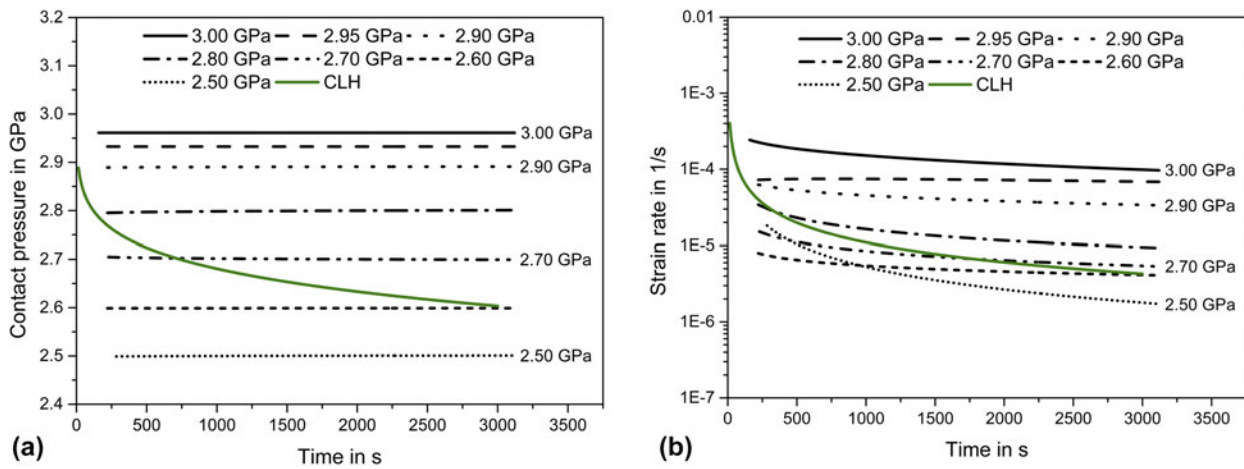


Figure 4: (a) Evaluated contact pressure data for the CLH and CCP experiments versus time and (b) strain rate versus time on the UFG CuZn30.

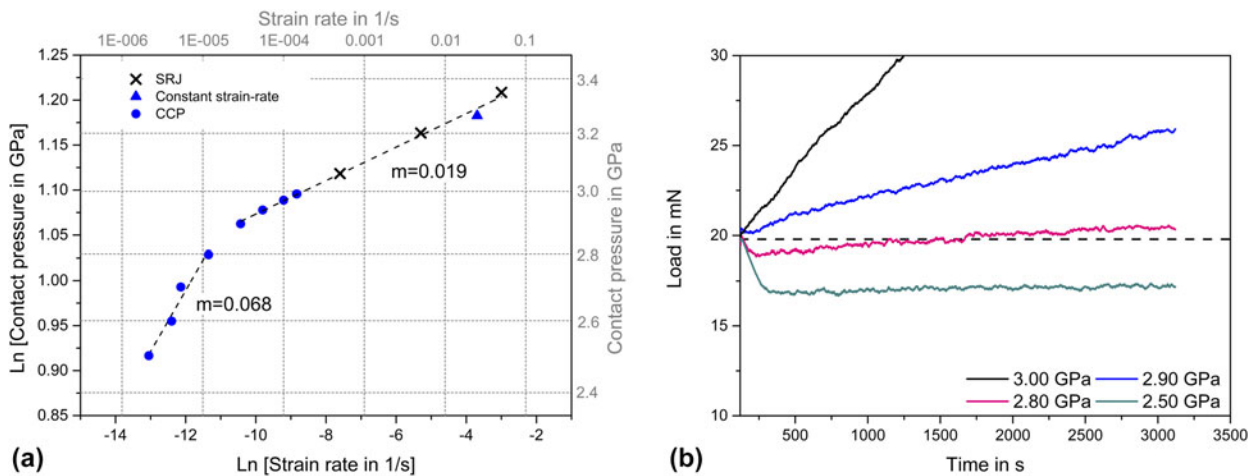


Figure 5: (a) SRS  $m$  of CuZn30, based on SRJ and CCP tests. The contact pressure in the initial loading segment of the CCP experiment is marked as constant strain rate. (b) Corresponding load versus time plot for different contact pressures. The dashed line represents the load at the target depth.

strain rates for all experiments have been evaluated according to Eq. (4) and are plotted in Figs. 4(a) and 4(b).

The hardness for the CLH experiments starts at a higher value and continuously declines, crossing the values from the CCP tests [Fig. 4(a)]. The same applies to the strain rates, which are initially relatively high for the CLH test and continuously decrease with time. The strain rates during the CCP test initially decrease slightly and reach a certain saturation level after a short time period, which depends on the set contact pressure value. The strain rates during the CLH test and the contact pressure thereby cross the values found during the CCP test [Figs. 4(a) and 4(b)].

Even though the contact pressure is kept constant at 2.5 GPa, the strain rate at this contact pressure exhibits a similar decline as in the CLH test. This means that at this low contact pressure, a similar relaxation process is taking place as in the CLH experiment, which will be discussed later on.

From the data on contact pressure and strain rate, it can be concluded that in the CLH test, the stress in the material is continuously decreasing, resulting in a transient behavior of the strain rate, which still continuous after a creep time of 3000 s. Therefore, a steady-state condition is never achieved, and all reported data stem from transient in the creep behavior at reduced mean contact pressures. In the CCP method, a plateau in strain rate is reached after 1500 s (for high contact pressures). Apparently, in the CCP test, the applied stress in the material is controlled and the material reaches a steady-state condition at a nearly constant deformation rate.

In Fig. 5(a), the strain rates that were obtained from the CCP are compared with the results from SRJ tests, analyzing the hardness values at different strain rates in a log/log plot. The SRS  $m$  is there simply given as the slope in the diagram. It was found that the  $m$  value is constant for a wide range of contact pressures and strain rates, and the results of SRJ and

CCP tests nicely overlap with each other. The SRS is constant for contact pressures between 2.90 and 3.35 GPa, and strain rates are in the range of  $1.0 \times 10^{-1} \text{ s}^{-1}$  to  $2.9 \times 10^{-5} \text{ s}^{-1}$ . At lower contact pressures, a change in the  $m$  value is observed. Apparently, the deformation behavior and the deformation condition during the CCP test are changing. This can be understood by analyzing the load versus time data at different contact pressure values [Fig. 5(b)].

A small drop in load can take place even at high hardness values of 3 GPa, and with the decrease in the applied contact pressure (2.5 GPa), this drop becomes more pronounced. The contact stiffness remains constant during this small drop (unloading segment) due to an elastic recovery of the material. At very low contact pressure values, the plastic zone extends negligible and the test condition is changing from CCP to CLH. After transition, the continuously increasing load can be observed, even for low contact pressure values. The system keeps the mean stress underneath the tip constant, and indentation depth increases slightly to keep contact pressure invariable and as a result CCP (hardness values).

In the following analysis, the results of CCP, CLH experiments, and SRJ tests are compared for fused silica (FQ) and HPT CuZn5 and CuZn30. The hardness values from the SRJ test can be overestimated due to pile-up effects, which were not considered in the original analysis [24]. Therefore, in the current data set, Sneddon's equation [Eq. (2)] was applied, similar to the CLH and CCP experiments. Generally, the strain rates (Fig. 6) from the CCP for all tested materials are lower than those applied during SRJ by one order of magnitude. The cause of this difference can be found in the method sequence. It was reported [26] that high strain rates lead to a higher dislocation density. Since the standard CSM is used with the standard strain rate ( $0.025 \text{ s}^{-1}$ ) to reach target depth, after which the control mode is changed and as it was mentioned earlier a small unloading can take place in the meantime, leading to dislocation annihilation and rearrangement. Strain rates found during the CCP tests for the all samples (Fig. 6) are in good accordance with the low strain rates in the SRJ experiments. Nevertheless, the maximum contact pressure which can be achieved and kept constant during CCP test is slightly lower in comparison to the SRJ tests. In contrast to the CLH test, where relaxation takes place, the evaluated strain rates from the CCP method approach a plateau value after a short transient time. Thus, a steady-state condition is reached. For all tested materials, also a change in the SRS exponent is found for lower contact pressures. For keeping the low contact pressure, the applied indentation load is reduced by roughly 20%. The depth of the indentation is only slightly increasing and the load level is approaching the initial indentation load. For these test conditions, the expansion of the plastic zone is strongly

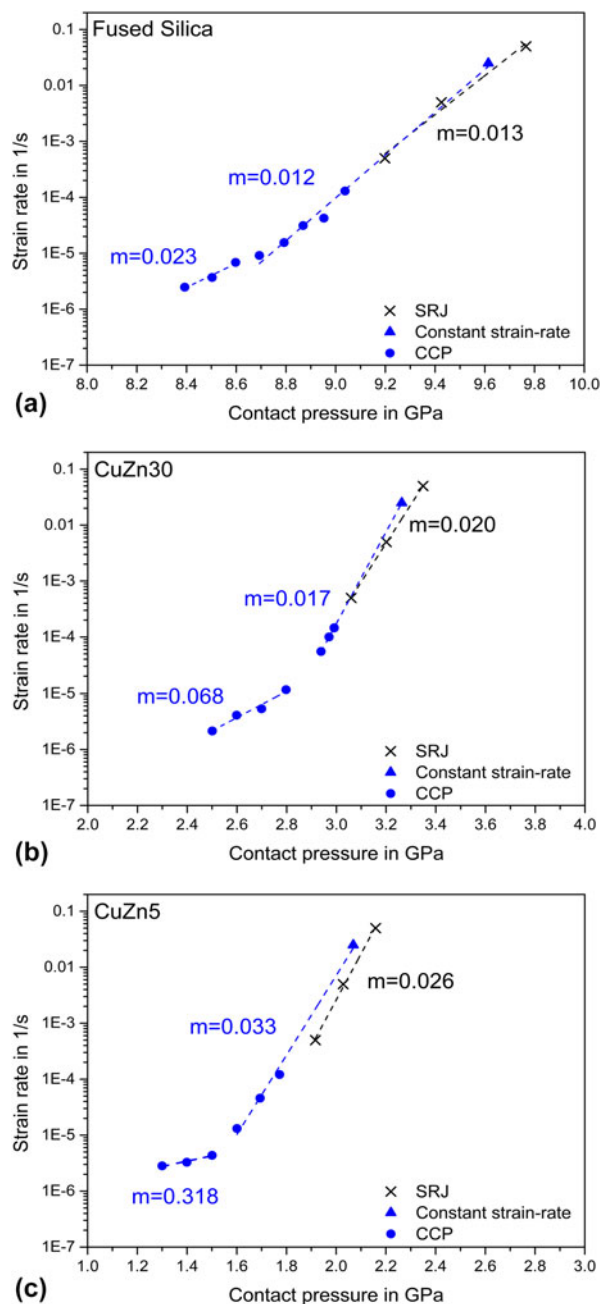


**Figure 6:** Results from nanoindentation CCP, CLH, and SRJ test of (a) fused Silica, (b) HPT CuZn30, and (c) HPT CuZn5.

reduced and mainly relaxation processes within the plastic zone are taking place, leading to a much higher rate sensitivity of the material. This change in deformation condition appears at strain rates between  $10^{-5}$  and  $10^{-6} \text{ s}^{-1}$ , which cannot be controlled in SRJ experiments.

To analyze the expansion process of the plastic zone, the residual indentation depths after CLH at an applied load of 20 mN and CCP at a contact pressure of 3 GPa were determined using a 3D-LASER scanning microscope (LEXT OLS4000, Olympus, Pennsylvania, USA). Depth profiles after different

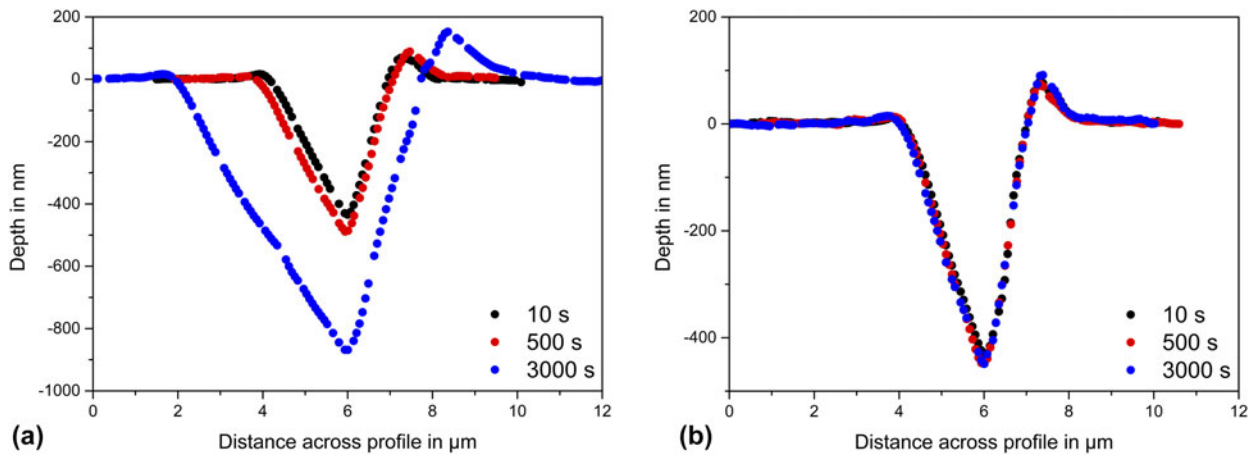


Figure 7: Depth profiles after (a) CCP and (b) CLH experiments on CuZn30.

TABLE I: SRS  $m$  and activation volume  $A$  obtained by nanoindentation for HPT CuZn30, HPT CuZn5, and FQ in this study.

Material	Method	Strain rate sensitivity $m$		Activation volume $A^a$ in $\text{nm}^3$
		High pressure	Low pressure	
CuZn30	CCP	0.017	0.068	0.411
	SRJ	0.020	...	0.343
CuZn5	CCP	0.033	0.318	0.370
	SRJ	0.026	...	0.414
FQ	CCP	0.012	0.023	0.097
	SRJ	0.013	...	0.088

<sup>a</sup>Calculated for the high contact pressures.

creep times were investigated and the depth increase is plotted in Figs. 7(a) and 7(b). Depth increase in the CCP test after the 3000 s of creep is around 440 nm, and for the CLH, it is only 20 nm using the same contact pressure value. Nevertheless, the depth profile analysis can show only the general tendency of the depth increase, because the average depth increase can vary from indent to indent.

Table I gives an overview of the obtained activation volume and SRS. It is not fully clear that only one mechanism is contributing to the thermal activation, and therefore, the activation volumes numbers are only representative of the material response under the described testing condition. The SRS exponent  $m$  of 0.12 was found for the FQ in CCP experiment and activation volume around  $0.088 \text{ nm}^3$ , which is in good agreement with the literature data. Zehnder et al. determined the  $m$  value of 0.0143 and an activation volume of  $0.0793 \text{ nm}^3$  [27]. Bruder et al. reported  $m$  values of 0.028 and 0.018 for CuZn5 and CuZn30, respectively [20]. Besides the well-reproduced  $m$  values at high stresses, also the data at low contact pressures are presented. Here a strong increase in  $m$  as well as activation volume at a CCP is found. During the lower stress values, the plastic zone is only slightly expanding

and the higher  $m$  values obtained are thought to be representative for relaxation processes taking place within the plastic zone. The interpretation of the different deformation regimes for the different materials is beyond the scope of the current publication but opens new directions for further future research.

## Conclusion

A new long-term nanoindentation creep method based on the constant contact pressure has been developed. In contrast to the already existing CLH creep method, CCP method is controlled by  $P/S^2$ . Constant stress can be hold over an extended period of time due to the minimization of the thermal drift effects. Moreover, an applied stress levels can be controlled. This method gives a possibility to study the deformation resistance of the material at various stress levels and strain rates several magnitudes smaller than during SRJ test can be achieved.

The method has provided SRS data from CuZn30, CuZn5, and FQ. The strain rates obtained from the CCP experiment lie between  $5 \times 10^{-4}$  and  $5 \times 10^{-6} \text{ s}^{-1}$  depending on the applied stress level. Using the CCP method, slow strain rates with constant stress levels can be held for a long period of time. On the other hand, for the SRJ experiments, a longer time is required to achieve the slow strain rate, which can be crucial due to the thermal drift effect. SRS values for the CuZn30, CuZn5, and FQ were found to be 0.017, 0.033, and 0.012 at high stress levels, respectively, which is in good accordance with the obtained results from the SRJ method. At lower stress values, we find a higher SRS for all materials, indicating a different deformation regime. The CCP method opens new possibilities in assessing the deformation and creep mechanism at constant contact stresses over a wide range of strain rates.

## Materials and sample preparation

The materials used in this study were FQ, UFG CuZn30 (29.4 at.% Zn), and UFG CuZn5 (4.87 at.% Zn). The UFG copper-based solid solutions were selected since they show a strain rate sensitive behavior at room temperature [7, 8, 20]. Fused silica is generally used as a reference material for tip-shape calibration, as it shows a large elastic recovery without any pile-up. The CuZn30 and CuZn5 samples were processed by HPT using samples in the form of solid disks.

Nanoindentation experiments were performed with a Nanoindenter G200 (Keysight Technologies) equipped with a three-sided Berkovich indenter tip. The machine stiffness and the tip shape calibrations were performed in accordance with the Oliver–Pharr method [4]. The samples were ground and diamond polished down to 0.25  $\mu\text{m}$ , followed by final vibration polishing, to remove the surface deformation layers.

Nanoindentation SRJ tests, according to the method developed by Maier et al. [8, 20], were performed to investigate the local SRS. A minimum of nine indentation SRJ tests were performed using strain rates of 0.05, 0.005, and 0.0005  $\text{s}^{-1}$ . For the CLH method [8] and for the CCP method, a minimum of four tests were performed. The experiments were first run with CSR up to target depth and then CLH, SRJ, and CCP approaches were used. For all experiments, a unified target depth of 500 nm was used.

## Acknowledgments

Authors gratefully acknowledge funding from Deutsche Forschungsgemeinschaft (DFG) within the framework of the project “Indentation creep: New machine and test methodology development at various length scales, high temperatures and low deformation rates” (DU 424/11-1). O. Prach is grateful to the German Academic Exchange Service (DAAD) for the financial support.

## References

1. **W.C. Oliver and G.M. Pharr:** An improved technique for determining hardness and elastic modulus using load and displacement sensing indentation experiments. *J. Mater. Res.* **7**, 1564 (1992).
2. **W.C. Oliver and G.M. Pharr:** Measurement of hardness and elastic modulus by instrumented indentation. Advances in understanding and refinements to methodology. *J. Mater. Res.* **19**, 3 (2004).
3. **J.L. Hay and G.M. Pharr:** Instrumented indentation testing. Kuhn, H., and Medlin, D. In *ASM Handbook Volume 8: Mechanical Testing and Evaluation*, 10th ed. (ASM International, Materials Park, 2000), pp. 232–243.
4. **J. Hay:** Introduction to instrumented indentation testing. *Exp. Tech.* **33**, 66 (2009).
5. **B.R. Lawn and D.B. Marshall:** Hardness, toughness, and brittleness: An indentation analysis. *J. Am. Ceram. Soc.* **62**, 347 (1979).
6. **P.S. Phani and W.C. Oliver:** A direct comparison of high temperature nanoindentation creep and uniaxial creep measurements for commercial purity aluminum. *Acta Mater.* **111**, 31 (2016).
7. **V. Maier, K. Durst, J. Mueller, B. Backes, H.W. Höppel, and M. Göken:** Nanoindentation strain-rate jump tests for determining the local strain-rate sensitivity in nanocrystalline Ni and ultra fine-grained Al. *J. Mater. Res.* **26**, 1421 (2011).
8. **V. Maier, B. Merle, M. Göken, and K. Durst:** An improved long-term nanoindentation creep testing approach for studying the local deformation processes in nanocrystalline metals at room and elevated temperatures. *J. Mater. Res.* **28**, 1177 (2013).
9. **T.O. Mulhearn and D. Tabor:** Creep and hardness of metals: A physical study. *J. Inst. Met.* **89**, 7 (1960).
10. **K. Durst and V. Maier:** Dynamic nanoindentation testing for studying thermally activated processes from single to nanocrystalline metals. *Curr. Opin. Solid State Mater. Sci.* **19**, 340 (2015).
11. **V. Maier, A. Leitner, R. Pippan, and D. Kiener:** Thermally activated deformation behavior of UFG-Au: Environmental issues during long-term and high-temperature nanoindentation testing. *JOM* **67**, 2934 (2015).
12. **M.J. Mayo, R.W. Siegel, A. Narayanasamy, and W.D. Nix:** Mechanical properties of nanophase  $\text{TiO}_2$  as determined by nanoindentation. *J. Mater. Res.* **5**, 1073 (1990).
13. **W.R. Lafontaine, B. Yost, and R.D. Black:** Indentation load relaxation experiments with indentation depth in the submicron range. *Mater. Res.* **5**, 2100 (1990).
14. **W.H. Poisl, W.C. Oliver, and B.D. Fabes:** The relationship between indentation and uniaxial creep in amorphous selenium. *J. Mater. Res.* **10**, 2024 (1995).
15. **D. Caillard and J.L. Martin:** *Thermally Activated Mechanisms in Crystals Plasticity*, 1st ed. (Elsevier Science, Cambridge, UK, 2003); pp. 13–51.
16. **M.J. Mayo and W.D. Nix:** A micro-indentation study of superplasticity in Pb, Sn, and Sn–38 wt% Pb. *Acta Metall.* **36**, 2183 (1988).
17. **R. Goodall and T.W. Clyne:** A critical appraisal of the extraction of creep parameters from nanoindentation data obtained at room temperature. *Acta Mater.* **54**, 5489 (2006).
18. **B.N. Lucas and W.C. Oliver:** Indentation power-law creep of high-purity indium. *Metall. Mater. Trans. A* **30**, 601 (1999).
19. **A. Rar, S. Sohn, W.C. Oliver, D.L. Goldsby, T.E. Tullis, and G.M. Pharr:** On the measurement of creep by nanoindentation

- with continuous stiffness techniques. *MRS Proc.* **841**, R.4.2.1 (2004).
20. **E. Bruder, P. Braun, H. ur Rehman, R.K.W. Marceau, A.S. Taylor, R. Pippan, and K. Durst:** Influence of solute effects on the saturation grain size and rate sensitivity in Cu-X alloys. *Scr. Mater.* **144**, 5 (2018).
21. **B. Backes, Y.Y. Huang, M. Göken, and K. Durst:** The correlation between the internal material length scale and the microstructure in nanoindentation experiments and simulations using the conventional mechanism-based strain gradient plasticity theory. *J. Mater. Res.* **24**, 1197 (2009).
22. **K. Durst, B. Backes, and M. Göken:** Indentation size effect in metallic materials: Correcting for the size of the plastic zone. *Scr. Mater.* **52**, 1093 (2005).
23. **V. Maier-Kiener, X. An, L. Li, Z. Zhang, R. Pippan, and K. Durst:** Influence of solid solution strengthening on the local mechanical properties of single crystal and ultrafine-grained binary Cu–AlX solid solutions. *J. Mater. Res.* **32**, 4583 (2017).
24. **A. Bolshakov and G.M. Pharr:** Influences of pileup on the measurement of mechanical properties by load and depth sensing indentation techniques. *J. Mater. Res.* **13**, 1049 (1998).
25. **R.B. King:** Elastic analysis of some punch problems for a layered medium. *Int. J. Solids Struct.* **23**, 1657 (1987).
26. **J. Chen, Y. Shen, W. Liu, B.D. Beake, X. Shi, Z. Wang, Y. Zhang, and X. Guo:** Effects of loading rate on development of pile-up during indentation creep of polycrystalline copper. *Mater. Sci. Eng., A* **656**, 216 (2016).
27. **C. Zehnder, S. Bruns, J-N. Peltzer, K. Durst, S. Korte-Kerzel, and D. Möncke:** Influence of cooling rate on cracking and plastic deformation during impact and indentation of borosilicate glasses. *Front. Mater.* **4**, 1 (2017).

---

## **Publication B**

Reproduced full text article with permission from Springer Nature.

Copyright (2021), Journal of Materials Research.

---



# Nanoindentation creep testing: Advantages and limitations of the constant contact pressure method

Christian Minnert<sup>1,a)</sup> , Karsten Durst<sup>1</sup>

<sup>1</sup>Physical Metallurgy, Materials Science Department, Technical University of Darmstadt, Darmstadt, Germany

<sup>a)</sup>Address all correspondence to this author. e-mail: c.minnert@phm.tu-darmstadt.de

Received: 28 July 2021; accepted: 19 November 2021

Different loading protocols have been developed in the past to investigate the creep properties of materials using instrumented indentation testing technique. Recently, a new indentation creep method was presented, in which the contact pressure is kept constant during the creep test segment, similar to the constant stress applied in a uniaxial creep experiment. In this study, the results of constant contact pressure creep tests are compared to uniaxial and constant load hold indentation creep experiments on ultrafine grained Cu and CuAl5. The constant contact pressure method yields similar stress exponents as the uniaxial tests, down to indentation strain rates of  $10^{-6} \text{ s}^{-1}$ , whereas the constant load hold method results mainly in a relaxation of the material at decreasing applied pressures. Furthermore, a pronounced change in the power law exponent at large stress reductions is found for both uniaxial and constant contact pressure tests, indicating a change in deformation mechanism of ultrafine grained metals.

## Introduction

Creep properties have been determined for a long time with standardized, macroscopic test methods (e.g. [1–3]). However, sample and test preparation of these standardized experiments are quite time-consuming. Furthermore, it is not possible to test individual phases such as those found e.g. in Ni-based superalloys using macroscopic test procedures. Macroscopic creep testing methods require relatively large sample volumes, which is critical for the analysis of the creep response in small volumes of e.g. thin coatings [4].

Indentation testing, moreover, allows to perform a multitude of creep tests semi-automatically on a single polished sample surface, which significantly increases the sample throughput. The small volume probed allows the mechanical properties of individual microstructure components or thin films to be investigated [5, 6]. Therefore, various indentation creep and relaxation test procedures have been developed for investigating the local, time-dependent mechanical properties. These test procedures promise to provide results comparable to macroscopic tests [7–14]. However, a direct comparison of macroscopic and indentation loading protocols reveals significant differences.

In an uniaxial creep experiment, the applied stress is kept constant for the entire creep segment and the time-dependent strain and strain rates are analyzed. In the most commonly used

constant load hold (CLH) indentation creep method, the load is kept constant and the time-dependent change of hardness and indentation depth are analyzed. For self-similar pyramidal indenters, the resulting strain gradient distribution below the indent is often interpreted as a constant representative strain whereas the hardness can be understood as a representative stress acting within the plastic zone [15]. Indentation testing results thereby in a complex triaxial stress state and the plastically deformed volume is expanding throughout the experiment as described e.g. by Johnson's expanding cavity model [16, 17]. Moreover, both, hardness and indentation strain rate decline with increasing creep time during a constant load and hold experiment, which is in contrast to uniaxial creep testing.

To overcome the limitations of the constant load and hold test, namely the declining indentation stress and indentation strain rate, we have recently presented a new constant contact pressure (CCP) indentation creep method [11], in which the contact pressure, respectively, the stiffness based hardness [8, 11, 18]:

$$H = \frac{4P\beta^2 E_r^2}{\pi S^2} \quad (1)$$

is kept constant throughout the entire creep segment by controlling  $P/S^2$ , where  $P$  is the applied load and  $S$  is the contact

stiffness,  $\beta$  is a geometrical constant and  $E_r$  is the reduced modulus. The contact stiffness is determined using the continuous stiffness measurement (CSM) technique, where the loading signal is superimposed with an additional sinusoidal dynamic displacement. The contact stiffness is thereby determined at an oscillation frequency of 45 Hz, applying a dynamic displacement amplitude of 2 nm. Based on the contact stiffness, the contact pressure can be easily evaluated by using Eq. 1, which was introduced by Joslin and Oliver [18]. Since the contact stiffness is directly related to the contact area, Eq. 1 can be used to determine directly the contact pressure, assuming a constant and depth independent Young's modulus. This contact pressure, determined at a frequency of 45 Hz, is thus based on the current contact situation and is independent of pile-up or thermal drift effects [8, 11, 18].

During a CCP test, the indenter tip is first indentation strain rate controlled loaded onto the surface up to a predefined load or depth, and then the contact pressure is kept constant, but at a lower level compared to the initial hardness value. To keep the average indentation stress inside the plastic zone (the mean contact pressure) constant, the applied load  $P$  has to increase continuously, which is in contrast to uniaxial testing (Fig. 1). The plastic zone thus expands with the increasing load, while the resulting indentation strain rate declines with creep time until a plateau in the indentation strain rate is reached [11].

The contact stiffness, determined during the creep segment is also used to assess the contact depth  $h_c$  using Eq. 2 [8]:

$$h = h_c + \frac{\varepsilon P}{S} \quad (2)$$

with indentation depth  $h$ , and a geometrical constant  $\varepsilon = 0.75$  for a three-sided pyramidal Berkovich indenter. The indentation strain rate  $\dot{\varepsilon}_{ind}$  can be defined via Eq. 3:

$$\dot{\varepsilon}_{ind} = \frac{\dot{h}}{h} = \frac{1}{2} \left( \frac{\dot{P}}{P} - \frac{\dot{H}}{H} \right) \approx \frac{1}{2} \frac{\dot{P}}{P} \quad (3)$$

whereas the indentation creep rate is defined as  $\dot{\varepsilon}_{ind} = \dot{h}/h$  in the CCP and CLH method.

Another advantage of the CCP test method is that the nanoindenter adjusts the loading rate, in order to keep the contact pressure constant and only has to monitor changes in load or indentation depth vs time in order to determine the strain rate. This allows to assess much smaller strain rates in comparison with constant strain rate (CSR) and strain rate jump (SRJ) experiments, which keep the strain rate constant and allow only a limited variation in indentation strain rate ( $10^{-1} - 10^{-3} \text{ s}^{-1}$ ). Further details and results of experiments performed with the CCP test methodology on fused silica and ultrafine grained alloys can be found in [11].

The strain rate sensitivity can be analyzed by the strain rate dependent change in deformation resistance or stress (Eq. 4) [7]:

$$m = \frac{d(\ln H)}{d(\ln \dot{\varepsilon}_{ind})} = \frac{d(\ln \sigma)}{d(\ln \dot{\varepsilon}_{uni})} \quad (4)$$

with indentation strain rate  $\dot{\varepsilon}_{ind}$  and uniaxial strain rate  $\dot{\varepsilon}_{uni}$ . The activation volume is associated with the active deformation mechanisms and is given for uniaxial and indentation test by Eq. 5 [7, 8]:

$$m = \frac{1}{n} = \frac{\sqrt{3}kT}{V\sigma_f} = \frac{C\sqrt{3}kT}{VH} \quad (5)$$

with stress exponent  $n$ , Boltzman constant  $k$ , absolute temperature  $T$  and uniaxial flow stress  $\sigma_f$ . It should be noted, that the absolute number of  $V$  is not sufficient to describe the complete deformation behavior, since several mechanisms may be active simultaneously. The Berkovich hardness and uniaxial flow stress at a representative strain of about 7.2% can be converted in each other using a strain-rate independent constraint factor  $C$ , for metals a constraint factor of 2.8–3 was found [7, 8].

It should be noted, that even if the indentation strain rate plateaus during a constant contact pressure experiment and a steady state in deformation resistance is achieved, the deformation

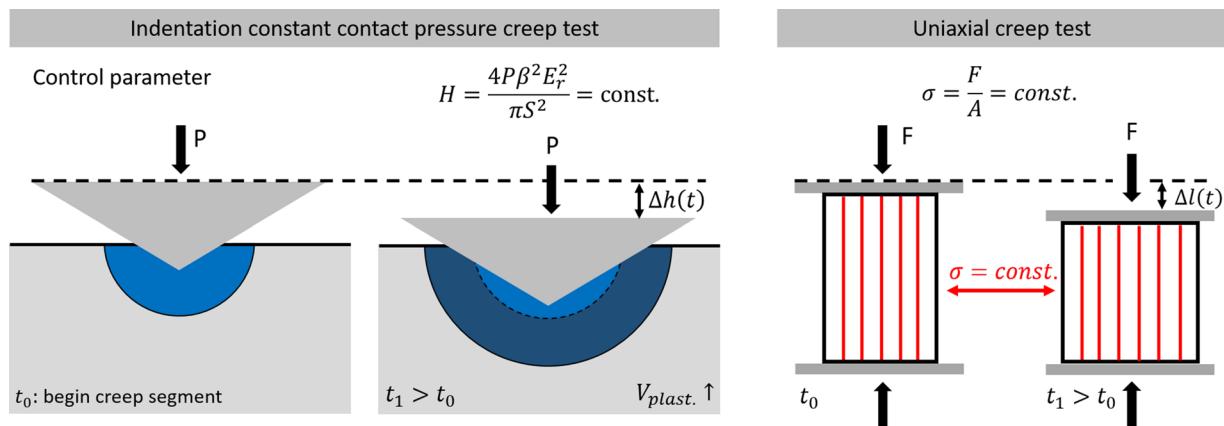


**Figure 1:** Comparison of the CCP nanoindentation creep method with a conventional uniaxial creep test. Adapted from [11].

microstructure is not necessarily in a steady state. This is caused by a continuous expansion of the plastic zone, whereby fresh, initially undeformed material is continuously being deformed. It is therefore not clear which creep mechanism dictates the minimum creep rate measured during an indentation test and how this relates to the minimum creep rate found in uniaxial creep experiments.

Comparing with literature, it should be noted that the CCP test protocol is quite similar to uniaxial stress dip tests, in which the sample is first loaded to a certain strain level and then partially unloaded, until the desired stress level is reached. Subsequently, the reduced stress is kept constant until the end of the experiment, analyzing the transient creep behavior [19–27]. Stress dip tests have been used in literature to investigate the materials response at different stress levels and a quasi-constant microstructure [25, 28–32], by Blum et al. e.g. [19–24, 31, 32] and Milička e.g. [25–27]. It has been observed that the resulting creep rate immediately after a stress drop depends on the magnitude of stress reduction which can be related to a changing deformation behavior.

Furthermore, Sun et al. used uniaxial stress dip tests inside a synchrotron to analyze the dynamic recovery behavior of nanocrystalline Ni and NiFe alloys [31, 32]. They found that the balance between dislocation nucleation and annihilation and thus the dislocation density changes depending on the amount of stress reduction during a stress dip test. At high stress levels and forward deformation, grain boundaries can act as sources but also as sinks for the dislocations. Strong stress reductions cause an inversion of the dislocation motion (backward deformation), leading dislocations to annihilate in the grain boundaries. This relaxation process leads to a reduction of the defect density and thus to a softening of the material. Thus, the equilibrium dislocation density correlates with the applied stress [20, 31–33].

A review on deformation mechanism of nanocrystalline and ultrafine grained fcc metals like Ni or Cu can be found in [8, 34–38]. The time-dependent deformation behavior of materials is strongly influenced not only by the homologous temperature and the applied stress, but also by loading history and the microstructure, respectively [20–22, 24, 25, 31, 32, 37–42].

From our previous publication [11] a few open questions remained, related to the contact situation after the indentation stress reduction, as well as for a possible change in deformation mechanism of ultrafine grained (UFG) materials. A pronounced increase in the strain rate sensitivity exponent was found for UFG CuZn30 after large indentation stress reductions, leading to low creep rates. It was not fully clear, which maximum indentation stress reductions are possible for a CCP test and if the observed changes in indentation strain rate sensitivity at low indentation stress levels and large contact pressure reductions are caused by the contact situation, or a

loading history effect, or if the enhanced strain rate sensitivity is indicative of a change in deformation mechanisms.

In the following, the long-term CCP indentation creep methodology is presented with respect to maximum indentation stress reduction and load history effects. The results of the CCP tests are compared to SRJ, as well as CLH indentation creep experiments. Furthermore, uniaxial compression SRJ experiments as well as stress dip tests were carried out on macroscopic compression samples of UFG Cu and a binary UFG Cu alloy with 5 wt% Al.

The UFG microstructures were generated by a semi-constraint high pressure torsion (HPT) process. More detailed information on sample processing and test parameters can be found in “Materials and methods” section. UFG Cu-alloys have been used as reference materials as they can be easily produced via a HPT deformation and show already a significant creep deformation at room temperature. In addition, good data sets on strain rate sensitivities and stress exponents are already available for Cu [33, 37, 38, 43–53] as well as for the investigated CuAl5 alloy investigated [53]. Furthermore, UFG materials do not show a pronounced indentation size effect and are thus nicely suited for indentation creep testing. The hardness is thus nearly independent of the indentation depth and data recorded at different indentation depths can be easily compared. This is in contrast to single crystalline materials, where an indentation size effect also needs to be considered [54].

## Results and discussion

### Indentation CCP testing

The CCP test procedure consists of two test segments, the initial loading with a constant indentation strain rate (here up to an indentation depth of 500 nm) and the subsequent creep segment where the contact pressure is kept constant (here for 0.8 h). Different contact pressures have been applied by varying the ratio of  $P/S^2$ , where the partial unloading at the beginning of the CCP segment was done in a single step. The load–displacement relationship for CCP tests on CuAl5 applying four different contact pressure reductions is shown in Fig. 2a. In total, the contact pressure was varied in eight different stages between 3.04 and 2.40 GPa (Fig. 2d). At the beginning of the creep segment (Fig. 2a), the indentation control is switched from strain rate control to a constant contact pressure control based on Eq. 1. Doing so, it is apparent that the slope of the load–displacement (Fig. 2a), or load–time data (Fig. 2b), is significantly dropping, when reducing the contact pressure. The  $P/S^2$  ratio is adjusted at the beginning of the creep segment (Fig. 2c) to set the desired contact pressure (Eq. 1) and then kept constant until the end of the experiment.

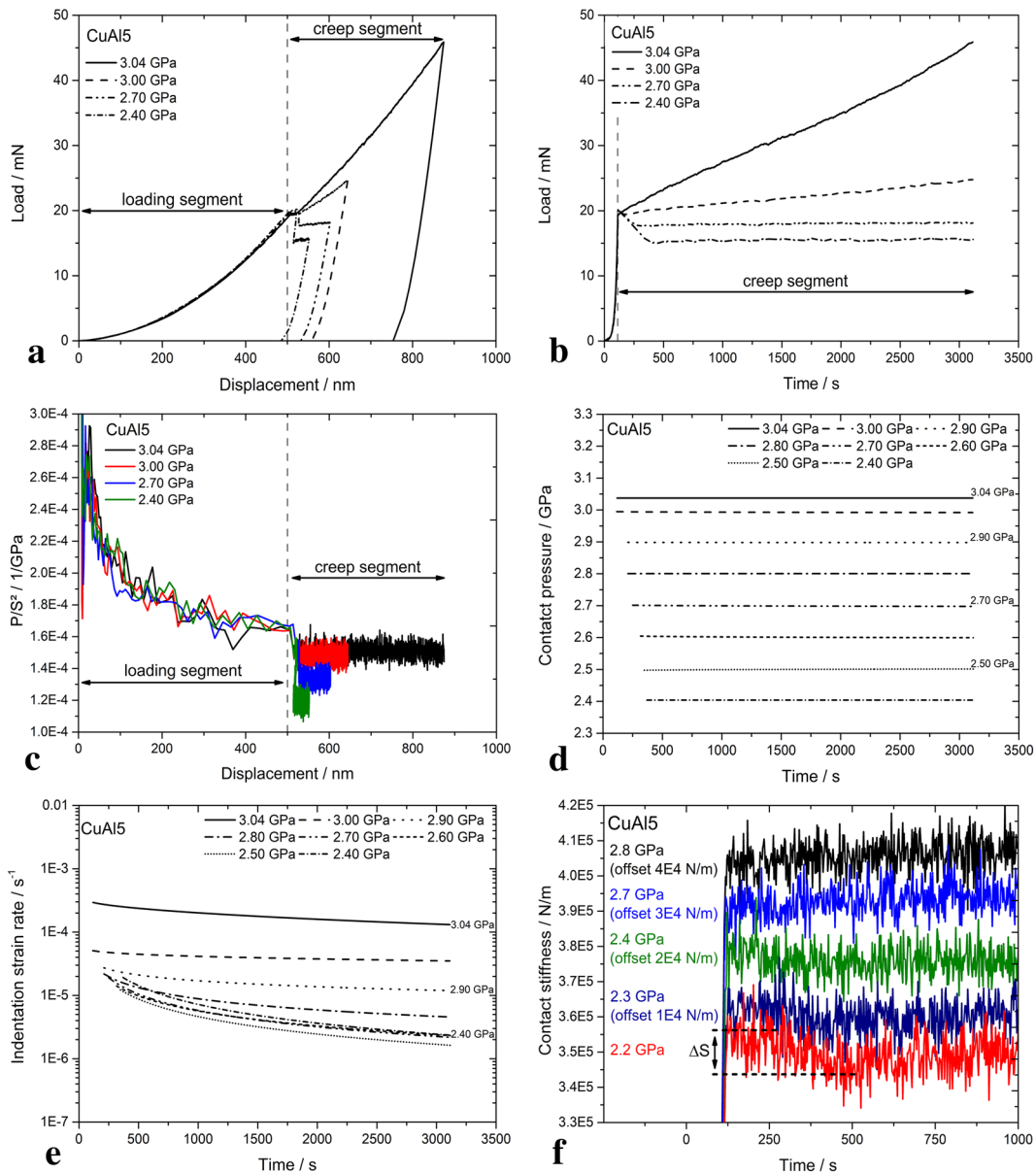


**Figure 2:** Indentation CCP tests on CuAl5 applying a single unloading event. In (a) the load vs. displacement, in (b) the load vs. time, (c) the  $P/S^2$  ratio vs. displacement, (d) the applied contact pressures vs. time, (e) indentation strain rate vs. time and (f) the contact stiffness vs. time is plotted for a single partial unloading event at the beginning of the CCP test segment. The individual stiffness curves are each shifted by an offset of  $1E4$  N/m for a better visibility.

A reduction in contact pressure results in a smaller increase in indentation depth during the creep segment (Fig. 2a). Based on the displacements, the resulting indentation creep strain rates are plotted in Fig. 2e. Here it is clear that both the indentation depth and the indentation strain rate declines with a reduction in indentation contact pressure. The corresponding data for Cu are shown in the Supplementary (S1). This data is later on (Sect. 3.3) used for a comparison with the uniaxial test results.

To analyze the maximum allowable indentation stress reduction, the contact stiffnesses for different contact pressures are shown in Fig. 2f. For low contact pressures (2.2–2.4 GPa) a slight decrease of up to 3.1% in  $S$  (Fig. 2f) can be found for  $H=2.2$  GPa in the beginning of the creep segment. Furthermore, an apparent increase in the indentation strain rate (not shown) was found for these low contact pressures, which cannot be justified physically and the test were discarded from a further analysis.

The exact reasons for this behavior are not fully clear, but the indenter could potentially lose contact during unloading, also due to the dynamic oscillation of the indenter tip. As a result of the, albeit marginal, unloading, the contact stiffness may no longer be determined correctly [55]. A pronounced decrease in  $S$  or at least a significant increase of its scattering would be an indication for contact issues if the tip would lose the contact temporarily due to the load reduction and the additional dynamic displacement (CSM technique). The scattering is independent of the applied pressure, however, a large reduction in contact pressure, can lead to changes in the contact situation and the material behavior could change from fully plastic to elastic-plastic deformation.

In this study and our previous publication on UFG Cu alloys and fused silica [11], the contact pressure could be reduced by approx. 12% (fused silica) to 37% (UFG Cu) (reference value at  $0.01 \text{ s}^{-1}$ ). For CuAl5, the contact pressure (Eq. 1) of 2.4 GPa, corresponding to a reduction of 25%, represents the lower limit. A detailed study of the indentation profiles is also given there.

### Load history effect

It is unclear whether the time-dependent deformation behavior is affected by the magnitude of sudden contact pressure reduction at the beginning of the creep segment. Therefore, additional

CCP tests were carried out on CuAl5 in which the contact pressure was reduced incrementally in order to investigate a possible load history effect.

The corresponding load-displacement curves as well as the contact pressure and depth as a function of time are plotted in Fig. 3a, b and c. Up to six successively decreasing contact pressures with a reduction in contact pressure of 0.1 GPa, and 0.2 GPa were applied in the two test series.

A decline in  $S$  at very low contact pressures can also be observed with the incremental test method (Fig. 3d), comparable to the original procedure (single unloading, Fig. 2f). The contact stiffness is thus exclusively affected by the reduction of the contact pressure in relation to the initial value at the end of the loading segment. The resulting indentation strain rates for the different contact pressures are compared in Fig. 5b to each other.

### Uniaxial constant stress testing

The results of the uniaxial constant stress tests on CuAl5 are shown in Fig. 4. In Fig. 4a, the stress strain response of tests with and without partial unloading segments are plotted. The samples were loaded up to total strains of 3%, reaching a saturation stress. Larger plastic strains caused shear failure of

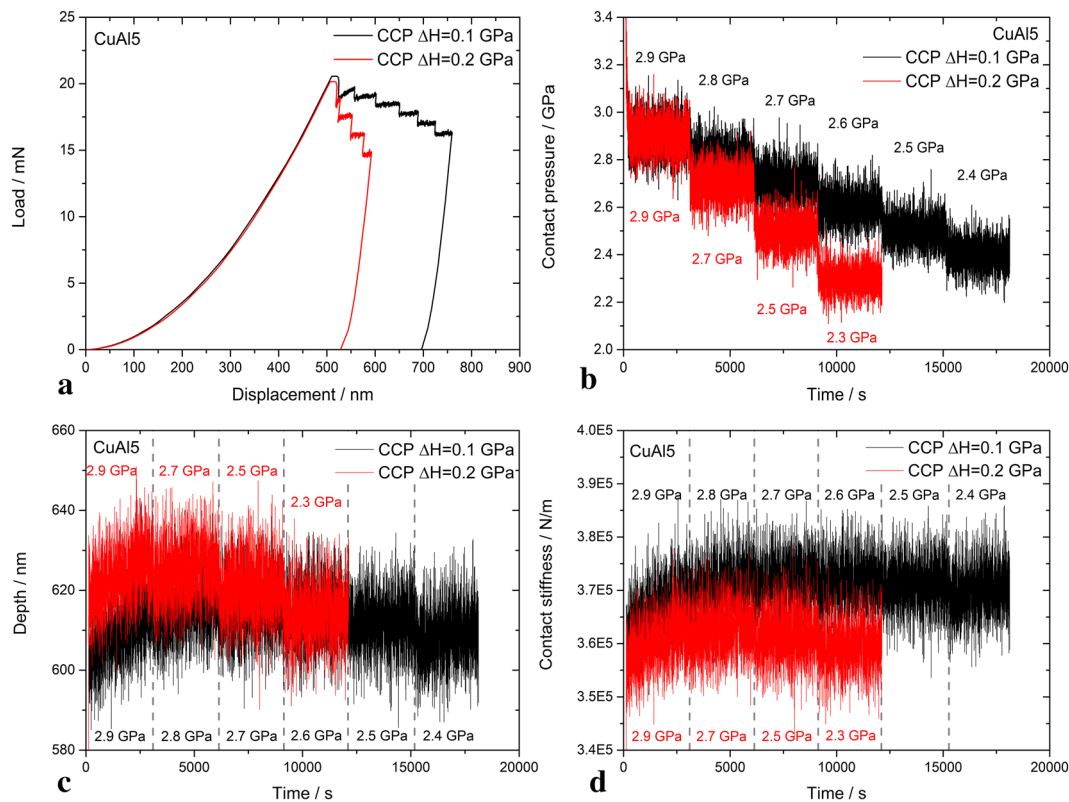


**Figure 3:** Indentation CCP tests on CuAl5 applying multiple partial unloading events. In (a) the load vs. displacement, in (b) the raw contact pressure vs. time, (c) the corrected indentation depth vs. time and (d) the contact stiffness vs. time is plotted.

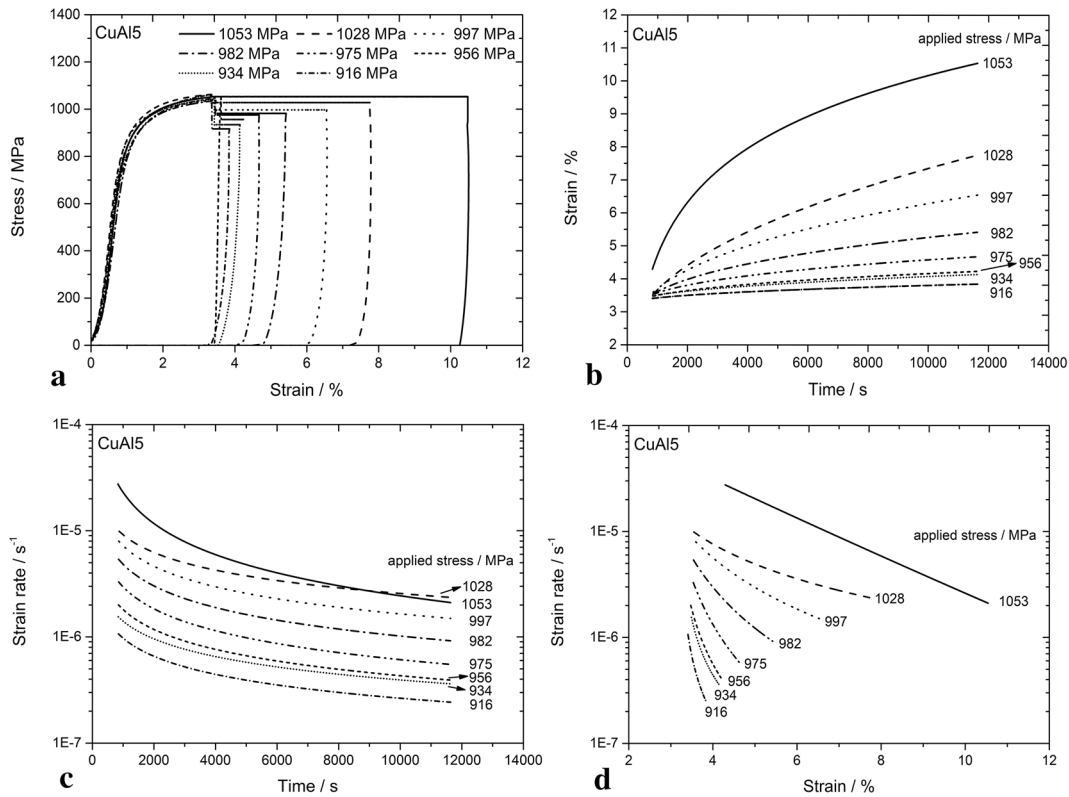


**Figure 4:** Uniaxial constant stress tests on CuAl5 with partial unloading at the beginning of the creep segment: stress vs. strain (a), strain vs. time (b), strain rate vs. time (c) and strain rate vs. strain (d).

the specimens and could not be applied. The partial unloading was done in displacement control. In the following creep segment, the engineering stress is kept constant for 10,800 s (3 h), resulting in a time dependent creep deformation as shown in Fig. 4b. The resulting creep strain rate as a function of test time and total strain is illustrated in Fig. 4c, d.

It is evident that the resulting strain and strain rate strongly depend on the applied stress level. For constant stress levels or small stress reductions, a high creep strain as well as a high strain rate can be observed during the test period (Fig. 4c). In contrast, a larger stress reduction results in a very low forward deformation of the sample and thus a low creep strain rate. However, a steady state creep condition is not reached during the experiment as the strain rate is continuously decreasing with the applied strain as illustrated in Fig. 4d. The uniaxial stress strain diagrams for Cu can be found in the supplementary (S2). Cu exhibits a similar behavior as CuAl5, except that the strain rate as a function of strain shows saturation at large stress reductions and large strains. The material approaches a steady state behavior.

### Comparison of strain rate sensitivity

The results of nanoindentation experiments (CSR, SRJ, CCP and CLH) are plotted in Fig. 5a for Cu and in Fig. 5b for CuAl5, whereas the results of the uniaxial tests (SRJ and constant stress) for Cu and CuAl5 are plotted in Fig. 5c, d respectively. The CSR data were determined in the initial loading segment of CCP tests, prior to partial unloading, and presented for comparison. The data from CCP tests was averaged over the last 500 s of the individual creep segments (between 2500 and 3000 s for CCP tests with a single unloading event). Data from constant stress tests were averaged in the creep segment between 2500 and 3000 s.

The data of the CSR, SRJ and CCP nanoindentation and uniaxial experiments agree well with each other and show two distinct regimes in the deformation behavior, with a lower strain rate sensitivity exponent in the high and a higher strain rate sensitivity exponent in the lower stress regime. The observed transition from the high to the low stress regime takes places at strain rates of about  $10^{-5} - 10^{-6} \text{ s}^{-1}$  for both uniaxial and indentation

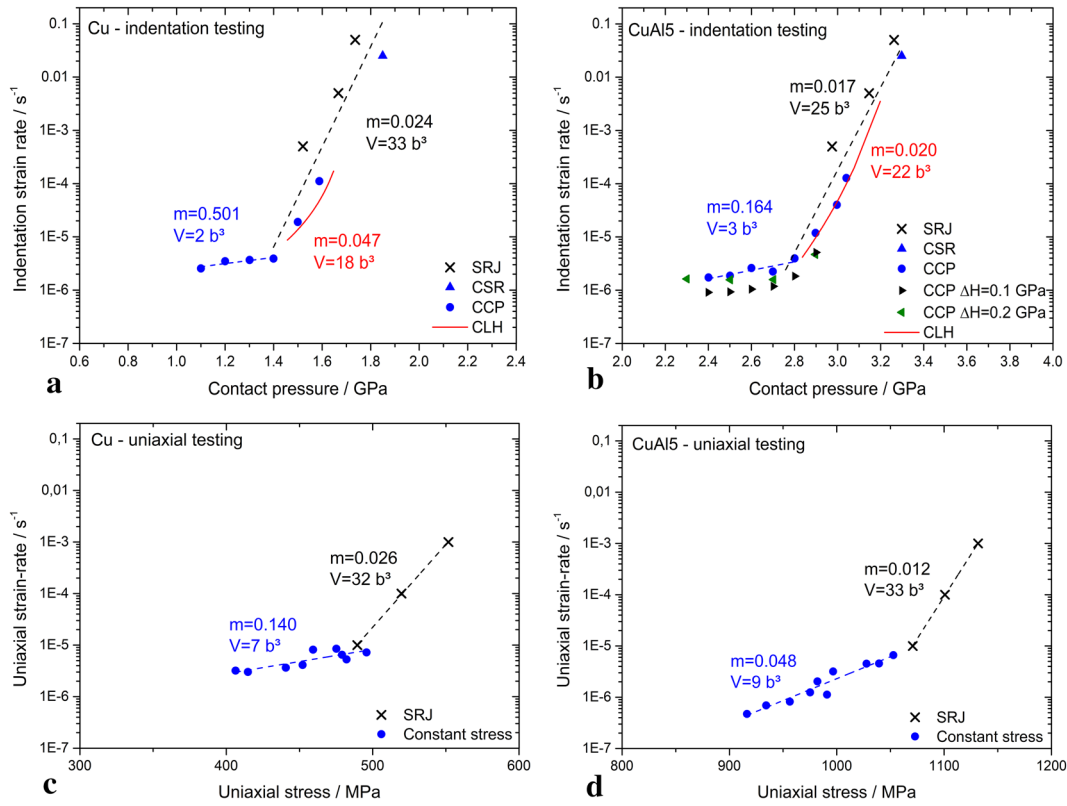


**Figure 5:** Comparison of the stress dependent equivalent strain rates from nanoindentation (a, b) and uniaxial experiments (c, d) on UFG Cu (left column) and UFG CuAl5 (right column). The CCP creep data was averaged over the last 500 s of the creep segments. Data from constant stress tests were averaged in the creep segment between 2500 and 3000 s.

test approaches. The observed transition in the deformation behavior is thus not a testing artefact of the CCP test method, but clearly results from a change in the deformation mechanism in the tested UFG Cu and UFG CuAl5. In Fig. 5b, also the results of the incremental unloading ( $\Delta H = 0.1 - 0.2$  GPa; black and green triangles) are shown in comparison to the results of CCP tests with a single unloading increment (blue circles). All three test series on CuAl5 (Fig. 5b) agree with each other and a history effect can thus be excluded for the current testing results.

In the high stress regime, a strain rate sensitivity value of  $m = 0.024$  was obtained for UFG Cu (Fig. 5a) by nanoindentation CCP, CSM and SRJ tests, which agrees with the exponent  $m = 0.026$  from the uniaxial strain rate jump tests (Fig. 5c). Both values are in good agreement with literature data of 0.009–0.031 [43–48, 51, 53]. CLH tests results in  $m = 0.047$  which is significantly larger than literature values. For UFG CuAl5, (Fig. 5b, d), SRS parameter of 0.012–0.017 (SRJ) and CCP tests) were found which are smaller by a factor of two than previously reported values of 0.024–0.026 [53] determined by SRJ indentation tests. The SRS coefficient determined by CLH tests is 0.020 and therefore comparable with the indentation SRJ/CCP data set ( $m = 0.017$ ). The results of CLH experiments follow to a certain extend the data from SRJ, CSR and CCP data. However there, a

continuous decline in indentation strain rate and contact pressure is found, leading to slightly larger strain rate sensitivity exponents compared to CCP, CSM and SRJ tests.

In the low stress regime, however, significantly larger  $m$  values in the range of 0.140–0.501 could be determined for UFG Cu by uniaxial constant stress and CCP indentation tests, respectively. The SRS has therefore increased by a factor of up to 21. A similar, but clearly less pronounced, trend was also observed for CuAl5, where  $m$  values of 0.048–0.164 were determined. The CLH experiments did not show the observed transition found in the other experiments after a test duration of 3000 s. A similar behavior was also observed by Yang et al. for relaxation tests on nanostructured Cu [38].

The corresponding activation volumes were calculated using Eq. 5 and the material specific Burgers vectors  $b$  [56]. The activation volumes determined in the high stress regime from SRS and CCP tests are quite similar for Cu ( $V_{Cu} = 24 - 26b^3$ ), while  $V$  from CLH tests is lower at  $18 b^3$  (Fig. 5a). For CuAl5,  $V$  of 12–20  $b^3$  were found with very similar values from the indentation tests of 17  $b^3$  and 22  $b^3$ . Activation volumes larger than 10  $b^3$  indicate that dislocation cross slip is the dominant deformation mechanism [57]. In contrast,  $V$  in the range of 2–9  $b^3$  were calculated for the low stress regime, with only minor differences

between the activation volumes from uniaxial constant stress and indentation CCP tests. The deformation behavior in the high stress regime is, thus, related to nucleation and motion of dislocations, where dislocation annihilation and grain boundary mediated processes becomes dominant in the low stress regime [37, 38, 57].

The calculated activation volumes only represent an average value and provide only limited information on the actual material behavior as several deformation mechanisms can be active at the same time. This is moreover true, since a steady state condition is not achieved and other transition mechanism, like grain coarsening could influence the calculated values. A detailed discussion of the deformation processes including microstructural influences will be prepared for a separate publication.

A direct comparison of different data sets determined by indentation and compression experiments are given in Fig. 6. We would like to point out that the uniaxial constant stress tests are only to be used for comparison with indentation tests. We are aware that the selected creep times are not sufficient to reach a steady state condition (e.g. Fig. 4c, d). However, uniaxial tests were performed in a similar manner to CCP tests but there are clear differences.

Hardness values were converted to equivalent uniaxial stresses using constant constraint factors of 2.8 for CuAl5 and 3 for Cu. The direct comparison of the indentation and uniaxial tests shows a good correlation for UFG Cu and the high stress regime of CuAl5. In the low stress regime of CuAl5, deviations between the data sets occur.

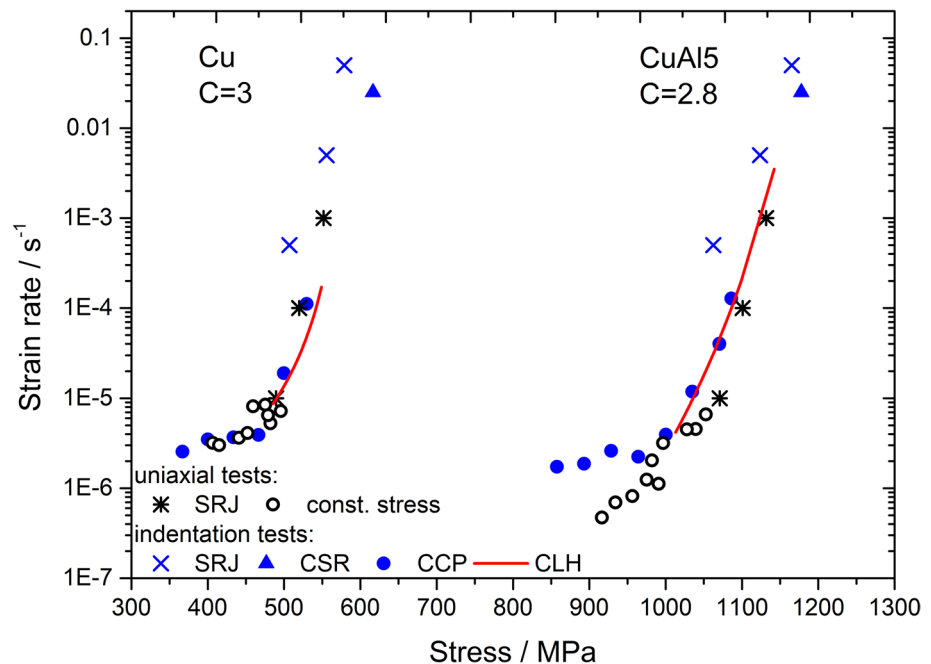
In CCP experiments, the average representative strain is constant, since a Berkovich indenter with a self-similar

geometry has been used whereas the probed volume increases with testing time. In contrast, the specimen volume is constant in a uniaxial test, but the applied strain increases continuously. The stress reductions are comparable for both test procedures but the absolute stresses within the plastic zone underneath the indenter are way higher than in the compression samples. Unstable microstructures are susceptible to high stresses, therefore changes in the microstructure like grain coarsening, are more likely to occur in the case of indentation tests than in a compression test [58–60].

Relaxation processes potentially assisted by grain growth is expected to occur particularly with UFG Cu as observed by Maier-Kiener et al. [53] during nanoindentation testing, while alloying Al leads to a pinning effect of the grain boundaries and thus to a more stable microstructure of CuAl5. This also becomes clear from the course of the strain rate as a function of time, respectively, strain. While the strain rate of UFG Cu (Online Fig. 10c, d) is in a kind of steady state, the decrease of the strain rate of CuAl5 (Fig. 4c, d) is still significant.

In CuAl5, the change in strain rate sensitivity or deformation mechanism takes place at similar stress reductions but is more pronounced for CCP indentation tests. Relaxation processes driven by the inversion of the dislocation motion during the stress dip is dominant for uniaxial testing while a slight grain coarsening is expected to occur during indentation testing [53] due to the higher indentation stresses and the indentation stress gradient within the plastic zone below the indenter.

**Figure 6:** Comparison of the results from indentation and uniaxial experiments performed on UFG Cu (a) and UFG CuAl5 (b).



### Advantages and limitations of the CCP method

The results from CCP tests revealed two deformation regimes for the UFG Cu and UFG CuAl5 alloy. This is similar to the results from uniaxial tests from this work and literature show a similar course as the CCP data [37, 42].

In the newly developed CCP method, the contact pressure within the plastic zone is kept constant by controlling  $P/S^2$ . The results (Fig. 5), are thus comparable to conventional uniaxial creep tests where the stress is kept constant, even at very low strain rates. The expansion of the plastic zone is much more pronounced than in a CLH test [11]. This is however compensated by a simultaneously, continuous increase in the applied load (Fig. 2a, b). In consequence, previously undeformed material is continuously being absorbed by the expanding plastic zone (Fig. 1). The material microstructure and plastic zone thus is never in a steady state condition, even though a steady state in contact pressure is achieved. However, also the uniaxial does not show a steady state behavior for the used testing conditions. A significant extension of the creep time and a temporally constant microstructure would be necessary to achieve this condition. Comparing the development of the creep rates of CCP and uniaxial tests (Figs. 2e and 4c), it is also noticeable that the minimum creep rate is reached much faster during the CCP than the uniaxial experiments.

The maximum possible stress reduction, i.e. the minimum contact pressure that can be applied during the CCP creep segment, correlates with  $S$ . In case of large contact pressure reductions (Fig. 2f), a slight drop in contact stiffness is indicative of changes in the contact situation and the reliability of the corresponding creep data is questionable.

The material response immediately after indentation stress reduction does not necessarily correspond to the actual creep behavior as investigated by Blum et al. e.g. [19–24, 31, 32] and Milička e.g. [25–27] using uniaxial stress dip tests. It has been observed that the resulting creep rate immediately after a stress drop depends on the magnitude of stress reduction which can be related to a changing deformation behavior. Small stress reductions causing dislocation glide and dislocation generation. Relaxation processes play a dominant role for large stress reductions.

Relaxation processes are caused by large stress reductions as the direction of dislocation motion can be reversed and dislocations will annihilate at grain boundaries. This can lead to a negative strain rate immediately after the stress drop, since the material response after partial unloading is determined by the net flow (forward and backward flow) of dislocations. However, with increasing test duration, dislocation nucleation will take place again due to the steadily progressing deformation. The dislocation density is changing until an equilibrium of dislocation nucleation and annihilation processes are

established. The resulting long-term deformation rate is thus related to the final, stress dependent dislocation density [19, 20, 24, 31, 32].

In this study, no significant differences were observed between the single and incremental partial unloading experiments (Fig. 5b). However, the data are not reliable as soon as the contact stiffness decreases during partial unloading event. This represents the limiting factor for the reduction of the contact pressure. The upper contact pressure limit is given by the maximum loading rate, which is limited by the control loops of the device.

Furthermore, the higher contact depths when applying multiple contact pressures in succession significantly did not affect the resulting creep rates. This demonstrates the robustness of the method dealing with long testing times and high contact stiffnesses.

### Conclusions

The recently developed constant contact pressure (CCP) indentation creep method was successfully validated by macroscopic compression tests. For this purpose, macroscopic SRJ tests as well as long-term constant stress creep experiments as well as nanoindentation CCP, SRJ and CLH tests were performed to determine the strain rate sensitivity of UFG Cu and CuAl5 as processed by high pressure torsion.

It could be demonstrated that the CCP method provides reliable creep data and strain rate sensitivity exponents at indentation strain rates down to about  $10^{-6} \text{ s}^{-1}$  whereas a high and low stress regime can be distinguished. In the high stress regime, a low strain rate sensitivity is observed compared to the low stress regime. The difference in strain rate sensitivity between the two regimes is more pronounced for UFG Cu in comparison to the UFG CuAl5 solid solution. Here, the deformation behavior is dominated by dislocation annihilation and grain boundary mediated processes. Furthermore, it could be shown that the well-established CLH method is more similar to a relaxation than a creep test. It gives thus deviating results to uniaxial creep experiments especially at very low strain rates. Applying several partial unloading events during a single CCP experiment does not affect the material's response (no history effect), as only the long term creep behavior was analyzed. The smallest achievable contact pressure is determined by the contact situation. Large reductions of the contact pressure lead to a reduction of the contact stiffness. The contact is then no longer fully plastic, which means that the elastic properties of the material influence the results and thus the correct creep behavior is no longer described correctly. The CCP method opens up the possibility of determining the creep properties of individual phases of materials under constant indentation stress conditions. The method is therefore ideally suited to analyze strain

rate dependencies and stress exponents at very low indentation strain rates, which cannot be achieved by any other indentation creep method. Interestingly, the indentation strain rate reaches an approximate constant value much faster than in uniaxial tests, which significantly reduces the testing time. This is an advantage especially for testing at elevated temperatures.

## Materials and methods

Experiments were performed on an ultrafine grained CuAl alloy containing 5 wt% Al (purchased from Wieland-Werke AG, Germany) as well as on technical pure Cu.

### Sample processing

The UFG microstructures were generated by severe plastic deformation (SPD) using a semi-constrained high pressure torsion press (Walter Klement GmbH, Austria). Therefore, discs with a diameter 20 mm and an initial height of 4.5 mm (approx. 3.3 mm after HPT processing) were deformed applying a compressive force of 1450 kN (pressure of approx. 4.5 GPa) and a rotational speed of 1 rpm until 25 revolutions were completed. The high degree of deformation applied to the material during HPT processing results in homogeneous grain refinement throughout the specimen. The upper anvil was actively cooled to dissipate some of the energy generated by plastic deformation in order to achieve a fine final grain size.

Afterwards, rectangular bars were cut out of the HPT samples, lathed and cut into compression specimens. This procedure is exemplarily shown in Fig. 7. The final cylindrical compression samples had a diameter of 2.5 mm and a length of 3.125 mm (aspect ratio of 1:1.25). The remaining sections of the HPT samples (Fig. 7c, left and right sections) were grinded and subsequently metallographically prepared using different diamond suspensions with particles sizes of 6, 3 and 1  $\mu\text{m}$ . An

oxide particle suspension (colloidal silica, particle size 0.04  $\mu\text{m}$ ) with additional ferrinitrate was subsequently used for the final (vibrational) fine polishing.

The resulting grain sizes after HPT processing were analyzed using a high-resolution scanning electron microscope (Mira3, Tescan, Czech) in backscattered electron (BSE) contrast imaging mode (Fig. 8) and a line intercept method. The grain sizes were analyzed at about the half radius ( $r = 5 \text{ mm}$ ) of the HPT disc in order to investigate a representative microstructure. The analysis yields average grain sizes of 425 nm for Cu and 133 nm for CuAl5.

### Nanoindentation testing

Nanoindentation experiments were performed with a G200 (Keysight, USA) indentation system equipped with a diamond Berkovich tip (Synton-MDP, Switzerland). The system was calibrated according to Oliver and Pharr [61, 62] using fused silica as reference material.

Strain rate jump tests according to Maier et al. [7] were performed in order to determine the strain rate sensitivity in the indentation strain rate range between ( $\dot{P}/P = 0.05 - 0.0005 \text{ s}^{-1}$ ). Additional long term creep tests were carried out using the constant load hold (CLH) [8] and the recently developed constant contact pressure (CCP) method [11].

In both creep test methods, strain rate controlled loading occurs in the first test segment until a penetration depth of 500 nm is reached, followed by creep segment. In case of the CLH method, the applied load is hold constant during the creep time of 3000 s (0.8 h). In contrast, a continuously loading takes place in the creep segment of the CCP method in order to keep the previously selected contact pressure constant. The creep segment for the CCP tests lasted 3000 s. An indentation strain rate of  $0.025 \text{ s}^{-1}$  was applied in the initial, constant strain rate loading segment of both, CLH and CCP experiments.

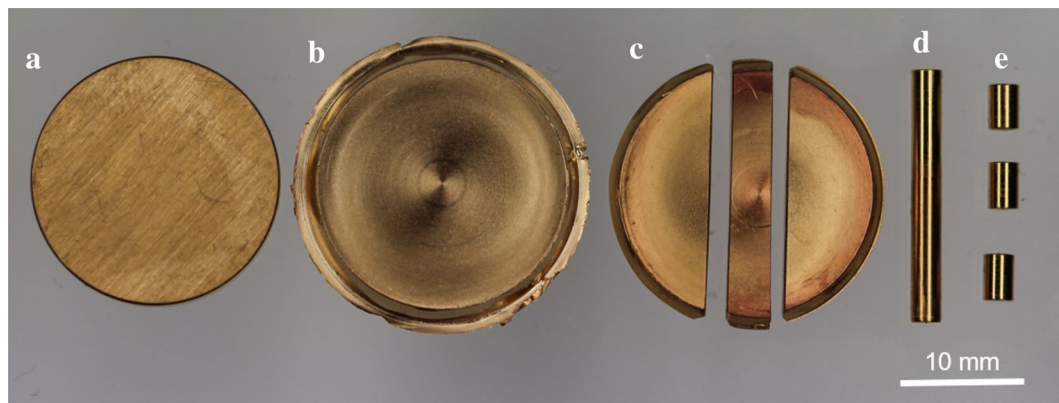


**Figure 7:** Sample Processing: (a) undeformed HPT sample, (b) sample after HPT processing, (c) cutted rectangular bar, (d) lathed bar and (e) final compression samples.

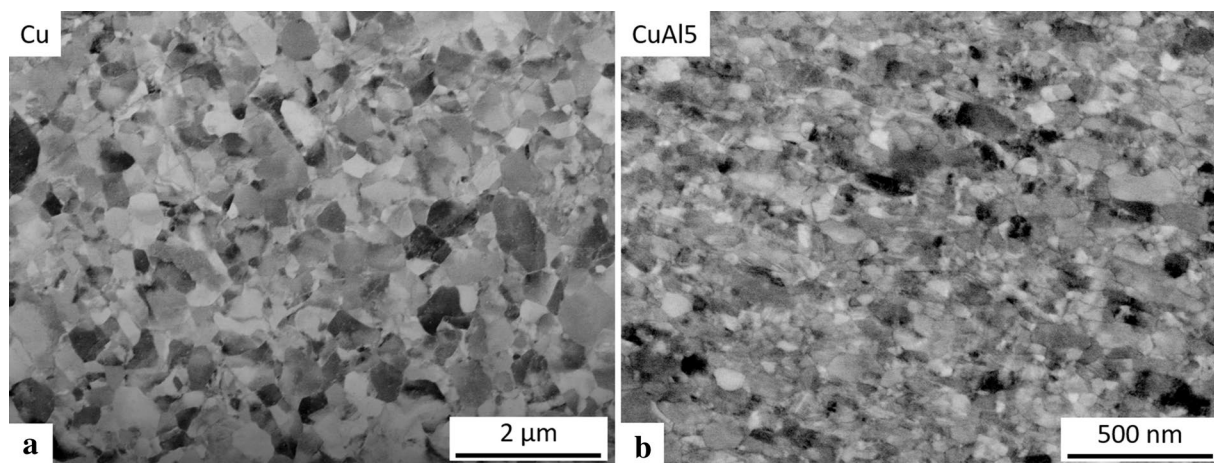


**Figure 8:** BSE images of (a) UFG Cu and (b) UFG CuAl5 after HPT processing.

In all three methods, the contact stiffness is continuously recorded and used for the calculation of the drift independent and pile-up corrected hardness, respectively, contact pressure according to Eq. 1. Therefore, a dynamic displacement of 2 nm was applied with a dynamic frequency of 45 Hz.

### Compression testing

Compression tests were performed using a universal testing device (Instron, Type 5967, USA) equipped with a 30 kN load cell and carbide punches. All compression experiments were carried out inside a closed cabinet in order to reduce the impact of thermal drift on the test results. The cross-sectional area was assumed to be constant.

Compression strain rate jump tests were carried out applying strain rates of  $10^{-3}$ – $10^{-5}$  s<sup>-1</sup>.

Additional compression experiments where the stress was hold constant were performed. The creep/constant stress segment started once an approximately constant stress level had been reached. A pyramidal Berkovich indenter generates a representative plastic strain of about 7.2% inside the plastic zone. This rather large plastic strain could not be achieved during compression testing due to shear fracture.

In the constant stress (creep) experiments, the stress level was varied at the beginning of the creep segment similar to the nanoindentation CCP method by changing the applied load. The partial unloading during these stress dip tests were performed displacement controlled with an unloading rate of 5 μm/s. The constant stress tests lasted 3 h.

### Acknowledgments

The authors thank Dr. Achim Kuhn (Wieland-Werke AG, Germany) for providing the CuAl5 solid solution alloy as well as Dr. Enrico Bruder and Leonie Frohnapfel for experimental support. Deutsche Forschungsgemeinschaft (DFG) is gratefully

acknowledged for financial support within the project No. 326946902.

### Funding

Open Access funding enabled and organized by Projekt DEAL.

### Data availability

The data are available upon reasonable request from the corresponding author (C.M.).

### Declarations

**Conflict of interest** The authors declare no conflict of interests.

### Open Access

This article is licensed under a Creative Commons Attribution 4.0 International License, which permits use, sharing, adaptation, distribution and reproduction in any medium or format, as long as you give appropriate credit to the original author(s) and the source, provide a link to the Creative Commons licence, and indicate if changes were made. The images or other third party material in this article are included in the article's Creative Commons licence, unless indicated otherwise in a credit line to the material. If material is not included in the article's Creative Commons licence and your intended use is not permitted by statutory regulation or exceeds the permitted use, you will need to obtain permission directly from the copyright holder. To view a copy of this licence, visit <http://creativecommons.org/licenses/by/4.0/>.

### Supplementary Information

The online version contains supplementary material available at <https://doi.org/10.1557/s43578-021-00445-6>.

## References

1. DIN, *DIN EN ISO 204:2018 Metallic Material—Uniaxial Creep Testing in Tension—Method of Test* (2018).
2. ASTM, *E139-11 Standard Test Methods for Conducting Creep, Creep-Rupture, and Stress-Rupture Tests of Metallic Materials* (2018)
3. DIN, Part 005: Uninterrupted creep and stress-rupture testing, in *DIN EN 2002-005 Aerospace Series—Test Methods for Metallic Materials* (2007)
4. S.J. Bull, Nanoindentation of coatings. *J. Phys. D* **38**(24), R393–R413 (2005)
5. K. Durst, M. Göken, Micromechanical characterisation of the influence of rhenium on the mechanical properties in nickel-base superalloys. *Mater. Sci. Eng. A* **387–389**, 312–316 (2004)
6. W.D. Nix, Elastic and plastic properties of thin films on substrates: nanoindentation techniques. *Mater. Sci. Eng. A* **234–236**, 37–44 (1997)
7. V. Maier et al., Nanoindentation strain-rate jump tests for determining the local strain-rate sensitivity in nanocrystalline Ni and ultrafine-grained Al. *J. Mater. Res.* **26**(11), 1421–1430 (2011)
8. V. Maier et al., An improved long-term nanoindentation creep testing approach for studying the local deformation processes in nanocrystalline metals at room and elevated temperatures. *J. Mater. Res.* **28**(9), 1177–1188 (2013)
9. P.S. Phani, W. Oliver, A direct comparison of high temperature nanoindentation creep and uniaxial creep measurements for commercial purity aluminum. *Acta Mater.* **111**, 31–38 (2016)
10. P.S. Phani, W. Oliver, G. Pharr, On the measurement of power law creep parameters from instrumented indentation. *JOM* **69**(11), 2229–2236 (2017)
11. O. Prach et al., A new nanoindentation creep technique using constant contact pressure. *J. Mater. Res.* **34**(14), 2492–2500 (2019)
12. D. Matschkal-Amberger et al., New flat-punch indentation creep testing approach for characterizing the local creep properties at high temperatures. *Mater. Des.* **183**, 108090 (2019)
13. P. Baral et al., A new long-term indentation relaxation method to measure creep properties at the micro-scale with application to fused silica and PMMA. *Mech. Mater.* **137**, 103095 (2019)
14. P. Baral et al., Indentation creep vs indentation relaxation: a matter of strain rate definition? *Mater. Sci. Eng. A* **781**, 139246 (2020)
15. D. Tabor, *The Hardness of Metals* (Clarendon Press, Oxford, 1951)
16. K.L. Johnson, The correlation of indentation experiments. *J. Mech. Phys. Solids* **18**(2), 115–126 (1970)
17. K.L. Johnson, K.L. Johnson, *Contact Mechanics* (Cambridge University Press, Cambridge, 1987)
18. D.L. Joslin, W.C. Oliver, A new method for analyzing data from continuous depth-sensing microindentation tests. *J. Mater. Res.* **5**(1), 123–126 (1990)
19. W. Blum et al., Two mechanisms of dislocation motion during creep. *Acta Metall.* **37**(9), 2439–2453 (1989)
20. W. Blum, P. Eisenlohr, F. Breutingger, Understanding creep—a review. *Metall. Mater. Trans. A* **33**(2), 291–303 (2002)
21. W. Blum, P. Eisenlohr, J. Hu, Interpretation of unloading tests on nanocrystalline Cu in terms of two mechanisms of deformation. *Mater. Sci. Eng. A* **665**, 171–174 (2016)
22. W. Blum, K. Durst, Kinetics of deformation and recovery of nanocrystalline Ni studied by stress reductions (2016)
23. W. Blum et al., Strain rate contribution due to dynamic recovery of ultrafine-grained Cu–Zr as evidenced by load reductions during quasi-stationary deformation at 0.5 Tm. *Metals* **9**(11), 1150 (2019)
24. R. Kapoor et al., Creep transients during stress changes in ultrafine-grained copper. *Scr. Mater.* **54**(10), 1803–1807 (2006)
25. K. Milička, Constant structure creep in metals after stress reduction in steady state stage. *Acta Metall. Mater.* **41**(4), 1163–1172 (1993)
26. K. Milička, Constant structure experiments in high temperature primary creep of some metallic materials. *Acta Metall. Mater.* **42**(12), 4189–4199 (1994)
27. K. Milička, Constant structure creep experiments on aluminium. *Kovove Mater* **49**, 307–318 (2011)
28. D. Caillard, J.L. Martin, *Thermally Activated Mechanisms in Crystal Plasticity*. Pergamon Materials Series, vol. 8, ed. R.W. Cahn (2003).
29. W. Osthoff et al., Creep and relaxation behavior of Inconel-617. *Nucl. Technol.* **66**(2), 296–307 (1984)
30. M.E. Kassner, Chapter 2—five-power-law creep, in *Fundamentals of Creep in Metals and Alloys*, 3rd edn., ed. by M.E. Kassner (Butterworth-Heinemann, Boston, 2015), pp. 7–102
31. Z. Sun et al., Dynamic recovery in nanocrystalline Ni. *Acta Mater.* **91**, 91–100 (2015)
32. Z. Sun et al., Grain size and alloying effects on dynamic recovery in nanocrystalline metals. *Acta Mater.* **119**, 104–114 (2016)
33. Y. Liu et al., Room temperature nanoindentation creep of nanocrystalline Cu and Cu alloys. *Mater. Lett.* **70**, 26–29 (2012)
34. C.L. Wang et al., Creep of nanocrystalline nickel: a direct comparison between uniaxial and nanoindentation creep. *Scr. Mater.* **62**(4), 175–178 (2010)
35. R.S. Kottada, A.H. Chokshi, Low temperature compressive creep in electrodeposited nanocrystalline nickel. *Scr. Mater.* **53**(8), 887–892 (2005)
36. W.M. Yin et al., Creep behavior of nanocrystalline nickel at 290 and 373 K. *Mater. Sci. Eng. A* **301**(1), 18–22 (2001)
37. X.-S. Yang et al., Time-, stress-, and temperature-dependent deformation in nanostructured copper: creep tests and simulations. *J. Mech. Phys. Solids* **94**, 191–206 (2016)

38. X.-S. Yang et al., Time, stress, and temperature-dependent deformation in nanostructured copper: stress relaxation tests and simulations. *Acta Mater.* **108**, 252–263 (2016)
39. W. Blum, Creep of crystalline materials: experimental basis, mechanisms and models. *Mater. Sci. Eng. A* **319–321**, 8–15 (2001)
40. M.A. Meyers, A. Mishra, D.J. Benson, Mechanical properties of nanocrystalline materials. *Prog. Mater. Sci.* **51**(4), 427–556 (2006)
41. M.A. Meyers, A. Mishra, D.J. Benson, The deformation physics of nanocrystalline metals: experiments, analysis, and computations. *JOM* **58**(4), 41–48 (2006)
42. Y.-J. Wang, A. Ishii, S. Ogata, Transition of creep mechanism in nanocrystalline metals. *Phys. Rev. B* **84**(22), 224102 (2011)
43. G.T. Gray et al., Influence of strain rate & temperature on the mechanical response of ultrafine-grained Cu, Ni, and Al-4Cu-0.5Zr. *Nanostruct. Mater.* **9**(1), 477–480 (1997)
44. Y. Wang, E. Ma, Temperature and strain rate effects on the strength and ductility of nanostructured copper. *Appl. Phys. Lett.* **83**(15), 3165–3167 (2003)
45. Y. Li, X. Zeng, W. Blum, Transition from strengthening to softening by grain boundaries in ultrafine-grained Cu. *Acta Mater.* **52**(17), 5009–5018 (2004)
46. Q. Wei et al., Effect of nanocrystalline and ultrafine grain sizes on the strain rate sensitivity and activation volume: fcc versus bcc metals. *Mater. Sci. Eng. A* **381**(1), 71–79 (2004)
47. S. Cheng et al., Tensile properties of in situ consolidated nanocrystalline Cu. *Acta Mater.* **53**(5), 1521–1533 (2005)
48. J. Chen, L. Lu, K. Lu, Hardness and strain rate sensitivity of nanocrystalline Cu. *Scr. Mater.* **54**(11), 1913–1918 (2006)
49. H. Chandler, A comparison between steady state creep and stress relaxation in copper. *Mater. Sci. Eng. A* **527**(23), 6219–6223 (2010)
50. W. Blum et al., Deformation resistance in the transition from coarse-grained to ultrafine-grained Cu by severe plastic deformation up to 24 passes of ECAP. *Mater. Sci. Eng. A* **528**(29), 8621–8627 (2011)
51. T. Suo et al., Compressive behavior and rate-controlling mechanisms of ultrafine grained copper over wide temperature and strain rate ranges. *Mech. Mater.* **61**, 1–10 (2013)
52. J. Hu et al., Plastic deformation behavior during unloading in compressive cyclic test of nanocrystalline copper. *Mater. Sci. Eng. A* **651**, 999–1009 (2016)
53. V. Maier-Kiener et al., Influence of solid solution strengthening on the local mechanical properties of single crystal and ultrafine-grained binary Cu–Al<sub>x</sub> solid solutions. *J. Mater. Res.* **32**(24), 4583–4591 (2017)
54. W.D. Nix, H. Gao, Indentation size effects in crystalline materials: a law for strain gradient plasticity. *J. Mech. Phys. Solids* **46**(3), 411–425 (1998)
55. B. Merle et al., Experimental determination of the effective indenter shape and  $\epsilon$ -factor for nanoindentation by continuously measuring the unloading stiffness. *J. Mater. Res.* **27**(1), 214–221 (2012)
56. K. Edalati et al., Influence of dislocation–solute atom interactions and stacking fault energy on grain size of single-phase alloys after severe plastic deformation using high-pressure torsion. *Acta Mater.* **69**, 68–77 (2014)
57. M. Monclús, J. Molina-Aldareguia, *High Temperature Nanomechanical Testing*. Handbook of Mechanics of Materials, ed. by C.H. Hsueh, S. Schmauder, C.-S. Chen, K.K. Chawla, N. Chawla, W. Chen, Y. Kagawa (2018).
58. K. Zhang, J. Weertman, J. Eastman, Rapid stress-driven grain coarsening in nanocrystalline Cu at ambient and cryogenic temperatures. *Appl. Phys. Lett.* **87**(6), 061921 (2005)
59. S. Brandstetter et al., Grain coarsening during compression of bulk nanocrystalline nickel and copper. *Scr. Mater.* **58**(1), 61–64 (2008)
60. W. Chen et al., Mechanically-induced grain coarsening in gradient nano-grained copper. *Acta Mater.* **125**, 255–264 (2017)
61. W.C. Oliver, G.M. Pharr, An improved technique for determining hardness and elastic modulus using load and displacement sensing indentation experiments. *J. Mater. Res.* **7**(6), 1564–1583 (1992)
62. W.C. Oliver, G.M. Pharr, Measurement of hardness and elastic modulus by instrumented indentation: advances in understanding and refinements to methodology. *J. Mater. Res.* **19**(1), 3–20 (2004)

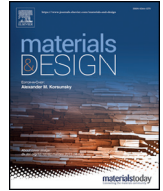
---

## **Publication C**

Reproduced full text article with permission from Elsevier Ltd.

Copyright (2020), Materials & Design.

---



# New ultra-high temperature nanoindentation system for operating at up to 1100 °C



Christian Minnert<sup>a,\*</sup>, Warren C. Oliver<sup>b</sup>, Karsten Durst<sup>a</sup>

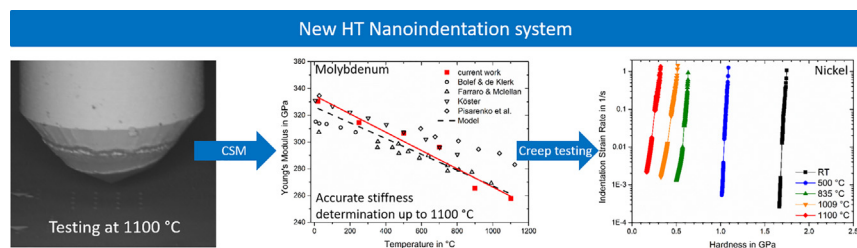
<sup>a</sup> Physical Metallurgy, Materials Science Department, Technical University of Darmstadt, Germany

<sup>b</sup> Nanomechanics Inc./KLA, Oak Ridge, TN, USA

## HIGHLIGHTS

- A new high-temperature and in-situ nanoindentation system was developed for testing temperature of up to 1100 °C.
- The sophisticated temperature management with tip and sample heating as well as actuator cooling leads to low drift rates.
- The determination of reliable hardness and Young's modulus data was presented by constant strain rate tests on fused silica for  $T < 300$  °C and Mo for testing up to 1100 °C.
- The applicability of the system to determine the creep behavior has been shown for single crystalline Ni up to 1100 °C was by using indentation strain rate jump and step load and hold methods.

## GRAPHICAL ABSTRACT



## ARTICLE INFO

### Article history:

Received 19 December 2019

Received in revised form 26 March 2020

Accepted 9 April 2020

Available online 13 April 2020

### Keywords:

High-temperature nanoindentation

Creep

Strain rate sensitivity

Hardness

Young's modulus

## ABSTRACT

In this work a new ultra-high temperature (UHT) nanoindentation system for testing at up to 1100 °C is presented. The system is capable to perform indents from small scale up to large indentation depths due to the combination of a 1 N actuator and a frame stiffness of  $>1 \cdot 10^6 \text{ N/m}$  even at 1100 °C. Dynamic testing allows a continuous determination of the contact stiffness (CSM) and thus also the depth-dependent hardness and indentation modulus. Low drift rates can be achieved by an independent tip and sample heating. Operating the nanoindenter inside a scanning electron microscope (SEM) equipped with a high temperature backscattered electron (BSE) detector opens the possibility of in-situ observations, as high vacuum minimizes oxidation effects. The HT capability of the system is demonstrated on three reference materials: fused silica, molybdenum assessing the change in modulus with increasing temperature using constant strain rate tests (CSR). The creep response of single crystalline Ni has been assessed by strain rate jump (SRJ) as well as a step-load and hold creep (SLH) method. The resulting modulus, hardness as well as the strain rate sensitivity from RT up to 1100 °C are in good accordance with literature data, highlighting the applicability of the system.

© 2020 The Authors. Published by Elsevier Ltd. This is an open access article under the CC BY-NC-ND license (<http://creativecommons.org/licenses/by-nc-nd/4.0/>).

\* Corresponding author.

E-mail address: [c.minnert@phm.tu-darmstadt.de](mailto:c.minnert@phm.tu-darmstadt.de) (C. Minnert).

## 1. Introduction

Over the past decades, the continuous development of new nanoindentation systems and new test protocols has made nanoindentation testing to a powerful tool for mechanical characterization on small length scales [1,2]. The advantages compared to conventional, macroscopic tests are not only the simple sample preparation and the rapid test rates, but also the variety of characterization options. Nanoindenters are used to determine hardness and Young's modulus on a local length scale. Furthermore, strain rate dependencies, fracture toughness, creep, fatigue behavior or adhesive strength of layers and coatings can be determined [3–7].

In order to increase the efficiency of jet engines or gas turbines for power generation, their operating or combustion temperature must be increased. However, this is often limited by the materials used [8]. Therefore, the development of new high temperature (HT) materials, such as Ni or Co-based alloys, as well as the improvement of thermal barrier coatings and bond coats, plays an important role in current research [8–14].

For this reason, nanoindentation systems have been developed for testing the local properties of materials and thin coatings at elevated temperatures [1]. Nanoindentation thereby enables to characterize the influence of alloying elements, chemical or microstructural gradients on a single phase of a material [15–17].

Thermal activated mechanisms can be analyzed by nanoindentation testing in terms of strain rate sensitivities/stress exponents, activation volumes and activation energies [3,5,14,18–22]. Therefore, tests with a controlled strain rate at different temperature or a changing strain rate have to be carried out. It has been shown that local, nanoindentation experiments, introducing a complex stress state in the material, provide comparable results to macroscopic, bulk and/or uniaxial experiments [3,5,19–21,23–26].

However, nanoindentation testing at elevated temperatures is quite challenging and several issues need to be considered [1]. Chemical reactions between tip and sample can lead to high tip wear, which strongly affects the measurements especially at low indentation depths [27]. In addition, a sophisticated temperature management is necessary to keep the drift rates as low as possible. Thermal drift can be caused by a temperature mismatch between tip and sample, therefore an independent sample and tip heating is required in order to match the temperatures [1]. Dynamic testing enables the possibility to measure the stiffness and, thus, the Young's modulus continuously. The stiffness data can also be used to calculate the hardness [5]. Environment assisted HT nanoindentation testing can be used to determine mechanical properties of e.g. superalloys under more application-related conditions where oxidation plays a role [28–30]. However, the oxidation of a material makes it more difficult to determine reliable material properties during nanoindentation. For this reason, experiments at high temperatures are preferably carried out in vacuum to minimize the influence of oxidation effects. The formation of thin oxide layers during heating cannot be completely avoided even in a high vacuum, but it can be significantly reduced [1,31–33].

The maximum reported testing temperature of the current HT nanoindentation systems is 1000 °C working in vacuum [32]. However, the determination of the contact stiffness data at these extreme temperatures is challenging due to high drift rates and insufficiently fast unloading rates [32].

In this work, nanoindentation tests from room temperature (RT) to 1100 °C were performed using an advanced commercial prototype, load-controlled in-situ system from Nanomechanics Inc./KLA. The ultra-high operating temperature of the system offers the possibility to determine mechanical properties as well as thermally activated processes of HT materials at their application temperature. Operating the nanoindenter inside a scanning electron microscope (SEM) equipped with a HT backscattered electron (BSE) detector opens the possibility of in-situ observations, as high vacuum reduces oxidation effects [32,34].

The testing capabilities of the new system is demonstrated on three different materials using the continuous stiffness measurement (CSM) method, strain rate jump (SRJ) tests and step load and the hold (SLH) creep method. The low T capabilities is shown on fused silica as a reference material for indentation testing. The high temperature tests were performed on polycrystalline body centered cubic molybdenum, for which temperature dependent modulus data is available. Single crystalline (SX) Ni with its face centered cubic structure is an important base metal for many high temperature materials as Ni-base superalloys and has been chosen as a reference for the creep tests.

### 1.1. Dynamic indentation testing for continuous property determination and measurement of thermally activated processes

Nanoindentation enables the determination of thermally activated mechanisms, by using different loading scenarios [3,5,18–21]. The following subsection gives a brief overview of the various nanoindentation test methods using a pyramid-shaped Berkovich indenter and their comparison to macroscopic, uniaxial tests.

Indentation testing relies on an accurate determination of the contact area  $A_c$ , which is based on Sneddon's equation, relating the contact stiffness  $S$  to the reduced modulus  $E_R$  and the contact area. The definition of  $S$  is shown in Eq. (1) [35,36]:

$$S = \frac{2\beta}{\sqrt{\pi}} \cdot E_R \cdot \sqrt{A_c} = S_{CSM} \quad (1)$$

with the constant  $\beta$  and the unloading stiffness  $S_{CSM}$  determined by a dynamic oscillating loading signal.

Thus, the contact area can be expressed as:

$$A_c = \frac{\pi}{4\beta^2} \cdot \frac{S^2}{E_R^2} \quad (2)$$

The correct contact depth  $h_c$  can now be calculated by knowing the correct tip area function  $f(h_c) = A_c$ :

$$f(h_c) = m_0 h_c^2 + m_1 h_c + m_2 h_c^{1/2} + m_3 h_c^{1/4} + \dots + m_n h_c^{2^{1-n}} = \sum_{i=0}^n m_i h_c^{2^{1-i}} \quad (3)$$

determined by calibration on a reference material like fused silica [36]. It has been discussed in literature that the hardness based on stiffness gives much more reliable hardness data, since it is unaffected by thermal drift, pile-up and sink-in [5].

The three different test methods used in this work are presented below. Further details on the used input parameters are given in subsection 3.1.

A constant strain rate  $\varepsilon$  is used in the continuous stiffness measurement (CSM) method, where the loading signal is superimposed by a sinusoidal oscillation. The definition of the strain rate, based on the work of Mayo and Nix [37], is given in Eq. (4) [5,38,39].

$$\varepsilon = \frac{h}{h} = \frac{1}{2} \left( \frac{P}{P} - \frac{H}{H} \right) \approx \frac{S}{S} \approx \frac{1}{2} \frac{P}{P} \quad (4)$$

with indentation depth  $h$ , applied load  $P$  and hardness  $H$ . The stiffness signal  $S$  can be determined continuously. Thus, it is possible to calculate the hardness and Young's modulus as a function of indentation depth. The hardness is defined by the ratio of the applied load and depth dependent projected contact area [5,38]:

$$H = \frac{P}{A_c} = \frac{P \cdot 4\beta^2 \cdot E_R^2}{\pi \cdot S^2} \quad (5)$$

with the reduced modulus  $E_R$  and the constant  $\beta$ . The Young's modulus  $E$  of the sample can be calculated with Eq. (6) [38]:

$$E_{\text{sample}} = \frac{(1-\nu^2)_{\text{sample}}}{\frac{1}{E_r} - \left(\frac{1-\nu^2}{E}\right)_{\text{indenter}}} \quad (6)$$

assuming a known modulus of the indenter material, as well as the Poisson's ratio  $\nu$  of the tip and sample material.

The SRJ method, developed by Maier et al. [3], is based on the CSM method mentioned above. In contrast to a CSM test is the strain rate changed within a single test (see Fig. 1). This allows to determine the strain rate sensitivity  $m$  in a "constant" volume/microstructure element. The strain rate sensitivity  $m$  of a material can be computed by comparing the strain rate dependent hardness values of the material:

$$m = \frac{1}{n} = \frac{d(\ln H)}{d(\ln \dot{\epsilon})} \quad (7)$$

with  $n$  being the stress exponent.

The correct analysis of strain rate dependencies of soft materials or at high temperatures can be rather difficult as the hardness changes only slightly with strain rate. The analysis becomes easier if the applied strain rate can be varied over several orders of magnitude. However, this is typically limited by about three orders of magnitude (e.g.  $\dot{\epsilon} = 10^{-1} - 10^{-41}/s$ ) with the SRJ method described above [18,26,40]. Therefore, the load and hold creep tests with an initial step load (SLH) according to Sudharshan Phani et al. [21,41] were performed (see Fig. 1) on single crystalline nickel. The big advantage of the SLH test is, that the strain rate can be varied by seven orders of magnitude within a single test [41]. Furthermore, the test duration is only 40 s, reducing the tip and sample interaction as well as thermal drift effects.

The test SLH protocol consists of two different test segments. In the first segment, the tip is slowly approaching the sample surface (no impact) and after contact, a step load is applied with a defined loading rate which results in very high strain rates in the beginning of the experiment. Afterwards, the load is kept constant for a short time e.g. 1.5 s, while the hardness is calculated by the applied load and the projected contact area, the strain rate is determined by  $\frac{h}{h}$ .

After 1.5 s the dynamics/sinusoidal oscillation was switched on. This marks the start of the second test segment, which is similar to a standard CSM test. Also here the load is kept constant, the strain rate is described by  $\frac{S}{s}$ . Thermal drift is a big issue in indentation creep testing,

therefore the stiffness based hardness was calculated in this test segment (Eq. (5)).

Hardness and strain rate determined by indentation testing has to be converted into uniaxial stress  $\sigma$  and strain rate  $\dot{\epsilon}$  using Eqs. (8) and (9) [21,25] in order to compare the results with literature data determined by macroscopic testing:

$$\sigma = \left(\frac{1}{Fc^2}\right) \left(\frac{L}{\pi(h \tan(\theta))^2}\right) \quad (8)$$

$$\dot{\epsilon} = \left(\frac{1}{c \tan \theta}\right) \left(\frac{1}{h}\right) \left(\frac{dh}{dt}\right) \quad (9)$$

with reduced contact pressure  $F$ , pile-up/sink-in parameter  $c$ , equivalent cone angle  $\theta$ , Load  $L$  and indentation depth  $h$ . The activation energy for creep can be calculated with Eq. (10) [19]:

$$\frac{H}{E} = G \cdot \exp\left(\frac{Q_c}{nRT}\right) \quad (10)$$

with pre-exponential coefficient  $G$ , activation energy  $Q_c$  in kJ/mol, stress exponent  $n$ , gas constant  $R$  and absolute temperature  $T$ .

## 2. New high temperature indentation system

The newly developed ultra-high temperature nanoindentation system is equipped with an actively cooled high load actuator with a maximum load of 1 N. Thereby the system is able to perform indents from small scale all the way up to large indentation depths in order to minimize the impact of tip blunting and surface oxidation on the test results. The indenter was designed for high machine stiffness, which is necessary for accurate data analysis at large indentation depths. The actuator can be driven at a high frequency, allowing a continuous determination of the contact stiffness. This is essential for determining the depth dependent material properties, like hardness and modulus. Furthermore, the contact stiffness can be used to determine pile-up and drift independent hardness values [5]. The active cooling of the actuator ensures that machine calibration during high temperature or long term testing remains constant and comparable to the RT properties. An accurate sample positioning is achieved by using a piezo-driven x-y stage (SmarAct GmbH) with a resolution of 20 nm.

The system is equipped with independent tip and sample heaters. K-type thermocouples are used to measure and control the temperature of the sample, tip and actuator housings. The temperature control is carried out via PID loops which allows an independently adjustment of

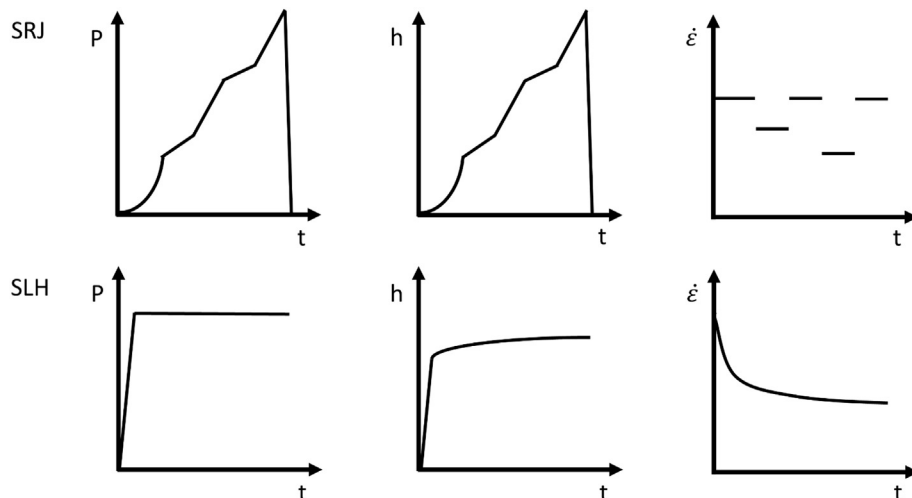


Fig. 1. Schematic illustration of the time dependent load, indentation depth and strain rate during SRJ and SLH tests.

the sample and tip temperature. Thus, low drift rates can be achieved after temperature matching between tip and sample. A detailed description of the system will be given in the subsequent sections.

### 2.1. Tip holder, shaft design and actuator

A schematic drawing of the indenter system is shown in Fig. 2. The centerpiece of the system is the 1 N actuator, the surrounding actuator housing can be actively cooled via a Peltier heat pump and the cool block on top of the housing. It is thermally insulated from the two Cu blocks on the side of the actuator housing. These lateral Cu blocks are connected with the base of the column via cooling springs. The temperature of these blocks is also controlled via Peltier elements located between the Cu blocks and the outer cooling blocks.

The magnetic driven and load controlled actuator is able to perform frequency specific loading experiments to determine the elastic stiffness of the sample continuously with a dynamic frequency of up to 1000 Hz. The maximum displacement range is 80  $\mu\text{m}$  with a resolution of 0.04 nm and a noise floor below 0.1 nm. The load is applied with a load resolution of 6 nN, the load noise floor of the system is 0.9  $\mu\text{N}$ . These specifications do not change while heating the system due to the active cooling of the actuator housing which keeps the actuator at room temperature. Thus, the optimal force and displacement resolution, as well as the low noise level will be maintained even at a temperature of 1100  $^{\circ}\text{C}$  (Appendix A.1). Active cooling also offers an advantage in long-term creep testing at RT, by continuously dissipating the heat generated in the actuator during holding periods.

A high frame stiffness is achieved by separating the resistive tip heater from the loading axis. This results in a frame stiffness higher than  $1 \cdot 10^6 \text{ N/m}$  even at maximum operation temperature.

### 2.2. Sample holder with integrated heating and cooling option

In contrast to standard RT systems, the specimen cannot be glued to the specimen holder as conventional adhesives cannot withstand these extreme temperatures. It is therefore clamped onto the sample heater using four 0.5 mm thick tungsten wires (see Fig. 2). Only a small amount of heat is transferred from the sample to the sample holder due to the small contact areas between the wires and the sample, reducing the required heating and cooling capacities. An additional molybdenum sheet is placed between the sample and sample heater to protect the heating element and prevents the sample from being welded to the heating element. A trench was etched into the molybdenum sheet in which the

sample thermocouple can be placed. Alternatively, the sample thermocouple can be inserted directly into the sample using a lateral drill hole, if available. This offers the possibility to measure the sample temperature close to the sample surface.

### 2.3. Cooling system

Cooling is provided by a closed loop cooling system consisting of a high-pressure pump, a water chiller and Peltier heat pump elements. The water is first pumped with a pressure of about 586 kPa (5.86 bar) through the cooling block on the sample side and afterwards through the three cooling blocks on the actuator housing. The water cooled block on the sample side of the system is in direct contact with the copper block surrounding the sample heater. The temperature of that block is kept close to RT by varying the water temperature via the water chiller in the delivery system.

The heat from the indenter tip is extracted at the base of the column. This is accomplished through cooling springs that provide a thermal path from the base of the column to the cooling system. Two of the water cooled blocks on the actuator side of the system are attached to the end of the heat extraction springs via two Peltier heat pumps. These pumps are controlled so that the base of the column that attaches to the actuator shaft remains at RT. The additional mechanical stiffness due to the cooling springs is reduced by using multiple thin springs instead of two thick springs at the same thermal cross section. The final water cooled block on the actuator side of the system is attached to the copper block surrounding the actuator through an additional Peltier heat pump that is controlled to maintain the actuator at room temperature at all times. A nickel plated heat shield between the tip heater and the actuator housing reduce the heating of the actuator caused by radiation.

### 2.4. Temperature control and adjustment

Numerous publications are dealing with the cause and effect of thermal drift on indentation test results [1,33,42–45]. In order to reduce the influence of thermal drift a temperature adjustment between tip and sample has to be carried out before testing at elevated temperatures to achieve a thermal equilibrium. Changes in displacement signal are caused by thermal drift. Thermal drift can be caused by a temperature mismatch between tip and sample (contact drift) and/or by a change in temperature of the whole gantry (system drift). The adjustment of tip and sample temperature is done by using a standardized, semi-automated temperature matching procedure developed by Nanomechanics Inc./KLA. A

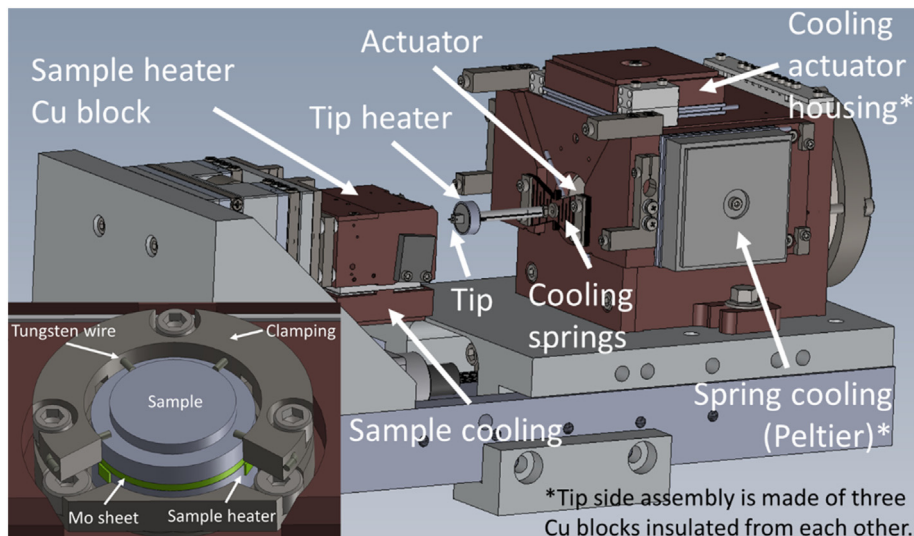


Fig. 2. Indenter set-up. The heat shield is not shown for illustration reasons.

detailed description of the temperature adjustment procedure is given in the [Appendix A.2](#).

### 2.5. Test environment

The indenter is installed inside a Tescan Vega 3 scanning electron microscope (SEM) equipped with a secondary electron (SE) detector and a water cooled backscattered electron (BSE) detector. In-situ experiments, sample positioning and imaging even at the maximum operating temperature can be carried out using the integrated water-cooled BSE detector. [Fig. 3](#) is taken with the water cooled backscattered electron detector at 1100 °C to demonstrate the imaging capability of the SEM at maximum operating temperature of 1100 °C. The high vacuum environment ( $\sim 10^{-3} - 10^{-4}$  Pa) reduces oxidation effects during testing. Low noise levels are achieved by an active vibration damping of the vacuum chamber.

## 3. Results and discussion

### 3.1. Testing of different materials for system validation

Nanoindentation experiments at elevated temperatures were performed using the continuous stiffness measurement (CSM) technique, strain rate jump (SRJ) and the step load and hold (SLH) test protocols. All tests were performed in batch mode. Fused silica was tested as it is widely used as a reference material due to its isotropic mechanical properties. Tip shape and frame stiffness calibration at room temperature were performed according to Oliver and Pharr [36]. Additional tests on fused silica were performed after testing at high temperatures in order to investigate changes in tip geometry. The results are presented in the [Appendix A.3](#).

For the CSM tests, a maximum load of 1 N and a constant input strain rate ( $\dot{P}/P$ ) of 0.2 1/s were applied, followed by a peak load hold time of 5 s and an unloading by 90% of  $P_{max}$ . The unloading has been performed in 1 s. Thermal drift was measured for 40 s after a settle time of 40 s at

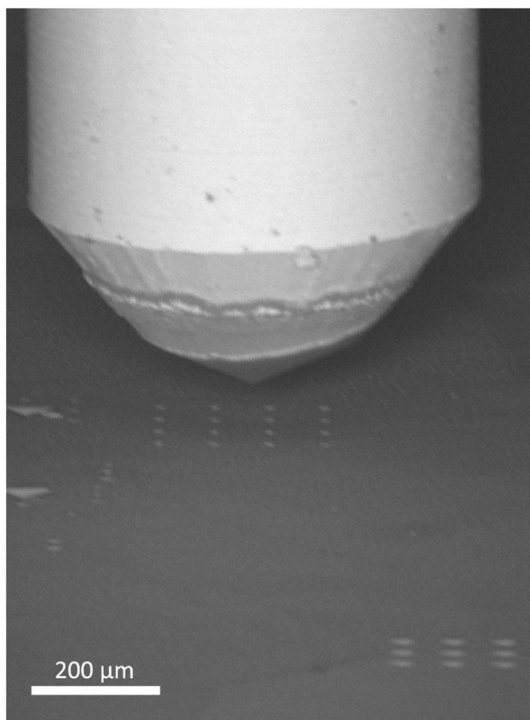


**Fig. 3.** Backscattered electron contrast image of a sapphire tip above a nickel sample at 1100 °C.

0.1  $P_{max}$ . For the superimposed CSM loading a target frequency of 100 Hz and a harmonic amplitude of 4 nm were used. SRJ tests were performed according to Maier et al. [3] with a change in strain rate ( $\dot{P}/P$ ) from 0.2 1/s to 0.05 1/s. Creep test with an initial step load were performed according to Sudharshan Phani et al. [21,41]. A step load of 95 mN was applied with a loading rate of 200 mN/s and hold constant for 1.5 s before switching on the dynamics (CSM) for 40 s.

Molybdenum was chosen as a reference material due to its high temperature mechanical properties which make it an interesting construction material for HT applications. The high thermal conductivity of Mo, compared to fused silica, causes higher drift rates if there is a temperature mismatch between tip and sample. An advantage compared to other materials is that Mo does not cause excessive tip wear due to chemical reactions with the sapphire tip used [27]. The sample thermocouple was placed into a lateral drill hole of the Mo sample. Thus, the temperature could be measured very close to the test locations.

Nickel is the base metal for a variety of high temperature alloys, the so called Ni-based superalloys and therefore an attractive material for future research. Furthermore, there is a good data set on the creep behavior, which can be used for comparison. The strain rate sensitivity of a Ni single crystal in (100) orientation was determined using SRJ and creep tests with an initial step load. Further information about the production and processing of the Ni single crystal can be found in [46,47].

### 3.2. Fused silica

Constant strain rate tests were performed as stated above, using a standard Berkovich diamond tip (MicroStar). Fused silica was tested at room temperature, 200 °C and 300 °C. The sample temperature was the set value, while the tip temperature was adjusted to achieve an isothermal contact. Temperature matching was carried out with the semi-automatic procedure described in the [Appendix A.2](#), using a maximum force of 30 mN and cycle load on/load off time of 30 s/90 s, until drift rates below 0.16 nm/s were achieved. The sample thermocouple was placed in the Mo sheet between sample and sample heater. A difference in tip and sample temperature of about 0.8 °C was determined during temperature matching at 200 °C.

The temperature change during testing was well below 0.01 °C ([Fig. 4](#)) which results in drift rates of 0.158 nm/s. The slight change in temperature at the end of the test segment is caused by a changing thermal contact between tip and sample due to partial unloading for thermal drift measurement. The measured temperature of the actuator was 22.5 °C respectively 23.8 °C during testing at 200 °C and 300 °C.

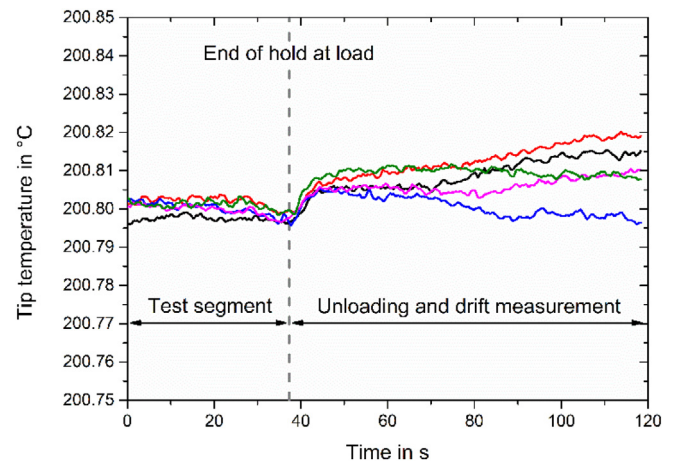


**Fig. 4.** Tip temperature during the indentation of fused silica at 200 °C. Temperatures are plotted for the test segment as well as the subsequent drift measurement segment.

The good temperature stability even at low temperatures like 200 °C demonstrates the capability of the system to control the heating power very well even at low current outputs.

The corresponding load-displacement data, as well as the dynamic contact stiffness are plotted in Fig. 5a and b. Hardness and modulus are shown in Fig. 5c and d. The indentation depth as well as the contact stiffness values are increasing with temperature. This leads to the well observed phenomena in literature, that the hardness of fused silica is

decreasing with temperature, while at the same time the Young's modulus is slightly increasing [2,33,43,44,48,49].

The measured hardness and modulus data in this study fit very well with literature (Fig. 5e–f). Higher drift rates have only a minor effect on the data due to the large contact depths achieved by the high load applied. The changing system stiffness during heating was compensated in order to get a depth independent, constant modulus of the sample. The frame stiffness is slightly decreasing

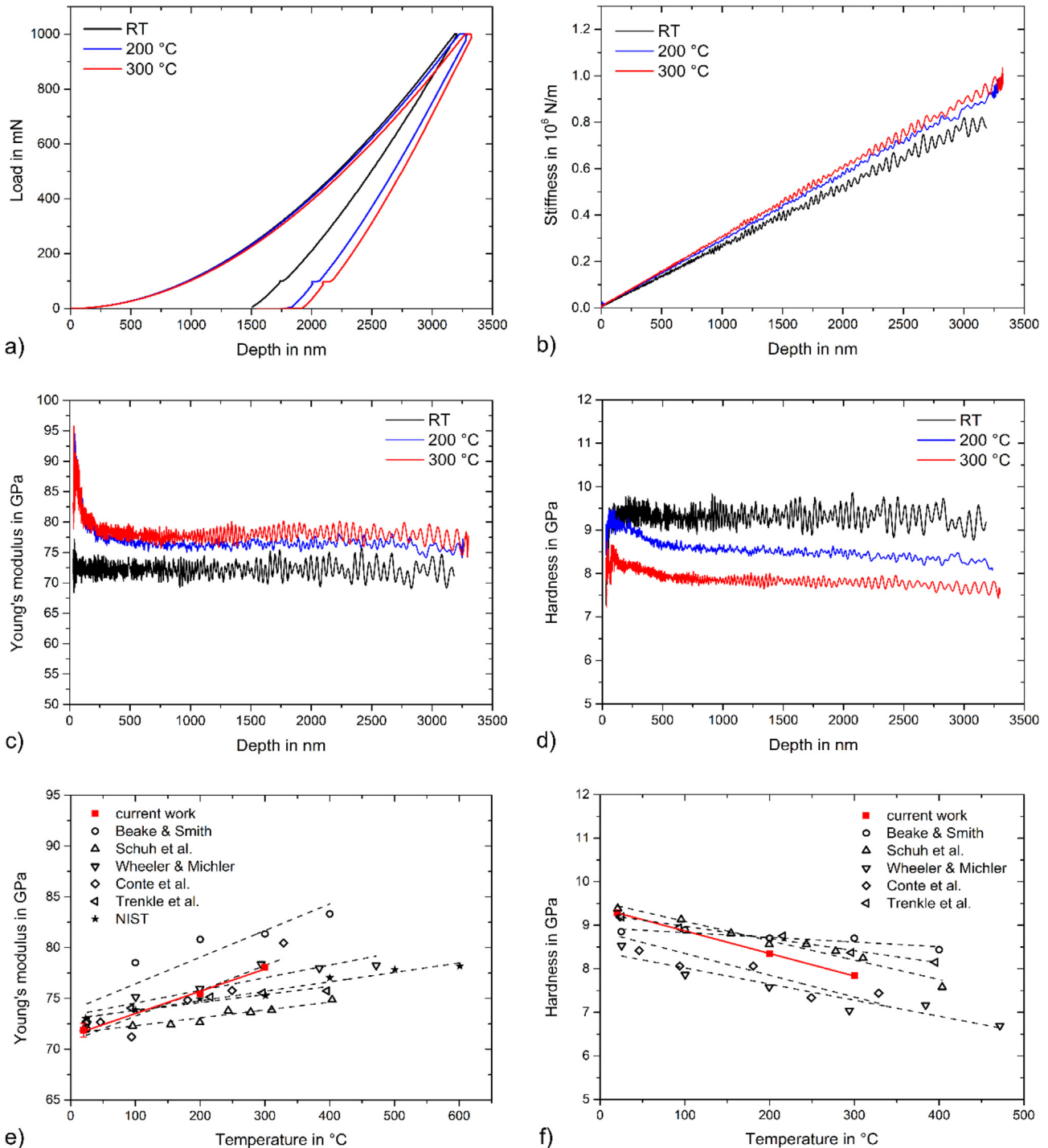


Fig. 5. a) Temperature dependent load displacement curve, b) contact stiffness vs. depth, c) Young's modulus vs. depth, d) hardness vs. depth, e) Young's modulus vs. temperature and d) hardness vs. temperature of fused silica. Literature data taken from [2,33,43,44,48,49].

from  $1.276 \cdot 10^6 \text{ N/m}$  at RT to  $1.136 \cdot 10^6 \text{ N/m}$  at  $300 \text{ }^\circ\text{C}$  and as such nearly independent of temperature.

### 3.3. Molybdenum

Ultra-high temperature nanoindentation experiments on a mirror finished, commercially pure (99,95%, ASTM-B-387 Type 361), polycrystalline Mo sample were carried out using an ultra-high temperature sapphire Berkovich tip (Synton MDP). More detailed information on

the tips used is given in the [Appendix A.3](#). All tests were carried out in batch mode applying the CSM test protocol as described above. Additional RT tests on fused silica were done between each test temperature to calibrate the tip area function according to the procedure developed by Oliver and Pharr [36]. The influence of thermal expansion of the tip on the tip area function can be neglected as it is already discussed in literature [2,27].

A temperature dependent Young's modulus of sapphire as well as a temperature dependent Poisson's ratio of molybdenum was used for the analysis [27,50]. The Poisson's ratio of Sapphire ( $\nu_{\text{Sap}} = 0.24$ )

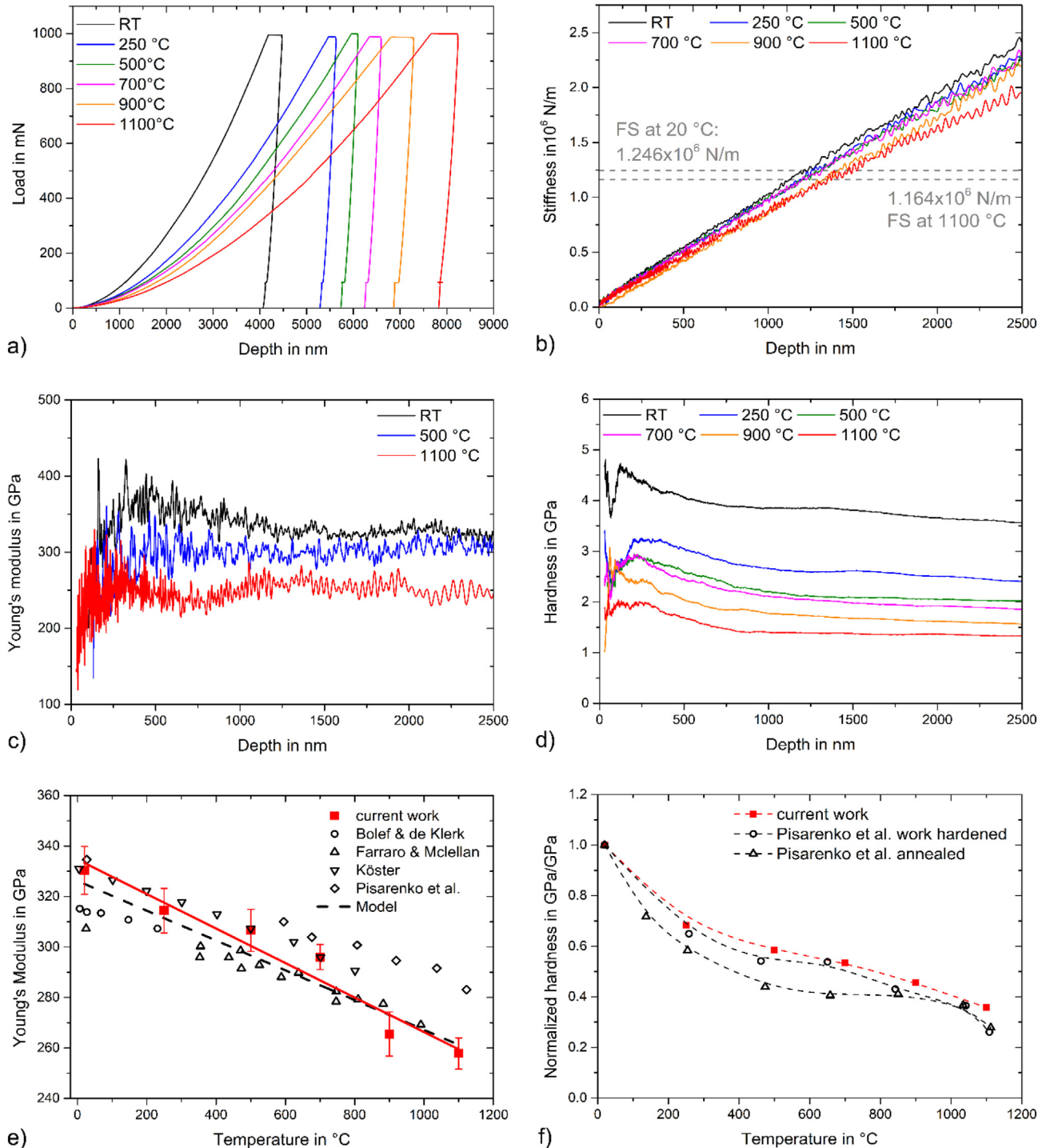


**Fig. 6.** a) Temperature dependent load displacement curve, b) contact stiffness vs. depth, c) Young's modulus vs. depth, d) hardness vs. depth, e) Young's modulus vs. temperature and d) hardness vs. temperature of molybdenum [51–53].

was assumed to be constant and T independent [27]. The frame stiffness was adjusted in order to get a depth independent Young's modulus. Therefore, the frame stiffness was reduced by about 6.6% from  $1.246 \cdot 10^6 \text{ N/m}$  at RT to  $1.164 \cdot 10^6 \text{ N/m}$  at 1100 °C (Fig. 8b). The actuator temperature was decreasing to 15.4 °C by testing at 1100 °C.

Representative, temperature dependent load-displacement curves as well as the temperature dependent stiffness data are plotted in Fig. 6a and b. The contact stiffness is slightly decreasing with increasing temperature. The stiffness follows a linear relationship for all T and depth ranges, except for the measurements at 1100 °C.

For this reason, were only data up to an indentation depth of max. 1500 nm analyzed. At this indentation depth the contact stiffness is similar to the frame stiffness of the system. At higher indentation depths, the frame compliance is larger than the contact compliance, which leads to increasing inaccuracy when determining Young's modulus, penetration depth and thus hardness. The modulus and hardness data as a function of indentation depth is plotted for several temperatures in Fig. 6c and d.

The comparison of measured hardness and Young's modulus data with literature data shown in Fig. 6e and f. Literature data for hardness were measured with a micro hardness tester, while the Young's modulus was determined by pulse-echo methods. Additionally, the Young's modulus was calculated according to the following model [54]:

$$E(T) = E(0 \text{ K}) \cdot \left(1 - 0.5 \frac{T}{T_m}\right) \quad (11)$$

with E (0 K), Young's modulus at 0 K and melting temperature  $T_m$ . The fit is normalized to a room temperature modulus of 325 GPa [55].

Young's modulus data are fitting very well to the data determined by pulse-echo methods and the model, even at a temperature of 1100 °C. The good consistency of measured and literature Young's modulus data indicates the correct determination of the projected contact area and thus of the measured hardness values. The temperature dependence of H matches nicely the literature data.

### 3.4. Single crystalline nickel

SRJ and SLH tests were performed on SX Ni as described above. All tests were performed with UHT sapphire Berkovich tips (Synton MDP). A temperature dependent tip modulus was used for the analysis, the Poisson's ratio of Ni was assumed to be constant [27]. The sample thermocouple was placed into the Mo sheet.

In SRJ tests, hardness values immediately before and after the strain rate jump were analyzed. An overview of test statistics and SRSs are given in Table 1. The frame stiffness of the nanoindenter was adjusted from  $1.166 \cdot 10^6 \text{ N/m}$ , at RT to  $1.001 \cdot 10^6 \text{ N/m}$  at 1100 °C. An actuator temperature of 14.4 °C was measured at the maximum test temperature.

**Table 1**  
Strain rate sensitivity of nickel determined with SRJ and step-load creep tests.

T in °C	SRJ tests			Creep tests		
	Number of tests	Max. drift rate in nm/s	m	Number of tests	Max. drift rate in nm/s	m
RT	6	0.065	0.001	4	0.037	0.001
499	6	0.072	0.013	4	0.095	0.010
835	5	0.069	0.027	3	0.108	0.028
1009	4	0.042	0.051	5	0.136	0.060
1100	4	0.180	0.055	2	0.767	0.098

The depth dependent hardness of the SRJ tests is plotted in Fig. 7a for different temperatures. Ni is strongly softening with temperature and mainly deforms plastic. The hardness data below 1000 nm are not representative of the material response, since strong tip rounding prevents a measurement of indentation size effects at low temperature. However, for larger depths, the hardness is nearly depth independent and only an influence of T and strain rate on the hardness is found. In Fig. 7b is the

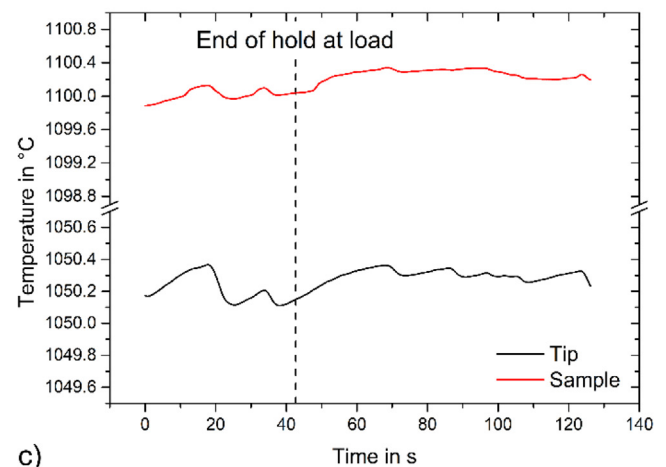
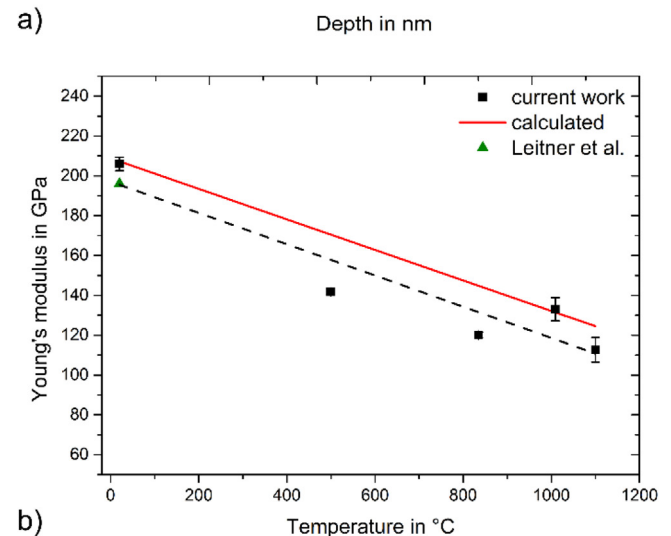
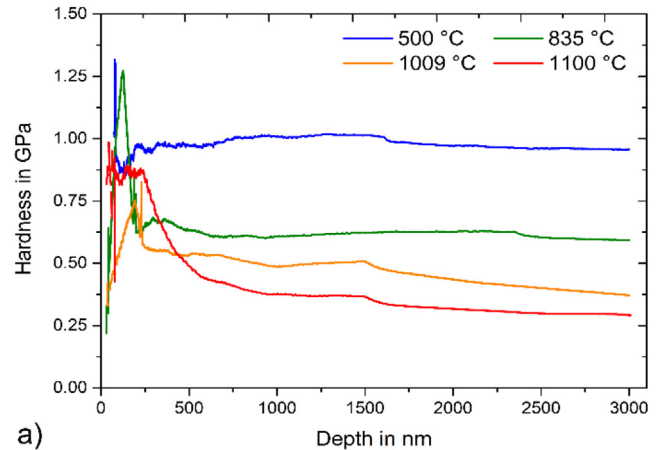


**Fig. 7.** a) Depth dependent hardness and b) temperature dependent modulus of SX Ni. Tip and sample temperature as a function of time during SRJ test on nickel at 1100 °C with a drift rate of 0.069 nm/s are shown in (c) [46,56,57].

temperature dependent Young's modulus plotted and compared to calculated data using Eqs. (12) and (13) [56]:

$$G(T) = 78.9(1 - 0.64(T - 300 \text{ K})/T_m) \text{ GPa} \quad (T_m = 1726 \text{ K}) \quad (12)$$

$$E(T) = G(T) \cdot 2(1 + \nu) \quad (13)$$

with temperature  $T$  and melting temperature  $T_m$  and Poisson's ratio  $\nu$ . The nanoindentation data are shifted to slightly lower values, but the temperature dependent related decrease described by the slope of the fitting lines is very similar. The temperature stability at 1100 °C (sample temperature is set temperature) is shown in Fig. 7c. The scattering is a bit higher than at lower temperatures (Fig. 4) but still good.

Fig. 8a shows the temperature dependent depth-time relationship during the performed step load and hold creep tests. The indentation strain rate as a function of hardness in Fig. 8b. High strain rates in the initial part of the tests can be achieved by applying a step load and hold the load for 1.5 s. In this first test segment is the hardness calculated by indentation depth whereas the hardness in the second part of the experiment is determined by the stiffness signal (Sneddon's hardness) using the CSM technique. The hardness values of the two test segments match very well, as can be seen from the linear relationship with the strain rate (Fig. 8b). Thus the influence of the thermal drift is low. This test protocol allows to vary the strain rate over five orders of magnitude within a single test.

The results of the SRSs determined by SRJ and creep tests are compared in Table 1. It could be demonstrated that  $m$  values determined via creep tests are in good accordance with SRJ tests. The relatively high drift rates during creep testing have a negligible influence on the results, since hardness is calculated based on the stiffness signal of the CSM measurement.

The measured hardness and strain rate were converted into uniaxial stress and strain rate using Eqs. (8) and (9) for comparison with literature data. The resulting temperature compensated uniaxial strain rate and normalized uniaxial stress data are compared with creep data from literature. This is shown in Fig. 8c. The results from SRJ and step load and hold tests show a similar behavior. Tests at 1100 °C show a small deviation, this can be attributed to the fact that a new tip was used for these tests.

The activation energy for creep can be calculated with Eq. (10) using two different strain rates. The activation energy for  $\dot{\epsilon} = 0.3 \text{ s}^{-1}$  is 140 kJ/mol, whereas the activation energy in the low strain rate regime ( $\dot{\epsilon} = 0.002 \text{ s}^{-1}$ ) 216 kJ/mol is. In literature activation energies in the range of 243–285 kJ/mol are determined. The difference to literature data can be explained by the fact that the steady state condition in the strain rate has not yet been reached, furthermore the complex stress state below the indenter.

#### 4. Conclusion

The results of the very first nanoindentation tests using the load controlled Prometheus UHT nanoindenter manufactured by Nanomechanics/KLA has been presented. Tests with diamond and sapphire Berkovich tips at temperatures between 20 °C and 1100 °C were performed on fused silica, molybdenum and SX nickel in  $\langle 100 \rangle$  orientation. The improved nanoindentation system offers for the first time the possibility to determine reliable Young's modulus and hardness data at temperatures up to 1100 °C using dynamic methods like the continuous stiffness measurement (CSM). Low drift rates even at ultra-high temperatures could be achieved by a sophisticated temperature management including multiple independent heating and cooling options. Additionally, a semi-automated temperature matching procedure has been presented.

The combination of the 1 N high load actuator and the high frame stiffness ( $\geq 1 \cdot 10^6 \text{ N/m}$ ) allows experiments to be carried out at higher

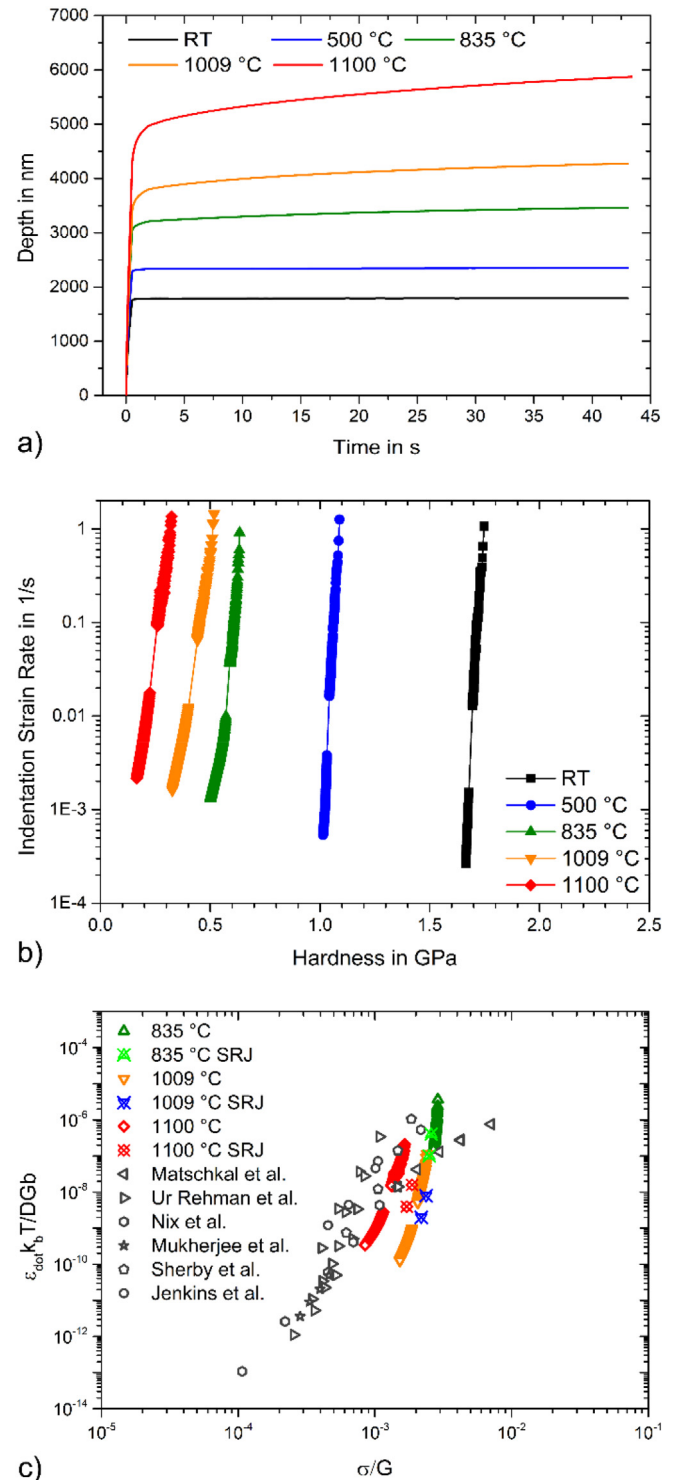


Fig. 8. A) Depth-time behavior of Ni at different temperatures using a step-load and hold test. B) Temperature dependent Indentation strain-rate as a function of hardness for nickel. C) Temperature compensated uniaxial strain rates vs. normalized uniaxial stress data [14,46,58–60].

indentation depths, which are less sensitive to tip wear and thermal drift. Tip and tip braze materials for operating at high temperature are still a pending issue which needs to be solved in future. Nevertheless, it could be shown that sapphire is a good tip material for testing molybdenum even at 1100 °C. Testing in nickel at high temperatures cause massive tip wear as already reported in literature [27]. The set up inside

a SEM allows in situ observations while the vacuum atmosphere minimize oxidation. It could be shown that imaging is possible up to the maximum temperature. A further improvement of the image quality will allow a good positioning or even in-situ experiments at 1100 °C in future. The temperature dependent hardness and Young's modulus data of fused silica are consistent with previous tests. The temperature control at low temperatures like 200 °C is challenging due to the low current output. Nevertheless, the excellent temperature stability at low temperature could be demonstrated. Tests at higher temperatures were performed on molybdenum and nickel. Young's modulus and hardness data correspond well with literature data. Also the temperature compensated uniaxial strain rates and normalized uniaxial stress data, as well as the determined activation energy for creep in Ni fit with literature data at least in the low strain rate regime. This demonstrated that nanoindentation experiments even under these extreme conditions give similar results as conventional uniaxial experiments.

### CRediT authorship contribution statement

**Christian Minnert:** Investigation, Formal analysis, Data curation, Visualization, Writing - original draft. **Warren C. Oliver:** Methodology, Writing - review & editing, Resources, Supervision. **Karsten Durst:** Conceptualization, Writing - review & editing, Supervision, Resources, Funding acquisition, Project administration.

### Declaration of competing interest

The authors declare no conflict of interest.

### Acknowledgement

The authors would like to thank Rich Anthony and Sam Bacon for technical support during the experimental part. The authors gratefully acknowledge Deutsche Forschungsgemeinschaft (DFG) for financial support within the framework of the project "Indentation creep: New machine and test methodology development at various length scales, high temperatures and low deformation rates" (DU 424/11-1). Further financial support was gratefully provided by the Open Access Publication Fund of the Technical University of Darmstadt.

### Data availability

The raw/processed data required to reproduce these findings cannot be shared at this time as the data also forms part of an ongoing study.

### Appendix A

#### A.1. Influence of temperature on the actuator calibration

As mentioned above is the actuator temperature is slightly changing during testing at non ambient temperatures. The maximum temperature of the actuator is controlled by an active cooling of the actuator housing. Whereas the lowest actuator temperature is controlled by the cooling water temperature which has to be reduced with increasing test temperature. In consequence, the actuator temperature was decreasing with increasing test temperature from RT to 14.4 °C, the maximum actuator temperature was 23.8 °C.

In order to investigate the influence of temperature on the calibration, the actuator was cooled down to 12 °C and heated up to 25 °C using the water circuit described above. In Fig. 9, the temperature dependent phase angle (Fig. 9a), compliance (Fig. 9b) and damping (Fig. 9c) are plotted. The data are nearly constant, only for the damping a small deviation could be observed, which is however in the range of the scattering [61–64].

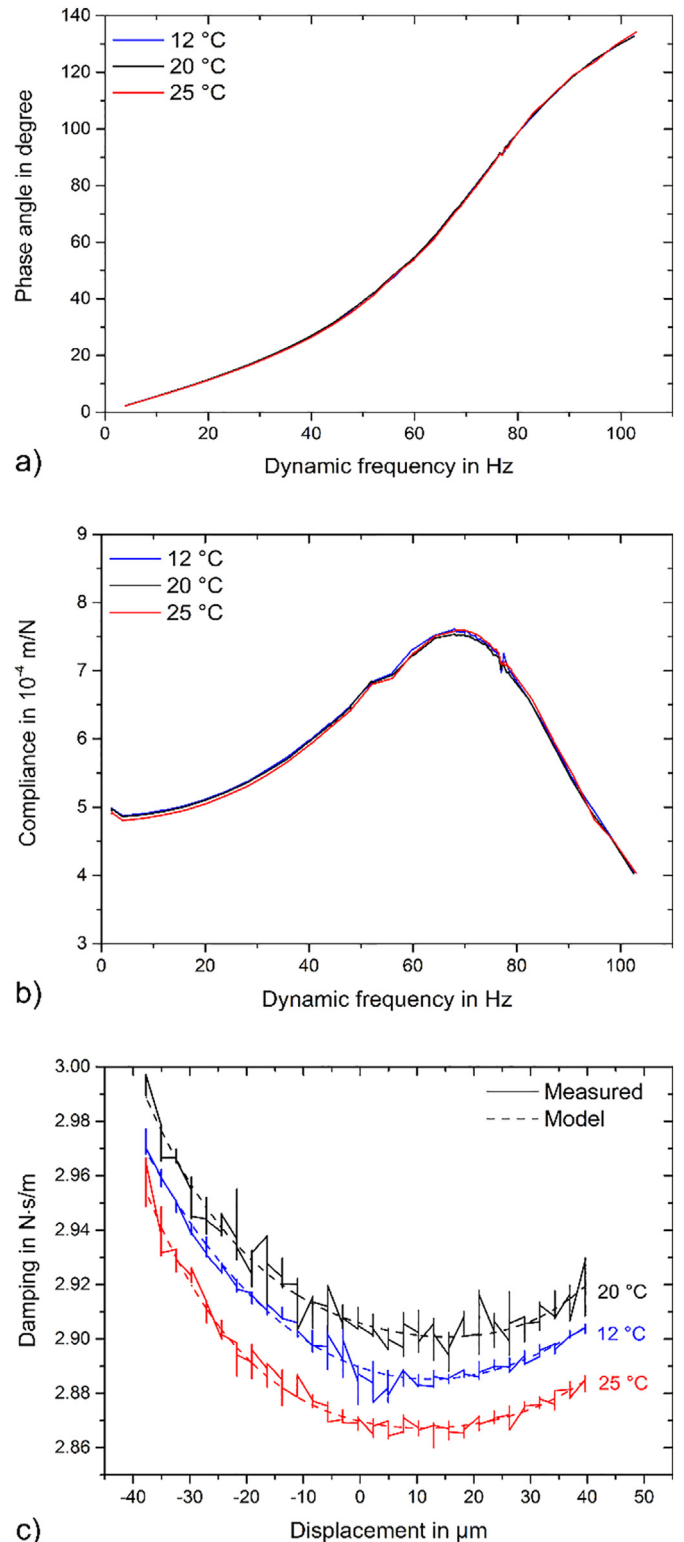


**Fig. 9.** Influence of temperature on calibration. A) Phase angle vs. Dynamic frequency, b) Compliance vs. Dynamic frequency and c) Damping vs. Displacement.

#### A.2. Semi-automated temperature matching procedure

Before starting the temperature matching process, the sample and tip are heated to the same temperature and hold there for a couple of minutes until temperatures are settled and thermal gradients caused

by fast heating (10 K/min) are minimized. During the T matching procedure, the tip is brought into contact with the sample for a few seconds using a predefined constant force e.g. 25 mN and then removed from the sample surface again (see Fig. 10a–b). This loading– unloading procedure is automatically repeated several times. The raw displacement (Fig. 10b) and the temperatures of the tip and sample are continuously recorded (Fig. 10c–d). Now, either the tip or the sample temperature has to be varied manually until the drift rate is steadily decreasing. The corresponding contact and system drift are calculated independently by the software (Fig. 10e–f).

The system drift is related to the displacement change between the individual loading cycles. This change is caused by thermal expansion or contraction of the system/gantry which affects the spacing between the tip and the sample surface. The system drift can therefore be calculated by the slope between the individual segments (overall slope) where the positive load is applied (see Fig. 10b and e). This overall displacement change will be superimposed with a displacement change due to the temperature mismatch of the contact. The tip side is more sensitive to temperature mismatches compared to the sample side due to the lower heat capacity (Fig. 10c–d). A changing tip temperature leads to a thermal expansion or contraction and thus to a change in displacement signal. The curvature of the displacement signal depends on the relative temperatures of tip and sample. Low thermal drift values result in a linear changing displacement. The change in displacement within a loading cycle (positive load applied) is related to the contact drift (Fig. 10b, f). It goes towards zero as soon as the system is in thermal equilibrium. The Influence of creep on the displacement signal will be reduced by continuously indenting at the same position.

The independent determination of system drift and contact drift allows to start the temperature setting of tip and sample already before the system/gantry is in thermal equilibrium which reduces the time for temperature adjustment significantly. In the example shown above (Fig. 10), the temperature of the sample was increased (Fig. 10d) until drift rates close to zero were reached. The difference in tip and sample temperature, here about 35 K, is mainly caused by a temperature gradient between the top and bottom side of the sample. The thermocouple

for measuring the sample temperature is placed in the Mo sheet close to the heater and is therefore not measuring the exact surface temperature of the sample. The surface temperature of the sample is lower due to radiation and heat transfer through the tungsten wires used for sample clamping. The small change in tip temperature (Fig. 10c) while loading and unloading is also effected by the relatively large alterations in displacement which causes different conditions in terms of heat transfer.

### A.3. Indenter tips

In this work a standard diamond Berkovich tip from MicroStar as well as three ultra-high temperature sapphire Berkovich tips manufactured by Synton MDP were used. All tests from RT to 300 °C, on fused silica were performed with the diamond tip. The maximum operational temperature of this tip is limited by the epoxy glue used to fix the tip in the holder. Molybdenum and Nickel were tested with the UHT sapphire tips. These tips were brazed at temperatures of 1500–1600 °C in a high vacuum environment and can therefore be operated up to 1100 °C.

The contact areas of the sapphire tips are plotted as a function of depth and temperature in Fig. 11. All tip area functions were determined at RT using fused silica as reference material. The sapphire tip show no excessive tip wear during testing Mo (see Fig. 11a) which is consistent with previous tests reported in literature [27].

Testing nickel at temperatures above 500 °C leads to a significantly changing tip area function (Fig. 11b). After testing at 1009 °C a huge change in the area function was observed, caused by tip wear or material adhesion to the tip. Therefore, two different tips were used in this study for testing Ni. The sapphire tips were sticking in the nickel sample at these extreme temperatures, high forces have to be applied to retract the tip from the sample surface.

It could also be demonstrated that the high temperature tips are able to withstand these ultra-high temperatures. The necessity for new tip materials for future long term creep experiments on nickel and nickel based alloys has been demonstrated.

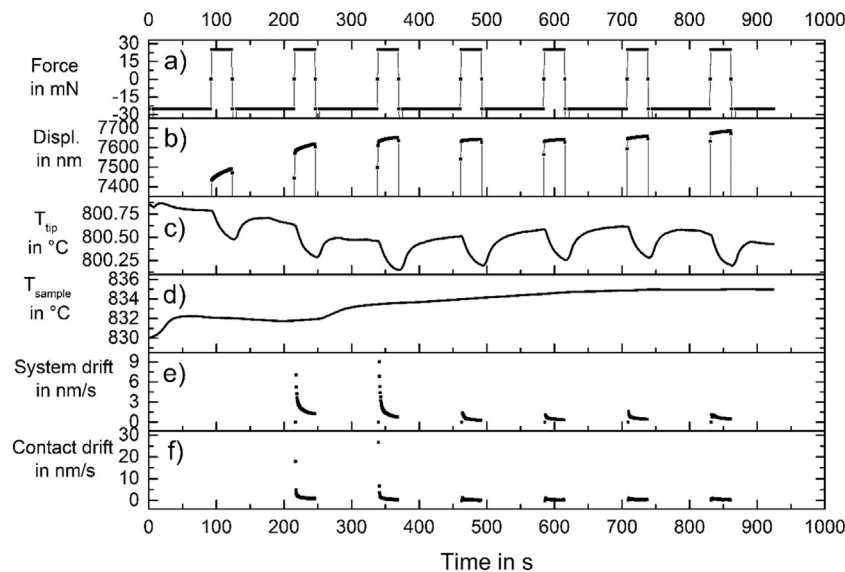


**Fig. 10.** Semi-automated procedure for temperature adjustment, shown exemplarily for Ni at 800 °C. A) Applied force, b) displacement, c) tip temperature, d) sample temperature, e) system drift and f) contact drift as a function of time.

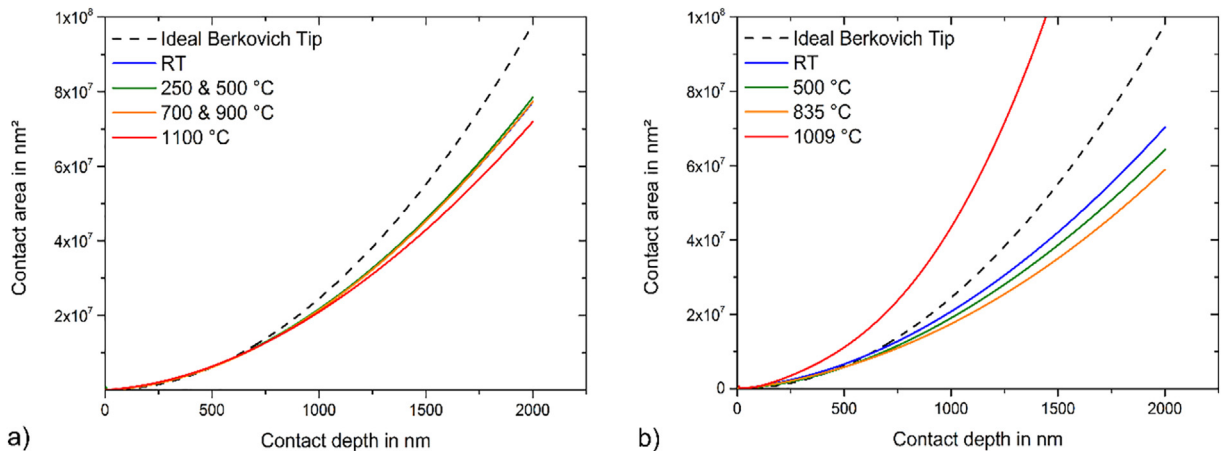


Fig. 11. Evolution of contact area as a function of contact depth and test temperature during indenting a) molybdenum and b) nickel with a sapphire Berkovich tip.

## References

- [1] J.M. Wheeler, et al., High temperature nanoindentation: the state of the art and future challenges, *Curr. Opin. Solid State Mater. Sci.* 19 (6) (2015) 354–366.
- [2] C.A. Schuh, C.E. Packard, A.C. Lund, Nanoindentation and contact-mode imaging at high temperatures, *J. Mater. Res.* 21 (3) (2006) 725–736.
- [3] V. Maier, et al., Nanoindentation strain-rate jump tests for determining the local strain-rate sensitivity in nanocrystalline Ni and ultrafine-grained Al, *J. Mater. Res.* 26 (11) (2011) 1421–1430.
- [4] J. Ast, et al., A review of experimental approaches to fracture toughness evaluation at the micro-scale, *Mater. Des.* 173 (2019), 107762.
- [5] V. Maier, et al., An improved long-term nanoindentation creep testing approach for studying the local deformation processes in nanocrystalline metals at room and elevated temperatures, *J. Mater. Res.* 28 (9) (2013) 1177–1188.
- [6] P. Cavaliere, Cyclic deformation of ultra-fine and nanocrystalline metals through nanoindentation: similarities with crack propagation, *Procedia Engineering* 2 (1) (2010) 213–222.
- [7] Y.-C. Huang, S.-Y. Chang, C.-H. Chang, Effect of residual stresses on mechanical properties and interface adhesion strength of SiN thin films, *Thin Solid Films* 517 (17) (2009) 4857–4861.
- [8] A. Saini, T. Pollock, High-temperature materials increase efficiency of gas power plants, *MRS Bull.* 37 (6) (2012) 550–551.
- [9] R. Weibler, et al., Evolution of microstructure and mechanical properties of coated Co-base superalloys during heat treatment and thermal exposure, *Mater. Sci. Eng. A* 628 (2015) 374–381.
- [10] R. Darolia, Development of strong, oxidation and corrosion resistant nickel-based superalloys: critical review of challenges, progress and prospects, *Int. Mater. Rev.* 64 (6) (2019) 355–380.
- [11] H. Long, et al., Microstructural and compositional design of Ni-based single crystalline superalloys – a review, *J. Alloys Compd.* 743 (2018) 203–220.
- [12] D. Bürger, et al., Creep properties of single crystal Ni-base superalloys (SX): a comparison between conventionally cast and additive manufactured CMSX-4 materials, *Mater. Sci. Eng. A* 762 (2019) 138098.
- [13] N. Volz, et al., Thermophysical and mechanical properties of advanced single crystalline Co-base Superalloys, *Metall. Mater. Trans. A* 49 (9) (2018) 4099–4109.
- [14] D. Matschkal-Amberger, et al., New flat-punch indentation creep testing approach for characterizing the local creep properties at high temperatures, *Mater. Des.* 183 (2019), 108090.
- [15] K. Durst, M. Göken, Micromechanical characterisation of the influence of rhenium on the mechanical properties in nickel-base superalloys, *Mater. Sci. Eng. A* 387–389 (2004) 312–316.
- [16] A. Barnoush, et al., In situ small-scale mechanical testing under extreme environments, *MRS Bull.* 44 (6) (2019) 471–477.
- [17] J. Kappacher, et al., Thermally activated deformation mechanisms and solid solution softening in W-re alloys investigated via high temperature nanoindentation, *Mater. Des.* 189 (2020), 108499.
- [18] K. Durst, V. Maier, Dynamic nanoindentation testing for studying thermally activated processes from single to nanocrystalline metals, *Curr. Opin. Solid State Mater. Sci.* 19 (6) (2015) 340–353.
- [19] J.M. Wheeler, et al., Activation parameters for deformation of ultrafine-grained aluminium as determined by indentation strain rate jumps at elevated temperature, *Mater. Sci. Eng. A* 585 (2013) 108–113.
- [20] P.S. Phani, W. Oliver, G. Pharr, On the measurement of power law creep parameters from instrumented indentation, *JOM* 69 (11) (2017) 2229–2236.
- [21] P.S. Phani, W. Oliver, A direct comparison of high temperature nanoindentation creep and uniaxial creep measurements for commercial purity aluminum, *Acta Mater.* 111 (2016) 31–38.
- [22] M. Chen, et al., Size-dependent plasticity and activation parameters of lithographically-produced silicon micropillars, *Mater. Des.* 189 (2020), 108506.
- [23] G. Mohanty, et al., Elevated temperature, strain rate jump microcompression of nanocrystalline nickel, *Philos. Mag.* 95 (16–18) (2015) 1878–1895.
- [24] J. Wehrs, et al., Comparison of in situ micromechanical strain-rate sensitivity measurement techniques, *JOM* 67 (8) (2015) 1684–1693.
- [25] C. Su, et al., Measurement of power-law creep parameters by instrumented indentation methods, *Journal of the Mechanics and Physics of Solids* 61 (2) (2013) 517–536.
- [26] G. Guillonneau, et al., Nanomechanical testing at high strain rates: new instrumentation for nanoindentation and microcompression, *Mater. Des.* 148 (2018) 39–48.
- [27] J. Wheeler, J. Michler, Invited article: indenter materials for high temperature nanoindentation, *Rev. Sci. Instrum.* 84 (10) (2013), 101301.
- [28] Y. Li, et al., In situ measurement of oxidation evolution at elevated temperature by nanoindentation, *Scr. Mater.* 103 (2015) 61–64.
- [29] Y. Li, et al., Effects of creep and oxidation on reduced modulus in high-temperature nanoindentation, *Mater. Sci. Eng. A* 678 (2016) 65–71.
- [30] Y. Li, et al., Microstructure evolution of FeNiCr alloy induced by stress-oxidation coupling using high temperature nanoindentation, *Corros. Sci.* 135 (2018) 192–196.
- [31] J. Langevoort, et al., On the oxide formation on stainless steels AISI 304 and incoloy 800H investigated with XPS, *Appl. Surf. Sci.* 28 (2) (1987) 167–179.
- [32] J.S.K.L. Gibson, et al., On extracting mechanical properties from nanoindentation at temperatures up to 1000 °C, *Extreme Mechanics Letters* 17 (2017) 43–49.
- [33] J.C. Trenkle, C.E. Packard, C.A. Schuh, Hot nanoindentation in inert environments, *Rev. Sci. Instrum.* 81 (7) (2010), 073901.
- [34] B.D. Beake, et al., Temperature dependence of strain rate sensitivity, indentation size effects and pile-up in polycrystalline tungsten from 25 to 950° C, *Mater. Des.* 156 (2018) 278–286.
- [35] I.N. Sneddon, The relation between load and penetration in the axisymmetric Boussinesq problem for a punch of arbitrary profile, *Int. J. Eng. Sci.* 3 (1) (1965) 47–57.
- [36] W.C. Oliver, G.M. Pharr, An improved technique for determining hardness and elastic modulus using load and displacement sensing indentation experiments, *J. Mater. Res.* 7 (6) (1992) 1564–1583.
- [37] M.J. Mayo, W.D. Nix, A micro-indentation study of superplasticity in Pb, Sn, and Sn-38 wt% Pb, *Acta Metall.* 36 (8) (1988) 2183–2192.
- [38] D.L. Joslin, W.C. Oliver, A new method for analyzing data from continuous depth-sensing microindentation tests, *J. Mater. Res.* 5 (1) (1990) 123–126.
- [39] B.N. Lucas, W.C. Oliver, Indentation power-law creep of high-purity indium, *Metall. Mater. Trans. A* 30 (3) (1999) 601–610.
- [40] O. Prach, et al., A new nanoindentation creep technique using constant contact pressure, *J. Mater. Res.* 34 (14) (2019) 2492–2500.
- [41] P. Sudharshan Phani, W.C. Oliver, Ultra high strain rate Nanoindentation testing, *Materials* 10 (6) (2017) 663.
- [42] J. Wheeler, P. Brodard, J. Michler, Elevated temperature, in situ indentation with calibrated contact temperatures, *Philos. Mag.* 92 (25–27) (2012) 3128–3141.
- [43] J.M. Wheeler, J. Michler, Elevated temperature, nano-mechanical testing in situ in the scanning electron microscope, *Rev. Sci. Instrum.* 84 (4) (2013), 045103.
- [44] M. Conte, et al., Novel high temperature vacuum nanoindentation system with active surface referencing and non-contact heating for measurements up to 800° C, *Rev. Sci. Instrum.* 90 (4) (2019) 45105.
- [45] G. Feng, A. Ngan, Effects of creep and thermal drift on modulus measurement using depth-sensing indentation, *J. Mater. Res.* 17 (3) (2002) 660–668.
- [46] H. ur Rehman, et al., On the temperature dependent strengthening of nickel by transition metal solutes, *Acta Mater.* 137 (2017) 54–63.
- [47] A. Sato, et al., On the mechanical behavior of a new single-crystal Superalloy for industrial gas turbine applications, *Metall. Mater. Trans. A* 43 (7) (2012) 2302–2315.
- [48] B.D. Beake, J.F. Smith, High-temperature nanoindentation testing of fused silica and other materials, *Philosophical Magazine A* 82 (10) (2002) 2179–2186.
- [49] R.G. Munro, NIST Interagency/Internal Report No. 6853, 2002.
- [50] H. Su, et al., Temperature-dependent Modulus of metals based on lattice vibration theory, *J. Appl. Mech.* 81 (4) (2013) 41017–041017–4.
- [51] R. Farraro, R.B. Mclellan, Temperature dependence of the Young's modulus and shear modulus of pure nickel, platinum, and molybdenum, *Metall. Trans. A* 8 (10) (1977) 1563–1565.

- [52] G. Pisarenko, V. Borisenko, Y.A. Kashtalyan, The effect of temperature on the hardness and modulus of elasticity of tungsten and molybdenum (20–2700 $\pm$ ), *Soviet Powder Metallurgy and Metal Ceramics* 1 (5) (1964) 371–374.
- [53] D.I. Bolef, J. De Klerk, Elastic constants of single-crystal Mo and W between 77 and 500 K, *J. Appl. Phys.* 33 (7) (1962) 2311–2314.
- [54] J. Roesler, H. Harders, M. Baeker, *Mechanical Behaviour of Engineering Materials*, Springer, 2007.
- [55] F. Caradelli, *Materials Handbook*, second edition Springer, 2008.
- [56] Y. Li, et al., Deformation kinetics of nanocrystalline nickel, *Acta Mater.* 55 (17) (2007) 5708–5717.
- [57] A. Leitner, V. Maier-Kiener, D. Kiener, Dynamic nanoindentation testing: is there an influence on a material's hardness? *Materials Research Letters* 5 (7) (2017) 486–493.
- [58] W.D. Nix, B. Ilshner, Mechanisms controlling creep of single phase metals and alloys, in: P. Haasen, V. Gerold, G. Kostorz (Eds.), *Strength of Metals and Alloys*, Pergamon 1979, pp. 1503–1530.
- [59] A.K. Mukherjee, J.E. Bird, J.E. Dorn, *Experimental Correlations for High-Temperature Creep*, 1968.
- [60] O.D. Sherby, P.M. Burke, Mechanical behavior of crystalline solids at elevated temperature, *Prog. Mater. Sci.* 13 (1968) 323–390.
- [61] J. Weertman, P. Shahinian, Creep of polycrystalline nickel, *JOM* 8 (10) (1956) 1223–1226.
- [62] G.J. Richardson, C.M. Sellars, W.J.M. Tegart, Recrystallization during creep of nickel, *Acta Metall.* 14 (10) (1966) 1225–1236.
- [63] S. Karashima, H. Oikawa, T. Motomiya, Steady-state creep characteristics of polycrystalline nickel in the temperature range 500 $\pm$  to 1000 $\pm$ C, *Trans. Jpn. Inst. Metals* 10 (3) (1969) 205–209.
- [64] H. Oikawa, T. Kato, S. Karashima, Activation parameters of high-temperature creep in nickel, and in Ni-9.5at% Cr and Ni-10.3at% W alloys, *Trans. Jpn. Inst. Metals* 14 (5) (1973) 389–395.

---

## **Publication D**

Reproduced full text article with permission from Springer Nature.

Copyright (2021), Journal of Materials Research.

---



# Thermally activated dislocation mechanism in Mo studied by indentation, compression and impact testing

Christian Minnert<sup>1,a)</sup> , Hamad ur Rehman<sup>1</sup>, Karsten Durst<sup>1</sup>

<sup>1</sup>Physical Metallurgy, Materials Science Department, Technical University of Darmstadt, Darmstadt, Germany

<sup>a)</sup>Address all correspondence to this author. e-mail: c.minnert@phm.tu-darmstadt.de

Received: 17 November 2020; accepted: 3 February 2021

Body-centered cubic metals like molybdenum and tungsten are interesting structural materials for high-temperature applications. These metals, are however, brittle at low homologous temperature, caused by the limited mobility of screw dislocations. In this study, the thermally activated deformation mechanisms in bcc Mo have been investigated using strain rate jump nanoindentation and compression tests as well as Charpy V-notch impact testing. The material shows a significant softening with increasing temperature and a maximum in strain rate sensitivity is found at the critical temperature, before decreasing again in the ductile regime. The activation volume, however, showed a distinct increase from about  $5 b^3$  at the onset of the brittle to ductile transition temperature. Here we propose to use temperature-dependent nanoindentation strain rate jump testing and the activation volume as a complementary approach to provide some indication of the brittle to ductile transition temperature of bcc metals.

## Introduction

Body-centered cubic (bcc), refractory metals like molybdenum or tungsten are interesting candidates for structural applications due to their high strength at elevated temperatures. The flow stress of these bcc metals at low homologous temperature is however mainly governed by the mobility of screw dislocations and therefore strongly dependent on temperature and applied strain rate. Thus, bcc metals exhibit a brittle behavior at low and a ductile behavior at elevated temperatures. The temperature at which the brittle to ductile transition (BDT) takes place is referred as the brittle to ductile transition temperature (BDTT). This well-studied behavior is caused by the crystal lattice and the activated slip systems:

In the low-temperature regime, the plastic deformation of bcc metals is mainly governed by the slip of  $\frac{a}{2}\langle 111 \rangle$  screw dislocations on  $\{110\}$  planes, whereas at high temperatures, additional  $\{112\}$  and  $\{123\}$  slip planes are activated [1–4]. A spreading of the screw dislocation core on  $\{110\}$  or  $\{112\}$  planes can take place due to the threefold symmetry of the  $\langle 111 \rangle$  dislocation line [5]. In consequence, the Peierls potential or the Peierls–Nabarro barrier will increase, resulting in a higher resistance of motion of the screw dislocations. The strength of this barrier is reduced by thermal activation and the formation of

kinks in the dislocation line. These kinks have an edge character and allow for the movement of dislocations over the barrier in steps. Thus, kink pairs are formed and they move through small kink steps instead of having to move the entire dislocation line at once. The nucleation and motion of these kink pairs is the rate controlling step, controlling the plastic deformation of bcc metals at low temperatures. Extrinsic effects like impurity atoms can constrain the kink mobility [3].

The dislocation velocity  $v_D$  is related to the applied plastic strain rate  $\dot{\epsilon}$  as described by the Orowan equation (Eq. 1) [5]:

$$\dot{\epsilon} = \rho_m b v_D \quad (1)$$

with mobile dislocation density  $\rho_m$  and Burgers vector  $b$ . The screw dislocation velocity  $v_D$  is given by Eq. (2) [5]:

$$v_D = \rho_K v_K h, \quad (2)$$

where  $\rho_K$  is the steady-state kink density,  $v_K$  the kink velocity and  $h$  the kink height. The kink pair nucleation rate  $J$  as well as the kink velocity are thermal activated processes and can therefore be expressed by Arrhenius-type equations (Eqs. 3 and 4). The kink pair nucleation rate  $J$  is [5]

$$J = J_0 \exp\left(-\frac{Q}{kT}\right) \quad (3)$$

with a frequency constant  $J_0$ , required energy for kink pair nucleation  $Q$ , Boltzmann constant  $k$  and absolute temperature  $T$ . It can be assumed that the energy required to initiate a kink movement  $Q_m$  is significantly lower than the energy  $Q$  required to form a kink pair. The resulting temperature-dependent kink velocity can be expressed by the following Arrhenius-type equation [5]:

$$v_k = 2av \sinh\left(\frac{\tau bha}{kT}\right) \exp\left(-\frac{Q_m}{kT}\right), \quad (4)$$

where parameter  $a$  is the distance which a kink is moving at each step,  $v$  is a frequency constant and  $\tau$  is the applied stress.

The plastic deformation is thus related to the formation and mobility of kinks. Both are thermally activated processes and therefore sensitive to test temperature and applied strain rate [6–9].

Seeger and Hollang [6] studied the temperature dependence of the flow stress of single-crystalline (SX) Mo. The data are shown in Fig. 1, with additional data from Cheng et al. [9], based on tensile tests carried out by Nemat-Nasser et al. [8] for coarse-grained (CG) Mo. It is apparent from the diagram that the flow stress of Mo consists of an athermal ( $\sigma_a$ ) and a thermal component ( $\sigma^*$ ). The athermal component is related to the long-range internal stresses and microstructural barriers [10, 11]. However, the aforementioned nucleation and motion of kink pairs of the screw dislocations affects the thermal component most and is responsible for the strain rate sensitivity (SRS) of Mo. The flow stress of Mo decreases with increasing test temperature as shown in Fig. 1, until the knee temperature  $T_k$ , also referred as athermal temperature, is reached and flow stress remains nearly constant [7, 9, 12]. The knee temperature is about 20% of the melting temperature for bcc metals [13]. For ultrapure single-crystalline Mo, a knee temperature of approx. 450 K was found [14]. Any further reduction of flow stress is

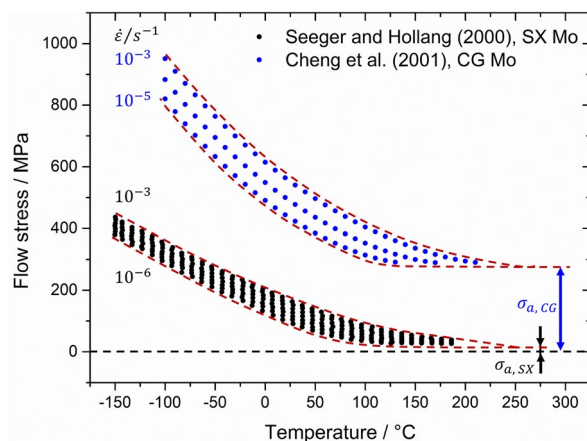


**Figure 1:** Temperature dependence of the flow stress of CG and SX Mo [6, 8, 9].

comparable to the temperature dependency of the shear modulus [9]. The deformation in the temperature range below  $T_k$  is controlled by the mobility of screw dislocations. It is apparent that the flow stress of the polycrystalline Mo from the tensile test data of Nemat-Nasser et al. [8, 9] is larger than that of single-crystalline Mo which is related to an increase in the athermal stress component due to grain boundary strengthening (see Fig. 1). The data will be used later as reference and discussion of the temperature-dependent change in strain rate sensitivity and activation volume.

This strong increase in the thermal stress component of bcc metals and the enhanced rate sensitivity below  $T_k$  lead to brittle fracture at low temperatures. The BDT is controlled by thermally activated dislocation mobility [15–18] and thus related to the applied strain rate (Eq. 1), microstructure [12] and testing conditions [19]. In consequence, the BDTT is an extrinsic material parameter. It is currently not fully understood how the thermal activation and strain rate dependency of the flow stress governs the brittle to ductile transition temperature and how different testing methods could be used for estimating the temperature range for the BDT behavior of bcc metals.

In the present work, nanoindentation and compression testing are used to assess the correlation between thermally activated processes with respect to strain rate sensitivity and activation volume and the brittle to ductile transition temperature in bcc metals determined by conventional Charpy impact testing. All experiments were performed on polycrystalline Mo, which is used as reference material.

There are several publications dealing with the BDT or the temperature-dependent mechanical properties of Mo and its alloys [18, 20–27]. In the most studies, tensile or impact tests were carried out. However, the authors of this study are not aware of any work that has used such a wide range of investigative methods to characterize the brittle to ductile transition of bcc Mo, particularly in terms of the strain rate sensitivity and activation volume underlying dislocation mobility. Different strain rate and stress conditions have been achieved by employing diverse mechanical testing methods.

In Charpy impact tests, a high strain rate is present and a triaxial stress state is formed in the region of the notch [28]. In compression tests, on the other hand, a uniaxial stress state is reached and very low strain rates are applied [29]. Therefore, indentation strain rate jump tests were carried out for comparison, in which a triaxial stress state is generated within the plastic zone below the indenter tip [30], bearing some similarity to the impact tests.

The deformation mode observed during impact testing is controlled by dislocation emission from the crack tip, which in turn depends upon the stress state and testing temperature. This dislocation emission is a thermally activated process [6, 15], thus, the energy absorbed by the specimen during impact

testing varies with temperature and strain rate. Furthermore, the dislocation mobility can lead to work hardening in the plastic zone next to the notch [15, 16, 31]. It is unclear how the thermally activated dislocation mobility changes in this high dislocation density region. In addition, different strengthening mechanisms, like grain boundaries or dislocation hardening, will influence the underlying mechanism and change the BDT behavior [6, 9, 26, 27].

The fracture properties, i.e., fracture toughness and BDTT of single-crystal bcc metals, vary with crystal orientation and active crack system. For tungsten, for instance, a change in BDTT of 100 K was found for different crystal orientations [16, 32]. In polycrystalline materials, grain boundaries can represent a preferred crack path, where the fracture stress depends on the misorientation, respectively the grain boundary energy, of neighboring grains [33, 34]. Segregations at the grain boundary can influence the grain boundary energy, resulting in an altered fracture behavior. Leitner et al. demonstrated how grain boundary segregations of carbon and boron change the fracture mechanisms from intergranular to transgranular resulting in a decreasing BDTT [35, 36].

The active, temperature-dependent deformation mechanisms can be analyzed on the basis of the strain rate sensitivity (SRS)  $m$  and activation volume. Changing the strain rate within a single test opens the possibility to determine the strain rate sensitivity of a material in a quasi-constant volume element or microstructure. The relationship between applied strain rate  $\dot{\epsilon}$  and resulting flow stress  $\sigma_f$  or hardness  $H$  is outlined in Eq. (5) [37]:

$$m = \frac{d(\ln\sigma_f)}{d(\ln\dot{\epsilon})} \cong \frac{d(\ln H)}{d(\ln\dot{\epsilon})} \quad (5)$$

for uniaxial und indentation testing [37].

The activation volume  $V$  is related to the process of kink formation when an obstacle is overcome by a jump of a dislocation line segment under an applied shear stress  $\tau$  (Eq. 6) [38].

$$V = kT \left( \frac{d(\ln \rho_m)}{d\tau} + \frac{d(\ln v_D)}{d\tau} \right) \quad (6)$$

The resulting activation volume can be calculated using Eq. (7) [37]:

$$V = \frac{\sqrt{3}kT}{m\sigma_f} \cong 3\sqrt{3} \frac{kT}{mH} \quad (7)$$

with Boltzmann constant  $k$  and absolute temperature  $T$  [37].

However, bcc metals show a well-known indentation size effect, i.e., the increase in hardness at low indentation depths, due to storage of geometrically necessary dislocations that are required to accommodate the large strain gradients induced by the indenter. This can lead to an overestimation of strain rate

sensitivity [39, 40]. The Nix–Gao [41] analysis can be applied in order to get a depth-independent hardness value using Eq. (8):

$$H = H_0 \sqrt{1 + \frac{h^*}{h}} \quad (8)$$

with the hardness  $H$  at an indentation depth  $h$  and a characteristic length  $h^*$ . This characteristic length depends on the shape of the indenter, the sample shear modulus and the hardness level for an infinite depth  $H_0$  [41]. However, the internal material length scale also changes with testing temperature [7].

This paper addresses the question whether quasi-static nanoindentation and compression tests can be used to study the temperature-dependent deformation mechanisms or in more particular the BDT and BDTT in bcc molybdenum as it is usually done with Charpy V-notch impact tests. Therefore, the strain rate sensitivities as well as the activation volumes were determined with different techniques causing different stress states in the material. The results are compared to literature data on single- and polycrystalline bcc Mo in terms of strain rate sensitivity and activation volumes.

## Results

### Impact testing

The absorbed energy determined in Charpy impact tests is plotted against temperature in Fig. 2a. A clear brittle fracture was observed at room temperature and below (Fig. 2b), with a low fracture energy in the order of 0.2 J. This is typical of fracture devoid of plasticity at the crack tip [15]. A mixed mode fracture is observed in the intermediate temperature range between 75 °C and 110 °C. The cleavage crack propagated directly from the notch and followed the pancake microstructure (Fig. 2c). At  $T > 125$  °C, the crack propagated in a ductile manner and plastic deformation was found next to the crack tip (Fig. 2d). A similar fracture behavior was observed by Babinsky et al. [27]. Dislocation slip becomes easier with an increase in temperature due to a reduction in the flow strength of Mo. Hence, more energy is absorbed by the samples in this regime. The brittle to ductile transition range is highlighted by the gray box in Fig. 2a.

### Compression strain rate jump tests

The results of compression strain rate jump tests in the brittle (RT), ductile (200 °C) and intermediate regimes (60 and 100 °C) are shown in Fig. 3a. A change in strain rate leads to a short transient in stress, e.g., the first strain rate jump from  $0.008 \text{ s}^{-1}$  to  $0.0008 \text{ s}^{-1}$ . This transition is caused by the mobility of the dislocation network as it is described by Eq. (1). Thermal activation of dislocations allows to overcome the Peierls barrier and the kink velocity increases (Eq. 4), resulting in a decrease in strength. The steady-state flow stresses at the constant strain

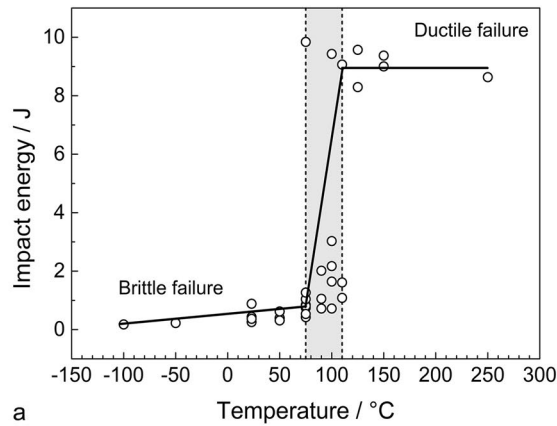


**Figure 2:** Charpy V-notch impact tests: (a) temperature-dependent energy absorbed by Mo samples during impact testing. The gray area indicates the brittle to ductile transition range (b–d). Samples fractured tested at room temperature (0.26 J), 100 °C (3.03 J) and 250 °C (8.64 J).

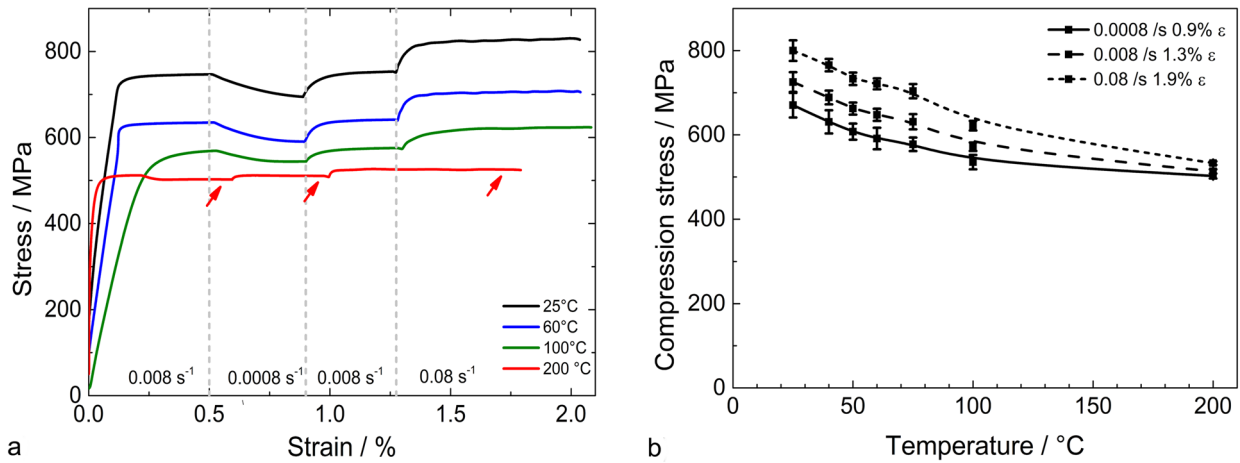


**Figure 3:** Compression strain rate jump tests: (a) stress over strain for different temperatures and (b) compression stress as a function of temperature for different strain rates.

rate marked by arrows (in Fig. 3a) are plotted as a function of temperature in Fig. 3b. These are later used to estimate the strain rate sensitivity and the activation volume.

### Indentation testing

The load displacement curves of nanoindentation strain rate jump tests are shown in Fig. 4a. As mentioned above,

the indentation size effect can lead to an overestimation of  $m$ . Therefore, Nix–Gao [41] fitting of the hardness displacement plots was performed and the indentation size effect was subtracted from the depth-dependent hardness. This ensured that the estimated rate sensitivity and the activation volume are independent of the material length scale and indentation size effect. The resulting rate-dependent hardness is shown in Fig. 4b. During strain rate jump tests, a short transition is

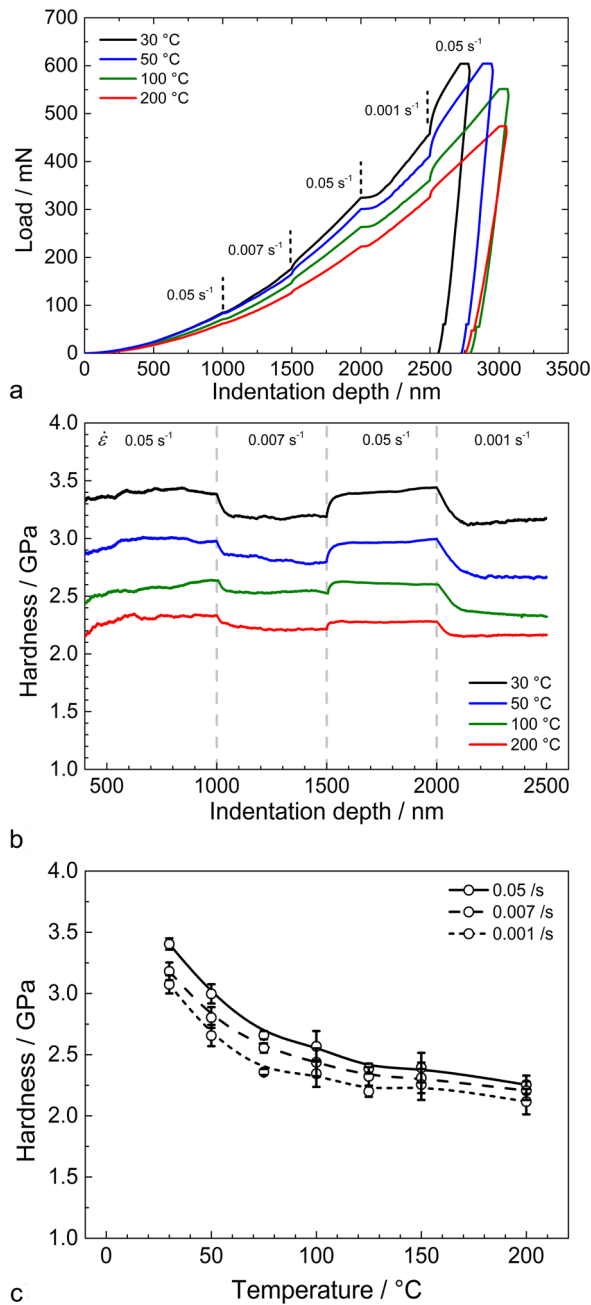


**Figure 4:** Nanoindentation tests: (a) load–displacement curve of the strain rate jump tests, (b) indentation size effect-corrected hardness from SRJ tests plotted against indentation depth, (c) hardness as a function of test temperature.

observed following a change in strain rate (Fig. 4b) similar to the compression SRJ tests.

The steady-state hardness from SRJ tests is decreasing with increasing test temperature as it is shown in Fig. 4c. It contains both the athermal and the thermal component of the flow stress, as the hardness can be converted into stress by multiplying with a constraint factor  $C$ . The hardness does

not decrease further with temperature beyond approx. 125 °C, indicating that the critical temperature has reached. The effect of deformation on the activation volume and the rate sensitivity will be discussed in the next section. Therefore, the strain rate sensitivity and the activation volume were estimated using Eqs. (5) and (7) [37, 38].

## Discussion

Thermally activated processes in bcc Mo have been investigated by using low strain rate indentation and compression experiments at various temperatures. It is not fully understood how the high strain rates and stress triaxiality at the notch during an impact test will influence the underlying dislocation mechanisms. Such stress triaxiality is also found in nanoindentation testing and this work aims at establishing the possibilities offered by nanoindentation testing as an approach for investigating thermally activated processes at elevated temperatures. The results are compared with uniaxial compression tests and literature data. The triaxial stress state during indentation testing makes it difficult to directly compare hardness and compression flow stress values. Therefore, strain rate sensitivity coefficient ( $m$ ) is first used to compare results from different testing approaches.

The rate sensitivity coefficients and corresponding activation volumes—determined from present experiments, single-crystal data from Seeger and Hollang [6] and a modified mathematical model for polycrystalline Mo by Cheng et al. [9]—are plotted as a function of test temperature in Fig. 5. The brittle to ductile transition range determined by impact testing is highlighted in gray for comparison. The present measurements, as well as the literature data, show a small SRS at low temperatures and an increase in the rate sensitivity in the intermediate temperature range (50–110 °C) before again a decrease at higher temperatures ductile regime (Fig. 5a). A similar behavior was also observed for bcc tungsten [42].

However, the absolute values of  $m$  are quite different for the different testing methods and microstructures. The highest SRS value is found for the single-crystal experiments by Seeger and Hollang [6], which is strongly increasing in the temperature range from approx. 50–110 °C. At this temperature range, the flow stress is strongly dropping with increasing temperature, however, the change in stress with strain rate remains largely constant.

The polycrystalline data by Cheng et al. [9] show a maximum in SRS in the temperature range from 50 to 80 °C. The SRSs determined from compression test data are almost identical to the literature values of Cheng et al., while the indentation technique provides significantly lower values. This indicates that the rate sensitivity is affected by the stress state inside the probed

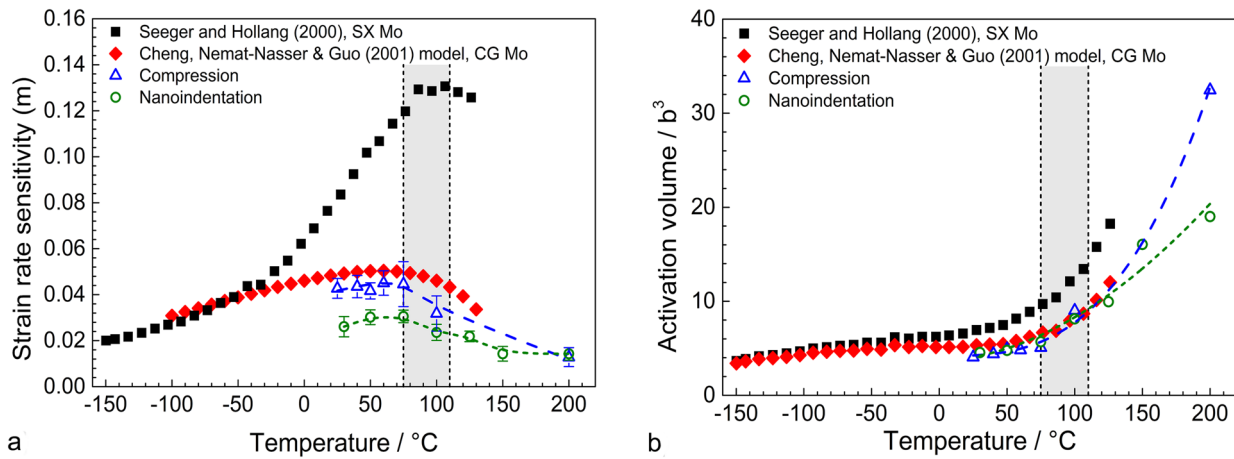


**Figure 5:** Temperature dependence of (a) strain rate sensitivity and (b) activation volume compared with literature from Seeger and Hollang [6] and mathematical model by Cheng et al. [8, 9]. The brittle to ductile transition range from Charpy V-notch impact testing is highlighted in gray for comparison.

volumes, whereas the applied strain rate has a negligible impact on the results.

Such discrepancies between individual testing methods and applied strain rates are caused by the interplay between the net flow stress and the strain rate sensitivity. The flow stress consists of a thermal component (temperature dependent) and an athermal component (grain size dependent). Therefore, the flow stress of polycrystalline Mo is larger than that of single-crystalline Mo due to grain boundary strengthening (see Fig. 1). Although the  $\Delta\sigma/\Delta H$  is similar at a constant temperature, the lower overall value of flow stress values for the single-crystal specimen results in a larger value of the SRS coefficient when it is estimated using Eq. (5). Therefore, as the net flow stress of Mo increases by grain boundary strengthening, the strain rate sensitivity decreases.

The activation volumes determined for single- and polycrystalline Mo (Fig. 5b) however differ only slightly and the activation volume for polycrystalline Mo is almost independent of the test method (uniaxial or triaxial stress state during indentation). The activation volume gives thus a much better representation of the deformation mechanism under these test condition, since both rate sensitivity and flow stress respectively hardness are considered in the analysis (Eq. 7). In comparison, at low temperature an activation volume of about  $5 \text{ b}^3$  is found, and similar values ( $4\text{--}7 \text{ b}^3$ ) are already reported for SX tungsten and chromium [43]. The activation volume is increasing to about  $30 \text{ b}^3$  at elevated temperatures.

Analyzing the temperature-dependent change of the activation volume in more detail, it is noticeable that a moderate, linear increase in the low temperature range can be observed. However, as soon as a critical temperature is reached, the gradient of the linear increase changes significantly. This behavior

is shown in Fig. 6 in more detail for the different data sets. In the following analysis, the critical temperature is determined by a line intercept method and is thus called as intersection temperature,  $T_{\text{int}}$ , in the following. Therefore, the activation volumes for the low and high temperature range are fitted in their linear regime (red dashed lines) and the intersections of the linear fitting lines are used as a measure for  $T_{\text{int}}$ . This results in  $T_{\text{int}}$  of approx.  $77 \text{ }^\circ\text{C}$  for the single-crystal data of Seeger and Hollang [4] and  $88 \text{ }^\circ\text{C}$  for the polycrystalline data of Nemat-Nasser [8] and Cheng et al. [9] (Fig. 6a, b). The same analysis for the SRJ tests yields an intersection temperature of  $76 \text{ }^\circ\text{C}$  for nanoindentation and  $79 \text{ }^\circ\text{C}$  for compression testing (Fig. 6c, d). Included in the diagram is also the range of the brittle to ductile transition temperature, as determined by the Charpy Impact test (Fig. 6c, d). It seems that the intersection temperatures are close to the lower limit of the BDT temperature range. At  $T_{\text{int}}$ , the SRS exhibits a maximum, whereas the activation volume is starting to increase significantly.

This leads to the question of the meaning of  $T_{\text{int}}$  and the underlying physical processes, which are activated and lead to the strong change in the activation volume.

The intersection temperatures of  $76\text{--}88 \text{ }^\circ\text{C}$  (Fig. 6) are significantly lower than the knee temperature of Mo single crystals, which is found to be  $T_k = 177 \text{ }^\circ\text{C}$  ( $450 \text{ K}$ ) [14]. The knee temperature is not necessarily identical to the BDTT. It rather represents an upper limit for the BDTT, i.e.,  $T_{\text{BDT}} \leq T_k$  [44] as the Peierls barrier disappears at  $T > T_k$  and the material can deform in a ductile manner. At temperatures below  $T_k$ , the deformation is limited by the mobility of the screw dislocations [12, 19]. However, the mobility can already be high enough to cause a “semi-ductile” material behavior. The discussion above shows that the intersection temperature must be

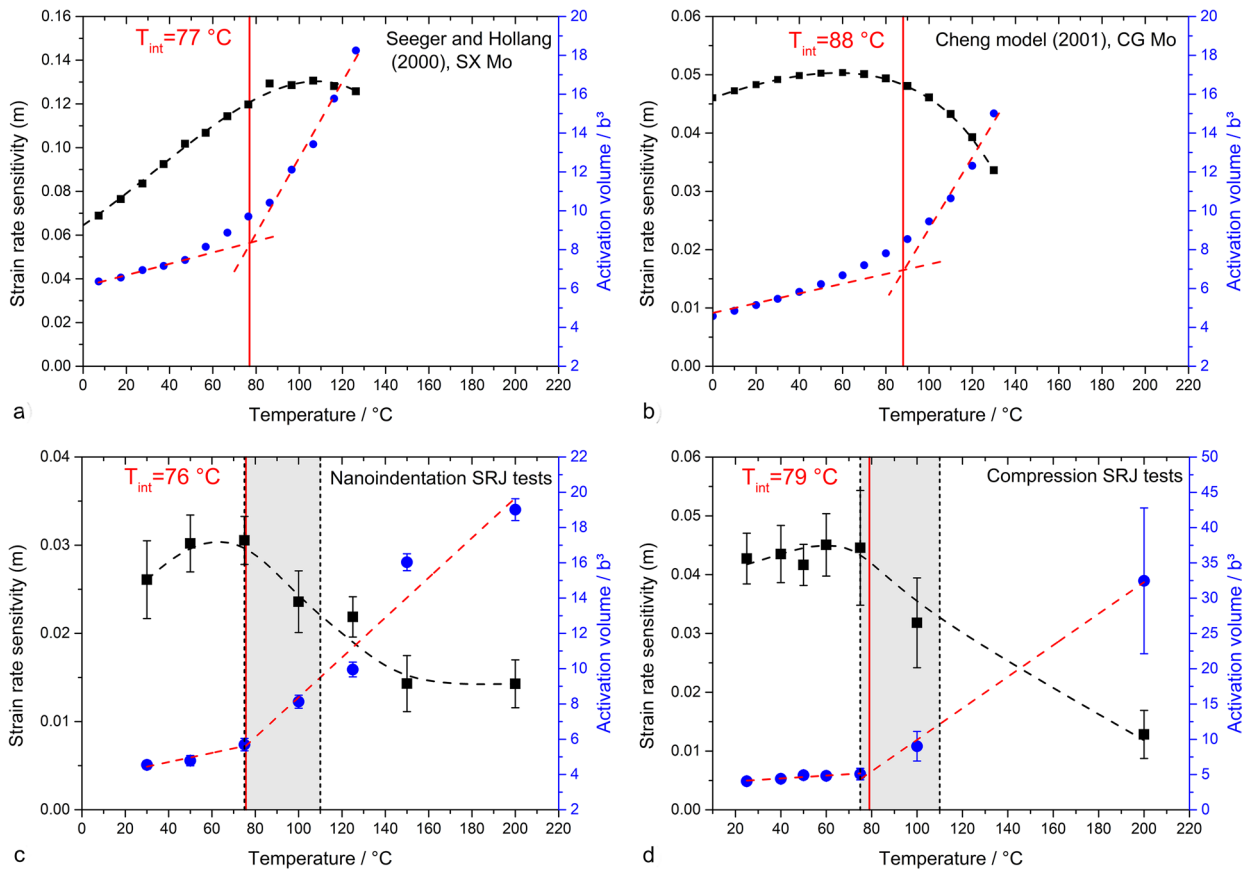


**Figure 6:** Determination of the intersection temperature for (a) SX Mo data from Seeger and Hollang [6], (b) Cheng–Nemat-Nasser model [8, 9], (c) nanoindentation strain rate jump tests and (d) compression strain rate jump tests. The brittle to ductile transition range from Charpy V-notch impact testing is highlighted in gray for comparison.

below  $T_k$ , so it has to be questioned how the BDTT is related to  $T_k$  and  $T_{int}$ . At temperatures below  $T_{int}$ , activation volumes of  $V \leq 5 b^3$  are found, which can be linked to a kink mechanism [43]. At temperature above  $T_k$ , the thermal energy alone is sufficient to overcome the Peierls barrier, the thermal component of the yield stress disappears (Fig. 1) and the mobility of screw and edge dislocations becomes equal [12, 19].

The  $T_{int}$  is thus close to the onset of the BDTT and the very good agreement of literature data and the data provided here make us confident that by analyzing the intersection of the activation volumes an estimate of the BDTT can be provided.

It should be noted, however, that this rather simple analysis procedure can only give an approximation of the brittle to ductile transition temperature. The temperature-dependent course of  $V$  can only be described with a linear fit to some extent. As shown in Fig. 6c, d, the data of this study show a well-defined change in  $V$  with increasing  $T$ , while the literature data (Fig. 6a, b) show a rather continuous transition. This complicates the definition of appropriate fitting functions.

This discussion clearly shows that the SRS coefficient can only provide a qualitative description of the thermally activated processes. A much better understanding of the deformation mechanisms can be achieved by comparing the activation volumes, since in that case the SRS is normalized by the flow stress and therefore independent of the stress state. Furthermore, the activation volume can be directly related to the spacing between the obstacles, i.e., the smaller the distance between obstacles, the lesser will be the activation volume and vice versa [45, 46]. Thus, the thermally activated mobility of screw dislocations is reflected in the activation volume. At low temperatures, the high Peierls stress does not allow the motion of dislocations and kinks must be nucleated for the dislocations to move resulting in a low activation volume of the order of  $5 b^3$ . At high temperatures, the deformation is controlled by the motion of kink pairs thereby resulting in a higher activation volume ( $> 20 b^3$ ) as shown in Fig. 5b. This is in agreement with literature data [8]. For tungsten, an increase in  $V$  to about  $200 b^3$  was observed at

$T > T_k$ , indicating dislocation interactions as observed in face-centered cubic materials [42, 43].

The most interesting finding of the present work is that irrespective of the testing method and stress state—triaxial indentation and uniaxial compression testing—a similar change in the activation volume is observed with an increase in test temperature. This clearly shows that the fundamental deformation mechanism controlling plastic deformation is the same in all the testing methods and the activation volume is the controlling parameter, which must be analyzed to compare the different test methods. The applied strain rates during impact testing are significantly larger than those employed during conventional indentation testing. However, the stress triaxiality during impact testing and the plastic zone underneath the indenter tip are quite similar.

The different methods differ not only in the stress state and the applied strain rate, but also in the microstructure being tested. Seeger and Hollang have performed experiments on single-crystalline Mo and thus obtain best data for the movement of screw dislocations, while Nemat-Nasser et al. have investigated polycrystalline Mo. These results are influenced by the different crystal orientations and grain boundaries. The results of the impact and compression tests carried out in this work are also influenced by grain boundary effects due to the size of the plastic zones. This is not necessarily the case for nanoindentation testing, as the probed volumes are small in respect to the grain size. In consequence, the information is obtained from individual grains or from a small number of grains depending on the grain size of the tested material. Thus, the influence of boundary effects is not as pronounced as in the other testing methods carried out in this study.

It could be assumed that, in general, the indentation technique provides more reliable results than tensile or compression testing. This is especially the case for highly anisotropic materials, as there the hardness is less influenced by the grain structure and texture due to the triaxial stress state inside the plastic zone. Although the indentation data are less dependent on crystal orientation than uniaxial test results, the orientation can still affect  $m$ ,  $H$  and in consequence the activation volume as these parameters depend on the number of active slip systems [43]. Thus, the intersection temperature is expected to depend on the crystal orientation. Furthermore, it has been shown in the literature that Mo exhibits only a marginal orientation-dependent hardness [47].

For the present data, the influence of crystalline orientation has not been specifically addressed. However, due to the small scatter in data, a strong influence of the crystal orientation on the determination of the brittle to ductile transition is not expected.

Recently, the development of non-ambient temperature nanoindentation systems has made significant progress. This opens the possibility for studying the BDT in a rather wide temperature range between  $-142$  and  $1100$  °C [48, 49].

In this study, the quasi-static tests show a slightly lower brittle to ductile transition temperature than Charpy impact tests with  $93.5$  °C [middle of the transition range ( $75$ – $110$  °C)]. This is in accordance with literature where a strain rate dependence of the BDTT was observed [15, 16, 26]. This phenomenon is due to an increase of the yield strength with increasing strain rate [26]. Additionally, a local temperature increase can occur within the plastic zone, which is more pronounced for high deformation rates, since the adiabatic energy generated by plastic deformation cannot dissipate due to the short time scale. This effect can also cause a small shift in the transition temperature. Furthermore, the determination of an exact transition temperature by using impact testing is only possible to a limited extent due to the scattering of the data. It is therefore more favorable to specify a temperature range for the BDT. This shows a further advantage of the methodology presented here, where the increase in activation volume provides a clear indication of the BDT and thus a more precise, strain rate-dependent BDTT can be determined.

## Conclusions

The active deformation mechanisms in bcc Mo have been investigated using different mechanical testing approaches and following conclusions could be drawn:

1. The absolute value of strain rate sensitivity parameter ( $m$ ) for bcc metals is dependent on the net flow stress. An increase in athermal component with grain boundary strengthening leads to a lower value of  $m$  and vice versa.
2. Indentation and compression SRJ tests show a low strain rate sensitivity in the brittle regime. It increases with temperature to a maximum at the onset of the brittle to ductile transition before decreasing in the ductile regime.
3. The significant increase in the activation volume can be used in order to determine the brittle to ductile transition temperature and gives information about the active deformation mechanism. In addition, unlike yield stress/hardness and strain rate sensitivity, it is independent of the microstructure and test method, since it depends only on the distance between thermal obstacles.
4. High-temperature nanoindentation strain rate jump tests can be used as a complementary approach to Charpy impact testing for investigating active deformation mechanisms

and for estimation of the brittle to ductile transition temperature.

## Material and methods

Polycrystalline Mo with a purity of 99.97% was purchased from Plansee GmbH as 5-mm-thick hot-rolled plates. The main impurities were tungsten (< 300 µg/g), oxygen (< 40 µg/g) and carbon with (< 30 µg/g). These samples had a grain size of 125 µm in the texture direction and a grain size of 37 µm perpendicular to the texture direction.

Nanoindentation strain rate jump tests [37, 38] were performed using the load-controlled G200 nanoindenter (Keysight technologies, USA) equipped with a diamond Berkovich tip and a Laser heating set-up (both from Surface System Technology, Germany) for testing up to 500 °C. The sample and the indenter tip could be heated independently with a temperature stability of 0.1 °C. A temperature adjustment procedure that ensures the accuracy of the tip and sample temperature is required for reliable measurements with low thermal drift rates at high temperatures [50]. The tip was therefore used as a probe by heating it with a constant laser power. Afterwards the sample temperature was adjusted until the change in tip temperature during contact with the sample was less than or equal to 0.1 K. At least six tests were performed at 30, 50, 75, 100, 125, 150 and 200 °C. The test locations were chosen arbitrarily; nevertheless mainly the interior of different orientated grains was tested. Forming gas (VARIGON H5, Linde, Germany) was used to prevent oxidation of the tip and sample. Strain rate jump tests were used to investigate the thermally activated mechanisms by varying the applied strain rate in the range 0.05 s<sup>-1</sup> to 0.001 s<sup>-1</sup>.

All indentation tests were performed on the same sample which was polished using the conventional metallographic polishing techniques followed by etching with a solution of 20 ml H<sub>2</sub>O<sub>2</sub> (30%) and 10 ml H<sub>2</sub>SO<sub>4</sub> (95%) in 70 ml deionized water. Finally, the deformation layers—induced by mechanical polishing—were removed by vibrational polishing using an oxide particle-based solution.

Rectangular samples with dimensions of 4 × 4 × 8 mm<sup>3</sup> were machined and polished plane-parallel for compression testing. Compression strain rate jump tests were performed using Z030 load frame (Zwick/Roell, Germany); it was equipped with a LVDT displacement sensor and a heating chamber, thus enabling measurements at 25, 40, 50, 60, 75, 100 and 200 °C. A preload of 250 N was applied to the samples before heating to the test temperature. The temperature was kept constant for 10 min before starting the test. This ensures a good thermal stability of the system. The strain rates during the jump tests consisted of 0.008 s<sup>-1</sup> till a displacement of 45 µm (0.5% ε), 0.0008 s<sup>-1</sup> till 75 µm (0.9% ε), 0.008 s<sup>-1</sup> to 105 µm (1.3% ε) and 0.08 s<sup>-1</sup> till

165 µm (2% ε). Further details about the machine set-up and control of strain rate can be found in [51].

Miniaturized Charpy V-notch impact tests (KLST) were used to investigate the brittle to ductile transition at high strain rates. Impact tests were performed at Karlsruhe Institute of Technology (IAM-WBM) at different temperatures between – 100 and 250 °C. The specimens were designed according to DIN 50,115. A notch with tip radius of 0.1 mm and opening angle of 60° was machined in at the middle of the rectangular specimen with dimension of 27 × 4 × 3 mm<sup>3</sup>. Impact tests were carried out using an impact testing device (Zwick/Roell, Germany) with an impact energy of 25 J resulting in an impact velocity of 3.85 m/s. The striker radius is 2 mm and the spacing between the supports is 22 mm. The system enables an automatic specimen cooling, heating and transporting in a test temperature range between – 180 and 600 °C.

## Acknowledgments

The authors gratefully acknowledge Dr. Ermile Gaganidze and Dr. Jarir Aktaa (both Karlsruhe Institute of Technology, Institute for Advanced Materials (IAM-WBM)) for the great support and for providing test equipment to perform the Charpy impact tests at elevated temperatures. Furthermore, Dr. Enrico Bruder, Dr. Sebastian Bruns, Dr. Kurt Johanns and Golo Zimmermann are thanked for experimental support. Deutsche Forschungsgemeinschaft (DFG) is gratefully acknowledged for financial support within the project No. 326946902. Additional financial support was provided by the Open Access Publication Fund of the Technical University of Darmstadt.

## Data availability

The data are available upon reasonable request from the corresponding author (C.M.).

## Compliance with ethical standards

**Conflict of interest** The authors declare no conflict of interests.

## Open Access

This article is licensed under a Creative Commons Attribution 4.0 International License, which permits use, sharing, adaptation, distribution and reproduction in any medium or format, as long as you give appropriate credit to the original author(s) and the source, provide a link to the Creative Commons licence, and indicate if changes were made. The images or other third party material in this article are included in the article's Creative Commons licence, unless indicated otherwise in a credit line to the material. If material is not included in the article's Creative Commons licence and your intended use is not permitted

by statutory regulation or exceeds the permitted use, you will need to obtain permission directly from the copyright holder. To view a copy of this licence, visit <http://creativecommons.org/licenses/by/4.0/>.

## References

1. D. Hull, D.J. Bacon, Chapter 6—dislocations in other crystal structures, in *Introduction to Dislocations*, 5th edn., ed. by D. Hull, D.J. Bacon (Butterworth-Heinemann, Oxford, 2011), pp. 109–136
2. V. Vitek, F. Kroupa, Dislocation theory of slip geometry and temperature dependence of flow stress in BCC metals. *Phys. Status Solidi B* **18**(2), 703–713 (1966)
3. T. Suzuki, S. Takeuchi, H. Yoshinaga, Dislocations in bcc metals and their motion. in *Dislocation Dynamics and Plasticity*. (Springer, New York, 1991), pp. 77–98
4. V. Vitek, Core structure of screw dislocations in body-centred cubic metals: relation to symmetry and interatomic bonding. *Philos. Mag.* **84**(3–5), 415–428 (2004)
5. M.S. Duesbery, G.Y. Richardson, The dislocation core in crystalline materials. *Crit. Rev. Solid State Mater. Sci.* **17**(1), 1–46 (1991)
6. A. Seeger, L. Hollang, The flow-stress asymmetry of ultra-pure molybdenum single crystals. *Mater. Trans., JIM* **41**(1), 141–151 (2000)
7. V. Maier et al., Microstructure-dependent deformation behaviour of bcc-metals—indentation size effect and strain rate sensitivity. *Philos. Mag.* **95**(16–18), 1766–1779 (2015)
8. S. Nemat-Nasser, W. Guo, M. Liu, Experimentally-based micro-mechanical modeling of dynamic response of molybdenum. *Scripta Mater.* **40**(7), 859–872 (1999)
9. J. Cheng, S. Nemat-Nasser, W. Guo, A unified constitutive model for strain-rate and temperature dependent behavior of molybdenum. *Mech. Mater.* **33**(11), 603–616 (2001)
10. D.H. Lassila, A. Goldberg, R. Becker, The effect of grain boundaries on the athermal stress of tantalum and tantalum-tungsten alloys. *Metall. Mater. Trans. A* **33**(11), 3457–3464 (2002)
11. G. Testa et al., Flow stress of bcc metals over a wide range of temperature and strain rates. *Metals* **10**(1), 120 (2020)
12. C. Bonnekoh et al., The brittle-to-ductile transition in cold rolled tungsten plates: impact of crystallographic texture, grain size and dislocation density on the transition temperature. *Int. J. Refract Met. Hard Mater.* **78**, 146–163 (2019)
13. A. Seeger, Why anomalous slip in body-centred cubic metals? *Mater. Sci. Eng. A* **319–321**, 254–260 (2001)
14. L. Hollang, M. Hommel, A. Seeger, The flow stress of ultra-high-purity molybdenum single crystals. *Phys. Status Solidi A* **160**(2), 329–354 (1997)
15. A. Hartmaier, P. Gumbsch, Thermal activation of crack-tip plasticity: the brittle or ductile response of a stationary crack loaded to failure. *Phys. Rev. B* **71**(2), 024108 (2005)
16. P. Gumbsch et al., Controlling factors for the brittle-to-ductile transition in tungsten single crystals. *Science* **282**(5392), 1293–1295 (1998)
17. A.A.N. Németh et al., The nature of the brittle-to-ductile transition of ultra fine grained tungsten (W) foil. *Int. J. Refract Met. Hard Mater.* **50**, 9–15 (2015)
18. A.Y. Koval, A. Vasilev, S. Firstov, Fracture toughness of molybdenum sheet under brittle-ductile transition. *Int. J. Refract Met. Hard Mater.* **15**(4), 223–226 (1997)
19. B.G. Butler et al., Mechanisms of deformation and ductility in tungsten—a review. *Int. J. Refract Met. Hard Mater.* **75**, 248–261 (2018)
20. F. Fang, Y.Y. Zhou, W. Yang, In-situ SEM study of temperature dependent tensile behavior of wrought molybdenum. *Int. J. Refract Met. Hard Mater.* **41**, 35–40 (2013)
21. A.S. Wronski, A.A. Johnson, The deformation and fracture properties of polycrystalline molybdenum. *Philos. Mag.* **7**(74), 213–227 (1962)
22. A.S. Wronski, A.C. Chilton, E.M. Capron, The ductile-brittle transition in polycrystalline molybdenum. *Acta Metall.* **17**(6), 751–755 (1969)
23. L.P. Loshmanov, P.V. Fedotov, Effect of the strain rate on the mechanical properties of metalceramic molybdenum in the ductile-brittle transition temperature range. *Russ. Metall.* **2009**(5), 412–415 (2009)
24. J. Wadsworth et al., A microstructural investigation of the origin of brittle behavior in the transverse direction in Mo-based alloy bars. *Metall. Trans. A* **15**(9), 1741–1752 (1984)
25. T. Takida et al., Mechanical properties of fine-grained, sintered molybdenum alloys with dispersed particles developed by mechanical alloying. *Mater. Trans.* **45**(1), 143–148 (2004)
26. Y. Hiraoka et al., Fracture and ductile-to-brittle transition characteristics of molybdenum by impact and static bend tests. *Mater. Trans., JIM* **36**(4), 504–510 (1995)
27. K. Babinsky et al., Fracture behavior and delamination toughening of molybdenum in Charpy impact tests. *Jom* **68**(11), 2854–2863 (2016)
28. R.A. Wullaert, *Applications of the Instrumented Charpy Impact Test Impact Testing of Metals* (West Conshohocken, ASTM International, 1970), p. 164
29. *Standard Test Methods of Compression Testing of Metallic Materials at Room Temperature*.
30. A.C. Fischer-Cripps, *Introduction to Contact Mechanics*, vol. 101 (Springer, New York, 2007).
31. E. Bitzek, P. Gumbsch, Mechanisms of dislocation multiplication at crack tips. *Acta Mater.* **61**(4), 1394–1403 (2013)
32. P. Gumbsch, Brittle fracture and the brittle-to-ductile transition of tungsten. *J. Nucl. Mater.* **323**(2–3), 304–312 (2003)

33. H. Kurishita et al., Misorientation dependence of grain boundary fracture in molybdenum bicrystals with various  $\langle 110 \rangle$  twist boundaries. *Trans. Jpn. Inst. Met.* **26**(5), 332–340 (1985)
34. S. Tsurekawa, T. Tanaka, H. Yoshinaga, Grain boundary structure, energy and strength in molybdenum. *Mater. Sci. Eng. A* **176**(1–2), 341–348 (1994)
35. K. Leitner et al., On grain boundary segregation in molybdenum materials. *Mater. Des.* **135**, 204–212 (2017)
36. K. Leitner et al., Grain boundary segregation engineering in as-sintered molybdenum for improved ductility. *Scripta Mater.* **156**, 60–63 (2018)
37. V. Maier et al., Nanoindentation strain-rate jump tests for determining the local strain-rate sensitivity in nanocrystalline Ni and ultrafine-grained Al. *J. Mater. Res.* **26**(11), 1421–1430 (2011)
38. K. Durst, V. Maier, Dynamic nanoindentation testing for studying thermally activated processes from single to nanocrystalline metals. *Curr. Opin. Solid State Mater. Sci.* **19**(6), 340–353 (2015)
39. G.M. Pharr, E.G. Herbert, Y. Gao, The indentation size effect: a critical examination of experimental observations and mechanistic interpretations. *Annu. Rev. Mater. Res.* **40**, 271–292 (2010)
40. K. Durst et al., Indentation size effect in metallic materials: modeling strength from pop-in to macroscopic hardness using geometrically necessary dislocations. *Acta Mater.* **54**(9), 2547–2555 (2006)
41. W.D. Nix, H. Gao, Indentation size effects in crystalline materials: a law for strain gradient plasticity. *J. Mech. Phys. Solids* **46**(3), 411–425 (1998)
42. D. Brunner, V. Glebovsky, Analysis of flow-stress measurements of high-purity tungsten single crystals. *Mater. Lett.* **44**(3–4), 144–152 (2000)
43. D. Kiener et al., Rate limiting deformation mechanisms of bcc metals in confined volumes. *Acta Mater.* **166**, 687–701 (2019)
44. V. Trefilov, Y.V. Milman, I. Gridneva, Characteristic temperature of deformation of crystalline materials. *Cryst. Res. Technol.* **19**(3), 413–421 (1984)
45. U. Kocks et al., *Prog. Mater. Sci.* **19**, 1–281 (1975)
46. D. Caillard, J.L. Martin, *Thermally Activated Mechanisms in Crystal Plasticity*. Pergamon Materials Series, ed. R.W. Cahn. vol. 8 (2003)
47. S. Jakob et al., Influence of crystal orientation and Berkovich tip rotation on the mechanical characterization of grain boundaries in molybdenum. *Mater. Des.* **182**, 107998 (2019)
48. A. Barnoush et al., In situ small-scale mechanical testing under extreme environments. *MRS Bull.* **44**(6), 471–477 (2019)
49. C. Minnert, W.C. Oliver, K. Durst, New ultra-high temperature nanoindentation system for operating at up to 1100 °C. *Mater. Des.* **192**, 108727 (2020)
50. J.M. Wheeler et al., High temperature nanoindentation: the state of the art and future challenges. *Curr. Opin. Solid State Mater. Sci.* **19**(6), 354–366 (2015)
51. E.A. Patterson et al., Temperature-dependent deformation and dislocation density in SrTiO<sub>3</sub> (001) single crystals. *J. Am. Ceram. Soc.* **99**(10), 3411–3420 (2016)